CRANFIELD INSTITUTE OF TECHNOLOGY

SCHOOL OF MECHANICAL ENGINEERING

Ph.D THESIS

Academic Year 1990-91

R I RAWLINSON-SMITH

Computational Study of Stalled Wind Turbine Rotor Performance

Supervisors: R L Hales & Professor J B Moss

January 1991

SUMMARY

Simplification of the aerodynamic control of large horizontal axis wind turbines (HAWTs) has been identified as an important step towards improved reliability and reduced cost. At present the majority of large HAWTs use active control to regulate power and loads. A simpler strategy is to use the inherent stalling of the rotor blades in high winds to limit power and loads.

Unfortunately the performance of stall regulated HAWTs is poorly understood; current performance models often fail to correctly predict peak power levels. The benefits of passive control of power and loads cannot be utilised because of this uncertainty.

This study examines the possible reasons for the poor performance of current prediction techniques in high winds with the objective of formulating a new model.

The available experimental evidence suggests that rotor stall is caused by turbulent separation at the rear of the blade aerofoil, growing in extent from the root in increasing wind. This 'picture' of the stalling HAWT rotor forms the basis of the approach. The new model consists of a prescribed vortex wake, first order panel method (extended to represent the viscous region of trailing edge separation) and three dimensional integral boundary layer directly coupled in an iterative scheme.

A sensitivity study of rotor performance to wake geometry indicates that the most important factor is the rate at which the wake is convected downstream. However, it is found that stalled power levels are insensitive to wake geometry; the study concludes that the problem of poor prediction of high wind performance lies on the rotor blades.

Before using the complete code to calculate the performance of a rotor it is first tuned for the aerofoils used on the blade. Aerofoil performance characteristics measured in a wind tunnel are synthesised by the model. Ideally these characteristics should include measured pressure profiles below and above stall.

Validation of the complete code against detailed measurements taken under controlled conditions on a three metre diameter machine indicates significant differences in the performance of aerofoil sections on a wind turbine blade when compared to the same section when tested in a wind tunnel. Derived lift coefficients show a reduced lift curve slope and more gentle delayed stall.

Similar results are found when the code is applied to two Danish stall regulated machines. These two machines although having very similar geometries and using the same family of aerofoils do however show differences in derived post stall drag. This is thought to be due to the different thickness distributions of the two rotors.

The validation and applications of the new model show that it can accurately predict the peak power level of stall regulated machines.

CONTENTS

TABLES

FIGURES

TABLES

FIGURES

ACKNOWLEDGEMENTS

Many people have given me assistance during the execution of this project and my heartfelt thanks go to all of them.

In particular, Richard Hales, my supervisor, provided guidance, constructive criticism and obtained funding for the work.

Also Professor Barrie Moss who read the initial drafts of this thesis and therefore aided me in its presentation.

And my wife, Julie, who has given me constant support and encouragement, particularly towards the end of the project.

This work was performed under contract to the United Kingdom Department of Energy.

CHAPTER 1. INTRODUCTION

Wind energy has become an integral part of European Community energy policy, [1.1], and has demonstrated its ability to provide bulk quantities of electricity as an alternative to fossil fuel plants in the United States of America, [1.2].

The development of commercial wind turbines began at the small scale and is progressing through medium and now on to large scale. The overriding concern in the research and development effort is to reduce the cost of energy produced by wind turbines.

Simplification of the aerodynamic control of large horizontal axis wind turbines (HAWTs) has been identified as an important step towards improved reliability and reduced cost.

1.1 Pitch regulation

At present the majority of large HAWTs use some form of pitch mechanism to turn all or part of the blades in and out of the wind to limit aerodynamic loading. For instance, full span pitch control which at low windspeeds optimises the energy capture of the rotor by altering the rotor blade pitch angle whilst in high winds the pitch angle is set to limit the power to the rated value preventing generator overload. The mechanisms used for pitch control require actuators, bearings and some form of control system; all of which add to the cost and complexity of the wind turbine rotor.

1.2 Stall regulation

One alternative to the pitch controlled rotor is the design of fixed pitch blades for stall regulation, the torque and loading in increasing winds being inherently governed by the progressive stalling of the blade from root to tip. This means of passive control simplifies the rotor reducing its weight and cost. Experience of stall regulation at medium scale, [1.3], has also indicated reductions in fluctuating loads in high winds which leads to increased fatigue life.

Therefore, if proved feasible at large scale, stall regulation would lead to structural and mechanical simplification, and hence reductions in weight and cost. However, active control will only be relinquished if there is sufficient confidence in the predictive methods to ensure benign behaviour of a fixed pitch rotor at low tip speed ratios. Unfortunately, such a high level of confidence cannot be supported by experience; a study, [1.4], of stall regulated Danish wind turbines contained the observation that while some machines have excellent stall properties, there are others which do not limit power and loads satisfactorily. The study reported in [1.3] also highlighted the difficulties of predicting the performance of a stall regulated rotor. A further uncertainty is the reduction in rotor efficiency caused by the use of passive control; power curves of stall regulated machines show a gradual reduction in slope around rated windspeed (see Figure 1.1) whereas the power curve of an equivalent pitch regulated machine has a sharp cut off at rated power.

Improved performance prediction at stall would allow more confident design, allowing the full benefits of stall regulation to be utilised.

1.3 Current performance prediction techniques

Most aerodynamic performance/structural load prediction methods for HAWTs use 2D aerofoil data with the assumption that a blade is made up of elements operating in independent streamtubes unaffected by their neighbours. This blade element method is often coupled to a momentum balance (actuator disc theory) in order to take into account the velocities induced by the rotor wake. This method of combined blade element and momentum theory, colloquially known as strip theory, is computationally straightforward and can produce acceptable estimates of power and loads under most operating conditions.

However, one important deviation is in high winds where all or part of the rotor blade (starting at the root) is stalled. In this area strip theory methods tend to underpredict power (Figure 1.1).

The tendency, using current prediction techniques, to poorly predict power in the stalled regime would indicate that the complex, three dimensional, rotor flowfield has a significant effect on the aerodynamic response which is not adequately modelled in terms of independent streamtubes.

The general point may be made that 'any uncertainty has to be covered by increased design margins and hence excessive machine costs'. The underprediction problem being especially significant if the machine has no blade pitch mechanism: if the inherent blade stall does not adequately limit power in this case, then all solutions (e.g. shutdown, slowdown, yawing or spoiling) will offset the benefits of stall regulation.

Not all of the difficulties associated with the use of stall regulation are due to poor aerodynamic performance prediction; Jamieson, [1.5], indicates that the peak power and loads of a stall regulated wind turbine can be significantly affected by small changes in rotor r.p.m., diameter and pitch setting which can fall prey to poor implementation of a design in the manufacturing and assembly phases. However, there is still an overriding need for accurate prediction of HAWT aerodynamic performance to obtain the full benefits of stall regulation.

1.4 Project objective

The current use of combined blade element and momentum theory in the design of HAWTs does not give consistent prediction of the performance of fixed pitch rotors for stall regulated operation.

The production of a refined and validated model of the performance of a stalled wind turbine rotor, implemented as a suite of computer programmes, in steady axial flow is the objective of the work described here. The new model will make use of more complex computational tools, treating the problem in three dimensions and including solutions of both the inviscid outer flow and viscous boundary layer flow.

The model should allow the aerodynamic design of a medium to large scale fixed pitch rotor to be tackled with confidence.

CHAPTER 2. AERODYNAMIC PERFORMANCE OF HAWTS AND PREDICTION METHODS

As stated in Chapter 1 the most common basis for HAWT performance prediction codes is combined blade element and momentum theory, colloquially known as strip theory.

According to Glauert, [2.1], strip theory methods are based upon the following assumptions

* the behaviour of a blade element is not affected by the adjacent elements of the same blade,

* two dimensional (wind tunnel) aerofoil characteristics can be used for the element.

The classical wake model used is based on the following statement

* the effective velocity of the element through the air is the resultant of the axial velocity and the rotational velocity less an allowance for the induced velocity estimated on the basis of a lightly loaded rotor (no slipstream expansion) with infinitely many blades.

The application of this approach is discussed by de Vries, [2.2]; the method has been encoded as a computer program by several groups, notably the PROP code of Wilson, Lissaman and Walker, [2.3], and its descendants such as PROPSH by Tangler, [2.4] and PROP (revised) by Hibbs and Radkey, [2.5].

These methods are computationally straightforward and provide accurate results for the majority of the operating regime of a HAWT. However, in high winds, where the rotor is partially or wholly stalled, strip theory methods often underpredict rotor power. The possible reasons for this poor prediction of high wind performance have been the subject of experimental and theoretical examination for some time.

The performance prediction problem can be split into two parts; firstly the modelling of the wake and secondly, the factors affecting the performance of the aerofoil sections making up the rotor blades.

These two areas of rotor performance are discussed. The way in which they are modelled in various prediction codes and the observed behaviour of the rotor flowfield are examined. The shortcomings of present prediction techniques, particularly at stall, will thus be highlighted.

2.1 Wake Modelling

A rotor blade when generating lift can be considered as a line vortex with varying strength equal to the local bound circulation. Since a line vortex can only end at a wall, this line of varying vorticity produces a helical vortex sheet from the trailing edge of each blade, convected downstream at the wake velocity. These sheets comprise (see Figure 2.1):

* the trailing vortex system of helical vortex lines normal to the rotor blade's trailing edge, associated with the spanwise change of circulation along the blade,

* the shed vortex system of radial vortex lines parallel to the trailing edge, associated with azimuthal changes in bound circulation due to flow unsteadiness or yaw.

This study will only consider steady, axial flow and so only the trailing vortex system need be included in any wake model.

The effect of the HAWT rotor on the fluid can be represented as the induced velocity of this complete vortex system.

The various components and features of the wake are discussed in the light of currently available wake models.

It should be noted that the form of the wake in high winds is expected to be helical. The turbulent wake and vortex ring states (Glauert, [2.1]), characterised by reversed flow in the wake of the rotor, are only expected to occur for low blade pitch settings and at low windspeeds, when the thrust on the rotor is incompatible with the momentum lost by the fluid.

Strip theory methods, [2.3], [2.4], [2.5], use actuator disc theory which models the vortex system as an infinite number of vortex rings distributed along a cylinder generated by a blade element; this is valid for the case of a large number of lightly loaded blades.

Other models of the rotor wake, [2.6], [2.7], [2.8], [2.9], [2.10], [2.11] (collectively known as vortex wake models), have been produced which attempt to more realistically represent its physical aspects. The physical representation of the rotor wake has two areas of consideration;

* the elements over which the wake vorticity is to be distributed

* the wake geometry

The elements used in vortex wake models, [2.6], [2.7], [2.8], [2.9], [2.10], [2.11], vary from straight line vortex filaments to vortex sheets and cylinders depending on the complexity of the model and the method used to deal with the singularities, Figures 2.2 and 2.3. The exact distribution of the vorticity amongst the elements is dependent upon the blade bound circulation distribution and the roll-up of vorticity , especially near the tip. Lowson & Brocklehurst, [2.12], have emphasised the importance of a discrete tip vortex that forms due to roll-up of vorticity in the wake.

Due to lack of quantitive experimental evidence for use in wake models three types of geometry definition are used

* A free wake calculation which allows the geometry of the wake to develop under the mutual influence of the wake elements

* A prescribed wake in which the exact geometry of the wake form part of the input to the model

* A rigid wake in which negligible expansion is assumed and the wake is convected downstream at freestream velocity (this is of course covered by the term prescribed wake but forms a special case within that definition)

Both the UTRC 'Wecsper' model, [2.6], and the Toledo University 'helical vortex method', [2.7], utilise a rigid wake analysis as it provides a simple first step to realistically model the constituent elements of the wake. In these methods the wake consists of a series of straight line vortices trailing from the rotor blades which describe constant pitch and diameter helices. The vortices are assumed to trail from the junctions between adjacent blade elements and their vorticity is defined by the blade bound circulation gradients. The Biot-Savart law is used to calculate the velocities induced at the rotor plane.

When compared to strip theory methods, e.g. [2.7], the results using these rigid wake analyses show very similar results with some improvement in performance prediction in light winds.

Since the turbine extracts energy from the wind, it may be expected that the flow is retarded and expands. The thrust on the rotor is directly related to the momentum extracted from the wind; the greater the rotor loading the greater the retardation and wake expansion. But in strip theory wake expansion is neglected because the rotor is assumed to be multi-bladed and therefore lightly loaded. This assumption is used in the derivation of the axial momentum equation and in both the Prandtl and Goldstein tip loss corrections, see section 2.2. In practice, however, a wind turbine rotor has only one, two or three blades, suggesting that the light loading assumption is invalid.

The wake helix angle is dependent on the transport velocity of the wake and the rotational velocity imparted to the wake by the rotor. In rigid wake analyses, it is assumed that this is constant and that the helical vortex is convected downstream with constant pitch and helix angle along the slipstream. For the propeller, Bocci & Morrison, [2.13], have suggested the use of a true wake helix angle which accounts for the induced velocities at the rotor (Figure 2.4).

Flow visualisation reported by Savino and Nyland, [2.14], has indicated the presence of wake expansion at low windspeeds. However, as windspeed increases (and rotor efficiency decreases) the expansion decreases and for most of the operating range the tip vortex forms a helix of diameter equal to that of the rotor, these observations are in line with those detailed in [2.15].

Afjeh and Keith, [2.8], extended the helical vortex method to a prescribed wake analysis in order to model expansion of the wake through the rotor. Noting the lack of experimental data regarding wake expansion they calculated the wake expansion from a momentum balance and used an exponential function to define the expansion rate. They found that (as may be expected) to obtain correlation with experimental results the rate of expansion must be varied with rotor geometry and operating conditions. It was found that prediction of rotor power showed some dependence on the wake expansion rate. The results presented show the code to perform well in light to moderate winds, which is consistent with the observations in [2.14] and [2.15], but do not go into stall.

A free wake analysis, [2.10], requires many wake elements and that the velocity field in the wake be well defined which results in a complicated and time consuming iterative calculation. Due to this complexity full free wake analyses are rarely used for performance prediction work; their computational expense outweighing the improvement in results. Simplified free wake analyses, [2.11], see Figure 2.3, have been shown to compare favourably with more complete codes. These methods simplify the calculation by reducing the number of wake elements to a few (less than 10, say) line or ring vortices rather than considering the vorticity to be distributed amongst many elements. When free wake results are compared with experiment, [2.11], good agreement is found in light to moderate winds. However, Miller, [2.16], reports that to obtain good correlation in high winds the input data to the blade element model requires modification, Figure 2.5.

Most wake models assume a semi-infinite helical wake. Other prescribed wake models , e.g. [2.8], use only the part of the wake which makes substantial difference to velocities induced at the rotor. The overall effect of the rotor wake is dependent on how long its structure remains coherent. Flow visualisation , [2.14], [2.15], has shown the wake structure to remain intact approximately two diameters downstream of the rotor. The breakup of any coherent structure signifies the end of any quantifiable effect on the induced velocities at the rotor.

2.1.1 Conclusions

There is presently little evidence to support any alternative to the assumption of a helical rotor wake, particularly in high winds. Also little consensus exists in the way the elements of a vortex wake should be represented. Further, the assumption of a semi-infinite wake appears to overestimate the coherent structure of the wake.

A study of the sensitivity of predicted performance to wake geometry, vorticity distribution and wake dissipation would allow more informed debate.

2.2 Blade Aerodynamic Performance

Blade element models, [2.3] [2.4], [2.5], assume independent blade elements to behave as two dimensional aerofoils. They use wind tunnel test data to define the behaviour of the blade elements.

2.2.1 Rotating blade performance

The performance of aerofoils on rotating blades has been studied in several experiments.

Himmelskamp, [2.17], found considerable differences in the performance of aerofoils on a two bladed impeller. At the inboard stations near the root he found increased Cl_{max} with this effect being inversely proportional to radial station, Figure 2.6. However a number of experimental uncertainties are associated with the high values of lift found in the blade root region, as discussed by Himmelskamp himself, the most significant of these are :

* the pressure and force coefficients at each blade element require a knowledge of the local air velocity; this was derived from a strip theory calculation which depends on knowledge of the aerofoil section behaviour;

* in order to convert the measured blade pressures into lift and drag a knowledge of the local incidence was required; uncertainty was associated with the measurement of this angle;

* surface friction was neglected as only pressure measurements were used;

* the portion of the blade near the root was 'subject to the considerable influence of the hub flow';

* over the Reynolds number range in question (0.12-0.36 million) the flat bottomed Gottingen 625 aerofoil section is dramatically Reynolds number sensitive, see [2.18].

Himmelskamp therefore wrote that the results should be regarded as being of a preliminary nature. He made a number of recommendations as to how the sensitive measurements might be improved.

Flow visualisation using threads showed evidence of a skewed boundary layer flow, with chordwise flow outside the boundary layer and outwardly radial flow developing inside the boundary layer towards the trailing edge. Himmelskamp explained the high values of lift in terms of a thinning of the boundary layer due to this radial flow.

An experimental study by Rebont et al, [2.19], showed correlation between the stalling incidence of a propeller blade and radial flows in its wake. The stall was found to be delayed when compared with two-dimensional data and the extent of this delay was related to the magnitude of radial flows. Radial flow in the wake can be caused by the presence of spanwise pressure gradients, tip and hub vortices. Blade element models neglect radial flows assuming only chordwise flow in the vicinity of the rotor.

Observations on the transition of the boundary layer on fan blades, [2.20], showed that compared to two dimensional wind tunnel tests transition was delayed on the suction surface of the blades. The authors suggested that this difference was caused by the existence of radial flow in the boundary layer. In addition, during the round table discussion at the Fluid Dynamics Symposium in Toronto, [2.21], Bass described a series of propeller experiments in which both blade tip Mach number and Reynolds number were held constant, varying only the rotational speed. Large differences in performance were observed which could, therefore, only be attributed to rotational effects.

Milborrow and Ross, [2.22], measured the angle of attack distribution and derived lift and drag on a model rotor using laser anemometry. These measurements indicated discrepancies between the lift and drag on the rotor when compared to wind tunnel data for the NACA 4415 section used on the rotor blades. They also looked at the boundary layer flow using tufts and found the flow to radially migrate particularly near the trailing edge of the blade where the flow was probably separated.

Savino and Nyland, [2.14], have suggested that the trailing edge separation line on a rotating blade is further forward than that expected from two-dimensional data. From flow visualisation studies they attempted to correlate observed separation position with wind tunnel data. They calculated the effective angle of attack for the rotating blade and found a discrepancy between the observed and expected separation positions of between ten and twenty percent chord. Similar observations have also been reported by Pedersen and Madsen, [2.23].

Apparent differences in aerofoil performance were also found on the 90m diameter MOD-2 wind turbine, [2.24], pressure distributions measured at 65% span suggested that the aerofoil section was providing more lift than would be expected for the aerofoil in two dimensions. Nyland estimated the local effective angle of attack using a blade element model and compared the measured pressure distributions for the rotor with those for the same aerofoil at the estimated angle of attack measured in a wind tunnel.

At Imperial College, [2.25], an experiment to investigate the effect of rotation on maximum lift coefficient used a two bladed, constant chord, untwisted rotor, tested in a wind tunnel settling chamber. Pressure distributions were measured at four spanwise stations. The NACA 23018 section used on the blade showed marked differences in its performance when compared with its behaviour in a wind tunnel. Near the blade root very high suction peaks were found to occur at local blade speed ratios where the sections would have been expected to have stalled. The mechanism causing this is not known.

At Southampton University, [2.26], a small rotor (1m diameter) with geometry representative of a real wind turbine has been tested at high rotational speed in order to achieve reasonably large Reynolds numbers. Measured pressure distributions indicate higher lift at the root sections and lower values near the tip than would be expected from a blade element analysis.

Workers from FFA in Sweden, [2.27], operated a 5m diameter wind turbine in a large wind tunnel (cross sectional area $192m^2$). No quantitive results are available to date due to uncertainties over tunnel blockage corrections. However, the authors do conclude that combined blade element and momentum theory over-predicts the loading at the blade tip.

At SERI, USA, [2.28], a 10m diameter rotor has been operated in the field with instantaneous measurement of pressure distributions, at 80% span, using a fast data acquisition system. This has allowed not only observations to be made on the steady performance of the rotor but also yawed operation. The steady measurements have indicated a slight drop in lift curve slope and reduction in Cl_{max} when compared to two dimensional performance for this radial station.

At Risø, Denmark, [2.29], a novel blade element technique is being used to directly measure blade forces at three spanwise positions. A five hole probe was used to measure the relative inflow velocities about one chord length ahead of the rotor blade. Tests have been carried out with the rotor blade stationary in high winds and also rotating in both axial and yawed flow conditions. Preliminary results suggest significant differences in the behaviour of the aerofoil sections on the rotor blade with similar results on the outboard stations as those found at SERI and increases in expected normal force near the root.

At Cranfield, [2.30], a 3m diameter rotor has been tested under controlled flow conditions with a fast data acquisition system measuring several rotor performance parameters including pressure distributions at two spanwise stations. A tentative comparison, [2.31], between the data from this experiment and that at Risø has shown good qualitative agreement in the measurement of normal force coefficient.

Studies performed at Risø laboratories, [2.32], on the Vestas 15 metre diameter HAWT have suggested that values of drag coefficients used in power prediction models are too high. Lift and drag coefficients were synthesised at each blade station in such a way that predictions of power and root bending moment closely fitted the measured data. The synthesised drag coefficients were substantially less than published two dimensional wind tunnel data over the whole range of incidence. However, the experimental and analysis details can only support this as a preliminary conclusion; in contrast, the impeller test of Himmelskamp, [2.17],and rotor test of Milborrow and Ross, [2.22], suggested that drag is increased on the rotor.

Attempts have been made to empirically correct the aerofoil performance data used as input to blade element codes, e.g. [2.33], [2.34], by generating aerofoil data to fit the measured performance of a particular rotor. However, these have failed to produce universal corrections due to geometry dependence. Rasmussen et al, [2.34], used measurements of power, thrust and flapwise bending moments to generate 'three dimensional' aerofoil coefficients for the 22m diameter Danwin 180 kW machine. Although these, highly modified, data showed very good agreement with all measurements, when they were applied to a geometrically very similar rotor of 17m diameter they were found to over-predict rotor power.

2.2.2 The use of two dimensional aerofoil characteristics

In the design of a rotor blade the section geometry is defined at a number of radial stations, with aerofoil section, chord and pitch angle specified. These designated stations are joined by smooth interpolation to form the entire blade. Therefore the exact section geometry is uncertain at intermediate stations. In order to perform a blade element calculation aerofoil performance characteristics are required at, say, ten spanwise stations. There is therefore uncertainty in defining appropriate aerofoil performance data. This is especially true in the root region where for structural reasons quite thick and/or truncated sections are used. Thick (in excess of 25% chord) and truncated sections have only recently been tested in the wind tunnel, [2.35], and then only at low angles of attack.

Due to radial chord and effective airspeed variation the blade Reynolds number changes with spanwise position, [2.36]. The range of variation depends on the size and speed of the turbine, but it is likely that the blade root region falls in the sensitive range of Reynolds number less than one million. In general a section's aerodynamic behaviour (lift curve slope, maximum lift, stall type and drag bucket) depend on Reynolds number. However aerofoils vary in their sensitivity to Reynolds number (Galbraith et al, [2.37]), so the variation along the blade has different effects for different sections. The work reported in [2.38] suggests that Reynolds number variation may have only a small effect on the stalled power of a wind turbine as post stall performance of the NACA 44xx sections tested is little affected by changes in Reynolds number. Any modifications to aerofoil performance can in fact be included in a blade element analysis at very little 'cost', [2.36].

Glauert, [2.1], quotes flat plate theory for a linear cascade indicating that for a typical wind turbine the lift curve slope at the root, where the high solidity of the rotor would suggest cascade like behaviour, may be increased by about 5 percent above the isolated aerofoil value. It thus appears that blade to blade interference could contribute to increased power at the root.

During operation, wind turbine blades become dirty due to insects, bird lime and the like, ,[2.39]. This introduces a surface roughness which results in degradation of the wind turbine performance and is difficult to emulate in wind tunnel testing of aerofoils.

In general, roughness on a lifting surface destabilizes the laminar boundary layer, promoting transition, and weakens the turbulent boundary layers resistance to adverse pressure gradients. These effects combine to reduce the maximum lift available from a particular section.

Experiments have been performed which have attempted to model the introduction of surface roughness on aerofoil sections for wind turbine use , e.g. [2.40]. However, the effects of roughness are determined by its size in relation to the boundary layer thickness. So care must be exercised in the use of wind tunnel data obtained using artificially applied roughness strips; some assurance is required that the scale and extent of the roughness used is typical of that found on HAWT blades. The effects of roughness will also depend on the particular aerofoil section. It appears though, that in the absence of a specific study on HAWT blade roughness, its effect can only be modelled by a certain degree of empiricism, either in two dimensional aerodynamic characteristics in the case of a blade element model or in the viscous sublayer modelling of a boundary layer treatment. There is nothing to suggest that surface roughness has any impact on the rotor stall problem other than on the peak value of power which may suffer as roughness increases.

Two dimensional wind tunnel test data are often assumed to be obtained in controlled flow conditions. Kucheman, [2.41], warned however, that even if the steady outer flow is two dimensional there is no reason to suppose that separated flows are two dimensional or steady. This suggests that there is an inherent limitation in the use of post stall data in a blade element model: no matter how carefully carried out post stall experiments in the wind tunnel will represent a three dimensional flow field.

2.2.3 Stall and separation

A rotor performance code for use in the stalled regime depends crucially on correct prediction of the stalling behaviour of the blade sections.

Blade element models use data which have been obtained in a wind tunnel where flow is essentially chordwise. When the same aerofoil is used on a rotating blade the flowfield can be quite different. On the HAWT blade, what is nominally the same aerofoil section will operate in the context of spanwise varying thickness, chord, incidence and airspeed. It would be suprising therefore if the stall behaviour of the section was exactly the same as that on a wind tunnel model.

Three 'pure' stall types have been classified by the separation process on the suction surface of a two dimensional aerofoil section, [2.42], [2.43]:

* trailing edge stall, (Figure 2.7), is characteristic of most thick aerofoil sections and is indicated by smooth and continuous variations in force and moment coefficients from zero lift to well beyond stall. This type of stall is caused by turbulent separation, the separation point moving progressively forward from trailing edge to leading edge as incidence is increased. At maximum lift the flow is separated over approximately half of the aerofoil; the post-stall rate of separation point progression is approximately the same as the pre-stall rate with incidence.

* leading edge stall, (Figure 2.8), is characteristic of most aerofoil sections of moderate thickness. The force and moment coefficients of these aerofoil sections show abrupt discontinuities when the incidence for maximum lift is exceeded. There is little or no attenuation of the lift curve slope as maximum lift is approached, and the peaks of the curves are sharp. This type of stall is associated with the bursting of a short bubble which is present near the leading edge at quite low incidences; from the attachment point the laminar boundary layer passes around the leading edge, through the pressure peak and separates. The detached laminar shear layer then grows and transition to turbulent flow occurs. The turbulent layer grows even faster so that pressure is recovered and the flow reattaches to the surface as a turbulent boundary layer. This localised region of separated flow is the laminar separation bubble, extending for just a few percent of aerofoil chord. The separation bubble is sensitive to the thickness of the boundary layer at separation, incidence, freestream turbulence and surface roughness. As incidence increases the bubble contracts until a point is reached when the turbulent layer can no longer reattach and the bubble bursts, causing a complete disruption of the flow over the entire suction surface. This is the point of maximum lift.

* thin aerofoil stall- not relevant to wind turbines which use moderately thick to thick aerofoils

It is not suggested that every aerofoil section fits uniquely into one of these three classifications; indeed under some conditions a section may exhibit stalling behaviour which is borderline or which combines the characteristics of two of the categories, as discussed below. Perhaps more importantly, a given aerofoil section may exhibit different stalling under different conditions. Since stalling is inseparably related to the behaviour of the boundary layer flow, the same factors which influence boundary layer growth (namely, pressure gradient, Reynolds number, free stream turbulence and surface roughness) also affect the stalling of aerofoil sections. A change in any one of these factors may cause the stall of a given section to change from one category to another.

Combined stall, (Figure 2.9), exhibits characteristics which are transitional between trailing and leading edge stall. The eventual stall type (and peak lift) may be seen as a race between the competing effects of turbulent separation and laminar or short bubble bursting.

Separation in three dimensions is described by Maskell, [2.44]. In three dimensions flow separation can occur at singular or ordinary points. A singular point is where there is zero surface friction and the flow downstream is reversed, two-dimensional separation is characterised by such a point. However, separation at an ordinary point is common in three dimensions and is not accompanied by zero friction or reversed flow; the only requirement for this separation is that the flow leaves the surface. On a plane of symmetry the separation occurs at a singular point; but at all other points on the separation line passing through the line of symmetry the flow separates at ordinary points. A picture of the limiting streamlines and trailing vortices due to separation before a strut in the boundary layer is shown in Figure 2.10.

On swept wings the boundary layer flow follows the curved streamlines shown in Figure 2.11. Physically it is the transverse pressure gradient in the external stream which produces the secondary crossflow in the boundary layer: the reduction in velocity in approaching the surface results in a decrease in the centrifugal force which outside the boundary layer is in equilibrium with the transverse pressure gradient. The surface (limiting) streamlines will always show the greatest deflection from the mainstream direction. If the limiting streamlines are turned into the spanwise direction then separation occurs.

The crucial issues are whether turbulent trailing edge separation on the two dimensional section in the wind tunnel may convert to the more abrupt leading edge separation on the rotating blade or that some mechanism acts to accelerate or delay the movement of the separation line.

2.2.4 Aspect ratio effects and tip loss corrections

Due to pressure difference between upper and lower surfaces of a finite aerofoil flow occurs around the tip. This leads to a progressive reduction in bound circulation as the tip is approached where no circulation can be supported. This reduction in circulation manifests itself as a reduction in lift curve slope for sections near the tip, Figure 2.12. This causes the power produced from the outboard section of the rotor blade to be reduced for angles of attack below the two-dimensional stall angle. Wind tunnel data for aerofoil section performance used in blade element models is rarely corrected for aspect ratio. A suitable correction to incidence and drag coefficient for a given lift coefficient is given by Glauert, [2.1] ; the correction for incidence is proportional to the lift coefficient, and that for the drag proportional to the square of the lift coefficient. The corrections are quite significant for large lifts. Various data on the effect of aspect ratio on measured lift coefficient are quoted by Miley, [2.18]. This force measured data indicates a thirty percent reduction of lift coefficient for the AR = 4 model compared to the AR = 8 model at the post stall secondary peak ($\alpha = 35°$), see also [2.38].

In strip theory methods aspect ratio effects are taken into account by utilising one of three tip loss models, [2.3], borrowed from helicopter and propeller theory:

* Effective rotor radius

The loss in circulation is allowed for by reducing the radius of the rotor (by a few percent) to an effective value which is used in the strip theory calculation.

* Prandtl tip loss model

The rotor wake is modelled as a set of vortex sheets each the same size as (and coaxial with) the rotor disc, with mutual distance dependent on the blade tip flow angle, each moving with a velocity equal to the axial induced velocity relative to the external flow. The reduction in potential difference between two vortex sheets approaching the tip is calculated. It is assumed that this reduction in potential difference is equal to the reduction of the circulation around the rotor blade. This correction is applied in the calculation of the wake induced velocities.

* Goldstein tip loss model

The wake (of a two or four bladed propeller) is modelled as a rigid helical vortex sheet for the case of optimum circulation distribution along the span of the blades, this gives a minimum rotational energy in the wake for a given thrust. This correction is also applied in the calculation of wake induced velocities.

Clearly the effective radius concept is convenient in its application, but must rely on some kind of detailed validation for its justification. For the other two methods a number of difficulties arise (see for instance Walker, [2.45], and de Vries, [2.2]). Firstly, the realism of the modelling assumptions can be questioned in relation to the HAWT which in high winds is heavily loaded in comparison with a propeller at design condition. Secondly, opinion differs on how best to apply the correction within the induced velocity calculation. Finally, it is noticed that the correction factor becomes dominant when the blade is stalled at low tip speed ratios. This indicates that the assumptions about the wake implicit in the vortex tip loss corrections warrant further discussion in their own right.

Viterna and Corrigan, [2.33], modified input data to a blade element model on the basis of aspect ratio and found improved correlation between prediction and measurements.

2.2.5 Unsteadiness of flowfield

Windshear, tower shadow and free stream turbulence constitute unsteadiness in the flow field of a HAWT rotor. The strip theory approach allows only axial and swirl components of velocity. It assumes a steady flow field with an absence of free stream turbulence. A dynamic stall response to this unsteadiness may be the explanation for differences between measured and predicted power. Aerodynamic models of the HAWT which account for dynamic stall have been developed, e.g. Hales & Garside, [2.46], and Hibbs, [2.47]. Since the dynamic stall models used are based on two dimensional pitching aerofoil test data, they are not necessarily appropriate for the performance prediction problem. Further, the induced velocity calculation should account for the non-uniformity of the flow velocity across the rotor disc. With these limitations the indications from this theoretical work are that power is little influenced by flowfield unsteadiness (except in the case of operation at large angles of yaw); the principal effects of dynamic stall being seen in variation of the out of plane loads.

The scale of free stream turbulence means that it cannot have a direct influence on the boundary layer on a wind turbine blade, [2.18]. Therefore the primary effect of free stream turbulence is on the local blade incidence; the unsteady aerodynamic effects of this have been adequately considered in the models mentioned above. Other effects such as on the dissipation of the turbine wake, and on the boundary layer of the turbine blade are secondary. Thus the indication is that the underprediction of power in high winds cannot be accounted for purely in terms of an unsteady flow field.

2.2.6 Aeroelastic deformation

The static aeroelastic deformation of large wind turbine blades in high winds could lead to alterations from the nominal blade geometry; most dramatic would be a coupling between the out of plane bending and the blade pitch distribution. It is conceivable that the increased bending in high winds could cause a progressive increment to blade element incidence towards the tip, leading to increased power.

2.2.7 Effect of hub blockage

The hub region of a wind turbine acts as a blockage in the flow field causing the flow to diverge. This has two effects :

(a) Radial flow component

In order to clear the blockage created by the hub a radial component is injected into the flow in the blade root region. An analysis by Klimas, [2.48], attempts to quantify the effect of this radial velocity component by modifying the lift coefficients of blade sections with respect to an effective local blade aerofoil yaw angle (i.e. introduce an effect similar to that of wing sweep).

The lift values and hence the maximum power from a predictive model using this model were found to increase for the Mod-0 machine.

Blade element models assume no radial flow component, with independent streamtubes across the blade span.

(b) Flow acceleration

Flow visualisation, [2.14], [2.15], has suggested that for the greatest part of a wind turbine's operation the flow pattern does not expand in passing through the rotor. This means that for the flow to diverge around the rotor hub/nacelle it must accelerate in the blade root region.

Accelerated flow would increase the local angle of attack (and thus possibly lift) and also the dynamic head. The power output from the blade root would therefore be higher than predicted by strip theory which assumes the rotor has no hub and that flow is uniform across the disc.

Flow acceleration would however bring forward the onset of stall (due to the increase in angle of attack) unless some other mechanism acted to delay stall.

These effects are of course dependent on the size of the machine hub and nacelle which for large machines is small in comparison to the rotor diameter.

The stall of a HAWT rotor blade begins at the root due to the low forward speed of the blade sections near the hub. As wind speed increases the amount of blade operating in stall increases. The stalled root region of the blades could act as a blockage in the rotor flow field - similar to that formed by the rotor hub and with the same effects. As a greater proportion of the blade becomes stalled so the blockage increases causing a redistribution of the flow towards the outer part of the blade; this therefore shows a greater possibility for affecting rotor power than hub/nacelle blockage.

2.2.8 Boundary layer behaviour

Tanner & Yaggy, [2.49], identified four influences on the boundary layer flow of a helicopter blade :

* Inflow effect - wake contraction due to increase in axial velocity

* Tip and hub vortices - trailed vorticity at blade extremities

* Spanwise pressure gradient due to variation of blade forward speed with radius

* Centrifugal pumping - flow thrown outwards by centrifugal force

When these influences are applied to a wind turbine blade, Figure 2.13, it is found that they act in a reinforcing manner on the suction side of the blade root possibly giving rise to radial outflow. This flow could remove fluid from the root region, thinning the boundary layer and hence delaying stall and giving enhanced values of lift coefficient. Enhancing of the lift produced by the inboard sections of a rotor blade would cause power output from such regions to be greater than would be expected especially near the stall.

Most power prediction codes are outer flow calculations that ignore boundary layer effects. The performance prediction code reported by Sørensen, [2.50], however, couples a boundary layer model to a strip theory type induced velocity calculation. This pioneering study showed there to be significant differences between the behaviour of aerofoil sections on a wind turbine rotor and that in a two dimensional environment. Unfortunately this study was limited by numerical difficulties but it showed how a complex three dimensional model could provide insight into the behaviour of a wind turbine rotor.

2.2.9 Conclusions

Most performance prediction codes rely on the use of two dimensional aerofoil characteristics. Experiments have shown the performance of aerofoils on a rotating blade to be different to that in a two dimensional wind tunnel. These differences are often considered to be due to the boundary layer behaviour in the rotating flowfield. Alternatively the inviscid outer flow through a wind turbine rotor, particularly at stall, may be significantly different from that seen in a two dimensional wind tunnel test and may alter behaviour of the aerofoil sections.

A three dimensional model of the flow over the blades of a wind turbine rotor should overcome the majority of the deficiencies found in strip theory methods. Such a model should include both the inviscid outer flow and the viscous boundary layer flow.

2.3 Objectives of this study

The performance of a HAWT rotor at stall is poorly understood. Much experimental work has shown significant differences in the behaviour of aerofoil sections when used on rotor blades when compared to two dimensional wind tunnel tests. The aim of this study is to quantify these differences by producing a validated model of the stalled HAWT rotor.

The discussion above showed three areas of the rotor flowfield that are not adequately modelled by the present state of the art blade element performance prediction codes. These are wake geometry, boundary layer behaviour and modifications to the outer flowfield through the rotor, the last two being closely coupled.

The new model developed in this study must address these areas if it is to be useful in the prediction of stall regulated rotor performance.

CHAPTER 3. ROTOR WAKE MODELLING

Chapter 2 illustrated the poor understanding of the HAWT rotor wake. The lack of quantifiable experimental evidence suggests that the definition (or prescription) of a wake model should be flexible.

This chapter outlines the development of a wake model and investigates the sensitivity of rotor performance to the effects of wake geometry.

3.1 Modelling requirements

It is apparent that although attempts have been made to realistically model the HAWT rotor wake no significant improvement has been made in the prediction of stalled rotor power/loads. This may still be due to inadequacies in the wake modelling and Miller, [2.16], suggests that there are still many areas where extensions to theory or additional measured data would enhance wake modelling for example

- Time history of vortex roll-up

- Vortex viscous core sizes

- Vorticity distribution outside the viscous core

- Number of vortex formations in inboard wake

- Formation of tip vortices at blade

Also wake expansion and decay rates require detailed examination through flow visualisation.

A measure of the effects of the above could be obtained by a sensitivity study on their importance to rotor power and loads. This would highlight the most important areas of investigation and also allow those with negligible effect to be discounted.

This study, therefore, requires a model which can provide an accurate physical representation of the rotor wake, and is flexible enough to allow a sensitivity study of critical parameters and also the incorporation of any experimental evidence to enhance its performance.

A rigid wake analysis (see 2.1) by definition does not fit these requirements. Free wake analyses have yet to show any significant advantages especially when their complexity and computational expense is taken into account. Therefore a prescribed wake analysis will be used.

No consensus is obvious regarding the constituent wake elements from the methods reviewed in Chapter 2. However, Johnson, [3.1], examines the various options when formulating a rotor wake model. He concludes that using a series of straight line vortex elements provides a simple and flexible approach without loss of accuracy.

3.2 The model definition

In order to undertake a study of the sensitivity of the performance of HAWTs to wake geometry a performance prediction code was produced, [3.2], coupling a prescribed wake model to a blade element model of rotor blade aerodynamic performance.

3.2.1 Structure of a HAWT rotor wake

Bound circulation from the wind turbine blade is trailed as vorticity into the wake. The way this vorticity behaves must be represented by the wake model. A recent study, at Risø by Pedersen & Antoniou, [2.15], shows that there is a strong tip vortex which maintains a helical path well downstream of the rotor. Inboard of the tip vortex the wake has a less coherent structure. The tip vortex shows some signs of wake expansion at low windspeeds but as the rotor becomes loaded this expansion is less noticeable and for the majority of the operational regime maintains a diameter equal to that of the rotor. These observations are broadly in line with those of Savino & Nyland in their earlier study of the Mod-0 turbine, [2.14].

The prescribed wake model employed here is based on discrete helices trailed from the rotor blade at any number of spanwise stations (defined by the user). This assumes that some roll-up of the vorticity occurs (as demonstrated by [2.14] and [2.15]).

3.2.2 The mathematical model

The first step is to define the end points of the straight line filaments used to represent the helical vortices in the rotor wake. The equations defining a helix in a co-ordinate system rotating with the 'first' blade are

$y = r\sin\theta$ (normal to the blade)
$z = r\cos\theta$ (radial along the blade)
$x = ut$ (axial)

where r is the radius of the helix

θ is the angle (in radians) defined by

$\theta = \omega t$

where ω is the relative rotation of blade and helix and u is the convection rate in the wake

The helices trailed from each blade are calculated with respect to the position of the 'first' blade which lies along the z-axis. The trailing vortex system is discretised to a set of points on each wake helix joined by straight line vortex filaments, Figure 3.1. Influence coefficients are calculated for each of the straight line filaments at N control points on the blade these coefficients represent the velocity induced by each filament if it were to have unit vorticity. The calculation of the influence coefficients uses the Biot-Savart law to calculate the velocity induced by an element of vorticity at a point with a correction for the core size (or smearing of the vorticity due to the viscous nature of a real fluid).

Johnson [3.1] derives the necessary equations by considering the situation shown in Figure 3.2. The velocity induced by the straight line filament of length s and strength Γ at the point P is (from the

Biot-Savart law)

$$\Delta\underline{v} = \frac{-1}{4\pi}\int \frac{\Gamma.\underline{r}\ \mathrm{x}\ d\underline{\sigma}}{r^3}$$

where $\underline{r}$ is the vector from the element $d\underline{\sigma}$ on the filament to the point P, r is $|\underline{r}|$ and x denotes the vector (cross) product.

Now write

$$\underline{r} = \underline{rm} - \sigma\ \underline{e}$$

where $\underline{rm}$ is the minimum (perpendicular) distance from the vortex filament (including its extension beyond its end points) to the point P and $\underline{e}$ is the unit vector in the direction of vortex. In terms of the filament end point, Figure 3.2, these are evaluated as

$$\underline{rm} = \frac{\underline{r1}(r2^2-\underline{r1}.\underline{r2}) + \underline{r2}(r1^2-\underline{r1}.\underline{r2})}{s^2}$$

$$\underline{e} = \frac{\underline{r1} - \underline{r2}}{s}$$

with the length of the vortex filament given by

$$s^2 = |\underline{r1} - \underline{r2}|^2 = r1^2 + r2^2 - 2\ \underline{r1}.\underline{r2}$$

The co-ordinate σ is measured from s1 to s2 along the filament, where

$$s1 = \frac{\underline{r1}.\underline{r2} - r1^2}{s}$$

$$s2 = \frac{r2^2 - \underline{r1}.\underline{r2}}{s}$$

Note that $\underline{rm}$ and $\underline{e}$ are perpendicular. It follows that

$$\Delta\underline{v} = \frac{\Gamma}{4\pi}\ \underline{r1}\times\underline{r2}\int\frac{d\sigma}{s\,(rm^2+\sigma^2)^{3/2}}$$

$$= \frac{\Gamma}{4\pi}\ \underline{r1}\times\underline{r2}\ \frac{s2\ r1 - s1\ r2}{s\ rm^2\ r1\ r2}$$

Substituting for s1, s2, s, and rm gives the velocity induced by this vortex element.

$$\Delta\underline{v} = \frac{\Gamma}{4\pi}\,\underline{r1}\times\underline{r2}\ \frac{(r1 + r2)(r1\ r2 - \underline{r1}.\underline{r2})}{r1\ r2\ [r1^2\ r2^2 - (\underline{r1}.\underline{r2})^2]}$$

$$= \frac{\Gamma}{4\pi}\,\underline{r1}\times\underline{r2}\left(\frac{1}{r1}+\frac{1}{r2}\right)\frac{1}{r1\ r2 + \underline{r1}.\underline{r2}}$$

Without a vortex core this result is singular as the vortex segment is approached. The influence of the vortex core is accounted for by multiplying the induced velocity by the factor

$$\frac{rm^2}{rm^2 + rc^2} = \frac{r1^2\ r2^2 - (\underline{r1}.\underline{r2})^2}{r1^2\ r2^2 - (\underline{r1}.\underline{r2})^2 + rc^2 s^2}$$

where rc is the vortex core radius.

Then the velocity induced by the finite length vortex filament is

$$\Delta\underline{v} = \frac{\Gamma}{4\pi}\,\underline{r1}\times\underline{r2}\ \frac{(r1 + r2)(1 - \underline{r1}.\underline{r2}/(r1\ r2))}{r1^2\ r2^2-(\underline{r1}.\underline{r2})^2+rc^2(r1^2+r2^2-2\ \underline{r1}.\underline{r2})}$$

Setting Γ to unity yields an influence coefficient for the straight line filament at the point P. The strength of the vorticity in the wake is defined by the blade bound vorticity distribution. This is calculated using the lift distribution on the rotor blade. The Kutta-Joukowski theorem is applied to calculate the vorticity at any station on the blade and the strength of each helix is defined by the spanwise change in vorticity on the blade.

The blade element model assumes that the rotor blade can be split into spanwise elements or strips, Figure 3.3. These elements are assumed to act independently of one another as two dimensional aerofoils. The velocity incident on the elements is calculated from the sum of the axial windspeed, the rotational speed and the wake induced velocities, Figure 3.4. As the blade elements are assumed to act as two dimensional aerofoils their behaviour is modelled using two dimensional wind tunnel data, suitably modified at the tip and hub stations as the lift generated at these points must be zero.

Because a vortex can only end at a solid boundary the circulation variation on a rotor blade causes vorticity to be trailed in its wake, Figure 3.5. The circulation is calculated using the Kutta-Joukowski theorem ($L=\rho U\Gamma$) for each spanwise station. The maximum bound circulation is found and depending on the radius of the wake helices each helical vortex is given a vorticity corresponding to the change in bound vorticity between helix radii.

The calculation process starts with zero vorticity assigned to the helices. The circulation distribution is calculated using the blade element model and the corresponding vorticities assigned to each helix. A new circulation distribution is calculated and the process repeated. The wake geometry remains fixed throughout and so the influence coefficients are not recalculated.

When five iterations on the wake induced velocities are complete the model is considered to have converged and so the resulting performance parameters are calculated.

3.3 The sensitivity study

The input to the wake model allows the prescription of

- the number of helices trailed from each blade
- the convection rate of each helix as a proportion of windspeed
- the swirl/rotational speed of each helix
- the initial radius of each helix
- the radial (linear) expansion of each helix throughout the extent of the wake as a function of initial radius
- the core radius of each helix as a function of rotor radius
- the number of straight line vortex filaments used to make up each helix
- the azimuthal step size associated with each straight line filament

Figure 3.1 shows one wake helix.

Initially the calculated circulation distribution on rotor blades was examined to see where it may be expected to find discrete/rolled up filaments of vorticity due to rapid variations in the bound circulation distribution. This showed little evidence for discrete trailed vortices anywhere other than at the blade root and tip. A typical circulation distribution is shown in Figure 3.6 which illustrates this point.

Using only tip and hub vortices the effect of the vortex core size, physical extent of the wake model and the resolution in azimuthal step size were examined to indicate their required values before the wake induced effects converged (this assumes a coherent structure throughout the wake with no decay of vorticity).

Figure 3.7 shows the effect of varying the core radius of the tip vortex which indicates the importance of this parameter on induced velocities at the tip. There is no hard experimental evidence for a particular core size but Johnson, [3.1], suggests a core size of approximately 5-10% local blade chord. A value of 5% local blade chord was used throughout the sensitivity study.

Figures 3.8-10 show that the induced velocities due to the wake are particularly dependent on the near wake and that the number of azimuthal elements has negligible effect except at the tip. Because of the somewhat arbitrary definition of core size, the effect of a small deficiency in induced velocity calculation introduced by using a smaller number of azimuthal steps was considered unimportant. Therefore to reduce computational effort only 12 azimuthal steps were used in the sensitivity study.

Figure 3.11 shows that good convergence of induced velocities is achieved after 12 spirals of the rotor wake have been included.

So a standard wake with two helices trailed from each rotor blade consisting of twelve spirals, each with twelve azimuthal elements and core size of 5% local chord was defined.

Following this preliminary investigation, a sensitivity study was made for each of the five turbines listed in Table 3.1. In the study, the effects on performance of tip speed ratio and the wake geometry parameters were systematically investigated. For each turbine, ten wake geometries were analysed for each of four tip speed ratios, a total of forty cases per turbine. The parametric values are summarised in Table 3.2 and the computer run numbers are listed in Table 3.3.

The input data for blade element type performance codes can influence the accuracy of the resulting prediction. The input data used here was selected with no special attention given to such a problem (the same data is used in the Strip Theory predictions shown for comparison in Figures 3.12-19). This is compatible with the philosophy of a sensitivity study where trends are of greater importance than accurate results for individual machines.

3.3.1 Discussion of Results

To illustrate the effect of wake geometry on rotor performance predicted power coefficient will be used, similar effects being present in the prediction of rotor thrust.

The dependency of predicted power coefficient on the wake geometry is most noticeable in the high tip speed ratio regime with sensitivity decreasing with tip speed ratio. Figures 3.12-17 show that at high windspeeds the predicted power coefficient is only marginally affected by variation of the wake geometric parameters but at low windspeeds the spread of results is much larger.

The reason for this trend is the aerodynamic performance of the blade elements; essentially the wake geometry determines the angle of attack distribution on the blade: in low winds the aerodynamics of the blade elements is linear, but in moderate to high winds as the blade stalls the lift curve slope reduces and so changes in angle of attack become less important.

The most important feature of the wake geometry is the convection rate (see Figures 3.17-19).

Further investigation has shown that the effect of wake geometry is dominated by the helix trailed from the tip of the blade, the hub vortex being of secondary importance with more locally defined effects.

As there is no quantitive experimental evidence concerning wake geometry all the parameters in the wake prescription were set to unity for the rest of the work described here.

3.4 Summary

A review of the literature, see Chapter 2, showed a poor physical understanding of the HAWT rotor wake and little consensus in the definition of a theoretical model.

In an attempt to understand the behaviour of the rotor wake a prescribed model was developed and used to undertake a study of the dependence of rotor performance on wake geometry and constituent elements.

This showed that that the most important aspect of wake geometry is the convection rate and that the geometry of the rotor wake becomes less important as windspeed increases; in very high winds the geometry of the wake has a minimal effect on the prediction of peak rotor power.

This indicates that the problem of poor prediction of stalled rotor power is concentrated in the prediction of blade aerodynamic performance.

CHAPTER 4. ROTOR BLADE AERODYNAMIC PERFORMANCE MODELLING

In Chapter 3 the rotor wake modelling was examined to quantify its importance in the prediction of high wind performance. This concluded that the problem of high wind performance prediction was centred on blade aerodynamic performance.

This chapter deals with the modelling of the blade aerodynamic performance. Chapter 2 described the simplifications used in blade element analyses and the sort of discrepancies found between measured aerofoil performance on a rotor blade when compared with that in a wind tunnel. The simplifying assumptions in blade element analyses essentially concern the neglect of the three dimensional nature of the flow through a wind turbine rotor. Any modelling technique used should therefore attempt to account for the three dimensionality of the flowfield.

4.1 Requirements of the model

The requirements of a model to simulate the flow over a wind turbine blade are severe in computational fluid dynamics terms; blade performance has to be defined for a large range of angle of attack particularly at the root. The model must therefore be capable of dealing with large regions of separated flow.

In order to include the effects of separating flow the model must include a solution of the viscous boundary layer near to the surface. The link between this and the incident rotational, wind and wake induced velocities being an inviscid flow solver.

The flow should be defined on the surface of the rotor, (if possible the spinner) and should account for not only the interaction of the rotor and its wake but also that between the rotor blades themselves. In essence the wind turbine rotor should be modelled as a whole with as few assumptions about 'negligible' interference as is practicable.

4.2 Choice of method

With such a rigorous set of conditions imposed on the choice of a flow model (Section 4.1) one class of method immediately shows promise; the so called 'panel method' or Boundary Integral (B.I.) method (see review by Butter et al [4.1]) has received great attention in the past two decades as it provides a nominally exact means of calculating irrotational incompressible flow around real (two or three dimensional) geometries. It does this without many of the limiting simplifying assumptions often associated with say, thin aerofoil or lifting surface theories, [4.2]. Also it requires that boundary conditions be imposed only at the surface of the body unlike field methods (Euler) which also require that the flowfield local to the body be calculated as part of the solution.

Panel methods have been successfully used (Hess [4.3], Coton & Galbraith [4.4], Maskew & Dvorak [4.5], Williams [4.6] and Sørensen [2.50]) in both inviscid applications and in conjunction with boundary layer schemes and aerofoil wake models to calculate separated flows.

4.3 Mathematical foundations of panel methods

For completeness the mathematical foundations of the panel method are laid before explaining its use in separated flow modelling (this analysis follows that of Moran [4.7]).

Any incompressible irrotational flow can be represented by a distribution of sources and vortices (or doublets) over its bounding surfaces. The remainder of this sub-section is devoted to a proof of this theorem.

The proof rests on the divergence theorem

$$\int_v \nabla . U \, dv = - \int_S n . U \, dS \qquad (4.1)$$

here v is a region in space (a flowfield in this case). S is the boundary of v, and n is a unit vector normal to S and directed into v. Since equation (4.1) is basically a three dimensional form of the 'fundamental theorem of calculus'

$$\int \frac{df}{dx} \, dx = f(b) - f(a)$$

it is important that U be a continuous function of position inside v. This has implications to the design of the surface S that bounds v, which are hinted at in Figure 4.1 and will be detailed later.

The vector U to which equation (4.1) is applied is defined by

$$U = \phi \nabla \phi_S - \phi_S \nabla \phi \qquad (4.2)$$

where ϕ is the velocity potential of the flow in v, so that

$$V = \nabla\phi \tag{4.3}$$

is the fluid velocity in v, whereas ϕ_S is the potential of a source of unit strength at some arbitrary point P in v:

$$\begin{aligned} \phi_S &= \frac{1}{2\pi} \ln r && \text{in two dimensions} \\ &= -\frac{1}{4\pi}\frac{1}{r} && \text{in three dimensions} \end{aligned} \tag{4.4}$$

In either case r is the distance from P to the point at which U is to be evaluated, as shown in Figure 4.2. It should be noted that in the case of two dimensions the distance r should be scaled by some reference length, but this has been omitted here since it simply implies a constant shift to the potential defined above. As will be seen shortly this choice of U leads to a formula for ϕ at P in terms of data on the bounding surface S.

If the function U defined by equation (4.2) is to be continuous in v, so must ϕ, $\nabla\phi$, ϕ_S, and $\nabla\phi_S$. But ϕ_S and its derivatives are not defined at P. Therefore before integrating over v, a small circle (in two dimensions) or sphere (in three dimensions) centred at P and of radius ε is carved out of v, as shown in Figure 4.3. Let v_ε be the part of v outside that excluded region, and S_ε be the surface of the circle or sphere.

For the same reason, such entities as the vortex sheet trailed by a wing of finite span must be excluded from v , since the velocity $\nabla\phi$ is discontinuous across such a sheet. This can be done by the device illustrated in Figures 4.1 to 4.3, namely, by including in the bounding surface S a two sided component that sandwiches the vortex sheet. Then $\nabla\phi$ can be assigned its proper values on either side of the sheet while remaining continuous in v (and v_ε).

A similar device is necessary in two dimensions, consider flow past an aerofoil with circulation Γ. From the definition

$$\Gamma = \int_C V.dl$$

where C is a closed curve around the aerofoil as shown in Figure 4.4. Also by definition the difference ϕ between two points P_1 and P_2 is

$$\phi(P_2) - \phi(P_1) = \int_{P_1}^{P_2} \nabla\phi.dl = \int_{P_1}^{P_2} V.dl$$

Now if one goes from P_1 to P_2 on the part of C above the aerofoil and returns to P_1 on the other part of C, one gets

$$\phi(P_1) - \phi(P_1) = \int_C V.dl = \Gamma \qquad (4.5)$$

which shows ϕ to be multivalued; the value of ϕ at P_1 is not the same at the beginning and end of the trip. The solution is to insert a 'branch cut' in the domain of interest that prevents circumnavigation of the aerofoil, which is what was done in in Figures 4.1 to 4.3. This makes the region v 'simply connected' in mathematical parlance.

In summary the surface S generally has three components (Figures 4.3 and 4.5):

1. S_B, the surface(s) of the body(ies) immersed in the flow.
2. S_∞, a surface far from S_B.
3. S_C, a two sided surface that runs between S_B and S_∞ and which sandwiches discontinuities in ϕ and/or $\nabla\phi$.

Now the source potential ϕ_S satisfies Laplace's equation

$$\nabla^2\phi_S = 0$$

everywhere in v_ε, as does ϕ. Therefore the divergence of the vector U defined in equation (4.2) is

$$\begin{aligned}\nabla.U &= \nabla\phi.\nabla\phi_S + \phi\nabla.\nabla\phi_S - \nabla\phi_S.\nabla\phi - \phi_S\nabla.\nabla\phi \\ &= \phi\nabla^2\phi_S - \phi_S\nabla^2\phi \\ &= 0 \text{ in } v_\varepsilon \qquad (4.6)\end{aligned}$$

Thus applying equation (4.1) to the region v_ε gives

$$\int_{S_\varepsilon} \nabla.U \, dv = 0 = -\int_{S+S_\varepsilon} n.(\phi\nabla\phi_S - \phi_S\nabla\phi) \, dS \qquad (4.7)$$

where it can be observed from Figure 4.3 that the surface bounding v_ε is comprised of S, the surface bounding v, and S_ε, the surface of the small sphere or cylinder surrounding P. It is convenient to separate the integrals over these two surfaces and to rewrite equation (4.7) as

$$\int_{S_\varepsilon} n.(\phi\nabla\phi_S - \phi_S\nabla\phi) \, dS = -\int_{S} n.(\phi\nabla\phi_S - \phi_S\nabla\phi) \, dS \qquad (4.8)$$

Interesting things happen when ε, the radius of the sphere or cylinder surrounding P, is allowed to go to zero. Then ϕ and $\nabla\phi$ approach their values at P, ϕ_P and V_P, say, so that the left side of equation (4.8) becomes

$$\int_{S_\varepsilon} n.(\phi\nabla\phi_S - \phi_S\nabla\phi)\ dS \approx \phi_P \int_{S_\varepsilon} n.\nabla\phi_S\ dS - \nabla_P.\int_{S_\varepsilon} n\phi_S\ dS$$

The first integral on the right is just the volume flow rate through S_ε, which equals the strength of the source inside, namely unity. As for the second integral, r is constant (ε) on S_ε, and so, from equation (4.4), is ϕ_S. Taking ϕ_S outside the integral leaves

$$\int_{S_\varepsilon} n\ dS$$

which is zero by symmetry, so that equation (4.8) becomes in the limit what is known as Green's identity:

$$\phi_P = \int_S [(n.\nabla\phi)\phi_S - \phi(n.\nabla\phi_S)]\ dS \qquad (4.9)$$

this formula gives the value of ϕ at any point P in v, a region in which ϕ is a continuous solution of Laplace's equation, in terms of the values of ϕ and n.$\nabla\phi$ on the boundary of v.

The physical interpretation of this mathematical formula is of interest here.

First, look at

$$\int_S (n.\nabla\phi)\phi_S\ dS$$

The quantity ϕ_S, according to equation (4.4), depends only on the distance r between P and the dS whose contribution to the integral is under consideration. Thus, although introduced as the potential of a source of unit strength at point P, evaluated at a point on S that is a distance r away, it could also be taken as the potential of a source of unit strength at dS, evaluated at P. With this interpretation, the integral can be called the potential of a source distribution on S whose strength per unit area is $n.\nabla\phi$, the component normal to S of the local fluid velocity.

The integral

$$\int_S \phi n.\nabla\phi_S \, dS$$

has a similar interpretation. The gradient of a scalar is defined as the vector whose magnitude and direction are those of the maximum rate of change of the scalar. Thus $n.\nabla\phi_S$ is the rate of change of ϕ_S in the direction of n at the element dS. This can be represented as follows. As shown in Figure 4.6 let Q_1 and Q_2 be points a distance δ apart, on either side of dS, and arranged so that

$$Q_1Q_2 = \delta n$$

Let ϕ_1 and ϕ_2 be the values at Q_1 and Q_2, respectively, of the potential of a unit strength source at P. Then

$$n.\nabla\phi_S = \lim_{\delta\to 0} \frac{\phi_1 - \phi_2}{\delta}$$

However, as noted above, ϕ_1 and ϕ_2 can also be regarded as the values at P of the potentials of unit sources at Q_1 and Q2. Then $\phi_1/\delta - \phi_2/\delta$ is the difference between the potentials of two sources of strength $1/\delta$ at Q_1 and Q2. As $\delta\to 0$, they coalesce into what is called a doublet, whose strength is defined to be the product of the source strength and the distance between the sources, or, in this case unity. From the viewpoint of an observer at P, the second part of the integrand in equation (4.9) is, therefore, the potential of a doublet distribution over the surface S. The axes of the doublets are normal to S, and the strength per unit area of the distribution is ϕ, the local velocity potential.

Thus it has been shown that the velocity potential of any irrotational flow can be represented by a distribution of sources and doublets over its bounding surfaces. The strength of the source and doublet distributions per unit area are, respectively, the boundary values of the normal derivative of ϕ and of ϕ itself.

A related variation is to take ϕ in the above to be the perturbation potential, so equation (4.3) becomes

$$V = V_\infty + \nabla\phi \tag{4.10}$$

Then ϕ vanishes on S_∞, so that equation (4.9) can be used with S replaced by S_B+S_C (Figure 4.3).

4.4 Application of panel methods to separated flow modelling

The panel method is widely accepted as a powerful tool for the calculation of both two and three dimensional potential flows with its application to separated flow modelling split into two broadly defined categories, [4.1].

The first of these attempts to model the actual nature of the separated flow using a boundary layer method closely coupled to the potential flow solution using a viscous inviscid matching procedure, [4.6]. This approach has found particular favour in aerofoil design where the performance of an aerofoil up to the point of maximum lift is required. However as separation becomes more extensive the method falls down because the boundary layer assumptions become inappropriate, Sørensen, [2.50], (for large regions of separated flow Cross, [4.8], states that it would be necessary to solve the Navier Stokes equations). In his pioneering work in applying this approach to the performance of wind turbines Sørensen, [2.50], reported that, due to numerical instabilities, solutions could only be obtained when the local angle of attack of the rotor blade was less than twenty degrees. Clearly this limitation, though allowing Sørensen to make some important observations concerning the effect of blade rotation on aerofoil performance, does not allow the method to be used in an attempt to calculate the performance of a wind turbine rotor in high winds.

The second approach uses an approximation based on the physics of the external flow to model the effect of the viscous separated region on the pressure distribution over the aerofoil e.g. [4.4], [4.5]. In these particular methods the separated region is modelled as an area of constant dynamic head encapsulated by free shear layers which are trailed from the upper separation point and trailing edge of the aerofoil. Although some doubt has been cast on the validity of this model for small regions of separation (Butter, [4.9]) it is accepted that the shear layer model forms a good representation of the physical nature of flows with extensive separations i.e. particularly applicable to the case of a wind turbine rotor in high winds.

In order to discuss the misgivings aired by Butter, a full description of the method used in the wind turbine performance model is outlined below.

4.4.1 Description of the method

Hess & Smith [4.10] outlined the modelling of non lifting three dimensional flows using source singularities distributed over the body. For lifting flows circulation must be introduced via either vortex or doublet singularities. Maskew & Dvorak [4.5] (also Coton & Galbraith [4.4]) used vortex panel methods for modelling two dimensional separated flows.

4.4.2 Two dimensional application of shear layer model

In two dimensions the flow over an aerofoil is illustrated in Figure 4.7, several regions of this flow can be identified (this analysis closely follows that in [4.5] and differs only in small detail unnecessary to the understanding of the method).

Firstly the region exterior to the boundary layer and separated wake can be assumed potential since the shear is everywhere so low that viscous stresses impart a negligible rotation to the fluid.

Secondly the boundary layer close to the aerofoil surface.

Thirdly the thin flow regions fed by the separating boundary layer have rotation but only moderate shear. These regions can be described as 'free shear layers'.

Fourthly the wake between the two trailing shear layers is a region with low vorticity and insignificant viscous stresses.

An approximate model of the flow can be generated by the application of the following assumptions.

(i) The boundary layer and free shear layers do not have significant thickness and, hence, can be represented as slip surfaces across which there exists a jump in velocity.

(ii) The wake does not have significant vorticity and has constant total pressure (below the free stream total pressure). It is therefore taken to be a potential flow region.

The flowfield can be constructed by adding to the uniform stream, the so-called 'induced' velocities associated with a vorticity distribution of strength equal to the curl of the velocity field. Figure 4.7 shows the resulting flow which is everywhere irrotational except along sheets where the boundary layer and free shear layers have been squeezed to zero thickness. The mathematical problem is to find the vorticity sheet strength such that the appropriate boundary conditions are met. The position of the vortex sheets representing the free shear layers is not known a priori.

The boundary condition for the aerofoil surface is flow tangency or

$$V.n = 0$$

where n is the unit normal vector on the surface and V is the total velocity vector. This condition is modified when allowing for the boundary layer displacement effect (the right hand side becoming equal to the transpiration velocity, [2.50], [4.7]).

The free vortex sheets are located on streamlines and there is no static pressure drop across them. This condition is not applied directly but by an iterative process whereby an initial guess to the position of the sheets is modified by interrogation of the velocity field. Maskew & Dvorak also indicate that results are sensitive to the length of the vortex sheets and give a tentative guide to the wake length (or fineness ratio Figure 4.8) based on a correlation with aerofoil thickness to chord ratio and extent of separation.

The boundary condition of flow tangency on the aerofoil surface gives the integral equation:

$$\int_C K\gamma(s)ds + \gamma_L(\int_L Kds - \int_U Kds) - V_\infty.n = V_N \qquad (4.11)$$

where the constant value of the vorticity on the free shear layers is used and where the kernel function, K, is the normal velocity component (at the boundary point for which V.n is being enforced) due to a unit point vortex at the point associated with the element, ds, of the line of integration, and where the integration paths, C, L and U are the the aerofoil and the lower and upper free vortex sheet locations respectively. The unknowns are the vorticity strengths on the curve , C, and on the free sheets represented by $\gamma(s)$ and γ_L respectively. The former is a function of position on the aerofoil and the latter is a constant. There is one auxiliary condition, related to the Kutta condition, which specifies that the vorticity values at the separation points on the upper and lower surface are equal but opposite and have the value of the free sheets, γ_L.

The right side of equation (4.1), is zero for the initial potential flow solution. Following a boundary layer analysis, however, the displacement effect is represented by a piecewise constant source distribution; V_N then becomes the integrated normal velocity induced by the boundary layer source distribution.

In order to solve the integral equation it is discretised in the following manner; the aerofoil contour is represented by an inscribed polygon, Figure 4.8. Each of the individual panels representing the polygon has a variation of vorticity across it, the free vortex sheets are represented by a number of panels of uniform vorticity. So each aerofoil contour panel has a vorticity γ_i and the integral equation (4.1) becomes a set of algebraic equations in the unknowns $\{\gamma_i\}$. Initially there are N+1 unknowns for N panels but the auxiliary condition 'squares the matrix' so that a solution can be found.

4.4.3 Difficulties with use of the method

As stated earlier reservations have been expressed as to the validity of the free shear layer model of separated flow. Most of the points raised seem to be based on the independent investigation of the method, Butter [4.9]. Three areas of difficulty will be considered in turn.

Firstly the assumption of constant pressure in the separated region is not universally accepted and recent work by Cross [4.8], using a quasi-simultaneous scheme to calculate beyond separation, has shown evidence for a slight pressure gradient in this region. However this gradient is small and therefore affects integrated forces only very slightly. The assumption is therefore regarded as being within engineering accuracy for calculating the loads on a wind turbine.

Secondly the use of a vortex sheet to represent separation on the aerofoil can cause difficulties in the calculation of velocities near to the separation point. The vortex sheet must leave the surface of the aerofoil at an angle, thus introducing a discontinuity; Figure 4.8b is a detail of the panel nodes and control points around the point of separation. Butter states that "there would tend to be a stagnation at separation"; the text-book picture of (two dimensional) separation does indeed suggest a line of zero-velocity 'leaving' the wall at separation, bounding the zone of reversed flow. The model is required to furnish estimates of velocity at the top of the boundary layer: the boundary layer thickening is represented by the transpiration effect, up to (the last control point before) separation, and the surface velocity is assumed constant at all control points thereafter. However, the point at which the boundary layer calculation suggests separation need not coincide with the corner node at which the shear layer leaves the surface. In addition, the velocities that are calculated should not be confused with those that would occur around an angular body made up of flat quadrilateral panels. The flat panels represent the real geometry of the body and the calculated velocities are estimates of those at the top of the boundary layer, which is a smooth surface. The shear layer (a thin layer of concentrated vorticity across which the velocity is discontinuous) is but a hypothetical construction to represent the vorticity of the separated region, and does not constitute an extension of the solid surface of the body. Butter suggests that the relative position of corner and (control point of the panel containing) separation may be such as to cause a dip in the pressure distribution. This, and his predicted pressure profiles for the separating NACA 0012 aerofoil, suggests that he has calculated velocities beyond the point of separation; there is no justification for such a calculation using this method. Butter hints that smoothing could be introduced to eliminate any velocity dips which could 'mislead' the boundary layer code. Essentially, this is what is done in the present work, velocities being calculated by differentiating potential (see 4.4.4) - the smoothing inherent in this process is sufficient in practice to eliminate purely local fluctuations. In any case, even without smoothing, it is apparent that dips in the predicted pressure profile are not inevitable. Indeed the data presented by BUTTER et al [4.1], reproduced here as Figure 4.9, shows that good predictions may be obtained when the separation point is known a priori.

Thirdly the problem of correctly estimating the separation point itself is also highlighted by Butter, but this is a problem common to all separated flow models and is centred on the separation criteria used in the boundary layer analysis. It must be pointed out that Maskew's computer code, which Butter used in his investigation, contains its own boundary layer model - it is to this part of Maskew's code that this criticism is directed. The boundary layer model used in the present study is a three dimensional integral method developed by Cousteix, [4.11], at ONERA; it has been validated and successfully applied over the years to a wide range of configurations (swept wings, elliptical bodies, turbo-machinery, etc.). Over the past decade, there has been extensive investigation and debate on the relationship between separation and the singularities arising from the boundary layer model. Used in the direct mode, Cousteix and his coworkers have predicted the separation line as a convergence of the wall stream lines, or skin-friction lines.

In his report, Butter accepts that the shear layer model is valid for large regions of separation, but questions the validity of the model for incidences where the separation is close to the trailing edge. This is because the development of such a small region is dominated by the boundary layer behaviour; in this case, Coton & Galbraith [4.4] have suggested that the problem may be alleviated somewhat if the growth of the boundary layer is restricted.

Finally, Butter's conclusion is that the approach is probably reasonable for 'large' separations where the separation point is well forward of the trailing edge. Overall, it appears that his misgivings concern the methods used to estimate the point of separation, and that the free shear layer model as such is suitable for use as a practical tool for the performance prediction of the stalling HAWT rotor.

4.4.4 Extension to three dimensions

Use of constant strength vortex methods can cause difficulties in the calculation of the velocity field at the trailing edge of aerofoil sections due to the proximity of control points (see Figure 4.10). When extending their study of separated flows to three dimensions Maskew et al [4.12] used a doublet/source scheme.

The velocity field of a constant strength doublet panel can be replaced by that of a vortex, a pair of line vortices in 2D, or a ring vortex in 3D, [4.7]. Therefore using the external Neumman boundary condition of flow tangency for the solution of the boundary integral equation can result in the singular velocity field of a constant strength vortex method, Maskew, [4.13]. Maskew indicated that these singularities can be removed by working in terms of the velocity potential field which is then differentiated to obtain velocities. He further stated that because the velocities are calculated as the gradient of the potential, the potential formulation behaves as if it is one order higher than the velocity formulation for a given order of singularity distribution.

In Figure 4.11 a streamwise cut is taken through a wing and its wake. Splitting this idealised model into four regions; aerofoil (A), bubble (B), wake (W), and outer flow (O) assuming the existence of velocity potential fields Φ_A, Φ_B, Φ_W, Φ_O, that satisfy Laplace's equation through out the regions A, B, W, O respectively. By applying Green's theorem to each of these regions and combining the resulting contributions, the velocity potential at a point, P, situated in any of these regions can be written:

$$\begin{aligned}
\Phi_P = &\frac{1}{4\pi}\iint_{S_{OA}} \left\{ (\Phi_O - \Phi_A)n_O \cdot \nabla(\frac{1}{r}) - \frac{1}{r} n_O \cdot (\nabla\Phi_O - \nabla\Phi_A) \right\} dS_{OA} + \\
&\frac{1}{4\pi}\iint_{S_{BA}} \left\{ (\Phi_B - \Phi_A)n_B \cdot \nabla(\frac{1}{r}) - \frac{1}{r} n_B \cdot (\nabla\Phi_B - \nabla\Phi_A) \right\} dS_{BA} + \\
&\frac{1}{4\pi}\iint_{S_{OW}} \left\{ (\Phi_O - \Phi_W)n_O \cdot \nabla(\frac{1}{r}) - \frac{1}{r} n_O \cdot (\nabla\Phi_O - \nabla\Phi_W) \right\} dS_{OW} + \\
&\frac{1}{4\pi}\iint_{S_{OB}} \left\{ (\Phi_O - \Phi_B)n_O \cdot \nabla(\frac{1}{r}) - \frac{1}{r} n_O \cdot (\nabla\Phi_O - \nabla\Phi_B) \right\} dS_{OB} + \\
&\frac{1}{4\pi}\iint_{S_{BW}} \left\{ (\Phi_B - \Phi_W)n_B \cdot \nabla(\frac{1}{r}) - \frac{1}{r} n_B \cdot (\nabla\Phi_B - \nabla\Phi_W) \right\} dS_{BW} + \\
&\phi_\infty
\end{aligned} \tag{4.12}$$

where S_{OA}, S_{OB}, etc., are the common boundaries between the respective regions. Vectors n_O, n_B are unit normals to the surface directed into the regions O and B respectively. The quantity, r, is the distance between an element of surface and the point, P.

The above is an extension of the derivation given section in 4.3 (cf equation (4.9))

If the point, P, lies on one of the surfaces, say the S_{OA} facing region O, then the local contribution to ϕ_P is obtained by a limiting process using a small hemispherical distortion of the surface centred on P, [4.2]. The local contribution is

$$\Delta\phi_P = \left(\frac{\phi_O - \phi_A}{2}\right)_P$$

This is half the jump in potential across the surface at P. The surface integral over S_{OA} would exclude the point P in this case.

Each of the integral expressions represent the perturbation potential due to distributions of doublets and sources over the respective boundaries. For example, the first integral is the perturbation potential for a doublet distribution of strength (ϕ_O - ϕ_A) on the boundary, S_{OA}, plus the perturbation potential for a source distribution of strength $-n_O.(\nabla\phi_O - \nabla\phi_A)$.

For a given region there exists an infinite number of combined doublet and source distributions over the boundary of that region giving the same velocity potential field within the region but producing different solutions in other regions. Thus a unique solution for the idealised model shown in Figure 4.11 exists only if appropriate boundary conditions are imposed on both sides of each boundary surface, the general arrangement of the model in three dimensions is shown in Figure 4.12.

The boundary conditions used in the model are summarised thus:

(i) Inside the wing specify the internal Dirichlet boundary condition

$$\Phi_A = \Phi_\infty$$

(ii) On the exterior surface of the wing specify the Neumann boundary condition

(a) in the attached flow region on boundary S_0A

$$n_0 \cdot \nabla\Phi_0 = -\frac{\partial}{\partial s}(V_e\delta^*) + n_B.V_\infty$$

i.e. the source strength is set directly as the onset normal velocity including the transpiration effect of the boundary layer

(b) in the separated zone on boundary S_{BA}

$$n_B \cdot \nabla\Phi_B = n_B.V_\infty$$

(iii) the shear layer model is represented by doublet sheets which take their strength from the value of the doublet strength at separation

$$\Phi_0 = \Phi_{sep}$$

(iv) Kutta Condition; at each spanwise station the velocity potential surface gradients at the upper and lower separation points are set equal (see Appendix D).

(v) The downstream wake region, W, is an extension of the bubble region.

With the appropriate boundary conditions applied in the idealised model equation (4.2) is applied at points P on the surface of the wing:

$$
\begin{aligned}
0 = {} & \frac{1}{4\pi}\iint_{S_{OA}} \left\{ \phi_O \, n_O \cdot \nabla\left(\frac{1}{r}\right) - \frac{1}{r}\, n_O \cdot \left(-\frac{\partial}{\partial s}(V_e \delta^*) + n_O . V_\infty\right) \right\} dS_{OA} \; + \\
& \frac{1}{4\pi}\iint_{S_{BA}} \left\{ \phi_B n_B \cdot \nabla\left(\frac{1}{r}\right) - \frac{1}{r}\, n_B \cdot V_\infty \right\} dS_{BA} - \frac{\phi_P}{2} \; + \\
& \frac{1}{4\pi}\iint_{S_{OBU}} \left\{ \phi_{sepu} n_O \cdot \nabla\left(\frac{1}{r}\right) \right\} dS_{OBU} \; + \\
& \frac{1}{4\pi}\iint_{S_{OBL}} \left\{ \phi_{sepl} n_O \cdot \nabla\left(\frac{1}{r}\right) \right\} dS_{OBL} \qquad (4.13)
\end{aligned}
$$

where $\phi_O = \Phi_O - \Phi_\infty$ etc are the perturbation potentials. The integral over S_{OA} and S_{OB} excludes the point, P, when it lies on part of the boundary and the quantities ϕ_{sepu} and ϕ_{sepl} are functions of radial location.

4.5 Boundary layer modelling

The need for accurate prediction of the separation line on the rotor blade is paramount. In order to achieve this not only must the inviscid outer flow be well defined but also the behaviour of the viscous flow on the surface. As with the inviscid flow solver the boundary layer calculation should be three dimensional, taking into account the radial pressure gradients present on a rotating blade.

4.5.1 Available techniques

Boundary layer calculations are often split into two types; field methods, in which the governing partial differential boundary layer equations are solved, and integral methods, in which the same equations are integrated in the direction normal to the wall.

Integral methods are both faster and less complex in application than finite difference methods and therefore lend themselves more readily to the engineering approach of this project.

4.5.2 The method used

The calculation method used is that of Cousteix, [4.11]. This uses the global equations of entrainment and momentum. Although the solution is not performed in an external streamline coordinate system it is more conveniently presented by writing these equations in such an axis system. They are (see Figure 4.13);

Streamwise momentum

$$\frac{C_{fs}}{2} = \frac{\partial \theta_{11}}{\partial s} + \theta_{11}\left(\frac{H+2}{U_e}\frac{\partial U_e}{\partial s} - K_1\right) + \frac{\partial \theta_{12}}{\partial n} + \theta_{12}\left(\frac{2}{U_e}\frac{\partial U_e}{\partial n} - K_2\right) +$$

$$\delta_2\left(\frac{1}{U_e}\frac{\partial U_e}{\partial n} - K_2\right) + K_1\theta_{22}$$

Cross wise momentum

$$\frac{C_{fs}\tan\beta_0}{2} = \frac{\partial \theta_{21}}{\partial s} + \theta_{21}\left(\frac{2}{U_e}\frac{\partial U_e}{\partial s} - 2K_1\right) + K_2\theta_{11}(H+1) + \frac{\partial \theta_{22}}{\partial n} +$$

$$\theta_{22}\left(\frac{2}{U_e}\frac{\partial U_e}{\partial n} - K_2\right)$$

Entrainment

$$\frac{\partial \delta}{\partial s} - \frac{v_e}{U_e} = \frac{\partial(\delta-\delta_1)}{\partial s} + (\delta-\delta_1)\left(\frac{1}{U_e}\frac{\partial U_e}{\partial s} - K_1\right) - \frac{\partial \delta_2}{\partial n} - \delta_2\left(\frac{1}{U_e}\frac{\partial U_e}{\partial n} - K_2\right)$$

K_1, K_2 : geodesic curvature of the n and s lines

$$\delta_1 = \int_0^\delta (1 - u/U_e)\,dy, \quad \theta_{11} = \int_0^\delta u/U_e(1 - u/U_e)\,dy, \quad H = \delta/\theta_{11},$$

$$\theta_{21} = \int_0^\delta - wu/U_e^2\,dy, \quad \theta_{12} = \int_0^\delta w/U_e(1 - u/U_e)\,dy,$$

$$\delta_2 = \int_0^\delta - w/U_e\,dy, \quad \theta_{22} = \int_0^\delta - w^2/U_e^2\,dy,$$

$$\tan\beta_0 = \lim_{y\to 0} w/u = C_{fn}/C_{fs}$$

The above equations require closure relationships, the number of equations outnumbering the unknowns. Early methods used empirically devised relationships. Cousteix, however uses self similar solutions which by making assumptions on the development of the velocity profiles provides relations which reduce the set of equations to a system of ordinary differential equations which can then be integrated.

The calculation is in fact performed in a body fitted coordinate system formed by drawing lines on the surface of the rotor blade. The panel method must provide the external velocities in this coordinate system which is described in more detail in Appendix E.

The laminar leading edge solution for an infinite yawed wing was used to start the calculation. Transition was assumed to occur suddenly on laminar separation.

4.5.3 Viscous-inviscid coupling

As mentioned in section 4.4, the coupling of viscous and inviscid flow solvers can be approached in many ways. For attached flows, however, direct coupling should provide a good representation of the interaction. Maskew and Dvorak, [4.5], and Coton and Galbraith, [4.4], have used direct coupling along with the shear layer represenatation of separated flow with considerable success in predicting the performance of aerofoils in two dimensions and Maskew, Rao and Dvorak, [4.13], have extended the approach to three dimensions. Hirschel, [4.14], has also demonstrated the succesful use of direct coupling in estimating the position of separation on three dimensional bodies.

The link used between the viscous and inviscid flow solvers is that of effective transpiration velocity. This represents the growth of the boundary layer as an effective outflow from the surface, modifying the boundary condition for the inviscid calculation (boundary condition (ii), (a) in section 4.4.4).

The transpiration velocity is determined thus; introducing the concept of an equivalent inviscid flow, [2.50], (Figure 4.14).

The three dimensional equation of continuity is, for the viscous flow,

$$\frac{\partial u}{\partial x} + \frac{\partial v}{\partial y} + \frac{\partial w}{\partial z} = 0$$

and, for the inviscid flow,

$$\frac{\partial u_i}{\partial x} + \frac{\partial v_i}{\partial y} + \frac{\partial w_i}{\partial z} = 0$$

the difference between these two equations is

$$\frac{\partial}{\partial x}(u_i - u) + \frac{\partial}{\partial y}(v_i - v) + \frac{\partial}{\partial z}(w_i - w) = 0$$

where w denotes velocity in the z direction.

Integrating the last equation across the boundary layer from $y = 0$ to $y = \delta$ an expresssion for the normal velocity in the equivalent inviscid flow is obtained

$$v_{iw} = \frac{\partial}{\partial x}\int_0^\delta (u_i - u)\, dy + \frac{\partial}{\partial z}\int_0^\delta (w_i - w)\, dy$$

The displacement thicknesses in the x and z directions are then defined as follows

$$\delta^*_{xA} = \frac{1}{u_{iw}} \int_0^{\delta} (u_i - u)\, dy$$

$$\delta^*_{zA} = \frac{1}{w_{iw}} \int_0^{\delta} (w_i - w)\, dy$$

Hence, the transpiration velocity is given as

$$v_{iw} = \frac{\partial}{\partial x} (u_{iw}\delta^*_{xA}) + \frac{\partial}{\partial z} (w_{iw}\delta^*_{zA})$$

If there is no gradient of equivalent inviscid velocity across the boundary layer, the standard expressions replace those given above for the displacement thickness and so the transpiration velocity to a first order approximation is given by the following equation

$$v_{iw} = \frac{\partial}{\partial x} (U_e\delta^*_x) + \frac{\partial}{\partial z} (W_e\delta^*_z)$$

So by examining the rate of growth of the boundary layer it is possible to determine the equivalent normal velocity to be applied in the boundary conditions for the outer inviscid flow.

4.5.4 Separation

The concept of three dimensional separation is complex, Maskell, [2.44], but Hirschel, [4.14], gives six indicators which can be used to determine the position of separation on a three dimensional body.

These are;

1. local convergence of skin-fricion lines (or surface streamlines)
2. occurence of a minimum in skin friction
3. bulging of the boundary layer thickness or displacement thickness
4. wall shear stress approaching zero
5. sudden rise in streamwise shape parameter
6. sudden rise in transpiration velocity

These indicators were used to determine the position of turbulent separation on the rotor blade, the fifth being most useful.

4.6 Formulation for computational model

The general arrangement of the configuration of the three dimensional model is shown in Figure 4.12 relative to the co-ordinate axes. The rotor blade is modelled by a series of quadrilateral panels, see Figure 4.15, (Appendix C describes the way in which the panels are fitted to the blade surface), the interference effect of the other blades on the rotor is included by the method of images.

Over each of the flat quadrilateral panels the doublet and source distributions are assumed constant. The problem is therefore discretised and becomes one of matrix algebra, as described below.

Equation 4.13 can be summarised thus, [4.13], (see Figure 4.11),

$$\sum_{K=1,K\neq J}^{N_{OA}} (\mu_K C_{JK}) + \sum_{K=1,K\neq J}^{N_{OA}} (\sigma_K B_{JK}) + \sum_{K=1,K\neq J}^{N_{BA}} (\mu_K C_{JK}) + \sum_{K=1,K\neq J}^{N_{BA}} (\sigma_K B_{JK}) - 2\pi\mu_J +$$

$$\sum_{K=1}^{N_{OBU}} (\mu_K C_{JK}) + \sum_{K=1}^{N_{OBL}} (\mu_K C_{JK}) = 0 , \qquad J = 1,NOA + NBA \tag{4.14}$$

Where μ_K is the strength of the doublet distribution on panel K, σ_K is the strength of the source distribution on panel K, C_{JK} is the influence of a unit strength doublet distribution on panel K at panel J (calculated by the method described in Appendix B), and B_{JK} is the influence coefficient of a unit strength source distribution on panel K at panel J (calculated by the method described in Appendix A).

This forms a simple matrix algebraic problem which can be solved by Gaussian elimination.

4.7 Summary

A three dimensional model of blade aerodynamic performance has been constructed using a first order panel method and integral boundary layer calculation. The panel method has been extended to model trailing edge separation with direct coupling between the viscous and inviscid calculations ahead of separation.

The model should correctly deal with the effect of finite aspect ratio, blade interference, spanwise flows and radial pressure gradients due to rotation.

CHAPTER 5. MODEL VALIDATION

Chapters 3 & 4 described the modelling techniques applied in the new performance prediction model.

Before the model can be applied in earnest it requires validation. This is done in three stages; firstly, the panel method is applied to a series of idealised problems for which benchmark data are available; secondly, the panel method (including trailing edge separation modelling) and boundary layer model are used to synthesise two dimensional aerofoil characteristics obtained in the wind tunnel; finally, the complete model (including vortex wake) is applied to measurements taken from a highly instrumented 3m diameter rotor tested under controlled conditions.

5.1 Validation of inviscid calculation

Hunt, [4.2], stated the importance of validation of panel method codes against data produced by 'carefully constructed datum methods for... idealised problems'. Without the reassurance of such a validation full confidence cannot be expressed in the panel method when used to calculate real flow problems by coupling it to, say, a boundary layer model.

Due to the popularity of surface singularity methods in the aeronautical field Systma et al, [5.1], collated a set of datum results from third order models against which other models could be validated. This data set consisted of two wing configurations for a number of thickness to chord ratios and one nacelle problem. Only the external flow cases were used to validate the panel method used here and two of these will be described in detail.

The first is a swept wing using the NACA 0005 aerofoil section, known as the 'RAEWING', see Figure 5.1. The panel method was used to calculate the pressure distribution over this wing at 5° incidence. Figures 5.2 to 5.4 show comparisons between the results from the first order method used here and the third order method of Roberts, results presented in [5.1], for three spanwise stations, nominally 8%, 55% and 92%. The agreement is very good at the most inboard station with a very small but progressive deterioration towards the tip. This suggests that aspect ratio effects are not handled entirely correctly by the first order method with the suppression of the suction peak being too pronounced although the affect of this on lift and drag are small. More significantly the 92% station shows a 'fatter' pressure profile which would give rise to two possible affects when calculating the performance of a real aerofoil including the effects of the boundary layer. Firstly, the fatter profile would cause an over prediction in the drag and secondly, the lower pressures on the suction surface may cause a slight delay in the onset of separation.

The second test case is a straked wing using the same NACA 0005 aerofoil section, known as 'STRAKE', see Figure 5.5. Again the pressure distribution was calculated for the wing at an incidence of 5° with comparisons being made for spanwise stations of 10% and 90%, see Figures 5.6 and 5.7. Similar observations can be made about the performance of the first order method in this case with good agreement at both stations for what is a difficult test case for a first order method. For the outboard station the first order method again shows a fatter pressure distribution than the datum result although the difference between the two predictions is much smaller.

In conclusion the first order panel method is capable of calculating the aerodynamic performance of three dimensional wings with a good degree of accuracy.

5.2 Two Dimensional Verification of Panel Method Against Wind Tunnel Data

In order to gain confidence in the modelling of separated flows with the shear layer model a quasi two dimensional study was undertaken to verify the method against published wind tunnel data for the NASA LS(1)-0421mod aerofoil McGhee & Beasley, [5.2]; this section is particularly relevant as it has been popular in the U.K. wind turbine community for the past few years, e.g. [1.3]. It has also been used as a test case (in its unmodified form as the GA(W)-1) by Maskew et al [4.12]. Also the blunt, cusped trailing edge provides a stiff test for a panel method calculation.

The performance of the aerofoil at a Reynolds number of 2×10^6 was examined. Variation of Reynolds number was not undertaken as this would have a large effect on the boundary layer model alone.

The first stage of the verification exercise was to predict the aerofoil performance at a low angle of attack where the flow is fully attached.

Initially a problem was found with the definition of the rear loading present on the LS(1) series of aerofoils. This loading is due to the cusp at the trailing edge lower surface. It was necessary to accurately define this cusp and the trailing edge thickness in order to get a good representation of this loading.

Introducing the boundary layer transpiration effect also improved the shape of the C_p distribution in the vicinity of the trailing edge, by reducing the pressure on the upper surface and rounding the pressure distribution in the region of the cusp.

The final pressure distribution calculated for an incidence of 3.9° is shown in Figure 5.8. In this figure, and also Figures 5.9-10 and 5.12-13, the present prediction is labelled as "Predicted 3D"; in addition to the un-corrected wind tunnel data of McGhee & Beasley [5.2], these figures also show the prediction of a panel method without free shear layer, labelled as "Attached 2D". The predicted lift coefficient at an incidence of 3.9° is within 4 percent of the measured value and the pressure drag (no skin friction effects are accounted for) is 78 percent of the total measured value (which includes viscous effects).

The next case was for an angle of attack of 10.1°; this has a moderate amount of separation (20 percent of chord). Carrying over the results of the previous case produced encouraging results with the only real error being in the prediction of base pressure (Figure 5.9). This error is relatively small causing a slight overprediction in lift and a rather larger one in drag. The biggest cause of error however would be introduced by the boundary layer seeing this pressure gradient and incorrectly specifying the separation point.

This was not pursued further as this is the region where the shear layer model is known to poorly represent the flow, i.e. for moderate (20% chord) trailing edge separation.

Further increasing the angle of attack resulted in two further problems. These were centred around the shear layer and trailing edge geometry. The base pressure and lower trailing edge pressure distribution were found to be very sensitive to these shapes at the trailing edge.

Firstly, this manifested itself in either very large over or underprediction of base pressure (Figure 5.10). The problem appears to have been one of 'interference' between the wake panels and the panels on the aerofoil. This occurred at high angles of attack because the prescription of the lower wake geometry was initially the same as that for lower angles of attack. As the aerofoil was 'rotated' the fine detail in the trailing edge geometry meant that control points on the wing became very close to those on the lower wake panels (Figure 5.11). This distorted the application of the Kutta condition and so affected the base pressure considerably.

The problem could be partially removed by reducing the resolution of the panelling in the trailing edge region but required that the trailing edge thickness be reduced to zero to remove all trace of it. This did not seem an unreasonable change to the model as the upper surface is encapsulated by the shear layers and so its exact geometry has little effect on the overall solution. In fact this was taken to the extreme by reducing the resolution beyond the separation point quite considerably (the resolution up to separation being important for correct application of the Kutta condition and therefore the prediction of base pressure) without any real effect on the overall pressure distribution.

The other problem was the prediction of lower surface pressure distribution. At first this appeared to be due to the incorrect base pressure 'dragging' the lower surface pressures down. However when the base pressure problem was solved this remained. This was solved by a sensitivity study on the effect of panel sizes on the lower surface and those on the lower wake. It was found that if there was not enough resolution in the panelling on the aerofoil the cusp effect was lost (Figure 5.12), but that if the panels in the wake were too large in comparison with those on the aerofoil the interference effect showed itself causing an over prediction of the base pressure. A compromise was struck by increasing the resolution in the wake and aerofoil panelling at the trailing edge. The resulting pressure distribution is shown in Figure 5.13 for an angle of attack of 15.3 degrees. The lift coefficient is within 5 percent of the measured value.

The boundary layer model of Cousteix [4.11] was used throughout this study to check the location of separation point. Because of the difficulties that were found initially this was quite problematic but when the pressure distribution matched that of the experiment so did the separation point predicted by the boundary layer code.

5.3 Validation of complete code

Validation of the complete code (panel method with trailing edge separation modelling, boundary layer code and the vortex wake model) is achieved using measurements from a highly instrumented turbine of 3m diameter which has been tested under controlled conditions.

5.3.1 Measurements

At Cranfield a small turbine, Bellia & Hales, [2.30], has been developed for controlled velocity testing. The measurements taken include pressure distributions at two radial stations (35%R and 75%R) which are obtained at 128 azimuthal stations per revolution. There are no more than 19 pressure taps at each station which limits the detail of the measurement.

The measured data used in this study consists of four runs of approximately seven seconds duration (forty revs) over which the input to the turbine and its response (rotor torque) are considered steady.

5.3.2 Predictions

The Cranfield turbine uses a nominal NACA 4415 aerofoil section. In order to check the behaviour of the model for this section comparison was made with two dimensional data for the NACA 4412 profile, Hastings & Williams, [5.3], see Figure 5.14. This showed that the most significant problem lies in the trailing edge region where coarse panelling can lead to poor definition of the pressure distribution. This was overcome by using the following modification to the Kutta condition.

The Kutta condition matches the pressure on the trailing edge panel on the pressure surface with that on the separation panel on the suction surface. A good estimation of the base pressure is essential if the position of the separation line is to be calculated correctly.

Problems arise if fine panelling is used in an attempt to obtain a well defined pressure distribution in the trailing edge region, particularly if the blade is twisted or tapered, see section 5.2.

However, if the panelling is too coarse at the trailing edge then the control point on the pressure surface trailing edge panel is too far away from the trailing edge and so the estimate of suction surface base pressure is too high.

When attempting to model the NACA 4412 aerofoil it was found that good agreement between measured and predicted separation point and base pressure was obtained with relatively coarse panelling if the Kutta condition of equal pressures at the suction surface separation and pressure surface trailing edge was relaxed. This relaxation amounted to a difference in pressures of 10% for this aerofoil at the one condition available from [5.3].

The percentage difference in pressure allowed for in the modified Kutta condition will however vary with angle of attack and trailing edge geometry (cusped aerofoils requiring larger values, see Figure 5.15). Therefore a calibration exercise would normally be required for any particular aerofoil before applying it on a rotor. This was not performed for the Cranfield rotor however as pressure distribution data was available and so the calibration could be performed as the pressure distributions were produced by the model. This is further discussed in section 6.1.

The three dimensional prediction code was applied to the four separate runs starting with the lowest windspeed and moving progressively upwards. This has the advantage of using the converged solution at a lower windspeed as the starting point for the next, thus reducing computer usage.

The measured and predicted power, is shown in dimensionless form in Figure 5.16, along with a strip theory prediction (Hibbs & Radkey, [2.5]).

The predicted power is seen to follow the measured power quite well even at the lowest tip speed ratio (< 2.5). Some over prediction is seen here but this is exacerbated by the presence of 9 degrees of yaw in the measured data (the lack of high wind data meant that a small amount of yaw had to be accepted in this case).

5.3.3 Pressure distributions

Looking at the measured and predicted pressure profiles gives a greater insight into the performance of the model. All comparisons are made for measured pressures at top dead centre to avoid tower/nacelle blockage effects.

Taking the highest windspeed case the instantaneous measured pressure profiles at top dead centre for both the 35%R and 75%R stations are shown for all forty revolutions in Figures 5.17 and 5.18. These show a qualitative difference in the flowfields experienced by the two stations.

At the 75%R station the flow is essentially steady with a significant region of trailing edge separation.

At the 35%R station the pressure distributions indicate an unsteady flowfield, with a large suction peak being present in some cases and a fully stalled, flat topped profile evident in others. This is illustrated more forcefully in Figure 5.19, which shows pressure profiles at top dead centre for two consecutive revs. They suggest that with the small perturbations of free-stream turbulence, the blade root aerodynamics 'flips' unstably between two flow states. The problem is 'What do we expect the model to predict ?'.

This can be answered by describing the process of achieving a converged prediction. As mentioned earlier the blade aerodynamic performance for a particular flow condition is calculated in an iterative fashion. The inviscid flow is calculated to give a pressure distribution which is fed into the boundary layer model. The boundary layer model has essentially two outputs, a transpiration velocity which indicates the displacement effect of the boundary layer and the position of separation. These outputs modify the boundary condition for the inviscid flow and the process is repeated until the separation point for each radial station does not move from one iteration to the next. As windspeed increases the angle of attack seen by the blade does likewise and so the separation point moves forward on the blade. It was found that converged solutions were obtained for separation points between approximately 35% and 100% chord. However, if the separation point for a particular iteration was ahead of 35% chord then for subsequent iterations the separation moved rapidly to the leading edge. This indicates that the high suction peaks seen at the 35%R station are transients and that the underlying steady performance of this blade station for this windspeed is the fully stalled case. This is, of course, what the model predicts, Figure 5.20 (here the measured data is an average of the pressure profiles measured over 6 consecutive revs within the forty revs over which power is averaged).

Figure 5.20 shows the fully stalled profile at the 35%R station (predicted angle of attack = 36°). The significant difference here is at the trailing edge, particularly on the pressure surface. The model underpredicts the pressure in the trailing edge region, with the measured profile showing a pressure recovery in the separated region. This, as discussed futher in section 6.2, is partly due to the relatively coarse panelling used at the trailing edge. Another contributing factor could be the Kutta condition fixing the relative pressures at the trailing edge and separation point; the measured profile has a slight pressure gradient in the separated region.

Figure 5.21 shows the measured and predicted pressure distribution at the 75%R station (predicted angle of attack = 21°). This shows a region of trailing edge separation with a moderate suction peak. Again the predicted pressure on the pressure surface trailing edge is underpredicted. The predicted pressure distribution appears to be at a lower angle of attack than the measured data suggests; the suction peak is lower and the pressure distribution around the stagnation point is not as full. However, it should be remembered at this point that the measurements were taken at a yaw angle of 9° which would introduce some uncertainty in the dynamic pressure used to produce the measured Cp distribution. The angle of attack may be underpredicted because of an overestimate of the wake induced velocities. The rotor wake was defined on the basis of a sensitivity study with no input from field measurements. The convection rate has been set at its maximum value, equal to windspeed, and so the only possibility for reducing the induced velocities is to reduce the extent of the wake.

5.3.4 Lift and drag coefficients

Lift and drag coefficients are derived for each station in the performance prediction code. These are plotted in Figures 5.22 and 5.23 as individual spots each referring to a radial station for one of the four windspeed cases. On the same figures two dimensional wind tunnel data are plotted for the NACA 4415 section at the 75%R station Reynolds number of 0.37 million.

The drag coefficient shows no systematic difference from the two dimensional data.

The general trend of the predicted lift shows a reduced lift curve slope, an increase in the stall angle and a gentler stall. These characteristics may be due to the fairly low aspect ratio of the rotor blades (~ 6.5), [2.38]; similar observations have been made on larger machines by Butterfield (aspect ratio ~ 8.5), [2.28], and Madsen et al (aspect ratio ~ 10), [5.4].

The reduction in the lift curve slope corresponds to the lower slope of the measured and three dimensional predicted power curve when compared with that predicted by strip theory using the two dimensional input data, Figure 5.16.

In order to test the validity of this derived three dimensional data it was applied to the Vestas 15, [2.32], a 15m diameter rotor which uses NACA 44xx series aerofoils. The data was used in a blade element model which is linked to the same vortex wake model as used in the full code. The resulting power curve, Figure 5.24, shows good agreement for tip speed ratios above 2.5 (the lowest tip speed ratio examined in the validation exercise) and provides a much improved prediction when compared to one which uses two dimensional data at the appropriate Reynolds number (the flapwise root bending moment is also well predicted, Figure 5.25).

5.4 Summary

Before applying the panel method code to a real wind turbine problem it was required to validate the model against three types of data.

Firstly, inviscid flow cases were compared with benchmark data produced by a higher order (and therefore more accurate) code. The comparison was favourable, with aspect ratio effects being handled correctly. The only concern was a slight difference in the prediction of pressures at the trailing edge of the swept wing case near the wing tip.

The second exercise attempted to synthesise two dimensional behaviour of an aerofoil in a wind tunnel. This included the separated flow modelling using the shear layer model. The main conclusion from this study is that the panel method when coupled to the shear layer model for separated flows lacks some of the robustness it shows for attached flow predictions but still remains a powerful means of calculating aerofoil performance at high angles of attack.

The complete three dimensional performance prediction code was then applied to a highly instrumented 3m diameter rotor, tested under controlled conditions.

Slight modification of the assumptions made about the trailing edge pressure distribution was required in order to produce good agreement without resorting to detailed panelling in this region. This modification at the trailing edge also made the code more robust as fine panelling can lead to panel interference effects (see 5.2).

The resulting performance prediction showed reasonable agreement both for the integrated rotor power and also the performance of the aerofoil sections at the two instrumented stations.

An instability in the flowfield for the inboard station was identified in the highest windspeed case, this behaviour being imitated by the code.

The measured data showed a slight pressure gradient in the separated region which is not modelled by the code which assumes constant pressure aft of separation.

For the highest windspeed case at the 75%R station the predicted pressure distribution appeared to be at a slightly lower angle of attack when compared to the measured data, the suction peak being lower and the Cp curve being less rounded about the stagnation point.

Significant differences between the three dimensional behaviour of the rotor blade aerodynamic section (NACA 4415) were found when compared to two dimensional wind tunnel data for the same section. These differences could be partly attributed to the effect of aspect ratio.

The derived three dimensional aerofoil data was used in a blade element model to predict the performance of a 15m diameter rotor which also uses the NACA 44xx aerofoil family. The resulting prediction showed good agreement with measurement and considerable improvement over a prediction using two dimensional wind tunnel data for the appropriate Reynolds number.

CHAPTER 6. APPLICATION TO STALL REGULATED MACHINES

In order to understand the mechanism of stall regulation it is sensible to examine rotors which use it successfully. Only then can the concept be confidently extended to large scale.

Considerable interest has been shown in Danish wind turbines due to their successful use of stall regulation. In this chapter two similar stall regulating rotors are examined, both of which use blades manufactured by LM Glasfiber.

Firstly the 180kw Danwin machine at 22m diameter uses the LM 10.5 blade; measurements of power, thrust and bending moment are available for this rotor, [2.34].

Secondly the LM 17.2 m diameter prototype rotor, [6.1], for which both power and root bending moment measurements are available.

These machines have added interest as they were the subject of an exercise at Risø, [2.34], which synthesised three dimensional aerofoil performance data using the detailed measurements on the larger machine and then applied the derived lift and drag curves to the (very similar) smaller machine. The resulting prediction was disappointing with the maximum power considerably over-predicted.

6.1 Generation of lift curve for the NACA 632215 aerofoil at Re 3 million

No pressure distribution data is available concerning the NACA 632-200 aerofoils so the only way to calibrate the method is to use data of lift coefficient versus incidence. This is unsatisfactory as peculiarities of the aerofoil performance may be hidden in the lift curve; pressure distributions would be of much greater value. It should also be noted that the NACA 63 aerofoils do not form a 'series' in the conventional sense, the camber and thickness distributions being different for the various thicknesses. The data used here are for the NACA 632215 profile taken from [6.2].

In an exercise similar to that described in section 5.2 a two dimensional lift curve is generated by using the code to model a high aspect ratio (>30) wing. The lift is calculated at a series of incidence values on the linear part of the lift curve using fully attached flow but applying the boundary layer code to give the displacement effect of the boundary layer. Any separation predicted by the boundary layer is ignored until the separation moves ahead of 80% chord (this is because it is difficult to obtain a converged solution for small regions of separation). When the separation point moves ahead of the 80% chord position the panel method near wake is redefined to leave the suction surface at the back edge of the panel upon which separation is indicated to have occurred. The viscous and inviscid models are used in an iterative cycle until a converged solution occurs. This is when the modified Kutta condition (see 5.3) is brought into play; if the resulting converged solution produces too low a value of lift then the percentage difference between the trailing edge pressure and that at the suction surface separation point is increased and vice versa. For the NACA 632215 section it was found that no significant separation occurred up to an angle of incidence of 14°. The difference between the pressures at the separation point and trailing edge at this incidence was 22%; this value decreased progressively with incidence, 12% being required at 18° incidence. This variation of the Kutta modification with angle of attack was considered to be too complicated for use on the rotating blade for two reasons.

Firstly, the performance of the aerofoil in the context of a rotating three dimensional blade is expected to differ from that of the quasi two dimensional (high aspect ratio) wing. In particular the suction peak for a three dimensional wing would be suppressed due to aspect ratio effects so the required variation of Kutta modification with angle of attack would be different.

Secondly, when a solution is being obtained for a rotating blade case the angle of attack variation along the blade may change from one iteration to the next. This would make the application of any rule about Kutta modification versus angle of attack very difficult to apply.

In order to overcome these difficulties a 2-zone formulation of the modified Kutta condition was devised. This depends on the variation of the chordwise position of separation. The 2-zone model uses the following rules:-

For separation positions between 80% and 60% chord use a Kutta modification of 22%.

For separation positions ahead of 60% chord use a Kutta modification of 12%.

This simplified representation might be expected to have one detrimental effect on the modelling. By switching straight over to a value of 12% from 22% the onset of stall may be accelerated, with the post stall behaviour of the sections unaffected. Nonetheless, this formulation of the Kutta condition was applied to the Danwin 22m rotor without causing unwanted effects convergence.

6.2 The Danwin 22m rotor

The performance of the Danwin 180kW machine is documented in [2.34]. The power curve presented stops short of stalled performance although the curve shows evidence of the onset of stall at the highest windspeed of 16m/s.

6.2.1 Initial Power Curve

First attempts to produce power and thrust versus windspeed curves showed an improvement over a strip theory prediction, [2.5], but the slope of the power curve was much lower than the measurement, Figure 6.1. The thrust prediction showed very good agreement, Figure 6.2, as did the bending moments at all three radial stations, Figure 6.3, suggesting that the out of plane force is well represented by the model. An examination of the derived lift and drag coefficients shows that the lift curve slope is somewhat reduced for all spanwise stations when compared to the two dimensional data and the stall is much less pronounced, Figure 6.4. The reduction in the slope at the inboard stations is due to the blade only being modelled from the start of the aerodynamic surface, thus leaving a 'free tip' at the root; this unrealistic treatment may cause an overestimate of the effect of aspect ratio but should have a small effect on rotor power. More significantly the derived drag coefficients are much higher than the two dimensional values for incidences in the region 5°-20°, Figure 6.5. The higher values of drag in this region may be caused by one or more of the following.

Firstly, a three dimensional wing would show a reduced value of suction peak for any particular angle of attack when compared with two dimensional performance; this would result not only in a reduction in lift curve slope but also an increase in drag.

Secondly, the 2-zone model may give rise to a low value of base pressure for this incidence range which would give rise to higher drag.

Thirdly, the measurements at Cranfield, [2.30], showed the presence of pressure gradients in the separated regions of flow, these are not catered for in the model (which fixes base pressure at the suction surface separation point) and would have a greater effect on the drag than the lift in the incidence range concerned.

Fourthly, the calibration exercise on the NACA 632215 aerofoil used only lift and drag coefficients. Without pressure distribution data full confidence cannot be expressed in the calibration process.

6.2.2 The Effect of Drag Coefficient on Rotor Performance

In order to examine the effect of the increased drag coefficient on rotor performance the derived lift and drag curves were used in a blade element model. Figures 6.6 and 6.7 show the predicted rotor power and thrust using the derived lift curves but with modified drag curves which have drag buckets extending to the onset of stall, similar to those seen in the two dimensional data. The power is well represented although the thrust at higher windspeeds shows an increasing discrepancy.

The modification of the drag curve is somewhat crude - fixing the drag coefficient at the lowest value calculated below stall and then using the derived values beyond stall. Further modification would yield better agreement with measurement although such treatment can only be justified pragmatically.

6.3 LM 17.2m prototype rotor

The performance of this rotor is documented in [6.1], the power curve showing a fairly sharp stall at a windspeed of about 13 m/s (for a tip angle of 2.5°) and the root flapwise bending moment showing an upward trend throughout the windspeed range.

The performance was initially predicted using the panel method, boundary layer and vortex wake model. It was similarly found that the out of plane force was well predicted by the three dimensional model but the power was under predicted. The derived lift and drag coefficients were then used in a blade element model, the drag coefficient being modified in the incidence range 5°-20°; the resulting power curve is shown in Figure 6.8. The predicted peak power is in good agreement with the measurement but the performance at and around stall is not accurately represented.

This could be further improved by further modification to the drag but as stated above (see 6.2.2) such treatment can only be justified pragmatically.

6.4 Differences between '3D' data for the 22m and 17.2m rotors

As mentioned above an attempt was made in [2.34] to apply aerodynamic profile data derived from the Danwin 22m machine to the smaller LM 17.2m rotor. The result was disappointing with the resulting prediction of rotor power for the smaller machine showing a large discrepancy (over prediction) at high winds. This implies that the derived aerodynamic characteristics were not universal.

In order to examine this the data derived from the two successful applications of the three dimensional model should be compared. The data examined here is that derived directly from application of the three dimensional code before the drag was modified below stall.

Figure 6.9 shows lift coefficients derived from the three dimensional code for both the 22m and 17.2 m machines at about 50% span. In general there is very little difference between the two curves; slightly less lift being generated by the smaller rotor below stall, this is typical of the derived lift coefficients at all spanwise stations.

The drag coefficients in Figure 6.9 show two effects. The steepness of the drag curve post stall increases with span and for the same spanwise station the smaller machine shows higher drag post stall. This is thought to be due to the influence of aerofoil thickness, the larger machine having a greater variation in thickness from root to tip, with both rotors having 12% thickness at the tip; in [2.38] thinner sections were demonstrated to have steeper drag versus incidence curves post stall. Therefore the difference in the performance of the rotors' aerodynamic sections must be due to their different thickness distributions.

6.5 Summary

The ability of the code to predict peak power levels of stall regulated machines has been demonstrated by applying the code to two similar Danish rotors.

Lift and drag curves were used to calibrate the modified Kutta condition as no pressure distribution data were available. This lack of appropriate two dimensional characteristics resulted in the need for retrospective manipulation of the drag bucket.

Three dimensional derived lift and drag curves for the 22m and 17.2m rotors show a reduced lift curve slope, and a more gentle, delayed stall when compared with two dimensional data.

Comparison of two similar rotors, one 17.2m in diameter and the other of 22m diameter, suggests the difference in their detailed performance may be due to their different thickness distributions inboard. The aerofoil drag at and just after stall is a major contributor to stall regulation. Any attempt to develop a simple model of 'three dimensional aerofoil' characteristics should account for the thickness as well as spanwise effects on drag.

CHAPTER 7. CONCLUSIONS

The problem of stalled HAWT rotor performance involves a number of different aspects of computational aerodynamics. These 'components' have been assembled to provide an 'engineering solution' for the blade designer.

7.1 The performance model

No incontrovertible experimental evidence yet exists which points to any stalling mechanism peculiar to the rotor blade in steady conditions. Flow visualisation (and other) evidence suggests the stall is caused by turbulent separation at the rear of the aerofoil growing in extent from the root with increasing wind. The evidence suggests that flow is chordwise for the attached part and (roughly) spanwise in the shear region. This 'picture' of the stalling HAWT rotor has been modelled by the code.

Due to the complex nature of the HAWT rotor flowfield pragmatism played a part in the definition and development of the performance model.

A prescribed vortex wake model was chosen for the calculation of induced velocities. A first order panel method was used for the blade aerodynamic performance model as this approach has been successful in predicting the performance of real flow problems with few of the limiting assumptions associated with more idealised flow solvers. A three dimensional integral boundary layer calculation was used to determine the separation line on the rotor blade. Direct boundary layer coupling was used with an inviscid model of the strong interaction between the free shear layers enclosing the region of trailing edge separation.

The combination of these building blocks provides a detailed model of the flowfield. Detailed validation was achieved in three stages. The inviscid panel method was applied to idealised problems for which datum solutions are available. This showed the first order method to behave well for purely inviscid problems. The trailing edge separation model was then used to synthesise published two dimensional performance of the NASA LS(1)-0421 mod aerofoil. This showed that the approach lacked robustness for this particular type of aerofoil and pointed to problems when applying the code to a three dimensional rotor blade with twist and taper. Finally the complete code was used to model the performance of a highly instrumented 3m diameter wind turbine which had been tested under controlled conditions. This exercise yielded a modification to assumptions made about the trailing edge pressure distribution which restored robustness to the code.

7.2 Results

In an attempt to understand the behaviour of the rotor wake a prescribed model was developed and used to undertake a study of the dependence of rotor performance on wake geometry and constituent elements. This showed that the geometry of the rotor wake becomes less important as windspeed increases and that the most important aspect of wake geometry is the convection rate; in high winds the geometry of the wake has minimal effect on the prediction of rotor power. This indicated that the problem of poor prediction of stalled rotor power is concentrated in the prediction of blade aerodynamic performance.

During the validation of the code against measurements taken on a 3m diameter rotor significant changes in the aerodynamic performance of the aerofoil section were found when compared to its two dimensional characteristics. The lift curve slope was reduced and the stall more progressive and delayed. This behaviour is consistent with the effect of finite aspect ratio. These derived coefficients were then applied to a 15m diameter machine which uses the same aerofoil section family. The resulting performance prediction showed very good agreement with measurement and considerable improvement over a prediction using two dimensional wind tunnel data for the sections at the appropriate Reynolds number.

Application of the code to two similar Danish stall regulated machines also showed significant differences between the behaviour of the blade's aerofoil sections when compared to their behaviour in two dimensions. Again the lift curve slope was reduced and the stall more progressive and delayed. During this application it became necessary to modify the drag coefficients derived from the code in order to achieve good agreement with measurements below stall. This was due to the lack of two dimensional wind tunnel data for the aerofoil sections used, NACA 632-200, which prevented detailed two dimensional validation of the code before its application to the three dimensional rotor problem.

7.3 Concluding remarks

The objective of this project was to produce a validated performance model of a stall regulated wind turbine capable of predicting high wind performance. The applications of the code (Chapter 6) illustrate that this has been achieved.

No peculiar stalling mechanism has been postulated in the model. What the modelling has provided is a flexible method of estimating the velocity distribution over the blade which takes account of the extent of turbulent separation. In this sense, the treatment is genuinely three dimensional; accounting for relevant features such as aspect ratio. The applications of the code have shown that the treatment can provide an improved performance prediction, subject to the important requirement for reliable two dimensional characteristics for the aerofoils employed. The availability of measured pressure profiles typical of the pre-stall and post-stall flow states is crucial for the confident prediction of aerofoil drag, and hence peak rotor power.

The study of the instrumented 3m diameter rotor, [2.30], has proved most useful in the development of the prediction method. It is recommended that detailed studies of the instrumented rotors at SERI, [2.28], and Risø, [2.29], be carried out as the complete measurements become available.

APPENDIX A. CALCULATION OF SOURCE INFLUENCE COEFFICIENTS

The source influence coefficients of equation 4.14 are calculated from the geometry of the problem. Considering each flat panel in turn and calculating its influence at the control point of all other panels on the surface. The following description of this process is taken from [4.10].

The integration of the basic point-source formulas over one of the quadrilateral elements used to approximate three dimensional bodies is most conveniently performed in a co-ordinate system for which the element lies in a co-ordinate plane. Specifically, the quadrilateral is taken to lie in the xy-plane as shown in Figure A.1. The positive z-axis (upward in Figure A.1) of the co-ordinate system is in the direction of the unit outward normal to the element (see Appendix C). The four points at the corners of the quadrilateral are denoted by subscripts 1, 2, 3, 4, where the numbering denotes the order in which the corner points are encountered as the perimeter of the quadrilateral is traversed in the clockwise sense as seen from the positive z-axis. The co-ordinates of the corner points are ξ_k, η_k, 0, where k = 1, 2, 3, 4, and the maximum dimension of the quadrilateral is denoted by t. The origin of the co-ordinate system is taken as the centroid of the quadrilateral.

It is desired to calculate the potential induced by a quadrilateral panel having a constant strength source distribution at a point in space. The point in element co-ordinates is x,y,z. The distance between this point and a point on the quadrilateral $\xi,\eta,0$ is

$$r = \sqrt{(x-\xi)^2+(y-\eta)^2+z^2} \qquad \text{A.1}$$

For a unit value of source density, the potential due to the quadrilateral at point x,y,z is

$$\phi = \iint_A \frac{dA}{r} \qquad \text{A.2}$$

where A denotes the area of the quadrilateral. This integral can be obtained exactly by analytical means. Firstly a cylindrical co-ordinate system is introduced, whose axis is parallel to the z-axis with origin at x,y,0 as shown in Figure A.2. The polar angle θ is measured clockwise from any convenient reference direction, which is shown as the negative x-axis in Figure A.2. The distance from the axis of the cylindrical co-ordinate system is denoted by R, given by

$$R = \sqrt{r^2+z^2} \qquad \text{A.3}$$

and thus

$$\phi = \iint_0^R \frac{RdRd\theta}{\sqrt{R^2+z^2}} \qquad \text{A.4}$$

The R integration is carried from R = 0 to a point on the perimeter, and the θ integration is around the perimeter in the clockwise sense. The contribution of each side of the quadrilateral to the integral represents the plane triangle defined by the endpoints of the side and the point x,y,0. As the perimeter is traversed in the clockwise direction the incremental angle dθ is positive if the point x,y,0 lies to the right of the side and negative if it lies to the left. Thus when the potentials of the triangles corresponding to all four sides of the triangle are summed the contributions of the portions of the triangles outside the quadrilateral sum to zero, and the result is the potential of the quadrilateral itself.

Now

$$dr = \frac{RdR}{\sqrt{R^2+z^2}} \qquad \text{A.5}$$

and so the integral can be reduced to

$$\phi = \int\left[\int_{|z|}^{r} dr\right]d\theta = \int(r-|z|)\,d\theta \qquad \text{A.6}$$

since z does not depend on position on the perimeter, this can be written

$$\phi = \int r\,d\theta - |z|\Delta\theta \qquad \text{A.7}$$

where $\Delta\theta = 0$ if x,y,0 lies outside the quadrilateral

and $\Delta\theta = 2\pi$ if x,y,0 lies inside the quadrilateral

Thus the second term of the resulting integral is discontinuous as x,y,0 crosses a side of the quadrilateral. The first term has an equal and opposite discontinuity and thus the potential is continuous. The integral is calculated as the sum of the contributions of the four sides of the panel. To express the contribution of the side between the points $\xi_1,\eta_1,0$ and $\xi_2,\eta_2,0$ to the integral the following geometric quantities, most of which are illustrated in Figure A.3. must be defined. The length of the side is

$$d_{12} = \sqrt{(\xi_2-\xi_1)^2+(\eta_2-\eta_1)^2} \qquad \text{A.8}$$

The cosine and sine of the slope angle of the side with respect to the x-axis are, respectively

$$C_{12} = \frac{\xi_2 - \xi_1}{d_{12}} \qquad S_{12} = \frac{\eta_2 - \eta_1}{d_{12}} \tag{A.9}$$

A perpendicular to the side is drawn from $x,y,0$ and arc length s_{12} is measured along the side from the intersection of the perpendicular with the extension of the side. The positive direction of s_{12} is that from $\xi_1,\eta_1,0$ to $\xi_2,\eta_2,0$. The arc length associated with a general point on the side is

$$s_{12} = (\xi-x)C_{12} + (\eta-y)S_{12} \tag{A.10}$$

In particular the arc lengths associated with the corner points $\xi_1,\eta_1,0$ and $\xi_2,\eta_2,0$ are respectively,

$$s_{112} = (\xi_1-x)C_{12} + (\eta_1-y)S_{12} \tag{A.11}$$

and

$$s_{212} = (\xi_2-x)C_{12} + (\eta_2-y)S_{12} \tag{A.12}$$

The signed perpendicular distance of the point $x,y,0$ from the extension of the side is

$$R_{12} = (x-\xi_1)S_{12} - (y-\eta_1)C_{12} \tag{A.13}$$

This distance is positive if $x,y,0$ lies to the right of the side with respect to the direction from $\xi_1,\eta_1,0$ to $\xi_2,\eta_2,0$ and negative if $x,y,0$ lies to the left. The co-ordinates ξ_2,η_2 could replace

ξ_1,η_1 without changing the value of R_{12}. The distances of the point $x,y,0$ to the corner points $\xi_1,\eta_1,0$ and $\xi_2,\eta_2,0$ are respectively,

$$r_1 = \sqrt{(x-\xi_1)^2 + (y-\eta_1)^2 + z^2} \qquad \text{A.14}$$

and

$$r_2 = \sqrt{(x-\xi_2)^2 + (y-\eta_2)^2 + z^2} \qquad \text{A.15}$$

The required integral can be expressed in terms of the following two quantities:

$$Q_{12} = \ln\left(\frac{r_2 + s_{212}}{r_1 + s_{112}}\right) = \ln\left(\frac{r_1 + r_2 + d_{12}}{r_1 + r_2 - d_{12}}\right) \qquad \text{A.16}$$

and

$$J_{12} = \operatorname{sgn}(R_{12}) \left[\tan^{-1}\left(\left|\frac{z}{R_{12}}\right| \frac{s_{212}}{r_2}\right) - \tan^{-1}\left(\left|\frac{z}{R_{12}}\right| \frac{s_{112}}{r_1}\right)\right]$$

$$= \tan^{-1}\left[\frac{R_{12}|z|(r_1 s_{212} - r_2 s_{112})}{r_1 r_2 R^2_{12} + z^2 s_{212} s_{112}}\right] \qquad \text{A.17}$$

The second form of the logarithm in A.16 is to be preferred, since the first is indeterminate along the extension of the side. In the first form of A.17 the inverse tangents are evaluated in the principal value range $-\pi/_2$ to $\pi/_2$, and in the second form in the range $-\pi$ to π by considering the individual signs of the numerator and denominator of its argument. The contribution of the side between $\xi_1,\eta_1,0$ and $\xi_2,\eta_2,0$ to the integral is

$$\phi_{12} = R_{12}Q_{12} + |z|J_{12} \qquad \text{A.18}$$

The contributions of the other sides can be calculated from the above equations by advancing the sub and superscripts cyclically.

Thus the potential at the point x,y,z induced by the quadrilateral panel is

$$\phi = \phi_{12} + \phi_{23} + \phi_{34} + \phi_{41} - |z|\Delta\theta \qquad \text{A.19}$$

It may be verified from these equations that no difficulty is encountered in calculating the effects of an element at its own control point. The Q's are singular only on the sides of the quadrilateral panel and for $z = 0$ all the J's vanish. Incidentally $\Delta\theta$ is easy to evaluate; it is 2π if R_{12}, R_{23}, R_{34}, and R_{41} are all positive, and zero otherwise.

Evaluation of the above analytic expressions for the influence of a quadrilateral panel is quite time consuming involving logarithms, inverse tangents and square roots. The complicated nature of the formulae arises from the fact that they account for the effects of all the details of the shape of the quadrilateral. It is intuitively plausible that if the point x,y,z is sufficiently far from the quadrilateral, the details of the shape of the quadrilateral are unimportant, and the induced potential depend mainly on certain overall parameters that characterise that shape. This consideration leads to approximation by means of a multipole expansion of the type commonly used in electrostatics.

Again the situation is shown in Figure A.1. It is desired to approximate the integral of A.2 that gives the potential induced by the quadrilateral at the point x,y,z. To accomplish this, the integrand of A.2 which is simply 1/r, is expanded in a Taylor series in ξ and η about the origin. The coefficients in the series being independent of ξ and η, may be taken out of the integral. Through terms of second order the result of thus expanding A.2 is

$$\phi = I_{00}w - (I_{10}w_x + I_{01}w_y) +$$

$$0.5*(I_{20}w_{xx} + 2I_{11}w_{xy} + I_{02}w_{yy}) + .. \qquad \text{A.20}$$

where

$$I_{nm} = \iint \xi^n \eta^m \, dA \qquad \text{A.21}$$

and where w is the reciprocal of the distance r_0 from the origin of co-ordinates to the point x,y,z, that is,

$$w = \frac{1}{r_0} = \frac{1}{\sqrt{x^2 + y^2 + z^2}} \qquad \text{A.22}$$

The subscripts x and y denote partial derivatives with respect to these variables. These derivatives depend only on the location of the point x,y,z with respect to the origin of co-ordinates and are independent of the shape of the quadrilateral. On the other hand, the quantities I_{nm} depend only on the shape of the quadrilateral and are independent of the location of the point x,y,z. They may be evaluated once and for all for each quadrilateral. The I_{nm} are the moments of various orders of the area of the quadrilateral about the origin. In particular I_{00} is just the area of the quadrilateral, I_{10} and I_{01} are the first moments, and I_{20}, I_{11}, and I_{02} are the second moments or "moments of inertia". Higher order terms of the expansion consist of products of higher order derivatives of w and higher order moments of the area. Such an expansion may be rigorously shown to converge if the point x,y,z is farther from the origin than any point of the quadrilateral.

The designation multipole expansion arises from the fact that various terms in equation A.20 may be interpreted as the potentials of point singularities of various orders located at the origin. Thus the first term is the potential of a point source. The second term consists of the potentials of two point dipoles, whose axes lie along the x-axis and the y-axis, respectively. The third term contains the potentials of the three independent point quadrupoles with axes in the xy-plane. The strengths of the singularities are the various moments of the area of the quadrilateral. The effect of each successive higher order singularity decreases with a successively higher power of the distance r_0. Thus the expansion may be interpreted as giving the effect of the quadrilateral in terms of its overall geometric properties "in order of their importance" at some distance from the quadrilateral.

In actual calculation the expansion is not carried beyond the second order terms shown. Since the centroid of the area of the quadrilateral is used as the origin of the co-ordinates, the first moments I_{10} and I_{01} are zero. There are no dipole terms in the expansion which can be written

$$\phi = I_{00}w + \frac{1}{2}(I_{20}w_{xx} + 2I_{11}w_{xy} + I_{02}w_{yy}) \qquad \text{A.23}$$

where w and its derivatives are

$$\left.\begin{aligned}
w &= r_0^{-1} \\
w_{xx} &= -(p+2x^2)r_0^{-5} \\
w_{yy} &= -(q+2y^2)r_0^{-5} \\
p &= y_2 + z^2 - 4x^2 \\
q &= x_2 + z^2 - 4y^2
\end{aligned}\right\} \qquad \text{A.24}$$

These formulae seem somewhat lengthy however their evaluation requires only simple arithmetic and one square root. They thus require much less computing time than the exact formulae. For the same reason the multipole expansion is faster than a numerical integration over the panel, which employs point sources located at a set of mesh points and thus must evaluate a square root for each mesh point.

If the point x,y,z is far enough from the element, the quadropole terms of A.20 are not required. The quadrilateral may be approximated by a point source at its centroid. This is equivalent in accuracy to a source plus dipole. For the point source calculation there is no need to use a co-ordinate system based on the element, and the calculation may be performed in the reference co-ordinate system. Let x_0, y_0, z_0 be the reference co-ordinates of the centroid of the quadrilateral, and let x', y', z' be the reference co-ordinates of the point where potential and velocity are to be evaluated. If the element is approximated by a point source, the potential is calculated from

$$\phi = \frac{1}{r_0} I_{00} \qquad \text{A.25}$$

where

$$r_0 = \sqrt{(x'-x_0)^2 + (y'-y_0)^2 + (z'-z_0)^2} \qquad \text{A.26}$$

Thus there are three sets of formulae for calculating the potential induced by a panel at a point in space. The choice of which set to use is determined by the value of the ratio r_0/t where r0 is the distance of the point in question from the centroid of the panel and t is the maximum dimension of the panel. Hess & Smith quote the use of the point source formulae for values of $r_0/t > 4$, the dipole formulae if $r_0/t > 2.45$ and the exact formulae if $r_0/t < 2.45$ distances which they consider conservative. Any errors from using the approximate formulae appear negligible in comparison to those introduced by the representation of the body by flat panels with constant strength singularity distributions. The savings in computation time are quite significant and rise with number of panels. Since the criteria for deciding which set of formulae to use is based on the value of r_0/t the number of entries of the induced potential matrix computed by the exact and multipole formulae is approximately proportional to the number of panels N. The total number of entries in the matrix is proportional to N^2. Thus the greater the number of elements the greater the percentage of entries computed by the point source formulas.

APPENDIX B. CALCULATION OF DOUBLET INFLUENCE COEFFICIENTS

The doublet influence coefficients of equation 4.13 are calculated from the geometry of the problem. Considering each flat panel in turn and calculating its influence at the control point of all other panels on the surface. The following description of this process is taken from [B.1].

It is desired to calculate the potential induced by a quadrilateral panel having a constant strength doublet distribution at a point in space. The point in element co-ordinates is x,y,z . The distance between this point and a point on the quadrilateral $\xi,\eta,0$ is

$$r = \sqrt{(x-\xi)^2+(y-\eta)^2+z^2} \qquad \text{B.1}$$

For a unit value of doublet density, the potential due to the quadrilateral at point x,y,z is

$$\phi = \iint_A n.\nabla\left(\frac{1}{4\pi r}\right) dA$$

$$= \iint_A \frac{-r.n}{4\pi r^3}\, dA \qquad \text{B.2}$$

where A denotes the area of the quadrilateral.

From Figure B.1 for a flat panel $r.n$ is just the perpendicular distance z. So the above equation becomes

$$\phi = \iint_A \frac{z}{4\pi r^3}\, dA \qquad \text{B.3}$$

a change to polar coordinates (see Figure B.2) similar to the one in Appendix A converts this double integral into a summation of line integrals along the panel edges

$$\iint_A \frac{1}{r^3} = \sum_{i=1}^{4} \int_{\theta_i}^{\theta_{i+1}} \left(\int_0^r \frac{r\,dr}{(r^2+z^2)^{3/2}} \right) d\theta \qquad \text{B.4}$$

Performing the r integration yields

$$\iint_A \frac{1}{r^3}\, dA = \sum_{i=1}^{4} \int_{\theta_i}^{\theta_{i+1}} \left(\frac{1}{|z|} - \frac{1}{(r^2+z^2)^{1/2}} \right) d\theta \qquad \text{B.5}$$

To convert this equation to a line integral along the boundary of A consider Figure B.3

Along a typical side L of the boundary, $r^2=a^2+l$ and the variable of integration θ is related to l as follows:

$$\left.\begin{array}{l} \cos\theta = \dfrac{a}{\sqrt{l^2+a^2}} \quad , \quad \sin\theta = \dfrac{l\,\mathrm{sign}(a)}{\sqrt{l^2+a^2}} \\[2em] \tan\theta = l/a \quad , \quad d\theta = \dfrac{a\,dl}{l_2+a^2} \end{array}\right\} \qquad \text{B.6}$$

Thus equation B.5 becomes

$$\iint_A \frac{1}{r^3}\, dA = \sum_{i=1}^{4} \int_{l_i}^{l_{i+1}} \left(\frac{1}{|z|} - \frac{1}{\sqrt{l^2+g^2}} \right) \frac{a\,dl}{(l^2+a^2)} \qquad \text{B.7}$$

where

$$g^2 = a^2 + z^2 \qquad \text{B.8}$$

separating into two parts

$$\iint_A \frac{1}{r^3}\, dA = \sum_{i=1}^{4} \left(\frac{a}{|z|} I_1 - aI_2 \right) \qquad \text{B.9}$$

where

$$I_1 = \int_{l_i}^{l_i+1} \frac{dl}{l^2+a^2} = \frac{1}{|a|} \tan^{-1}\left(\frac{l}{|a|}\right)\Bigg|_{l_i}^{l_{i+1}} \qquad \text{B.10}$$

and

$$I_2 = \int_{l_i}^{l_{i+1}} \frac{dl}{(l^2+a^2)\sqrt{l^2+g^2)}} = \frac{1}{|a|.|z|} \tan^{-1}\left(\frac{|z|l}{|a|(l^2+g^2)^{1/2}}\right)\Bigg|_{l_i}^{l_{i+1}} \qquad \text{B.11}$$

Using these last two results, equation B.9 becomes

$$\iint_A \frac{1}{r^3}\, dA = \frac{1}{|z|} \sum_{i=1}^{4} \left(\frac{a}{|a|} \beta \right)\Bigg|_{l_i}^{l_{i+1}} \qquad \text{B.12}$$

where

$$\beta = \tan^{-1}\left(\frac{l}{|a|}\right) - \tan^{-1}\left(\frac{|z|l}{|a|(l^2+g^2)^{1/2}}\right) \qquad \text{B.13}$$

In this form four arc tangents must be computed for each side of Σ. To make more efficient computations, the two arc tangents in equation B.13 are combined into one

$$\beta = \tan^{-1} \frac{|a|l\left(\sqrt{l^2+g^2} - |z|\right)}{a^2\sqrt{l^2+g^2} + l^2|z|}$$

$$= \tan^{-1} \frac{|a|l}{g^2+|z|\sqrt{l^2+g^2}} \qquad \text{B.14}$$

With the aid of Figure B.4 and the relation

$$\frac{m}{|m|} \tan^{-1}|m| = \tan^{-1} m \qquad \text{B.15}$$

we obtain

$$\iint_A \frac{1}{r^3}\, dA = \frac{1}{|z|} \sum_{i=1}^{4} \beta \Big|_{l_i}^{l_{i+1}} \qquad \text{B.16}$$

where

$$\sin\beta = \frac{|a|l}{g\left(\sqrt{l^2+g^2} + |z|\right)}$$

$$\cos\beta = \frac{g^2 + |z|\sqrt{l^2+g^2}}{g\left(\sqrt{l^2+g^2} + |z|\right)}$$

$$\tan\beta = \frac{al}{g^2 + |z|\sqrt{l^2+g^2}} \qquad \text{B.17}$$

An additional efficiency is obtained by combining the difference $\beta_{i+1}-\beta_i$ into a single arc tangent. For simplicity, consider only a single side of Σ, with endpoints i=1,i+1=3.

Then

$$\beta_2-\beta_1 = \tan^{-1}\left(\frac{al_2}{c_2}\right) - \tan^{-1}\left(\frac{al_1}{c_1}\right) \qquad \text{B.18}$$

where

$$c_1 = g^2 + |z|s_1 \qquad s_1 = \sqrt{l_1^{\,2} + g^2}$$

$$c_2 = g^2 + |z|s_2 \qquad s_2 = \sqrt{l_2^{\,2} + g^2} \qquad \text{B.19}$$

Equation B.18 reduces to

$$\beta_2-\beta_1 = \tan^{-1}\left(\frac{a(l_2c_1-l_1c_2)}{c_1c_2 + a^2l_1l_2}\right) \qquad \text{B.20}$$

and equation B.16 becomes

$$\iint\limits_A \frac{1}{r^3}\,dA = \frac{1}{|z|}\sum_{j=1}^{4} (\beta_2-\beta_1)_j$$

$$= \frac{1}{|z|}\sum_{j=1}^{4} \tan^{-1}\left(\frac{a(l_2c_1-l_1c_2)}{c_1c_2+a^2l_1l_2}\right)_j \qquad \text{B.21}$$

where the sum is over the four sides of Σ and subscripts 1 and 2 are taken as the endpoints of side j.

Computing equations B.18 and B.19 with the single argument FORTRAN ATAN external function returns values of $\beta_2-\beta_1$ in the range $(-\pi/_2,\pi/_2)$. To use the double argument ATAN2 external function, so as to obtain values of $\beta_2-\beta_1$ in the range $(-\pi,\pi)$, we must also compute $\sin(\beta_2-\beta_1)$ and $\cos(\beta_2-\beta_1)$. These quantities are obtained from equations B.17, using the difference formulae for for sin and cos. The result is

$$\left.\begin{aligned} \sin(\beta_2-\beta_1) &= \frac{a(l_2c_1-l_1c_2)}{g^2d_1d_2} \\ \cos(\beta_2-\beta_1) &= \frac{c_1c_2+a^2l_1l_2}{g^2d_1d_2} \end{aligned}\right\} \qquad \text{B.22}$$

where

$$\left.\begin{aligned} d_1 &= s_1 + |z| \\ d_2 &= s_2 + |z| \end{aligned}\right\} \qquad \text{B.23}$$

Equation B.19 is then rewritten as

$$\iint\limits_A \frac{1}{r^3}\,dA = \frac{1}{|z|}\sum \tan^{-1}\left(\sin(\beta_2-\beta_1),\cos(\beta_2-\beta_1)\right) \qquad \text{B.24}$$

If $g^2d_1d_2 \neq 0$ then this can be written

$$\iint\limits_A \frac{1}{r^3}\,dA = \frac{1}{|z|}\sum \tan^{-1}\left(a(l_2c_1-l_1c_2),c_1c_2+a^2l_1l_2\right) \qquad \text{B.25}$$

The quantity $g = \sqrt{a^2+z^2}$ is illustrated in Figure B.5.

APPENDIX C. CALCULATION OF PANEL GEOMETRIC QUANTITIES

The calculation of the geometry of individual panels that model the rotor blades, the spinner and the near wake of the wind turbine involves the input of the node points that form these surfaces. From these input node points plane quadrilateral elements are formed using the method that follows, which is taken from [C.1], and various geometric parameters calculated. These geometric parameters are used to calculate the panel influence coefficients, see Appendix A and Appendix B.

The node points are input at several stations on the rotor blade and nacelle and linearly interpolated to form sets of chordwise 'node-lines'. Each panel is formed from two pairs of node points one on one node line and one on the adjacent line.

Let the reference co-ordinates of the input node points used to form an element be denoted x_k, y_k, z_k, $k = 1,2,3,4$. It simplifies equations to use vector notation so define

$$\underline{x}_k = x_k\underline{i} + y_k\underline{j} + z_k\underline{k} \tag{C.1}$$

where i,j,k are unit vectors along the axes of the reference co-ordinate system. The input node points $k = 1,2$ are on one, the 'first' node-line, and the node points $k = 3,4$ are on the next, or 'second' node-line (see Figure C.1). In what follows the subscripts F and S denote the first and second node line. The numbering is cyclic around the panel element. The adjustment of the input points to form a plane quadrilateral element is as follows.

First form the node-line vectors

$$\underline{p}_F = \underline{x}_2 - \underline{x}_1 \qquad \underline{p}_S = \underline{x}_3 - \underline{x}_4 \tag{C.2}$$

The two parallel sides of the trapezoid are taken as parallel to the weighted average of these two vectors. In the co-ordinate system of the panel element this is also the direction of the x-axis. The unit vector parallel to the two parallel sides of the trapezoid is denoted $\underline{i}_E$ to show it is also the unit vector along the x or ξ axis of the element co-ordinate system. It is computed from

$$\underline{i}_E = \frac{\underline{P}_F + \underline{P}_S}{|\underline{P}_F + \underline{P}_S|} \qquad \text{C.3}$$

where $|\underline{v}|$ means the absolute magnitude of the vector $\underline{v}$. This calculation ensures that each parallel side has the same midpoint and the same length as the segment of node-line from which it was formed. In fact, once the elements are formed the original node-line segments are replaced by these parallel sides. The side lengths are

$$d_F = |\underline{P}_F| \qquad d_S = |\underline{P}_S| \qquad \text{C.4}$$

the midpoints in vector form are

$$\underline{x}_F = (\underline{x}_1 + \underline{x}_2)/2 \qquad \underline{x}_S = (\underline{x}_3 + \underline{x}_4)/2 \qquad \text{C.5}$$

the endpoints of the parallel sides, which are thus the corner points of the trapezoidal element are, in vector form,

$$\left.\begin{array}{ll} \underline{x}_1 = \underline{x}_F - d_F\underline{i}_E/2 & \underline{x}_2 = \underline{x}_F + d_F\underline{i}_E/2 \\ \underline{x}_3 = \underline{x}_S + d_S\underline{i}_E/2 & \underline{x}_4 = \underline{x}_S - d_S\underline{i}_E/2 \end{array}\right\} \qquad \text{C.6}$$

The normal vector to the plane of the element is

$$\underline{N} = (\underline{x}_4 - \underline{x}_2) \times (\underline{x}_3 - \underline{x}_1) \qquad \text{C.7}$$

The unit normal vector is

$$\underline{n} = \frac{\underline{N}}{|\underline{N}|} \qquad \text{C.8}$$

This is also the unit vector along the z-axis of the element co-ordinate system. The unit vector along the y or η axis of the element co-ordinate system is

$$\underline{j}_E = \underline{n} \times \underline{i}_E \qquad \text{C.9}$$

In component form the three unit vectors are

$$\left.\begin{aligned} \underline{i}_E &= a_{11}\underline{i} + a_{12}\underline{j} + a_{13}\underline{k} \\ \underline{j}_E &= a_{21}\underline{i} + a_{22}\underline{j} + a_{23}\underline{k} \\ \underline{n} = \underline{k}_E &= a_{31}\underline{i} + a_{32}\underline{j} + a_{33}\underline{k} \end{aligned}\right\} \qquad \text{C.10}$$

The 3x3 array of a's is the transformation matrix that is used to transform co-ordinates of points and components of vectors between the reference and element co-ordinate systems.

Temporarily the origin of the element co-ordinate system is taken as the average of the four input points.

$$\underline{x}_{av} = (\underline{x}_F + \underline{x}_S)/2 \qquad \text{C.11}$$

With this origin, the element co-ordinates of the co-ordinate points are

$$\left.\begin{aligned} \xi_k^* &= a_{11}(x_k-x_{av}) + a_{12}(y_k-y_{av}) + a_{13}(z_k-z_{av}) \\ \eta_k^* &= a21(x_k-x_{av}) + a_{22}(y_k-y_{av}) + a_{23}(z_k-z_{av}) \end{aligned}\right\} \qquad \text{C.12}$$

$$k = 1,2,3,4$$

where in accordance with vector notation, x_k, y_k, z_k are the co-ordinates of $\underline{x}_k$ from A.3.6 it will turn out that

$$\eta_1^* = \eta_2^* \quad \text{and} \quad \eta_3^* = \eta_4^* = -\eta_1^* \qquad \text{C.13}$$

The width of the element is

$$w = \eta_1^* - \eta_3^* = 2\eta_1^* \qquad \text{C.14}$$

The slopes of the non-vertical sides of the element (Figure C.2) are

$$m_{32} = \frac{\xi_2^* - \xi_3^*}{w} \qquad m_{41} = \frac{\xi_1^* - \xi_4^*}{w} \tag{C.15}$$

with respect to the η axis. The co-ordinates of the centroid are

$$\left.\begin{aligned} \eta_0 &= \frac{w^2}{6} \, \frac{m_{32} - m_{41}}{\xi_3^* + \xi_2^* - \xi_1^* - \xi_4^*} \\ \xi_0 &= \frac{m_{32} + m_{41}}{2} \eta_0 \end{aligned}\right\} \tag{C.16}$$

The reference co-ordinates of the centroid are

$$\left.\begin{aligned} x_0 &= x_{av} + a_{11}\xi_0 + a_{21}\eta_0 \\ y_0 &= y_{av} + a_{12}\xi_0 + a_{22}\eta_0 \\ z_0 &= z_{av} + a_{13}\xi_0 + a_{23}\eta_0 \end{aligned}\right\} \tag{C.17}$$

The centroid is now taken as the origin of the element co-ordinate system and replaces the average point in all subsequent calculations. With respect to the centroid as origin, the element co-ordinates of the corner points are

$$\left.\begin{aligned} \xi_k &= \xi_k^* - \xi_0 \\ \eta_k &= \eta_k^* - \eta_0 \end{aligned}\right\} \tag{C.18}$$

where

$$\eta_2 = \eta_1 \quad \text{and} \quad \eta_4 = \eta_3 \tag{C.19}$$

These are the corner points used in all subsequent calculations. The maximum diagonal of the element is

$$t = \text{Max} \begin{cases} \sqrt{(\xi_2 - \xi_4)^2 + (\eta_2 - \eta_4)^2} \\ \sqrt{(\xi_3 - \xi_1)^2 + (\eta_3 - \eta_1)^2} \end{cases} \tag{C.21}$$

The length of the sides are

$$\left.\begin{aligned} d_{12} &= d_F & \qquad d_{34} &= d_S \\ d_{32} &= w\sqrt{1 + m_{32}^2} & \qquad d_{41} &= w\sqrt{1 + m_{41}^2} \end{aligned}\right\} \qquad \text{C.22}$$

Finally the moments of area of the panel elements are required. These are defined by

$$I_{nm} = \iint_E \xi^n \eta^m \, d\xi d\eta \qquad \text{C.24}$$

where the integration is over the element. The moments are calculated by a straightforward but lengthy set of formulas given below. The moments are first defined in terms of auxiliary functions

$$I_{nm} = -I_{nm}^{(32)} + I_{nm}^{(41)} + \frac{[\eta_1^{m+1}(\xi_2^{n+1}-\xi_1^{n+1})+\eta_3^{m+1}(\xi_4^{n+1}-\xi_3^{n+1})]}{(m+1)(n+1)} \qquad \text{C.25}$$

The auxilliary function $I_{nm}^{(32)}$ is as follows

If $|m_{32}| > 1$:

$$\begin{aligned} I_{nm}^{(32)} = {} & \frac{1}{(m+1)\,(n+1)}\,[\xi^{n+1}\eta^{m+1}]_3^2 - \\ & \frac{1}{(n+1)\,(n+2)}\,\frac{1}{m_{32}}\,[\xi^{n+2}\eta^{m}]_3^2 + \\ & \frac{m}{(n+1)\,(n+2)\,(n+3)}\,\frac{1}{m_{32}^{\;2}}\,[\xi^{n+3}\eta^{m-1}]_3^2 - \\ & \frac{m(m-1)}{(n+1)\,(n+2)\,(n+3)\,(n+4)}\,\frac{1}{m_{32}^{\;3}}\,[\xi^{n+4}\eta^{m-2}]_3^2 + \\ & \frac{m(m-1)\,(m-2)}{(n+1)\,(n+2)\,(n+3)\,(n+4)\,(n+5)}\,\frac{1}{m_{32}^{\;4}}\,[\xi^{n+5}\eta^{m-3}]_3^2 - \\ & \frac{m(m-1)\,(m-2)\,(m-3)}{(n+1)\,(n+2)\,(n+3)\,(n+4)\,(n+5)\,(n+6)}\,\frac{1}{m_{32}^{\;5}}\,[\xi^{n+6}\eta^{m-4}]_3^2 \end{aligned} \qquad \text{C.26}$$

If $|m_{32}| \leq 1$:

$$\begin{aligned} I_{nm}^{(32)} = {} & \frac{1}{(m+1)\,(m+2)}\,m_{32}\,[\xi^{n}\eta^{m+3}]_3^2 - \\ & \frac{n}{(m+1)\,(m+2)\,(m+3)}\,m_{32}^{\;2}\,[\xi^{n-1}\eta^{m+3}]_3^2 + \\ & \frac{n(n-1)}{(m+1)\,(m+2)\,(m+3)\,(m+4)}\,m_{32}^{\;3}\,[\xi^{n-2}\eta^{m+4}]_3^2 - \\ & \frac{n(n-1)\,(n-2)}{(m+1)\,(m+2)\,(m+3)\,(m+4)\,(m+5)}\,m_{32}^{\;4}\,[\xi^{n-3}\eta^{m+5}]_3^2 + \\ & \frac{n(n-1)\,(n-2)\,(n-3)}{(m+1)\,(m+2)\,(m+3)\,(m+4)\,(m+5)\,(m+6)}\,m_{32}^{\;5}\,[\xi^{n-4}\eta^{m+6}]_3^2 \end{aligned} \qquad \text{C.27}$$

where the bracketed symbols are defined by

$$[\xi^k\eta^p]_3^2 = \xi_2^k\eta_2^p-\xi_3^k\eta_3^p \qquad \text{C.28}$$

(The superscripts in the above equations denote simple powers except for the bracketed double superscript (32) which denotes the side of the panel.) The auxiliary function $I_{nm}^{(41)}$ is obtained from the above by an obvious subsitution of subscripts.

APPENDIX D. APPLICATION OF THE KUTTA CONDITION

In three dimensions the Kutta condition is difficult to apply as the usual method of equating pressures used in two dimensional problems is complicated by the cross flow. An iterative procedure could be used but in this case a direct method will be employed. Therefore a simplified form of the condition must be used which approximately equates chordwise velocities at the upper and lower separation points.

The panel method is performed in terms of perturbation potential and so the velocity at any point is calculated from the gradient of the perturbation potential plus the incident tangential velocity. So the 'Kutta condition' at each spanwise station is formulated thus;

$$V_{\infty sepu} + \frac{\phi_{sepu-1} - \phi_{sepu}}{du} = -V_{\infty sepl} + \frac{\phi_{sepl+1} - \phi_{sepl}}{dl} \qquad \text{D.1}$$

$$\frac{\phi_{sepu-1} - \phi_{sepu}}{du} - \frac{\phi_{sepl+1} - \phi_{sepl}}{dl} = -V_{\infty sepu} - V_{\infty sepl} \qquad \text{D.2}$$

where

V_∞ is the incident chordwise velocity

ϕ is the perturbation potential

and the subscripts sepu and sepl refer to the panels upon which separation occurs on the upper and lower surface respectively (du and dl being the distance along the aerofoil between the separation panels' control points and the next panels').

APPENDIX E. BOUNDARY LAYER CO-ORDINATE TRANSFORMATION

The boundary layer equations are formulated in a body fitted co-ordinate system consisting of constant ϕ and s lines on the wing surface (Figure E.1), y being normal to the wall. λ is the angle between the ϕ and s axes the metric elements along ϕ and s being h_1 and h_2. The length, ds, of an element on any curve on the surface is given by

$$ds^2 = h_1 d\phi^2 + 2g d\phi ds + h_2 ds^2$$

$$g = h_1 h_2 \cos\lambda$$

A point, P, on the surface is represented by

$$\cos\phi = 1 - X , \quad s = r/R \qquad \text{E.1}$$

This transformation gives a smooth function through the leading edge and allows the calculation of the boundary layer beginning at a stagnation point on the lower surface.

The metrical quantities required for the boundary layer equations, [4.11], are calculated from the formulae outlined below.

For two reference stations (0) and (1), Figure E.2, we assume we can evaluate Y and $\partial Y/\partial\phi$ at any chordwise point ϕ. The pitch axis along the blade is constant at $X = X_p$.

Now

$$\left.\begin{aligned} \sigma &= (r-r_0)/(r_1-r_0) \\ c &= (1-\sigma)c_0 + \sigma c_1 \\ \beta &= (1-\sigma)\beta_0 + \sigma\beta_1 \\ Y &= (1-\sigma)Y_0 + \sigma Y_1 \end{aligned}\right\} \qquad \text{E.2}$$

c being the blade chord and β the blade twist at any station

$$\left.\begin{aligned}
\frac{\partial Y}{\partial \phi} &= (1-\sigma)\frac{\partial Y_0}{\partial \phi} + \sigma\frac{\partial Y_1}{\partial \phi}\\
\frac{\partial X}{\partial \phi} &= \sin\phi\\
\frac{\partial c}{\partial s} &= \frac{c_1 - c_0}{s_1 - s_0}\\
\frac{\partial \beta}{\partial s} &= \frac{\beta_1 - \beta_0}{s_1 - s_0}\\
\frac{\partial Y}{\partial s} &= \frac{Y_1 - Y_0}{s_1 - s_0}
\end{aligned}\right\} \tag{E.3}$$

$$\left.\begin{aligned}
\frac{\partial \xi^1}{\partial \phi} &= c\frac{\partial X}{\partial \phi}\sin\beta + c\frac{\partial Y}{\partial \phi}\cos\beta\\
\frac{\partial \xi^2}{\partial \phi} &= c\frac{\partial X}{\partial \phi}\cos\beta - c\frac{\partial Y}{\partial \phi}\sin\beta\\
\frac{\partial \xi^3}{\partial \phi} &= 0
\end{aligned}\right\} \tag{E.4}$$

$$\left.\begin{aligned}
\frac{\partial \xi^1}{\partial s} &= \frac{\partial c}{\partial s}[(X-X_p)\sin\beta + Y\cos\beta] +\\
&\quad c[(X-X_p)\cos\beta\frac{\partial \beta}{\partial s} - Y\sin\beta\frac{\partial \beta}{\partial s} + \frac{\partial Y}{\partial s}\cos\beta]\\
\frac{\partial \xi^2}{\partial s} &= \frac{\partial c}{\partial s}[(X-X_p)\cos\beta - Y\sin\beta] +\\
&\quad c[-(X-X_p)\sin\beta\frac{\partial \beta}{\partial s} - Y\cos\beta\frac{\partial \beta}{\partial s} - \frac{\partial Y}{\partial s}\sin\beta]\\
\frac{\partial \xi^3}{\partial s} &= R
\end{aligned}\right\} \tag{E.5}$$

$$\left.\begin{aligned}
h_1^{\,2} &= \left(\frac{\partial\xi^1}{\partial\phi}\right)^2 + \left(\frac{\partial\xi^2}{\partial\phi}\right)^2 + \left(\frac{\partial\xi^3}{\partial\phi}\right)^2 \\
h_2^{\,2} &= \left(\frac{\partial\xi^1}{\partial s}\right)^2 + \left(\frac{\partial\xi^2}{\partial s}\right)^2 + \left(\frac{\partial\xi^3}{\partial s}\right)^2 \\
g &= \frac{\partial\xi^1\partial\xi^1}{\partial\phi\partial s} + \frac{\partial\xi^2\partial\xi^2}{\partial\phi\partial s} + \frac{\partial\xi^3\partial\xi^3}{\partial\phi\partial s} \\
\lambda &= \cos^{-1}\left(\frac{g}{h_1h_2}\right)
\end{aligned}\right\} \qquad \text{E.6}$$

REFERENCES

1.1 NACFAIRE H N & DIAMANTARAS K The European Community demonstration programme for wind energy and community energy policy, EWEC '89, Glasgow, July 1989

1.2 ROGERS L J United States wind energy research program, EWEC '89, Glasgow, July 1989

1.3 WARREN J G The WEG MS-2 stall regulated rotor study, ETSU-WN-5063, June 1988

1.4 LUNDSAGER P On the power regulation of small wind turbines based on experience with small Danish wind turbines, Fifth Biennial Wind Energy Conference, Washington, October 1981

1.5 JAMIESON P Evaluation of the concept of a stall limited rotor, Report for DEn contract number E/5A/CON/6026/2214, June 1990

2.1 GLAUERT H Airplane Propellers, Vol. IV, Division L in 'Aerodynamic Theory' ed. W F Durand, Springer, 1935

2.2 de VRIES O Fluid Dynamic Aspects of Wind Energy Conversion, AGARD-AG-243, July 1979

2.3 WILSON R E LISSAMAN P B S & WALKER S N Aerodynamic Performance of Wind Turbines, Oregan State University, NSF/RA-760228, June 1976

2.4 TANGLER J L Horizontal Axis Wind System Rotor Performance Model Comparison, RFP-3508, February 1983

2.5 HIBBS B & RADKEY R L Calculating rotor performance with the revised 'PROP' computer code, Aerovironment Report PFN-13470W, 1983

2.6 EGOLF T J & LANDGREBE A J The UTRC Wind Energy Conversion System Performance Analysis for Horizontal Axis Wind Turbines (WECSPER) Conference on Wind Turbine Dynamics, Cleveland, 1981, NASA CP 2185

2.7 JENG D R KEITH T G & AFJEH A A Aerodynamic Performance Prediction of Horizontal Axis Wind Turbines, Conference on Wind Turbine Dynamics, Cleveland, 1981, NASA CP 2185

2.8 AFJEH A A & KEITH T G
A Prescribed Wake Model for Performance Prediction of Horizontal Axis Wind Turbines, European Wind Energy Association Conference and Exhibition, 7-9th October 1986, Rome, Italy

2.9 BUGGE J A HANSEN K S & LARSEN A M
A refined Windmill Rotor Model AIAA/SF-R1 Wind Energy Conference 9-11th April, Boulder, Colorado

2.10 ZERVOS A HUBERSON S & HEMON A
Three Dimensional Free Wake Calculation of Wind Turbine Wakes, Department of Mechanical Engineering, National Technical University of Athens, Greece

2.11 AFJEH A A & KEITH T G
Simplified Wake Models of Horizontal Axis Wind Turbines, Seventh Biennial US Wind Energy Conference, San Francisco, August 1985, pp 469-475

2.12 LOWSON M V & BROCKLEHURST A
A preliminary analysis of 'Superstall' phenomena on wind turbines, Westland Helicopters, 1986

2.13 BOCCI A J & MORRISON J I
A review of ARA research into propeller aerodynamic prediction methods, Paper 5 in Aerodynamics and Acoustics of Propellers, AGARD CP 336, October 1984

2.14 SAVINO J M & NYLAND T W
Wind turbine flow visualisation studies, Seventh Biennial US Wind Energy Conference, San Francisco, August 1985, pp 559-564

2.15 PEDERSEN T F & ANTONIOU I
Vizualization of flow through through a stall regulated wind turbine rotor, EWEC '89, Glasgow, July 1989

2.16 MILLER R H
The Aerodynamics and Dynamics of Rotors - Problems and Perspectives, from Recent Advances in Aerodynamics, Proceedings of an International Symposium held at Stanford University, August 1983

2.17 HIMMELSKAMP H
Profile investigations on a rotating airscrew, PhD Thesis, Gottingen, 1945; Ministry of Aircraft Production, Volkenrode, Reports and translations No 843, VG 177, September 1946, ARC 10856

2.18 MILEY S J
A catalogue of low Reynolds number airfoil data for wind turbine applications, RFP-3387, February 1982

2.19	REBONT J MARESCA C & FAVIER D	Characteristic wake data for local blade propeller stalling, Journal of Aircraft, Vol. 14, No 1, January 1977, pp 56-59
2.20	HIGNET E T & GIBSON M M	Surface flow patterns as visualised by dust deposits on the blades of a fan, Journal of the Royal Aeronautical Society, Vol. 67, No. 633, September 1963, pp 589-594
2.21		Aerodynamics and Acoustics of Propellers AGARD CP 366, October 1984
2.22	MILBORROW D J & ROSS J N	Aerofoil characteristics of rotating blades, IEA LS-WECS meeting of experts, Developments in aerodynamic calculation methods, Copenhagen, October 1984
2.23	PEDERSEN T F & MADSEN H A	Location of flow separation on an 11m wind turbine blade by means of flow visualisation and a two dimensional airfoil code, BWEA10, London, March 1988
2.24	NYLAND T W	Chordwise pressure measurements on a blade of MOD-2 wind turbine, Sixth ASME wind Energy Symposium, Dallas, February 1987
2.25	BROWN C J & GRAHAM J M R	Investigation into the effect of turbine rotation on the maximum lift coefficient, Final Report, Imperial College, December 1989
2.26	BARNSLEY M J & WELLICOME J F	Design and testing of a horizontal axis wind turbine model for the investigation of stall regulation aerodynamics, EWEC '89 Glasgow, July 1989
2.27	RONSTEN et al	Pressure measurements on a 5.35m HAWT in CARDC 12 by 16m wind tunnel compared to theoretical pressure distributions, EWEC '89, Glasgow, July 1989
2.28	BUTTERFIELD C P	Three dimensional airfoil performance measurements on a rotating wing, EWEC '89, Glasgow, July 1989
2.29	MADSEN H A	Measured airfoil characteristics of three blade segments on a 19m diameter HAWT rotor, BWEA workshop 'Recent Developments in the Aerodynamics of Wind Turbines', Nottingham, February 1990

2.30	BELLIA J M & HALES R L	Mobile test results for the fully-instrumented rotor, Final Report of 'An experimental investigation of HAWT aerodynamics in natural conditions', July 1990
2.31	HALES R L & MADSEN H A	Personal communication
2.32	RASMUSSEN F	Blade and rotor loads for Vestas 15, Risø-M-2402, June 1983
2.33	VITERNA L A & CORRIGAN R D	Fixed pitch rotor performance of large horizontal axis wind turbines, In DOE/NASA workshop 'Large horizontal axis wind turbines', Cleveland, July 1981, NASA CP 2230
2.34	RASMUSSEN F PETERSEN S M LARSEN G KRETZ A & ANDERSEN P D	Investigations of aerodynamics, structural dynamics and fatigue on Danwin 180kW, Risø-M-2727, June 1988
2.35	REDDY M T	Wind Tunnel Tests on Thickened and Truncated Aerofoils for Wind Turbines, Department of Ship Science, University of Southampton, December 1987, Final Report to ETSU of Contract No. E/5A/CON/5054/1395
2.36	MUSIAL W D & CROMACK D E	Influence of Reynolds number on performance modelling of horizontal axis wind rotors, Journal of Solar Engineering, Volume 110, May 1988
2.37	GALBRAITH R A McD COTON F N SALIVEROS E & KOKKODIS G	Aerofoil scale effects and the relevance to wind turbines, BWEA 9, Edinburgh, April 1987
2.38	OSTOWARI C & NAIK D	Post Stall Studies of Untwisted Varying Aspect Ratio Blades with NACA 44xx Series Airfoil Sections - Part II, Wind Engineering, Vol. 9, No. 3, 1985
2.39	TANGLER J L & SOMERS D M	Advanced airfoils for HAWTs, presented at Windpower '85, San Francisco, California, August 1985
2.40	KHOO H & GRAHAM J M R	Wind Tunnel Tests on the Effect of Spoilers on Wind Turbine Blades, EWEC '89, Glasgow, July 1989

2.41	KUCHEMANN D	The Aerodynamic Design of Aircraft, Pergamon, Oxford, 1978
2.42	HORTON H P	Fundamental aspects of flow separation under high lift conditions, Paper 4 in Assessment of Lift Augmentation Devices, AGARD-LS-43, April 1970
2.43	GAULT D E	A correlation of low speed airfoil section stalling characteristics with Reynolds number and airfoil geometry, NACA TN 3963, 1957
2.44	MASKELL E C	Flow separation in three dimensions, RAE Aero R-2565, November 1955
2.45	WALKER S N	Performance and optimum design analysis/ computation for propeller type wind turbines, PhD Thesis, Department of Mechanical Engineering, Oregan State University, May 1976
2.46	HALES R L & GARSIDE A J	Design and analysis techniques for wind turbines in unsteady flow environments, Cranfield Institute of Technology, 06/691, July 1985
2.47	HIBBS B	HAWT performance with dynamic stall, SERI/STR-217-2732, February 1986
2.48	KLIMAS P C	Three dimensional stall effects, IEA Experts meeting on Aerodynamic Calculation Methods, October 1986
2.49	TANNER W H & YAGGY P F	Experimental boundary layer study on hovering rotors, Journal of American Helicopter Society, Vol. 11, No 3, July 1966, pp 22-37
2.50	SØRENSEN J N	Three level, viscous-inviscid interaction technique for the prediction of separated flow past a rotating wing, PhD Thesis, Technical University of Denmark, 1986
3.1	JOHNSON W	Chapter 13: Rotary Wing Aerodynamics III. Helicopter Theory Princeton University Press, 1980;
3.2	RAWLINSON-SMITH R I	HAWT Performance Prediction: A Prescribed Wake Model. Users' Guide, DEn Research Contract Number E/5A/CON/5087/1642, Cranfield reference 06/683/2, 1988

4.1 BUTTER D J
HUNT B
HARGREAVES G R
A Survey of Boundary Integral Methods, in Numerical Methods in Aeronautical Fluid Dynamics, ed. P L Roe, Academic Press, London, 1984.

4.2 HUNT B
Recent and anticipated advances in the panel method, Von Karman Institute lecture series, 1980

4.3 HESS J L
Calculation of Potential Flow About Arbitrary Three Dimensional Lifting Bodies, Final Technical Report, Oct 1972, MDC J5679/01

4.4 COTON F N
GALBRAITH R A McD
A Direct Viscid-Inviscid Interaction Scheme for the Prediction of 2-Dimensional Aerofoil Performance in Incompressible Flow, University of Glasgow, Dept. of Aeronautics & Fluid Mechanics, February 1987, GU AERO Report 8701; see also Aeronautical Journal, April 1988, pp 132-140.

4.5 MASKEW B
DVORAK F
The Prediction of Clmax using a separated flow model, Journal of American Helicopter Society, April 1978

4.6 WILLIAMS B R
Coupling Procedures For Viscous-Inviscid Interaction in External Aerodynamics, Fourth Symposium on Numerical and Physical Aspects of Aerodynamic Flows, Long Beach California, USA, 16-19 January 1989

4.7 MORAN J
An Introduction to Theoretical and Computational Aerodynamics, John Wiley & Sons, Inc., 1984

4.8 CROSS A G T
Separated Flow Calculations Involving Integral Boundary-Layer Methods and Quasi-Simultaneous Coupling, The Prediction and Exploitation of Separated Flows, The Royal Aeronautical Society, London, 18-20 April 1989.

4.9 BUTTER D J
Separated Flow Modelling, British Aerospace Report Number BAe-MAE-R-FDM-0078, 25th March 1981

4.10 HESS J L &
SMITH A M O
Calculation of potential flow about arbitrary bodies, Progress in Aeronautical Sciences, Vol 8, Pergamon press, 1967

4.11	COUSTEIX J	Three-Dimensional Boundary Layers; Introduction to Calculation Methods, paper 1 in Computation of Three-Dimensional Boundary Layers Including Separation, AGARD-R-741, February 1987 Also; Von Karman Institue for Fluid Dynamics, Lecture Series 1981, Separated Flows in Turbomachinery Components, Turbulence modelling and boundary layer caclulation methods
4.12	MASKEW B RAO B M DVORAK F A	Prediction of Aerodynamic Characteristics for Wings With Extensive Separations AGARD CP 291 1980
4.13	MASKEW B	Prediction of Subsonic Aerodynamic Characteristics: A Case for Low-Order Panel Methods, Journal of Aircraft, Vol. 19, No 2, February 1982
4.14	HIRSCHEL E H	Evaluation of results of boundary layer calculations with regards to design aerodynamics, Computation of Three-Dimensional Boundary Layers Including Separation, AGARD-R-741, February 1987
5.1	SYSTMA H S HEWITT B L & RUBBERT P E	A Comparison of Panel Methods for Subsonic Flow Computation, AGARDograph No. 241, February 1979
5.2	McGHEE R J & BEASLEY W D	Wind Tunnel Results for an Improved 21-Percent Thick Low-Speed aerofoil Section NASA Technical Memorandum 78650, 1978
5.3	HASTINGS R C & WILLIAMS B R	Studies of the flow field near a NACA 4412 aerofoil at nearly maximum lift, Aeronautical Journal, January 1987
5.4	MADSEN H RASMUSSEN F & PEDERSEN T	Aerodynamics of a Full-Scale HAWT Blade, ECWEC '88, Herning, Denmark, 6-10 June 1988.
6.1	RASMUSSEN F	Aerodynamic Performance of a New LM 17.2m Rotor, Risø-M-2466, November 1984
6.2	ABBOT I H & von DOENHOFF A E	Theory of Wing Sections, Including a Summary of Airfoil Data, McGraw-Hill Book Company, 1949

B.1	Johnson F T	A general panel method for the analysis and design of arbitrary configurations in incompressible flows, NASA CR 3079, May 1980
C.1	HESS J L	Calculation of potential flow about arbitrary three dimensional lifting bodies, Final Technical Report, October 1972, Report No MDC J5679-01, McDonnell

MACHINE/ BLADES	AEROFOIL SECTION	ROTATIONAL SPEED (rpm)	DIAMETER (m)
Cranfield turbine with Marlec 1kW blades	NACA 4415	333 395 458	3.85
Windmatic WM17S with LM blades	NACA 632-2xx	55	17
Windpower & Co (UK) WP-1	NASA LS(1)-0421m	39/59	17.5
WEG MS-2 with Gifford 12m fixed pitch blades	NASA LS(1)-0421m	48	25
Nibe B	NACA 44xx	33.4	40

Table 3.1 Machines used in the wake sensitivity study

Tip Speed Ratio 3.5<=λ<=10.0	$\frac{\text{Convection Rate}}{\text{Windspeed}}$	40% 60% 80% 100%
	$\frac{\text{Swirl Rate}}{\text{Rotor RPM}}$	100% 110% 120% 130%
	Expansion	0% 10% 20% 30%

Table 3.2 Sensitivity Study Test Cases

MACHINE	TIP SPEED RATIO	CONVECTION RATE (%WS)				SWIRL RATE (%RPM)				EXPANSION (%RAD)			
		100	80	60	40	100	110	120	130	100	110	120	130
CRANFIELD	10.0	81	85	99	93	81	97	101	105	81	109	113	117
	7.0	82	86	90	94	82	98	102	106	82	110	114	118
	5.0	83	87	91	95	83	99	103	107	83	111	115	119
	2.5	84	88	92	96	84	100	104	108	84	112	116	120
WINDMATIC	10.0	121	125	129	133	121	137	141	145	121	149	153	157
	7.0	122	126	130	134	122	138	142	146	122	150	154	158
	5.0	123	127	131	135	123	139	143	147	123	151	155	159
	2.5	124	128	132	136	124	140	144	148	124	152	156	160
WINDPOWER & CO. WP-1	10.0	201	205	209	213	201	217	221	225	201	229	233	237
	7.0	202	206	210	214	202	218	222	226	202	230	234	238
	5.0	203	207	211	215	203	219	223	227	203	231	235	239
	2.5	204	208	212	216	204	220	224	228	204	232	236	240
WEG MS-2 SR ROTOR	10.0	1	5	9	13	1	17	21	25	1	29	33	37
	7.0	2	6	10	14	2	18	22	26	2	30	34	38
	5.0	3	7	11	15	3	19	23	27	3	31	35	39
	2.5	4	8	12	16	4	20	24	28	4	32	36	40
NIBE B	10.0	121	125	129	133	121	137	141	145	121	149	153	157
	7.0	122	126	130	134	122	138	142	146	122	150	152	158
	5.0	123	127	131	135	123	139	143	147	123	151	153	159
	2.5	124	128	132	136	124	140	144	148	124	152	154	160

Table 3.3 Run numbers for the sensitivity study test cases

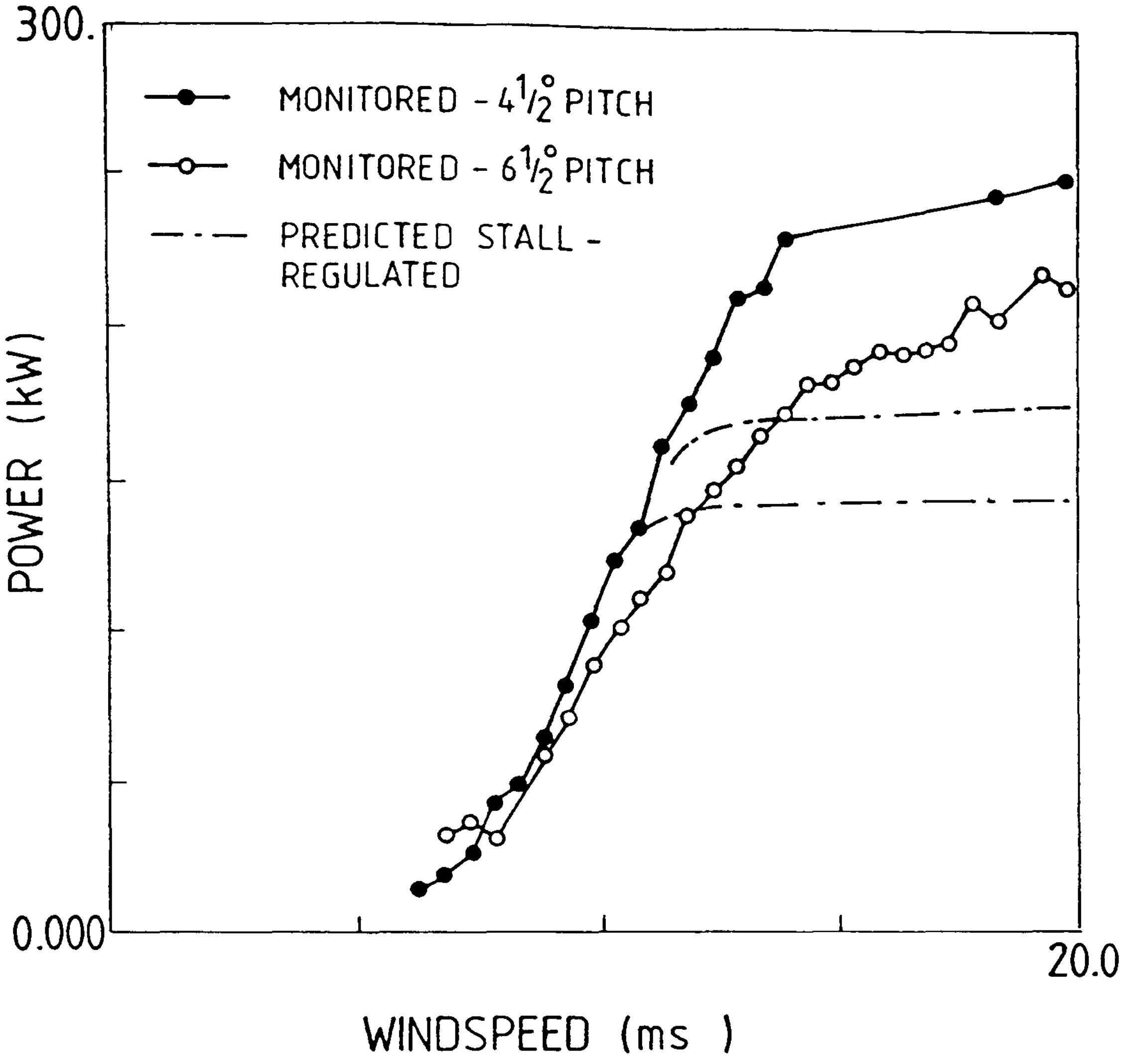

Figure 1.1 Underprediction of high wind performance using a strip theory method, [1.1]

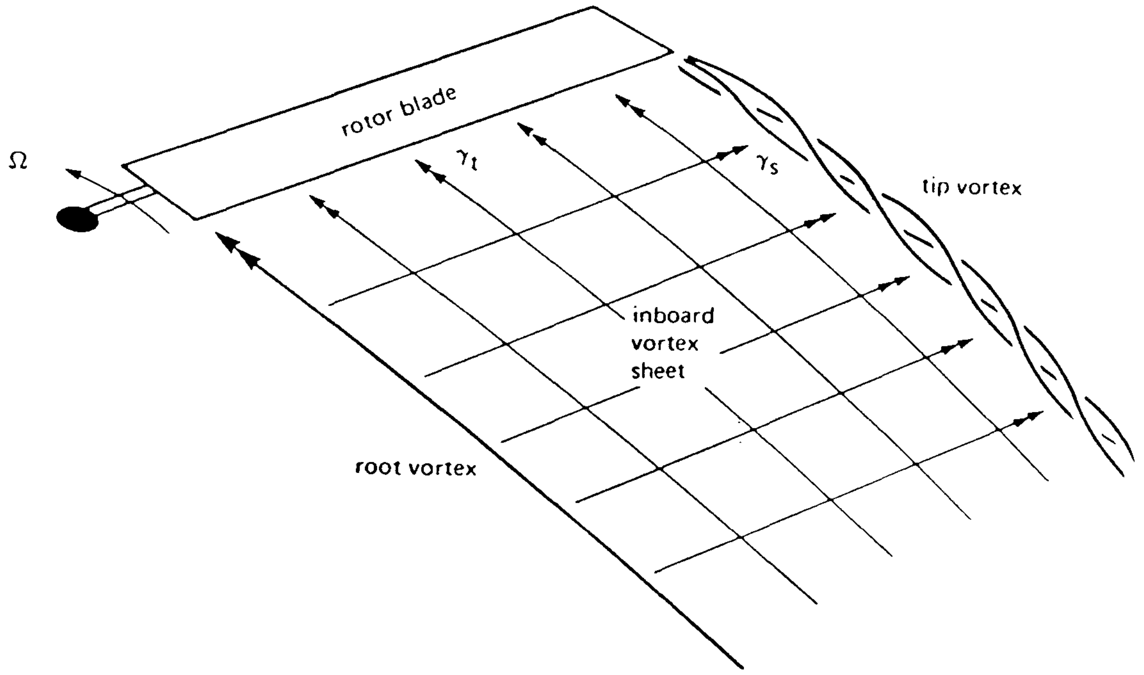

Figure 2.1 Trailed and shed vorticity in a rotor wake

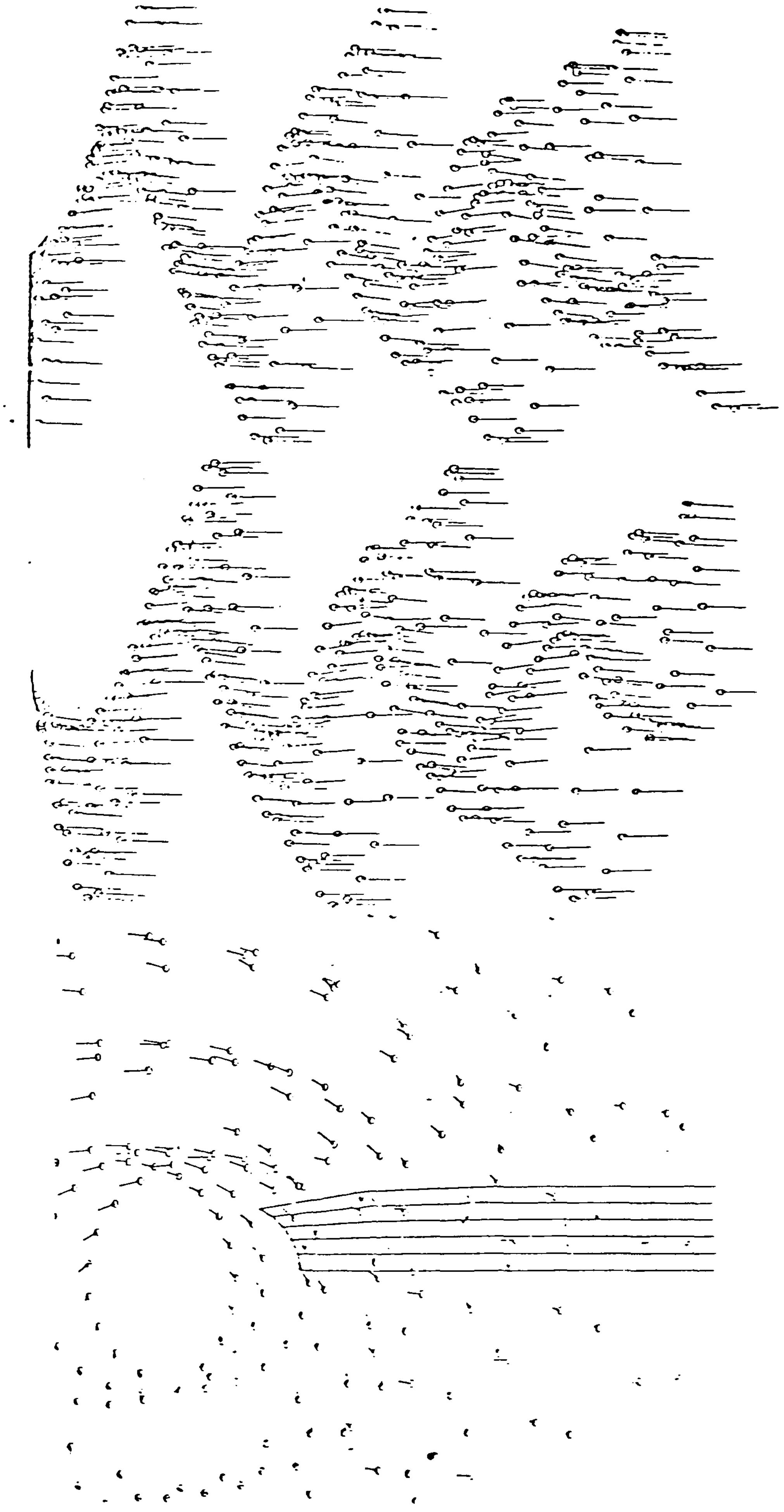

Positions of vortex particles and their velocity vectors at a given instant

Figure 2.2 **Complex nature of a full free wake analysis, [2.10]**

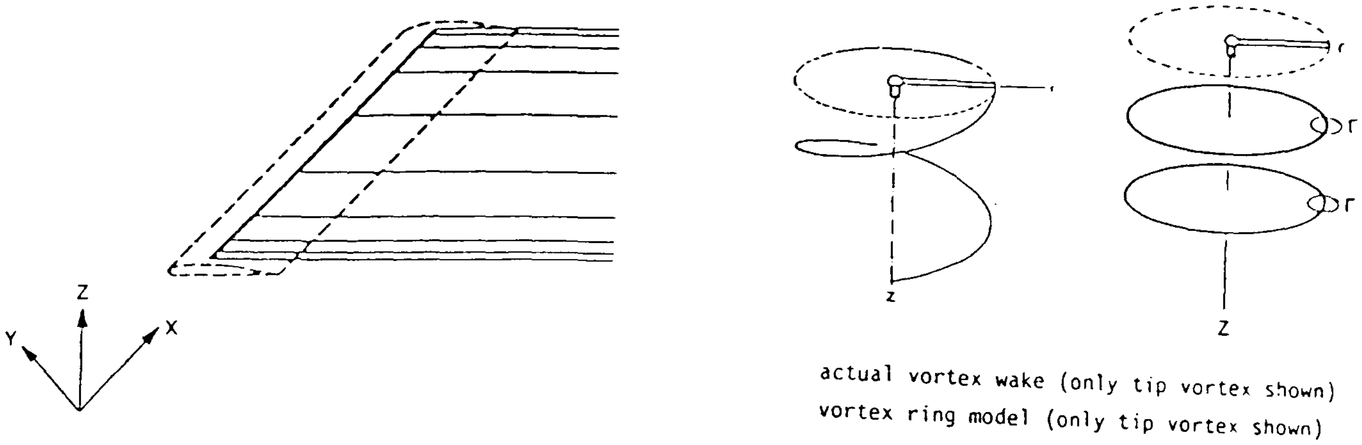

(i) NEAR WAKE VORTEX MODEL

(ii) INTERMEDIATE WAKE VORTEX MODEL

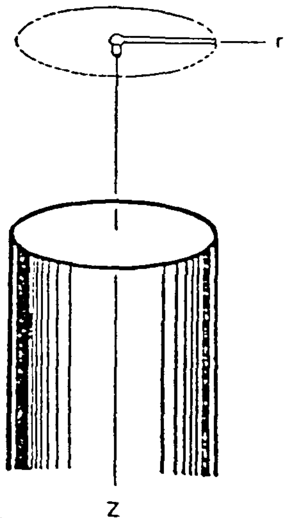

(iii) FAR VORTEX WAKE MODEL

(a) Fast Free Wake

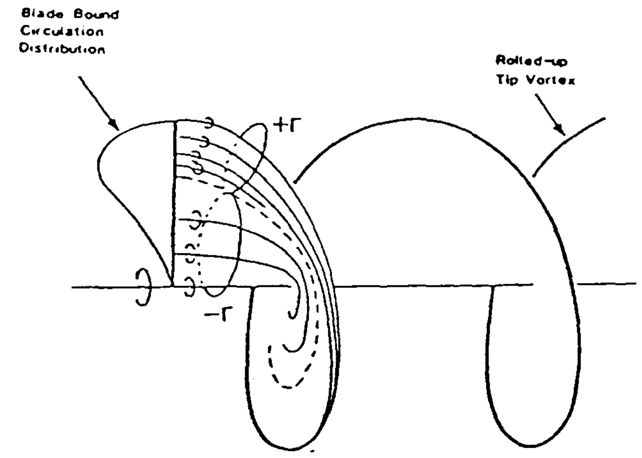

PHYSICAL MODEL OF THE FLOW FIELD USED TO DEVELOP SIMPLIFIED FREE WAKE MODEL

(b) Simplified Free Wake

Figure 2.3 Simplified free wake analyses use a reduced number of wake elements, [2.11]

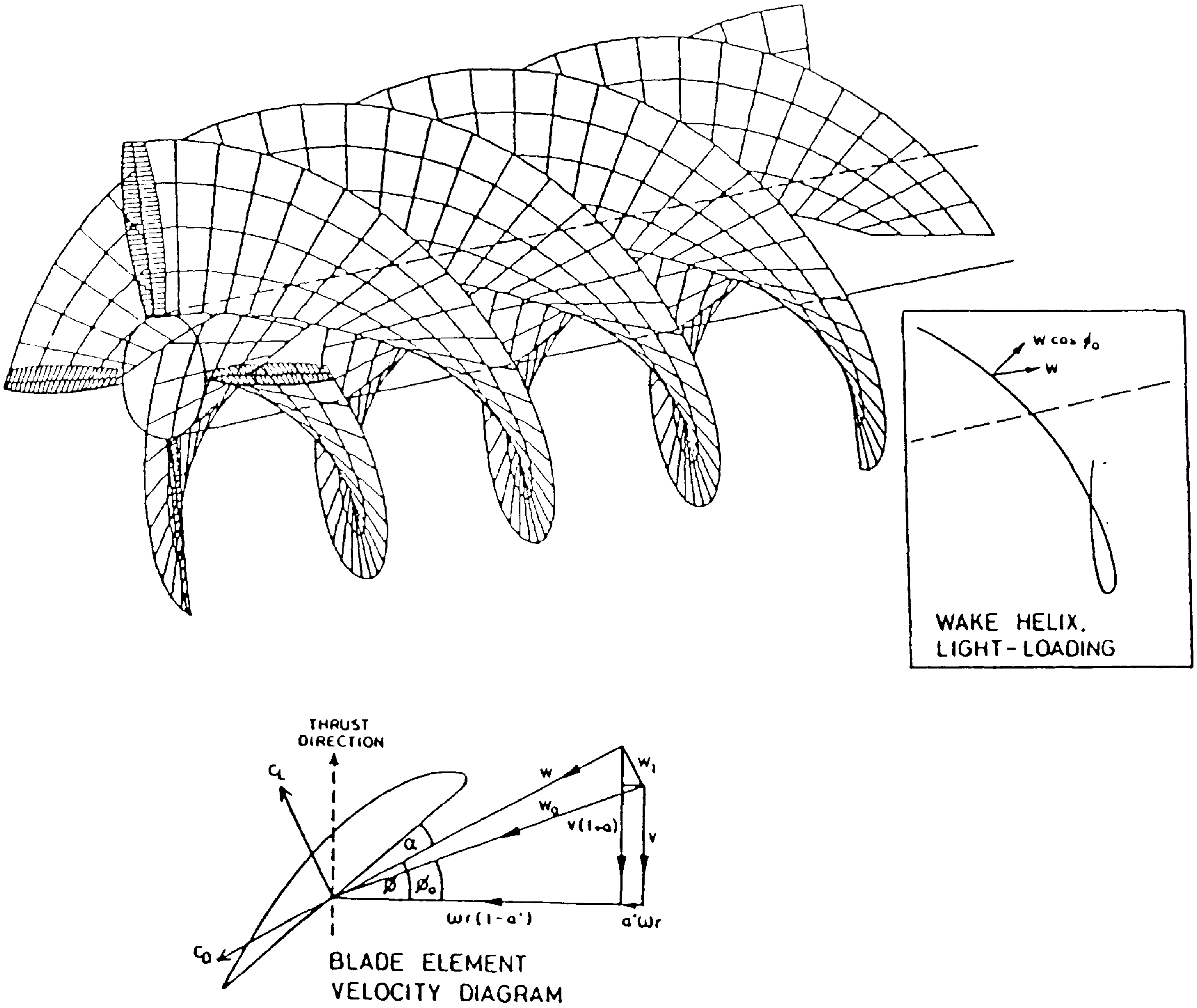

Figure 2.4 Rotor wake helix and true wake helix angle ϕ, [2.13]

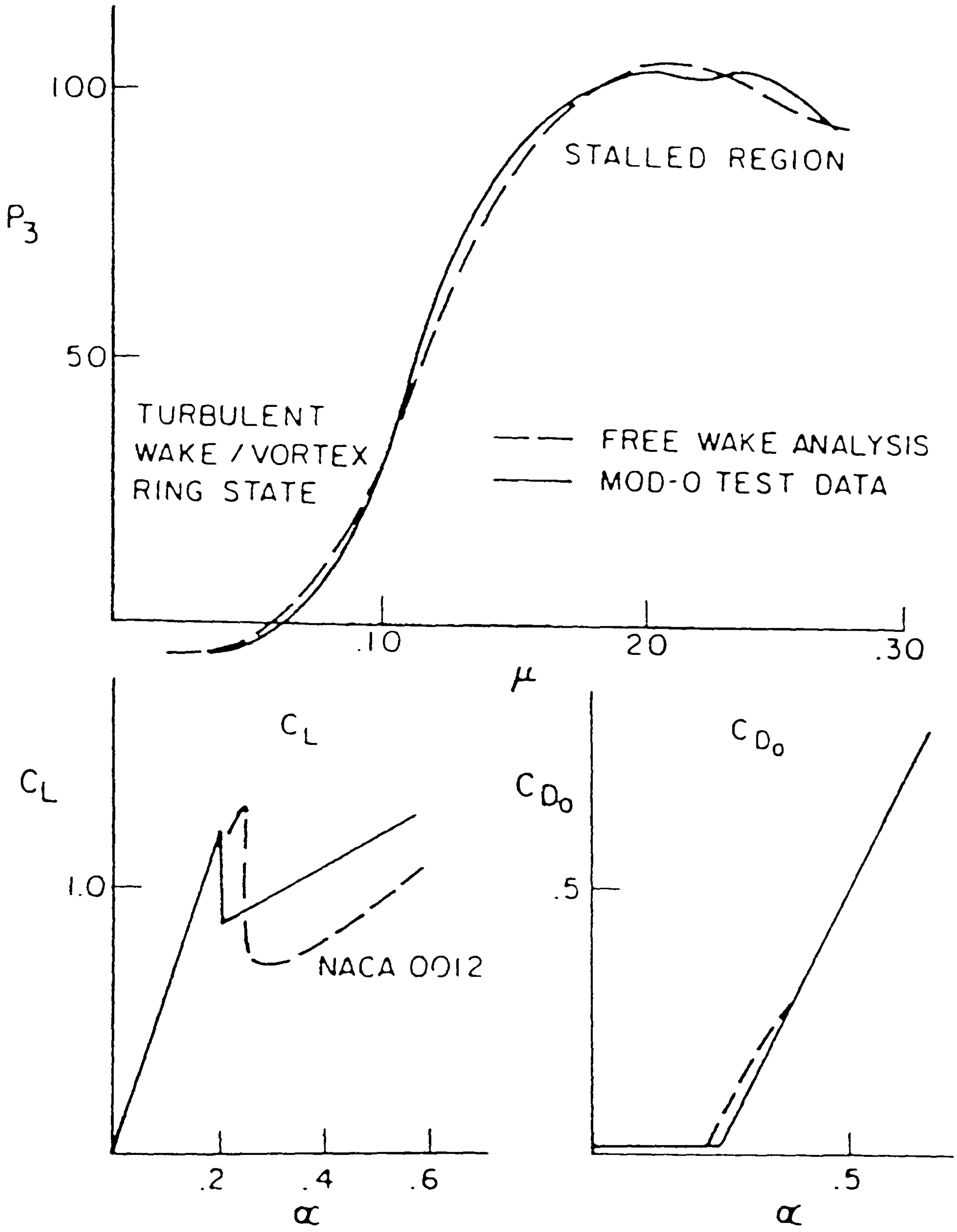

Figure 2.5 Modifications required to the blade element input data in a free wake performance code to obtain correlation with experiment, [2.16]

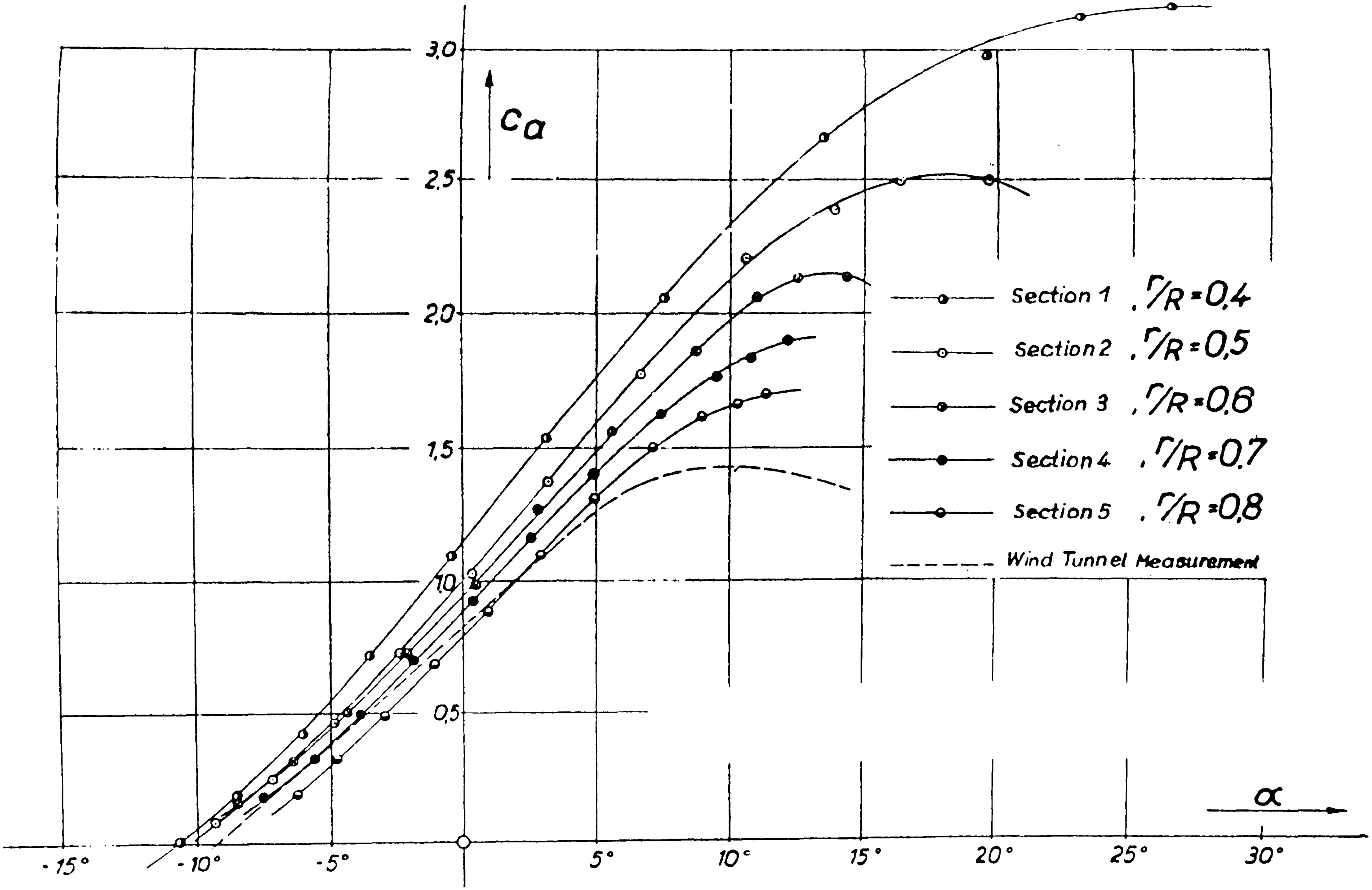

Figure 2.6 Lift coefficient versus angle of attack, Himmelskamp's results, [2.17]

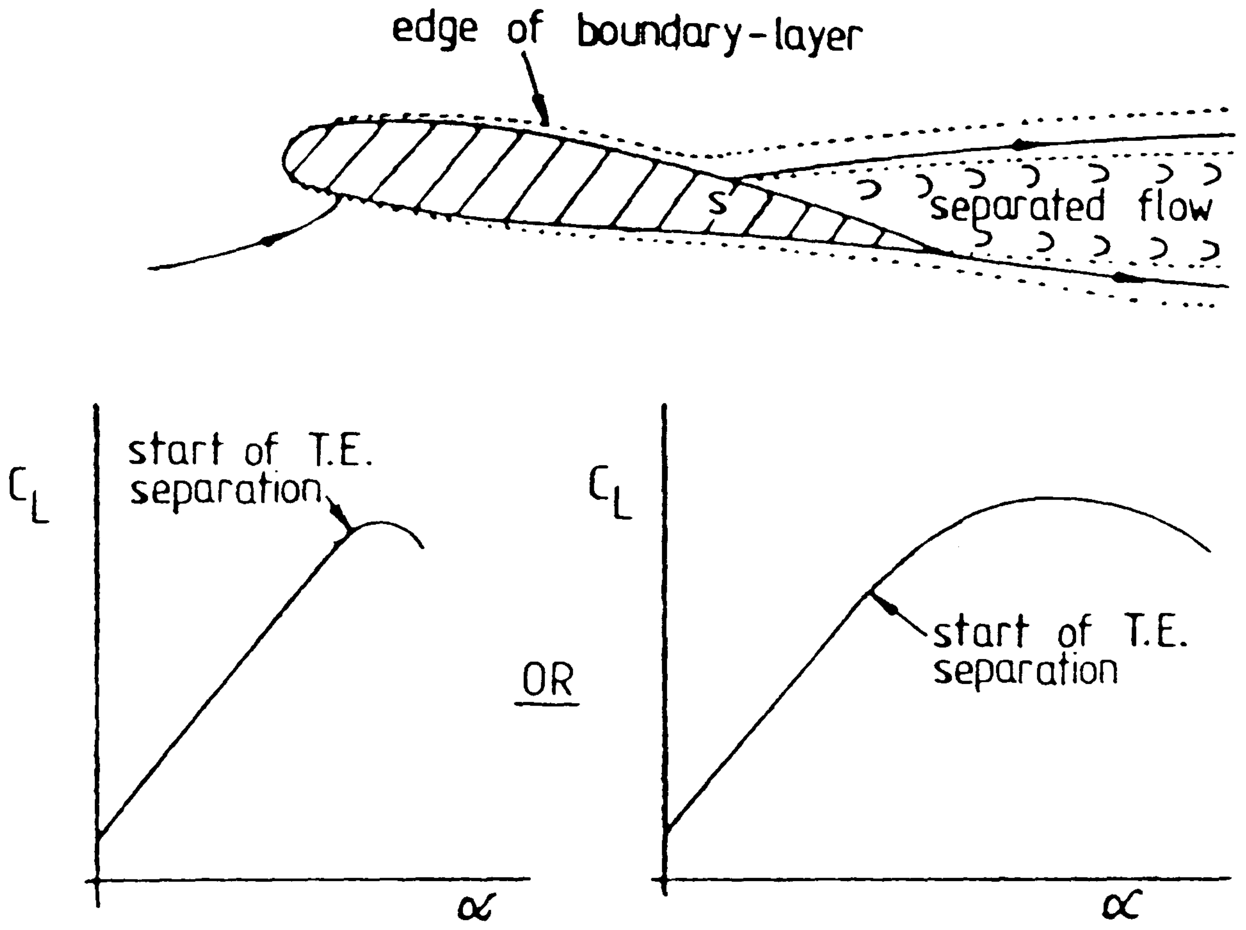

Figure 2.7 Trailing edge stall, [2.40]

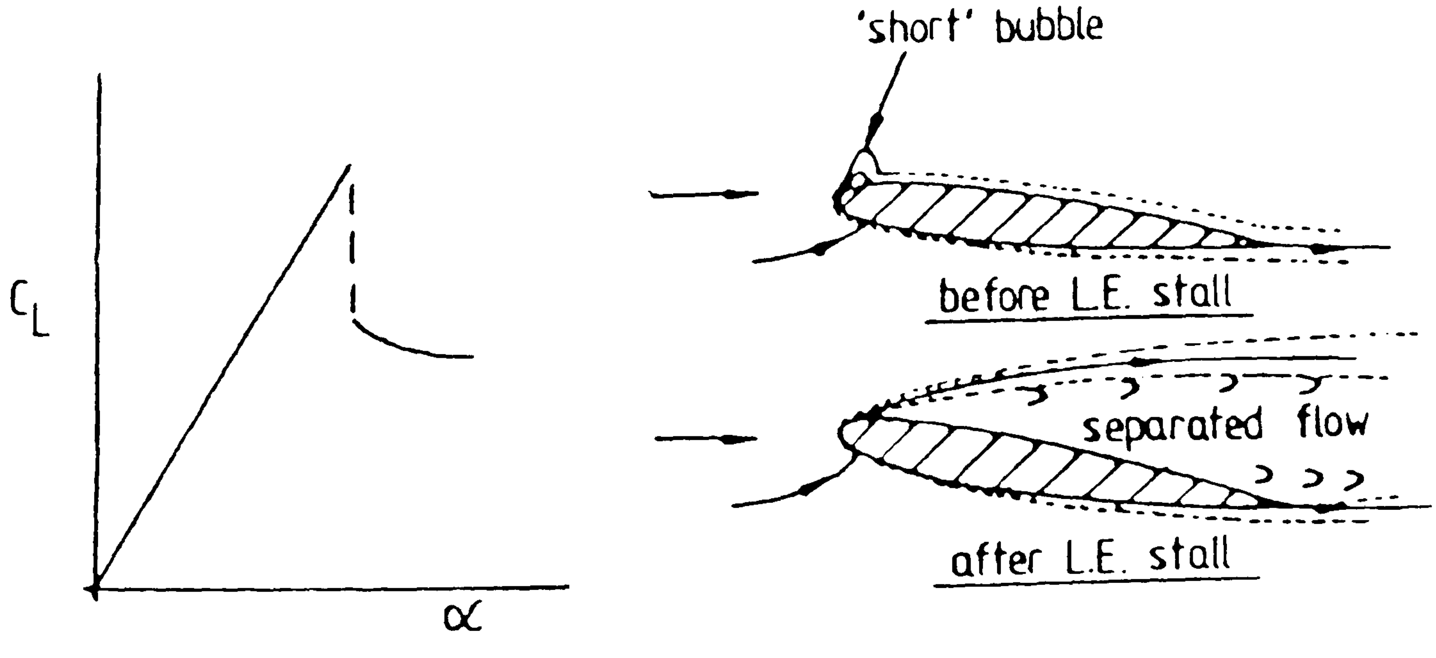

Figure 2.8 Leading edge stall, [2.40]

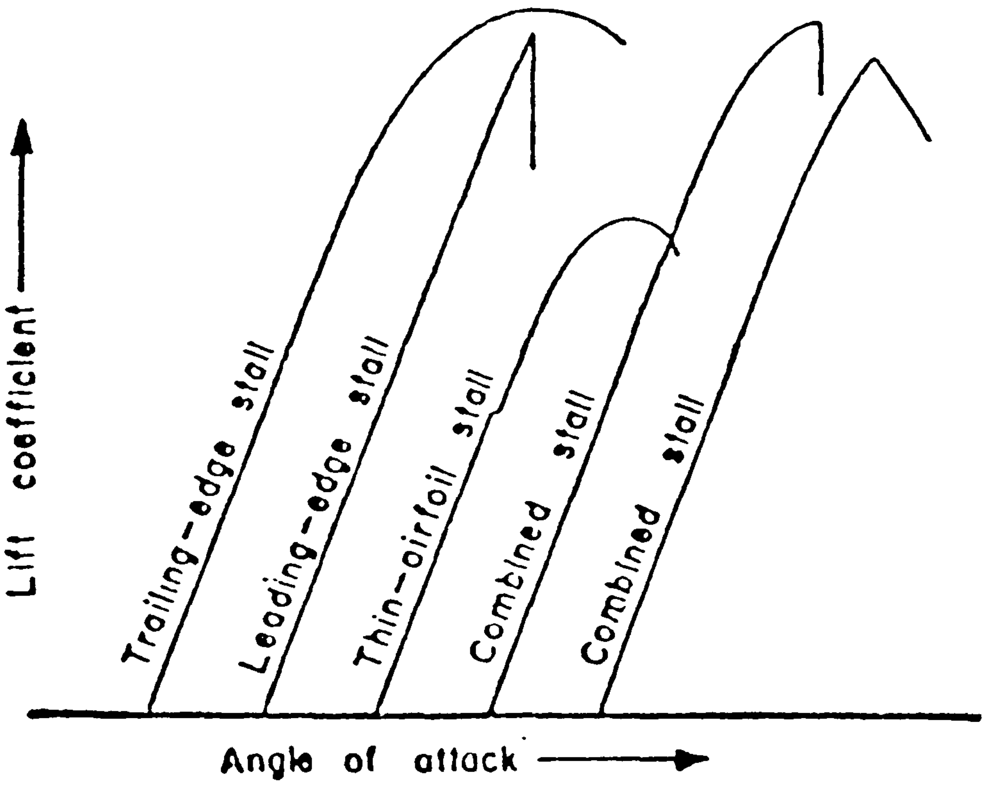

Figure 2.9 Typical lift characteristics for different stall types, [2.41]

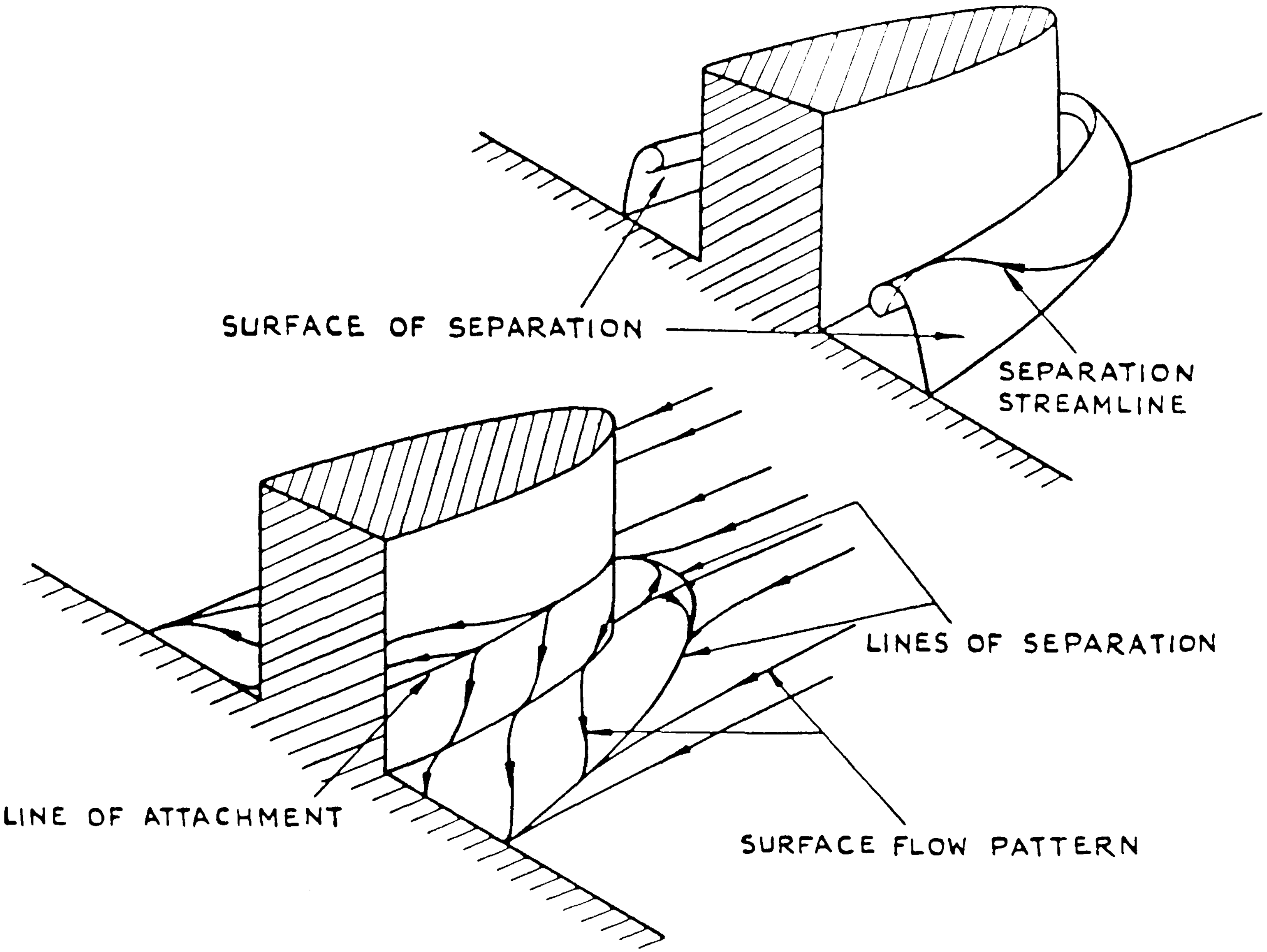

Figure 2.10 Formation of junction vortices, [2.42]

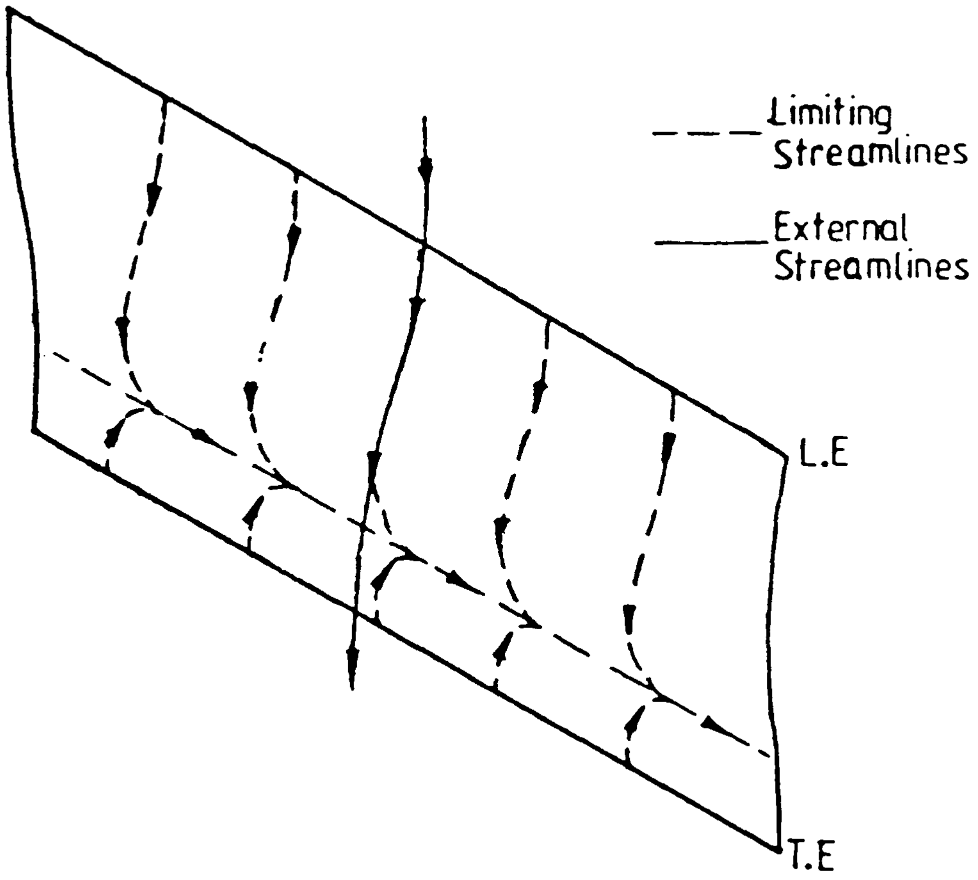

Figure 2.11 Separation from an infinite yawed wing, [2.40]

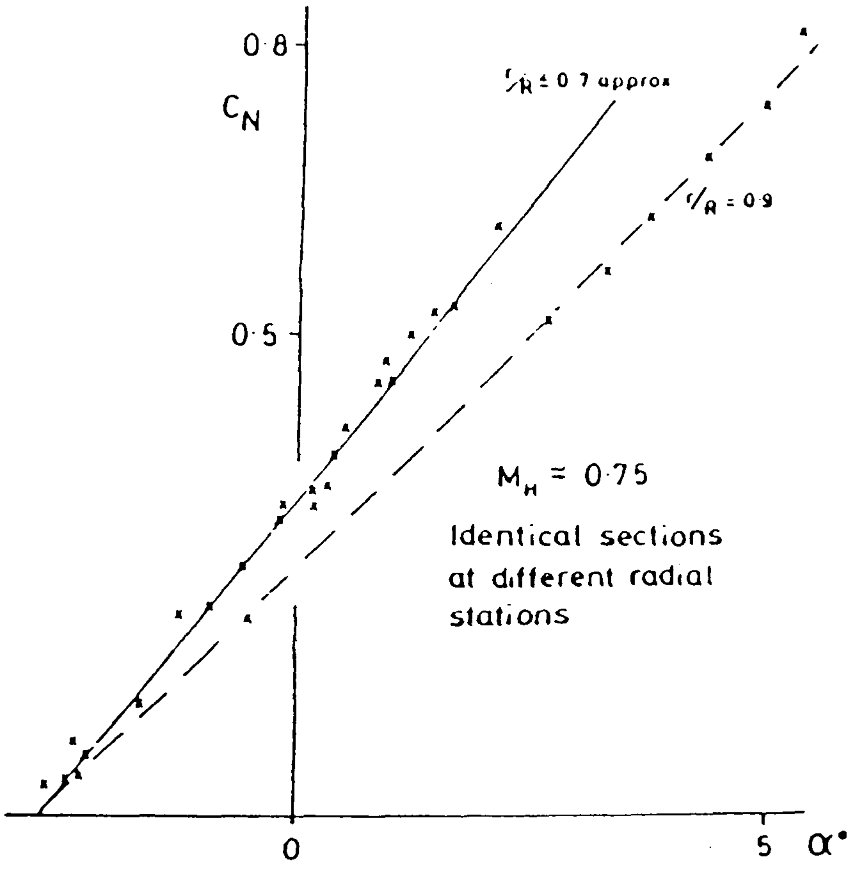

Figure 2.12 Reduction in lift curve slope near rotor tip due to tip loss, [2.16]

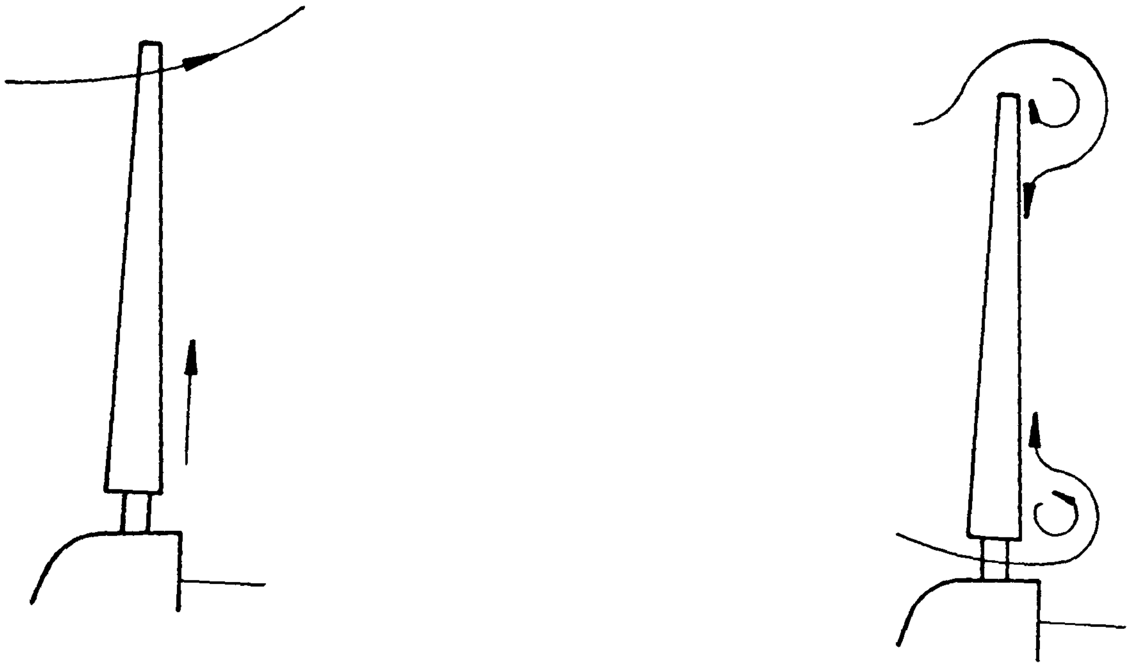

(a) 'Inflow' effect - wake expansion

(b) Tip and hub vortices

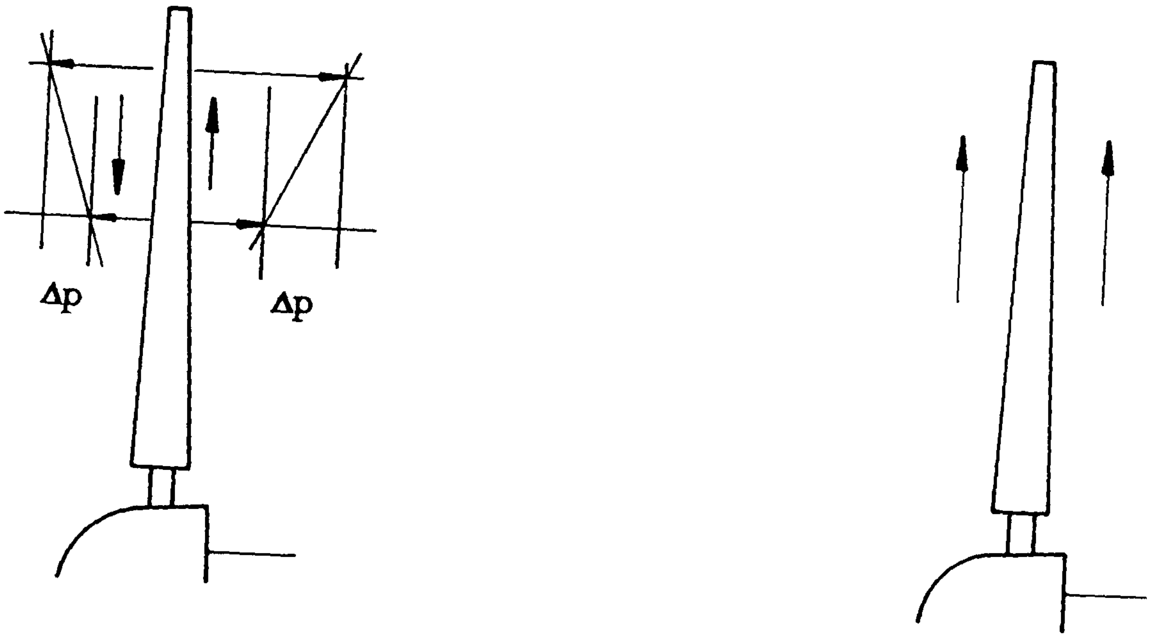

(c) Pressure gradients

(d) Centrifugal pumping

Figure 2.13 Factors causing radial flow in the boundary layer on a wind turbine blade

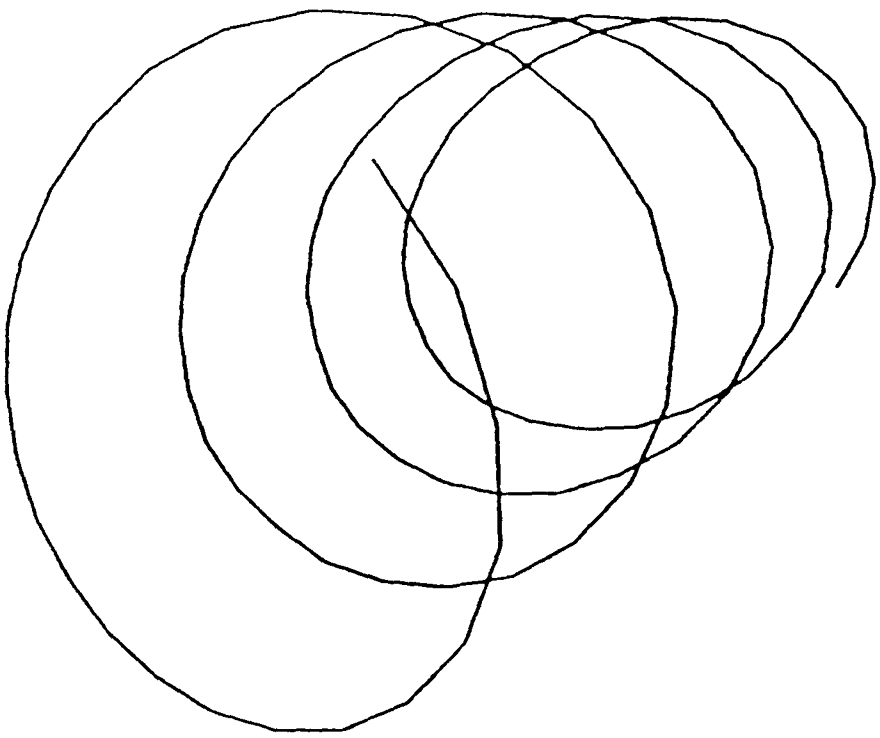

Figure 3.1 A Single Wake Helix

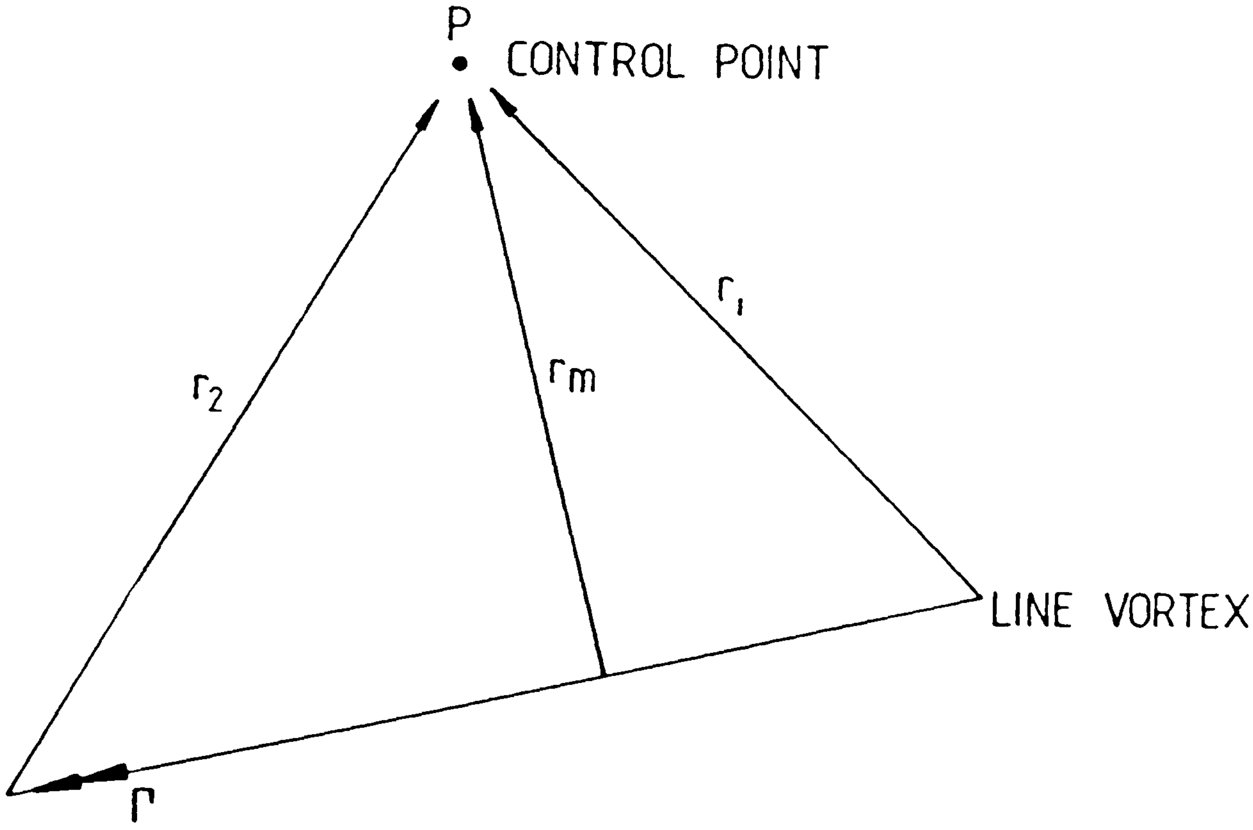

Figure 3.2 Calculation of Velocities Induced by a Line Vortex

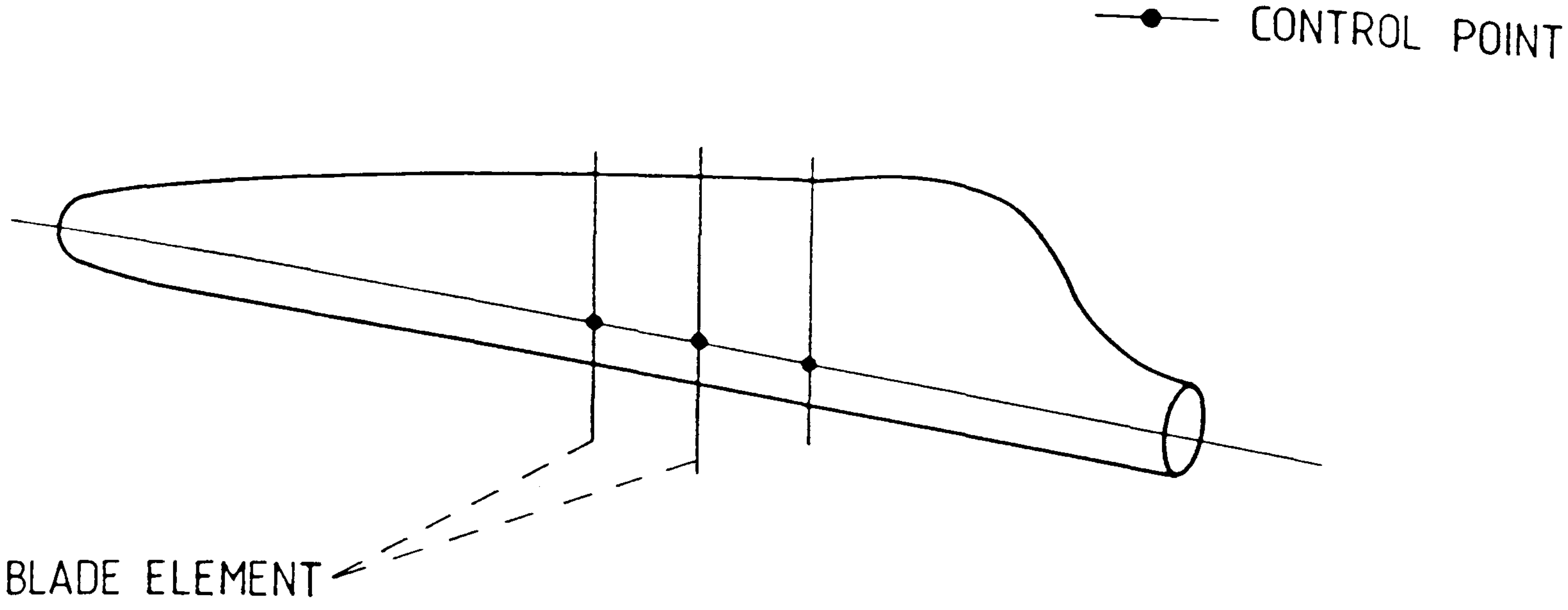

Figure 3.3 Blade Elements and Control Points

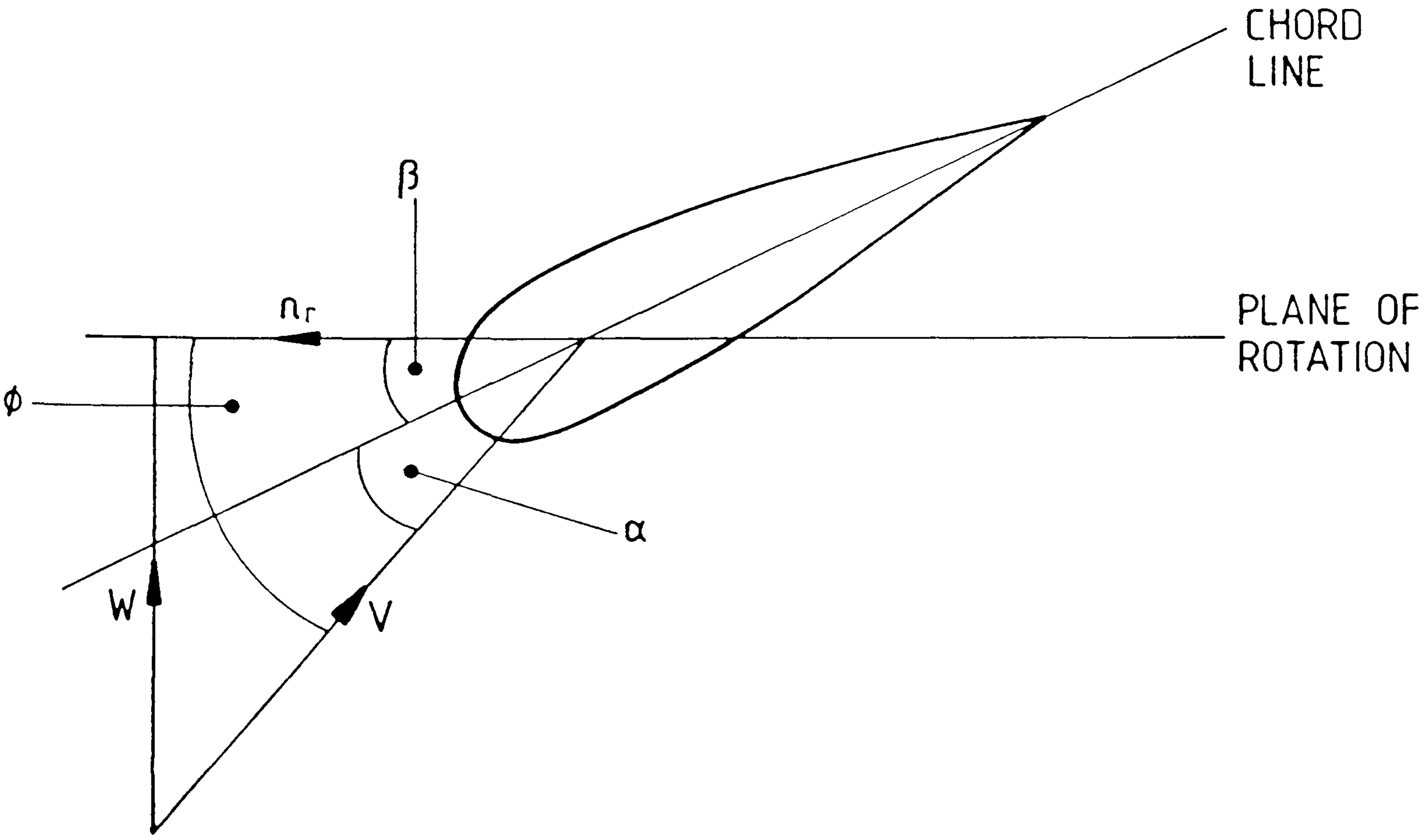

Figure 3.4 Blade Element Velocity Diagram

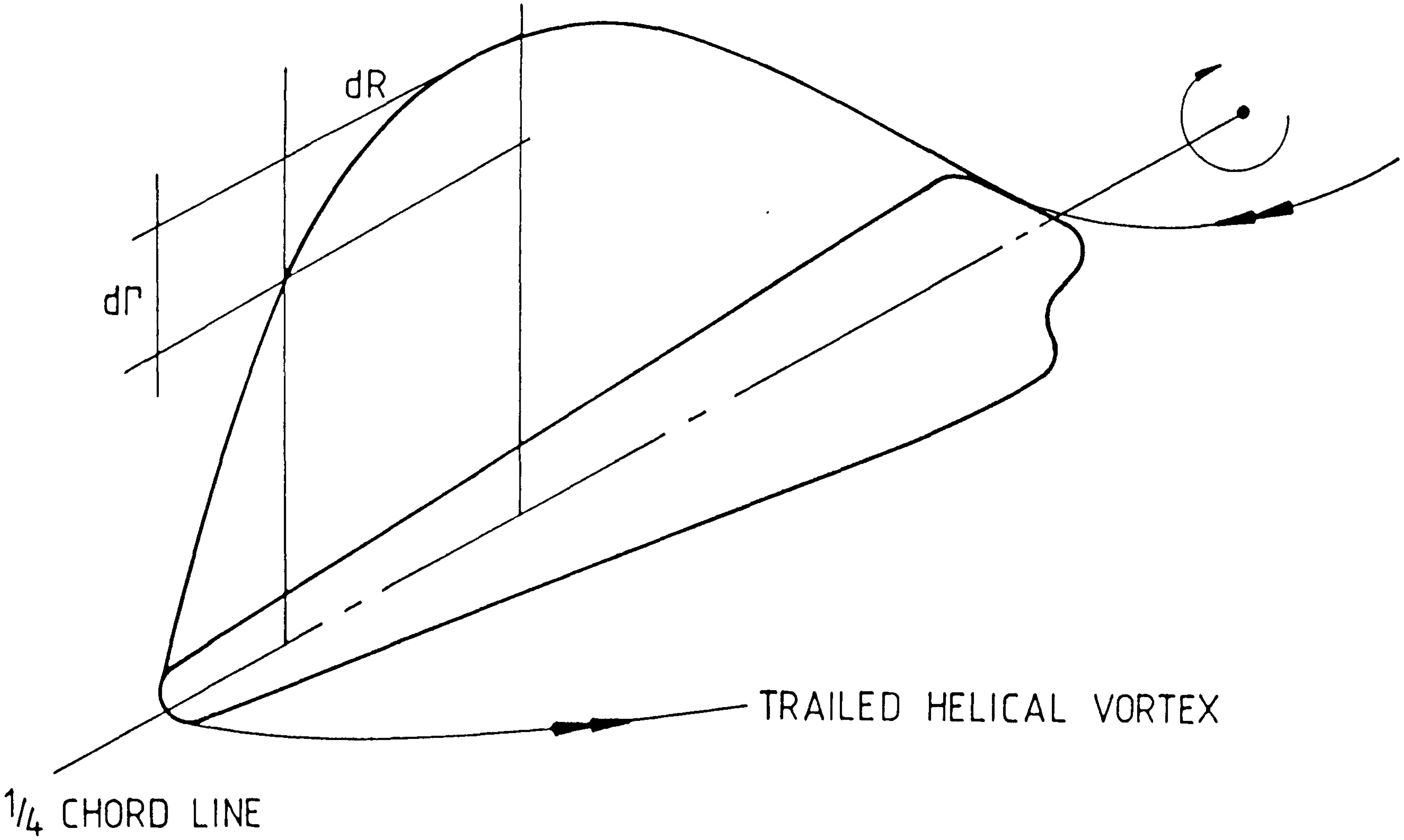

Figure 3.5 Bound Circulation Distribution and Method of Assigning Vorticity to Wake Elements

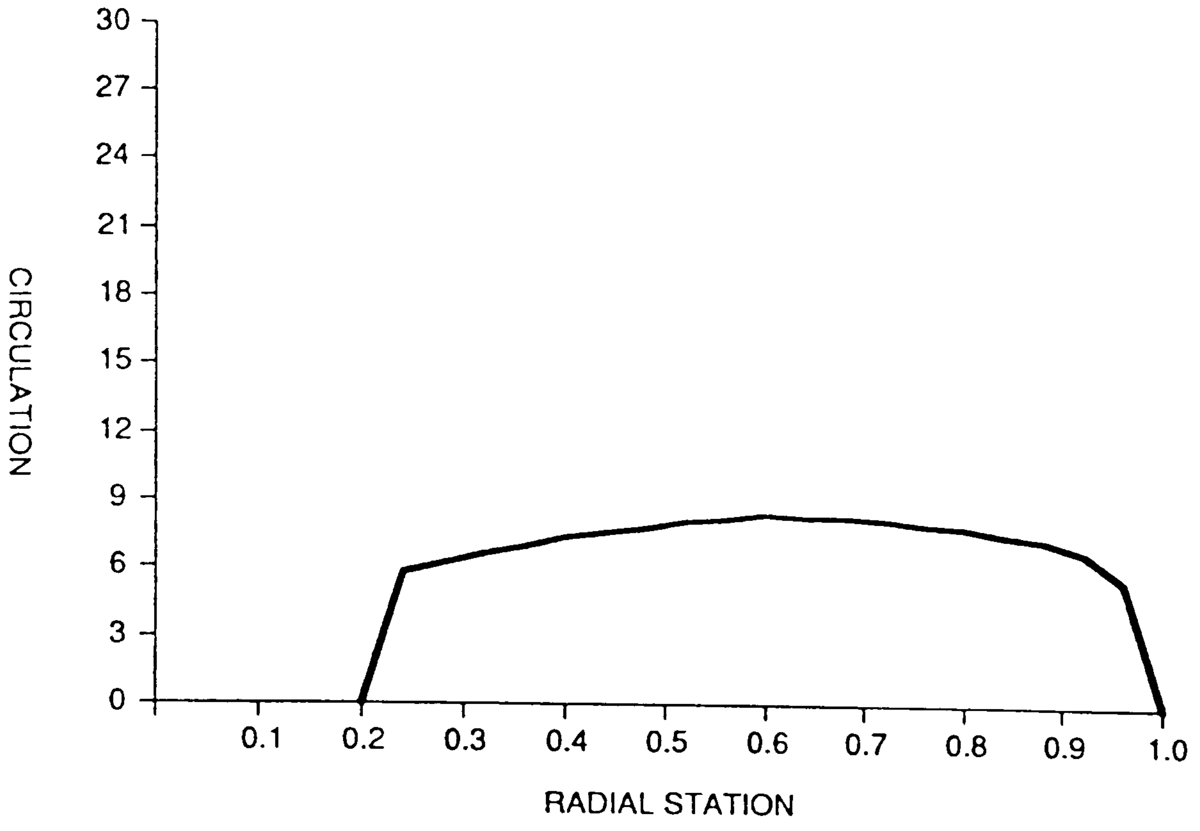

Figure 3.6 Typical Calculated Circulation Distribution.

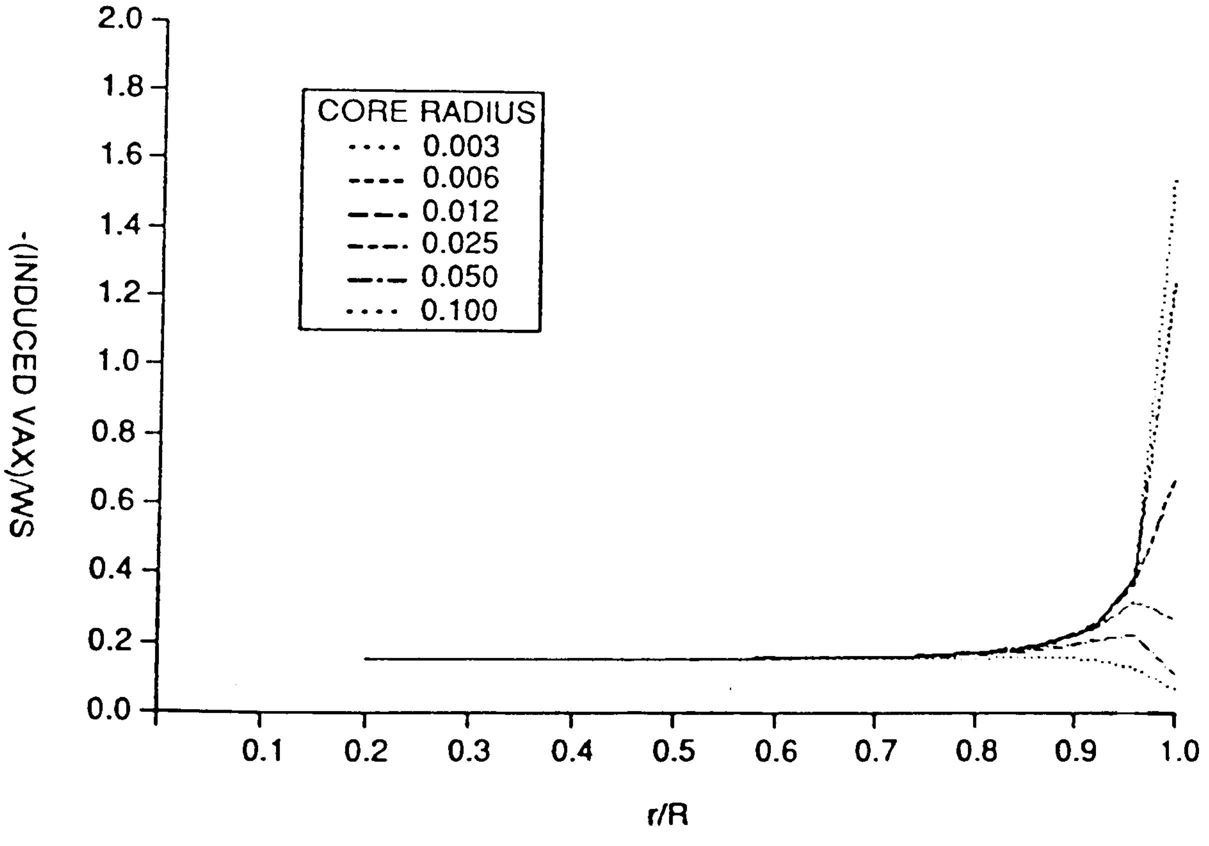

Figure 3.7 Effect of Core Radius on Induced Axial Velocity

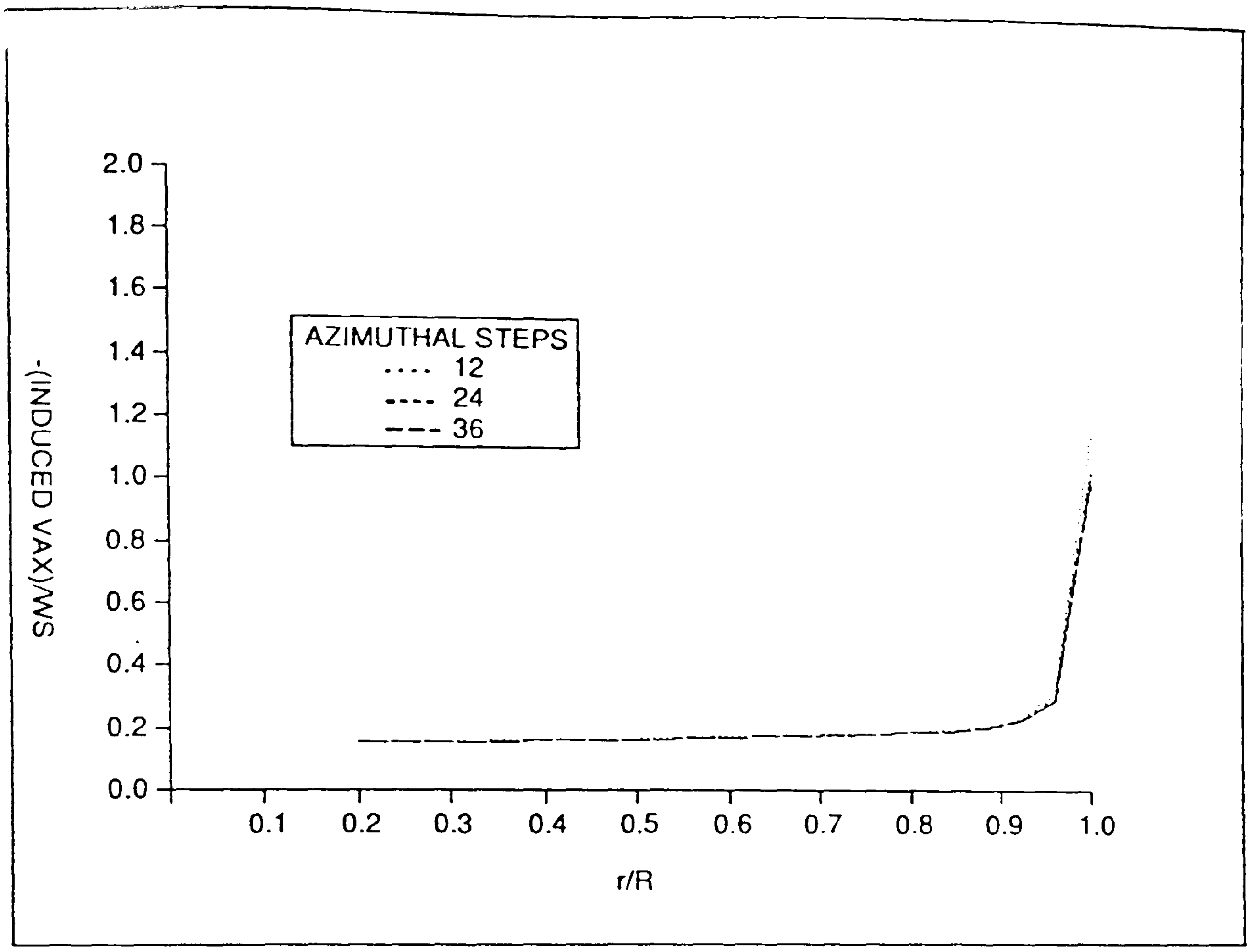

Figure 3.8 Effect of Varying Number of Azimuthal Elements for a Single Spiral/Helix

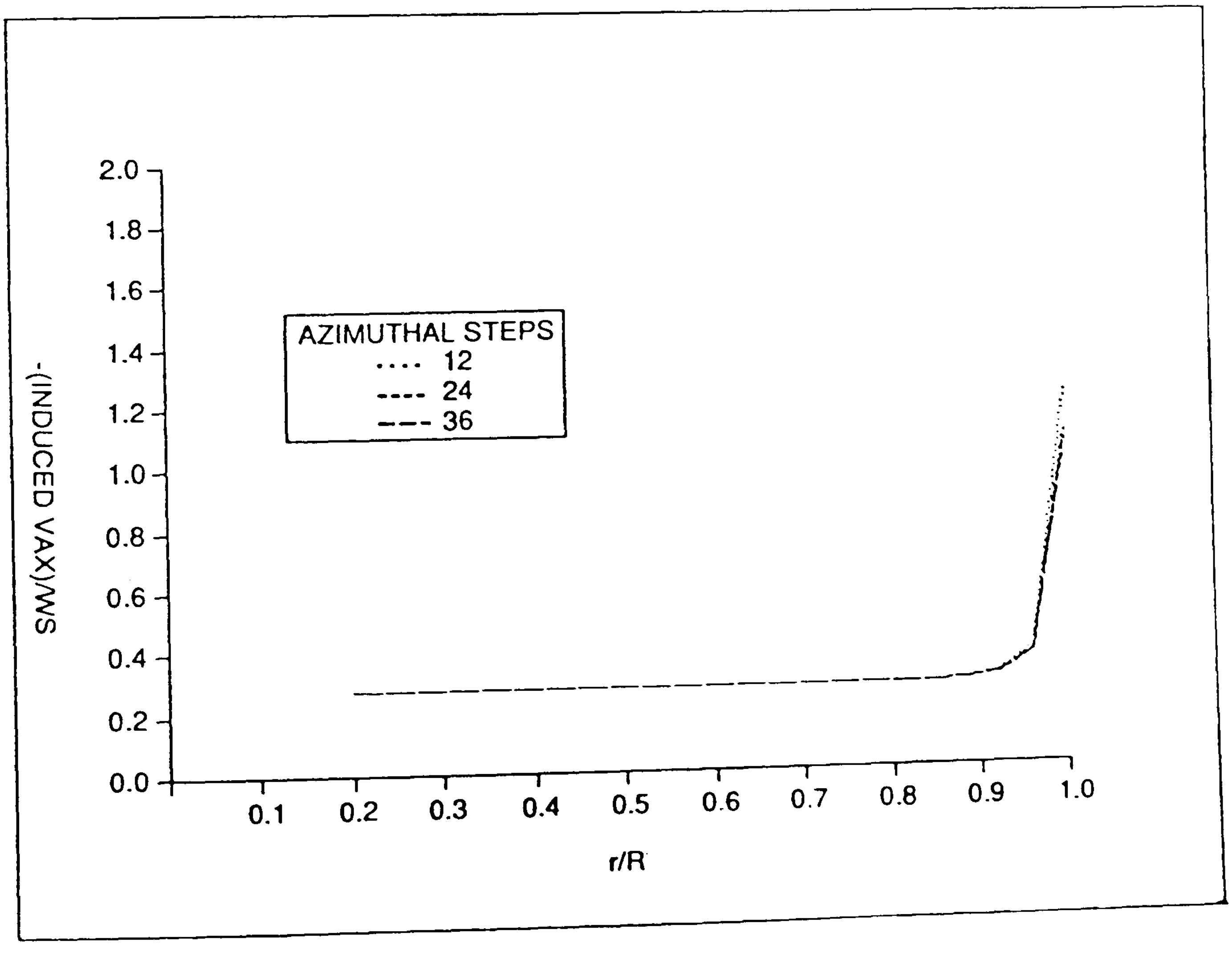

Figure 3.9 Effect of Varying Number of Azimuthal Elements for Three Spirals/Helix

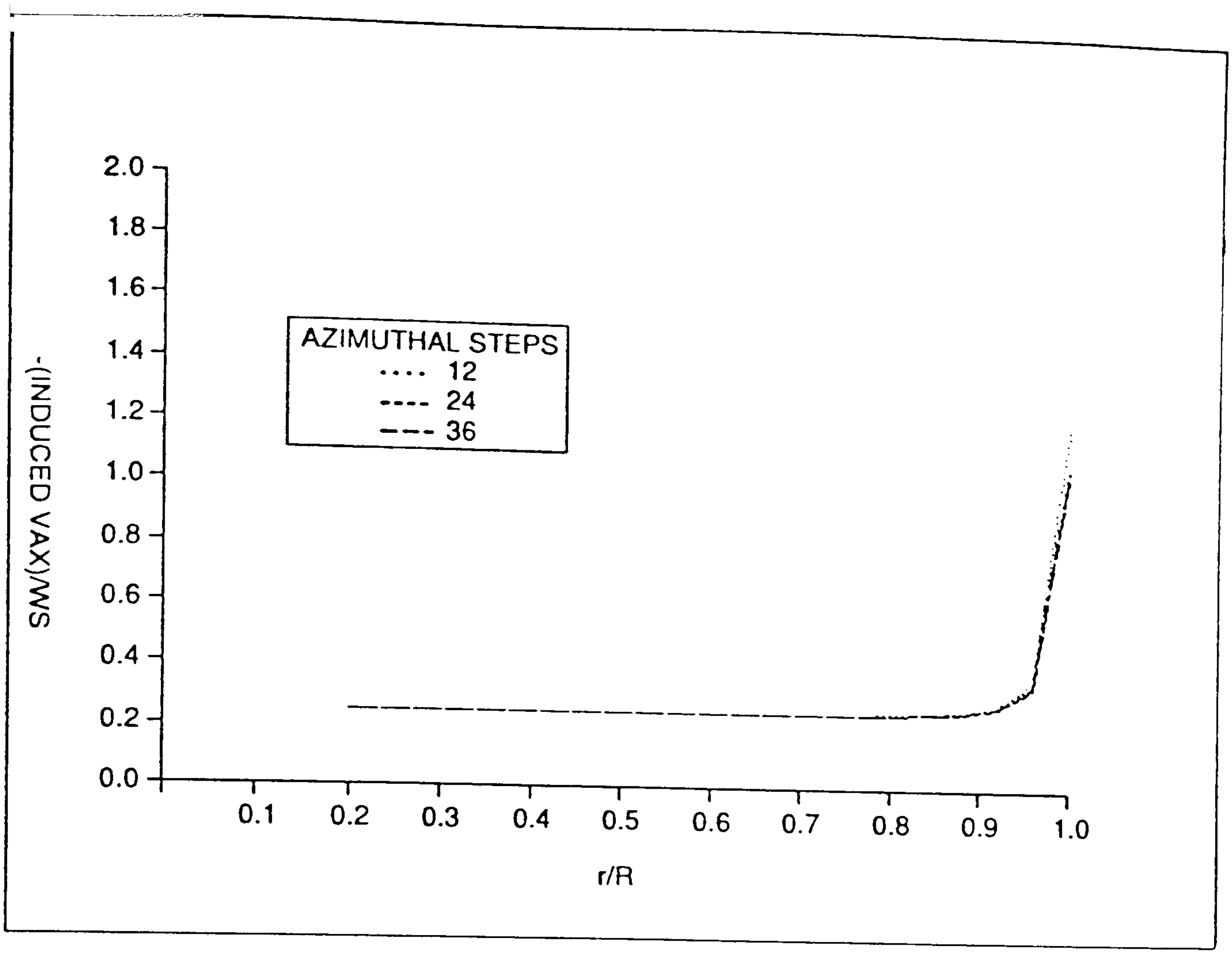

Figure 3.10 Effect of Varying Number of Azimuthal Elements for Twelve Spirals/Helix

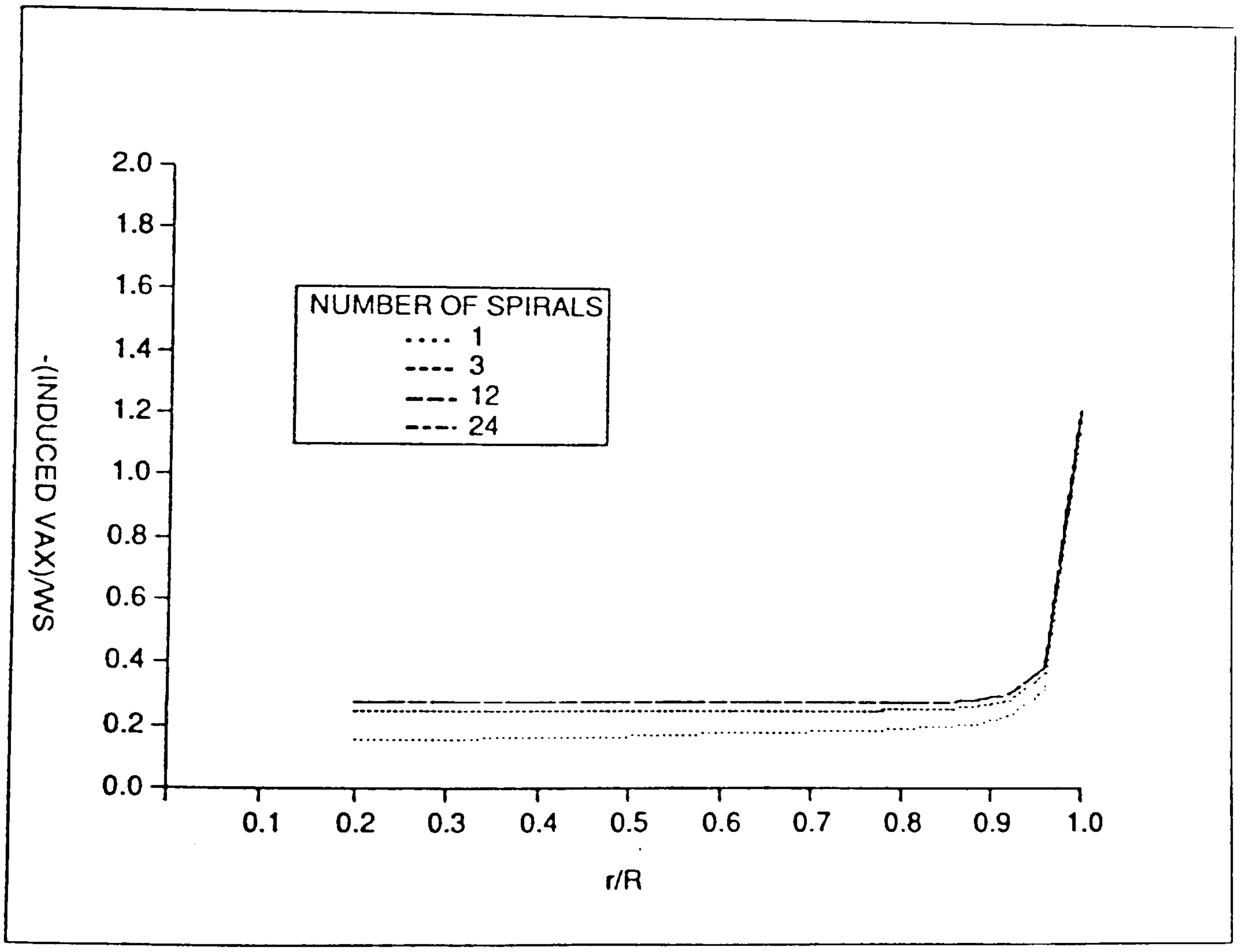

Figure 3.11 Convergence of Axial Induced Velocity With Increasing the Number of Spirals/Helix

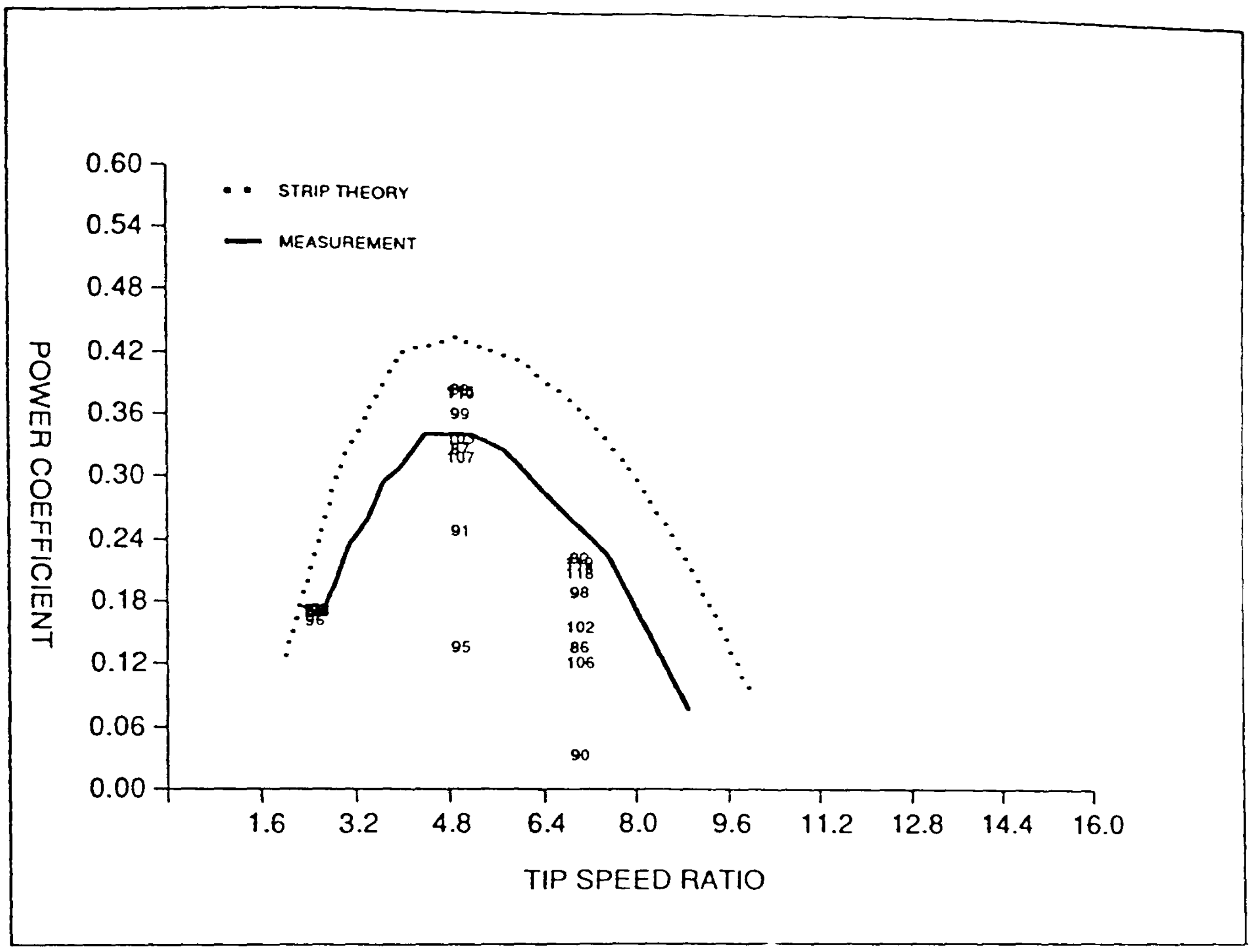

Figure 3.12 Cranfield 3m diameter turbine Predicted and Measured Power Coefficient

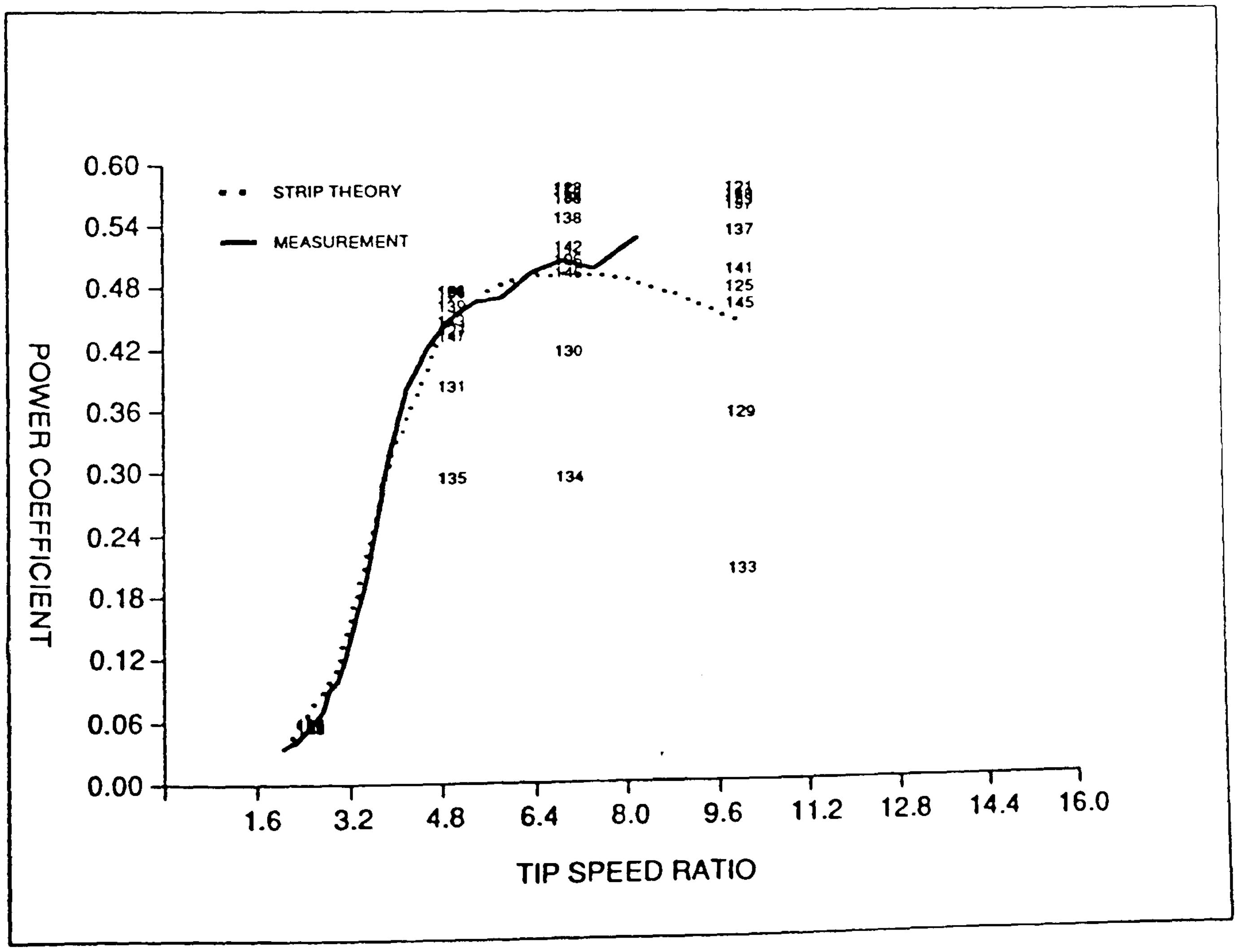

Figure 3.13 Windmatic WM17S Predicted and Measured Power

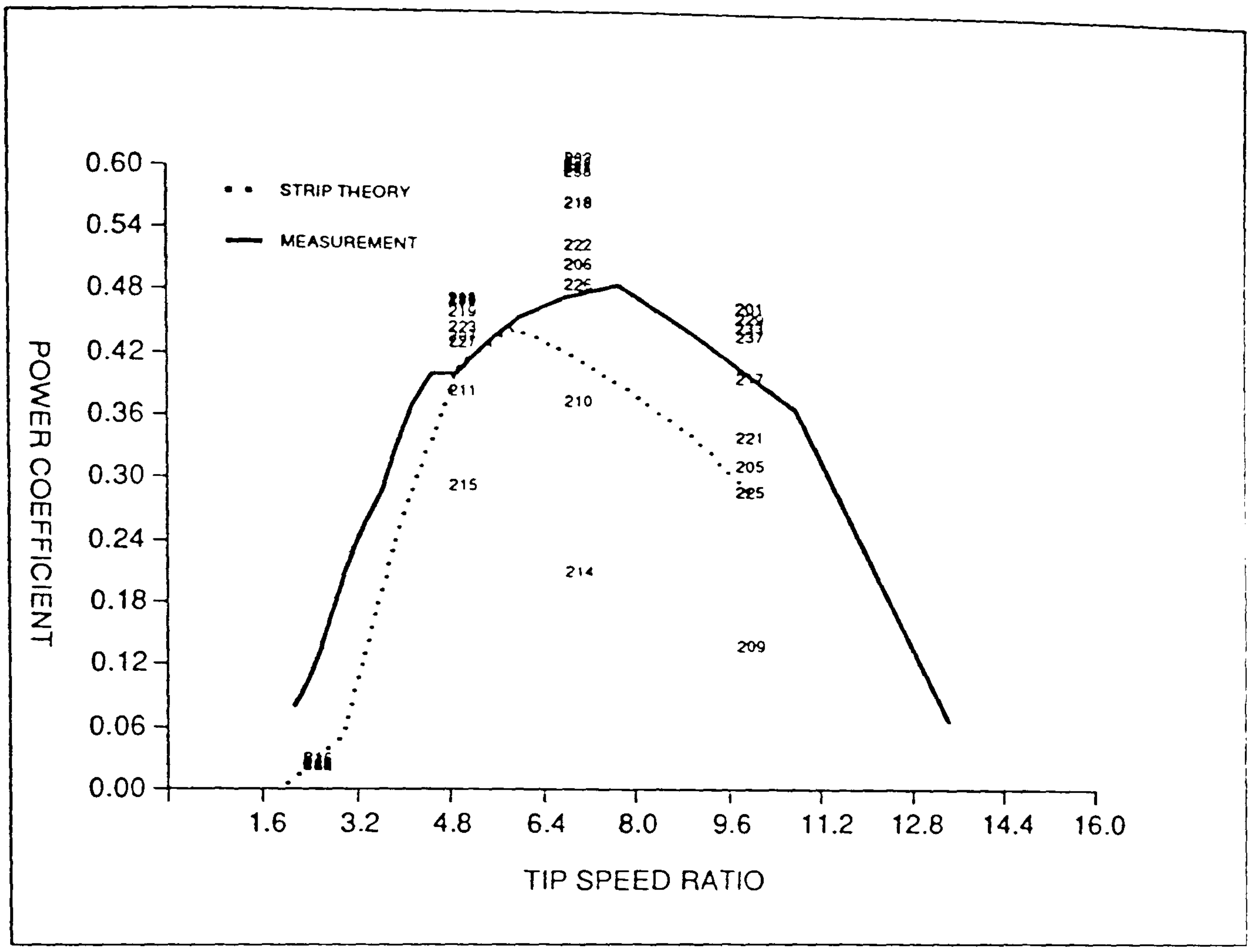

Figure 3.14 Windpower & Co (UK) Ltd WP-1 Predicted and Measured Power Coefficient

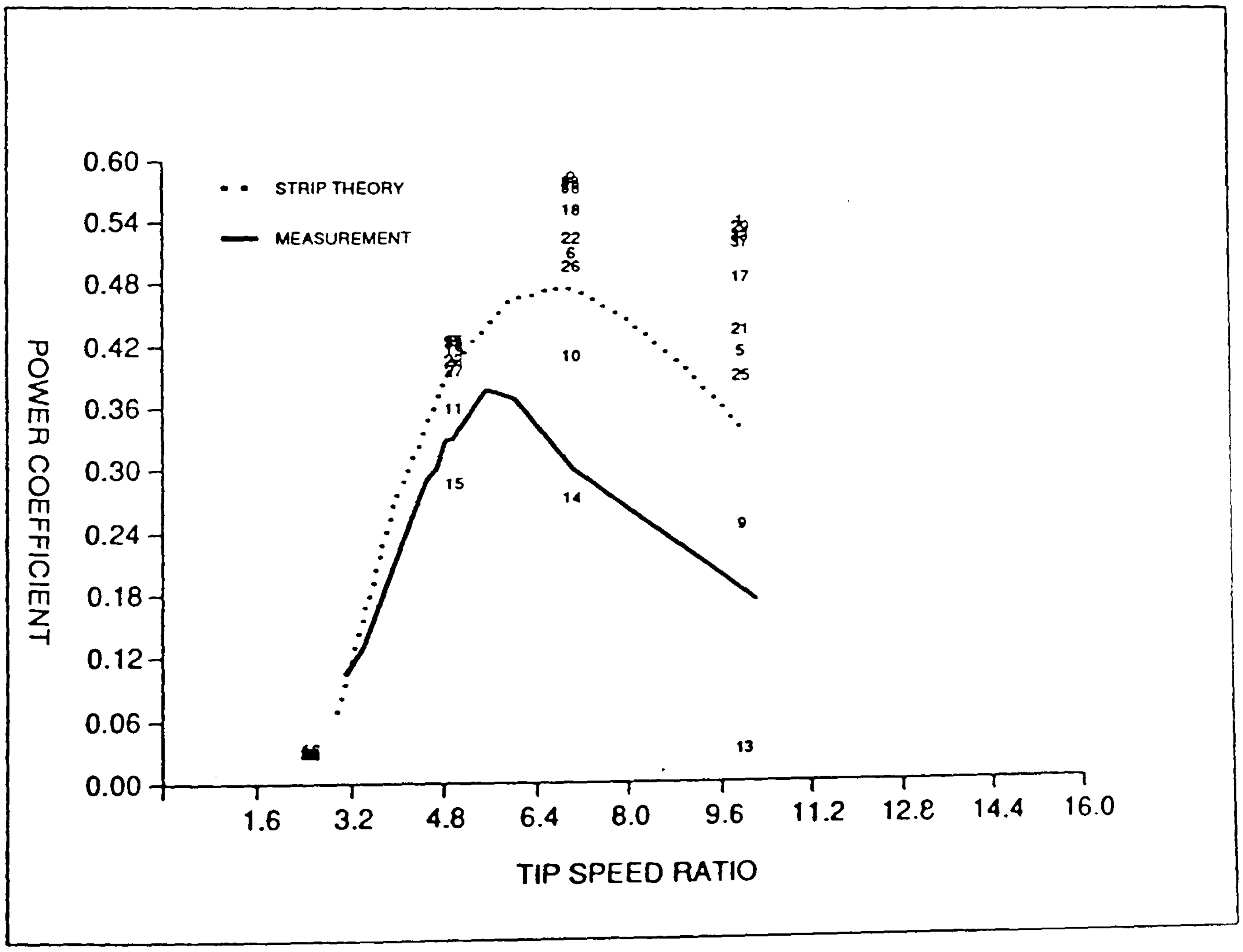

Figure 3.15 WEG MS2.SR Predicted and Measured Power Coefficient

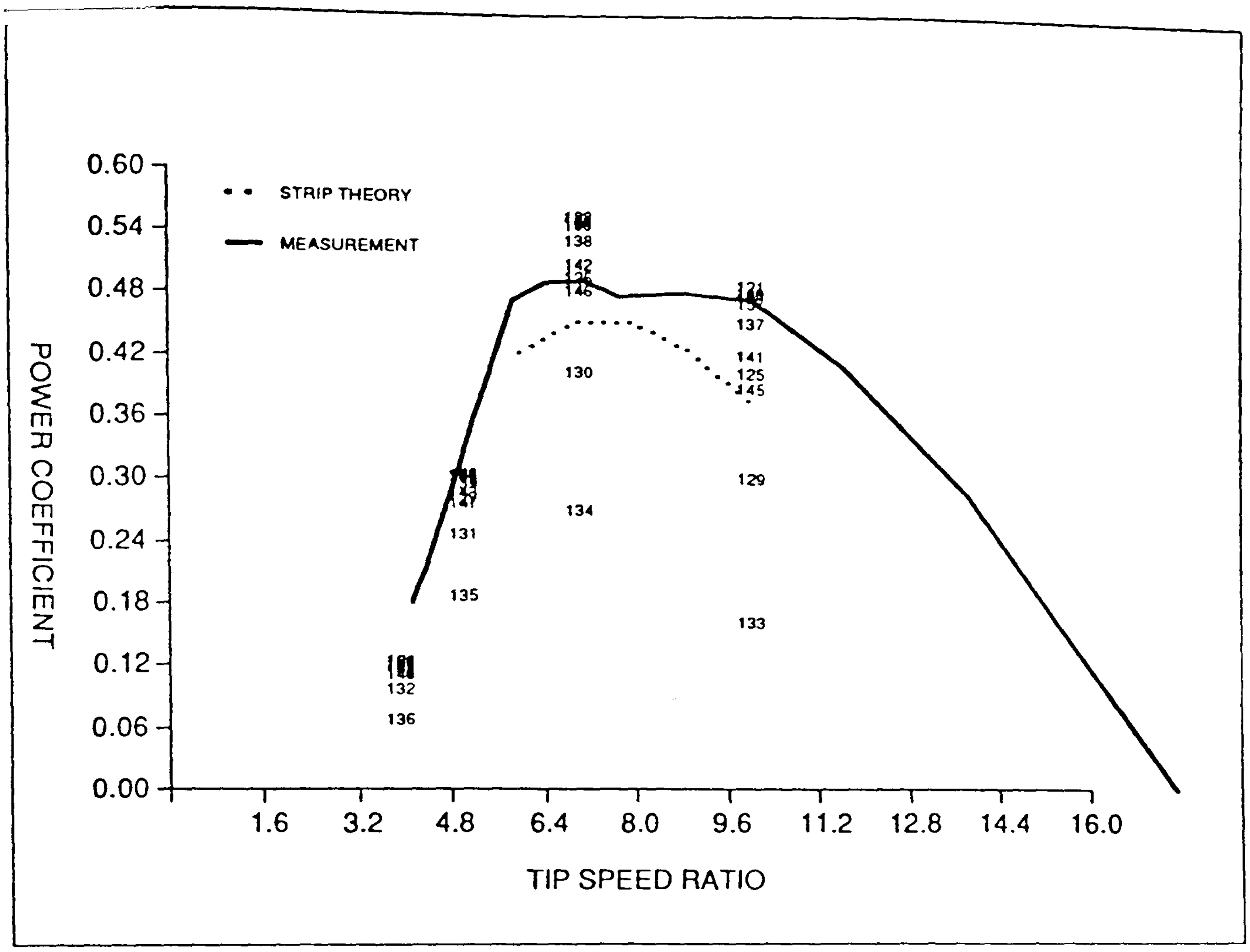

Figure 3.16 Nibe B Predicted and Measured Power Coefficient

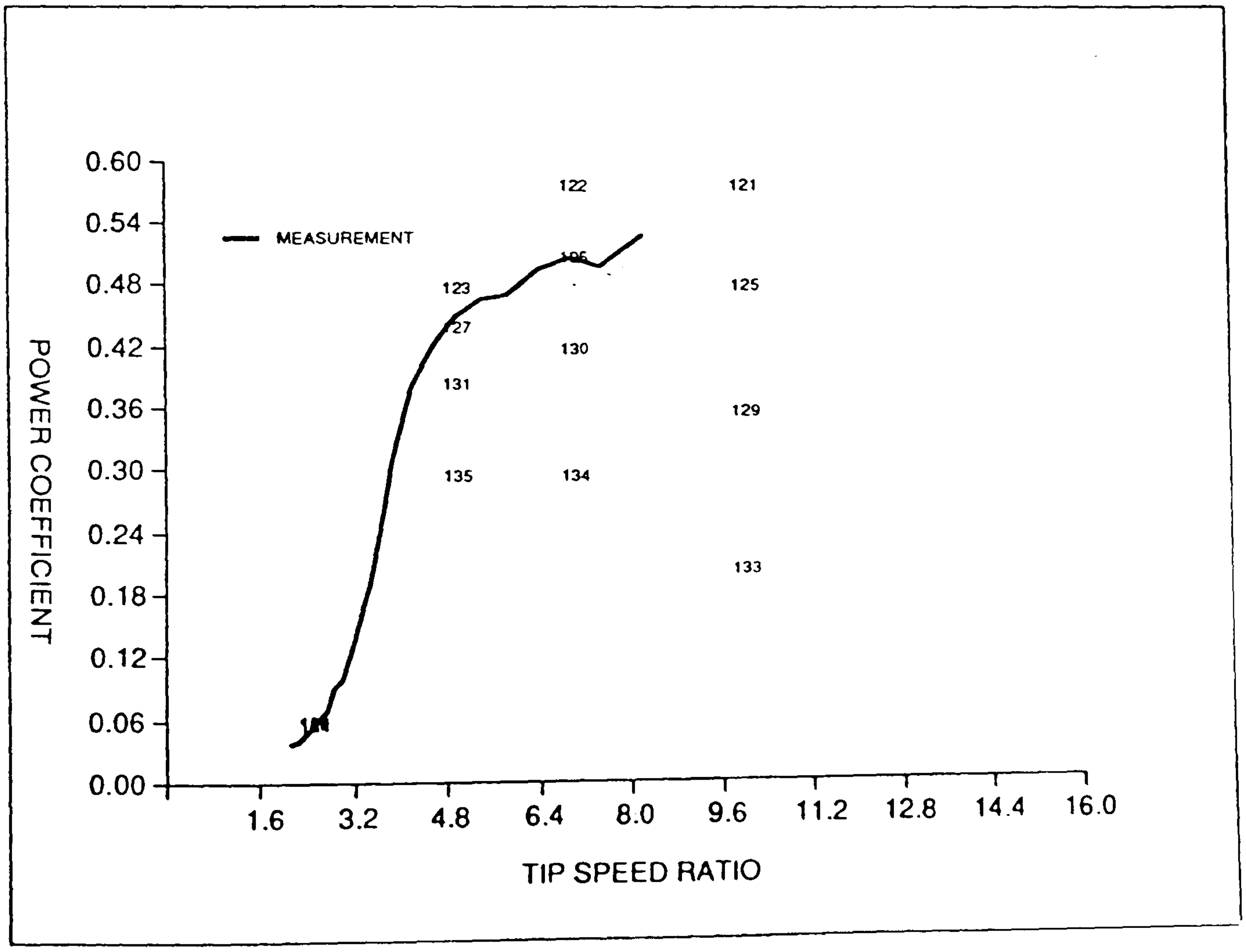

Figure 3.17 Windmatic WM17S Effect of Convection Rate on Predicted Power Coefficient

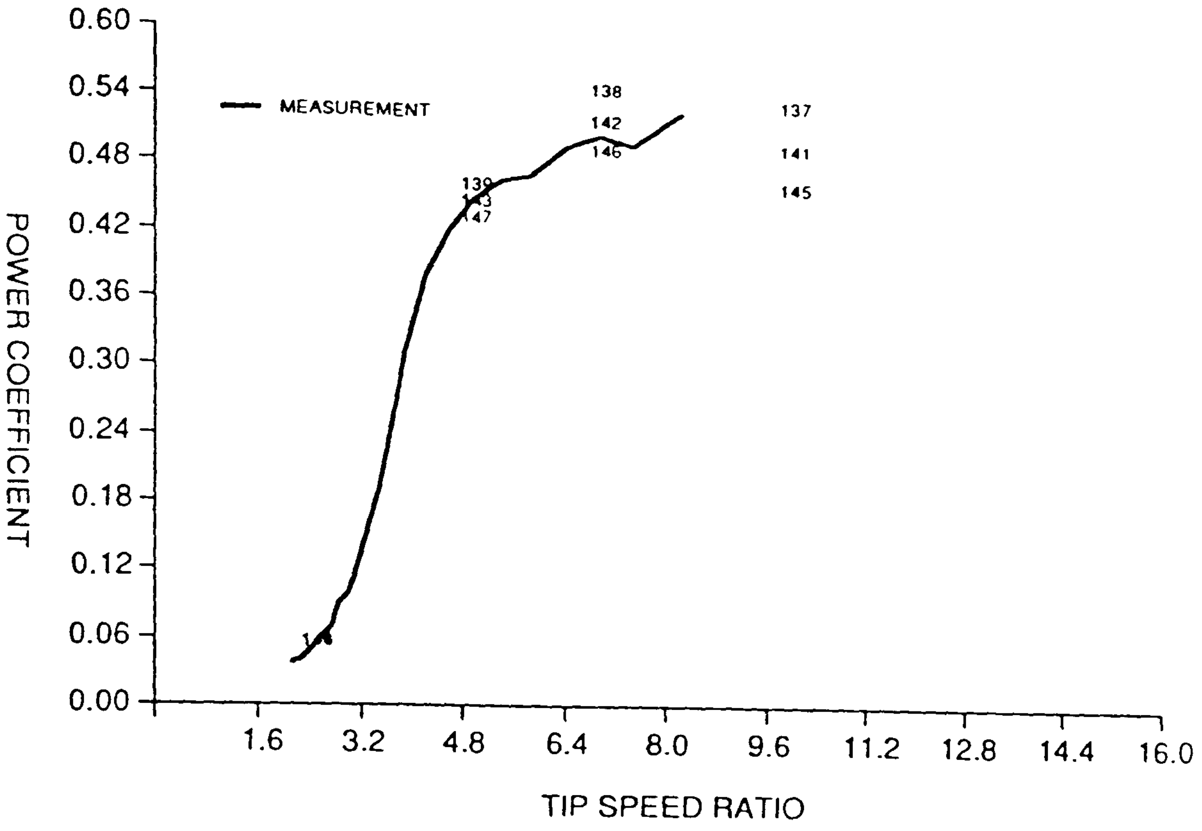

Figure 3.18 Windmatic WM17S Effect of Swirl Rate on Predicted Power Coefficient

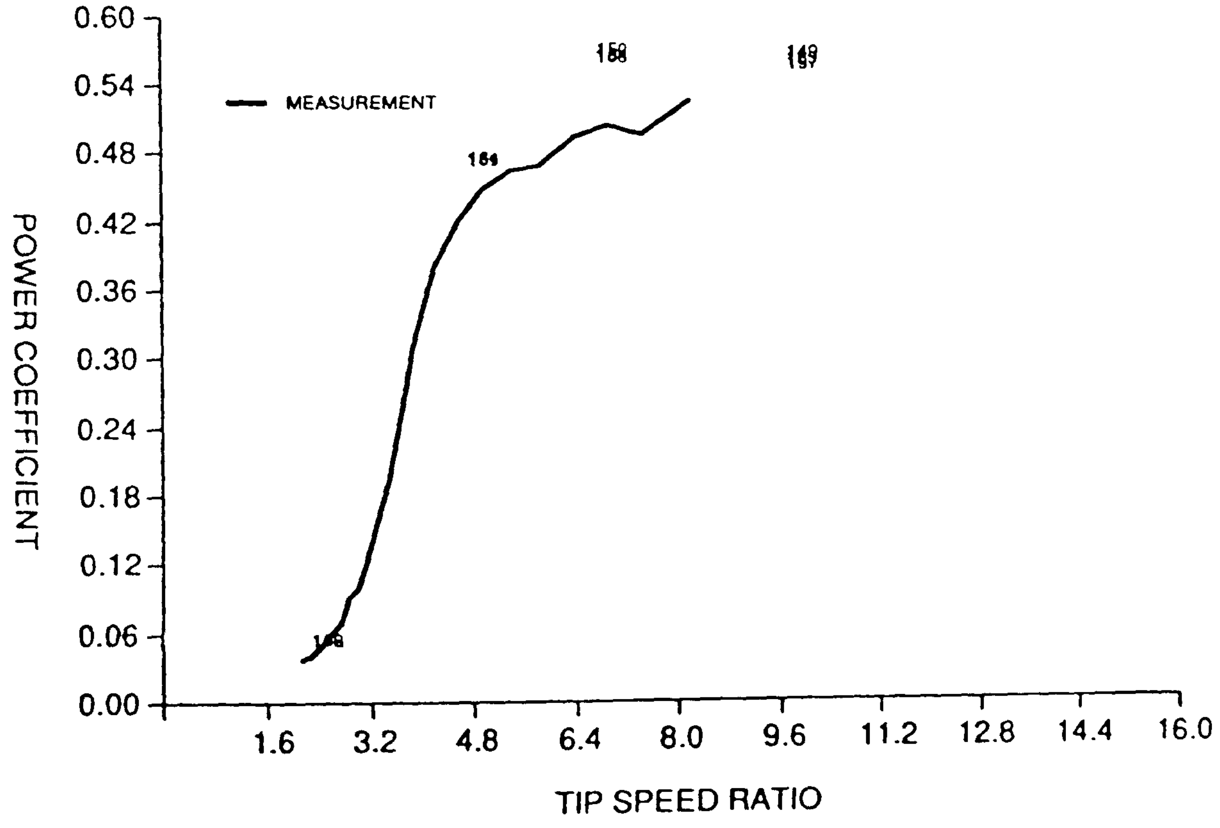

Figure 3.19 Windmatic WM17S Effect of Wake Expansion on Predicted Power Coefficient

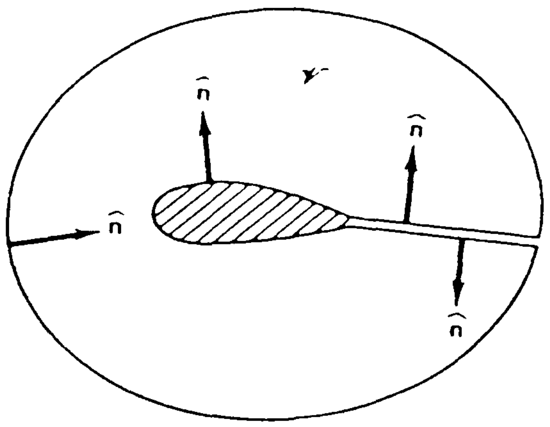

Figure 4.1 Control Volume for Application of Divergence Theorem, [4.7]

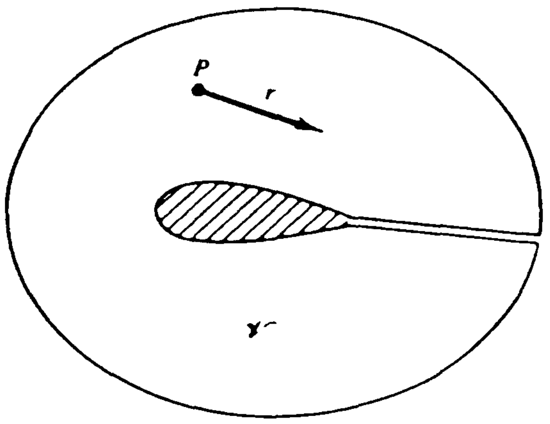

Figure 4.2 Nomenclature for Source Potential, [4.7]

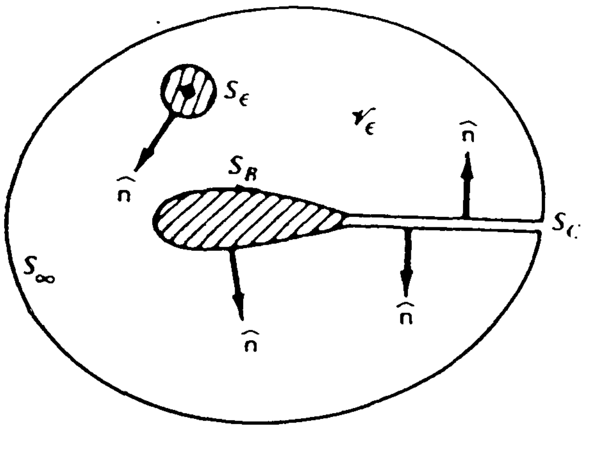

Figure 4.3 Nomenclature for Derivation of Green's Identity, [4.7]

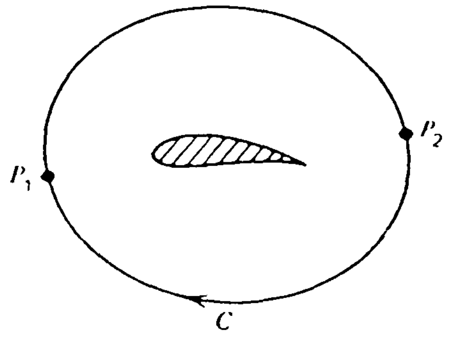

Figure 4.4 Multivaluedness of Potential of Flow Past a Lifting Aerofoil, [4.7]

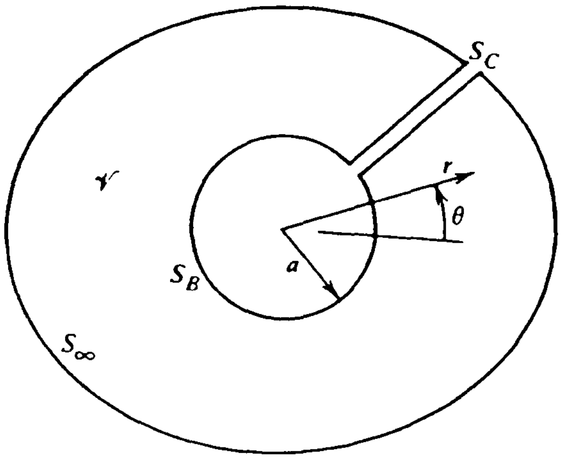

Figure 4.5 Need for a Branch Cut to make Potential Single Valued, [4.7]

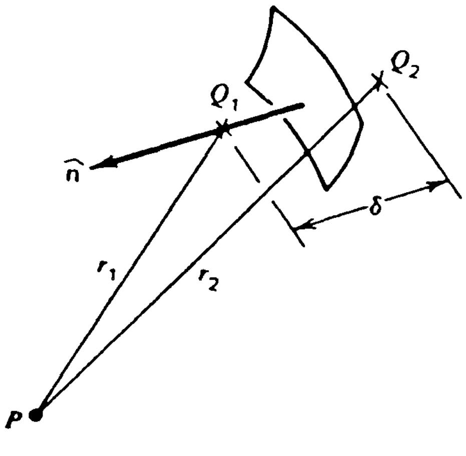

Figure 4.6 Interpretation of Second Integral in Equation (4.9) as a Doublet Distribution, [4.7]

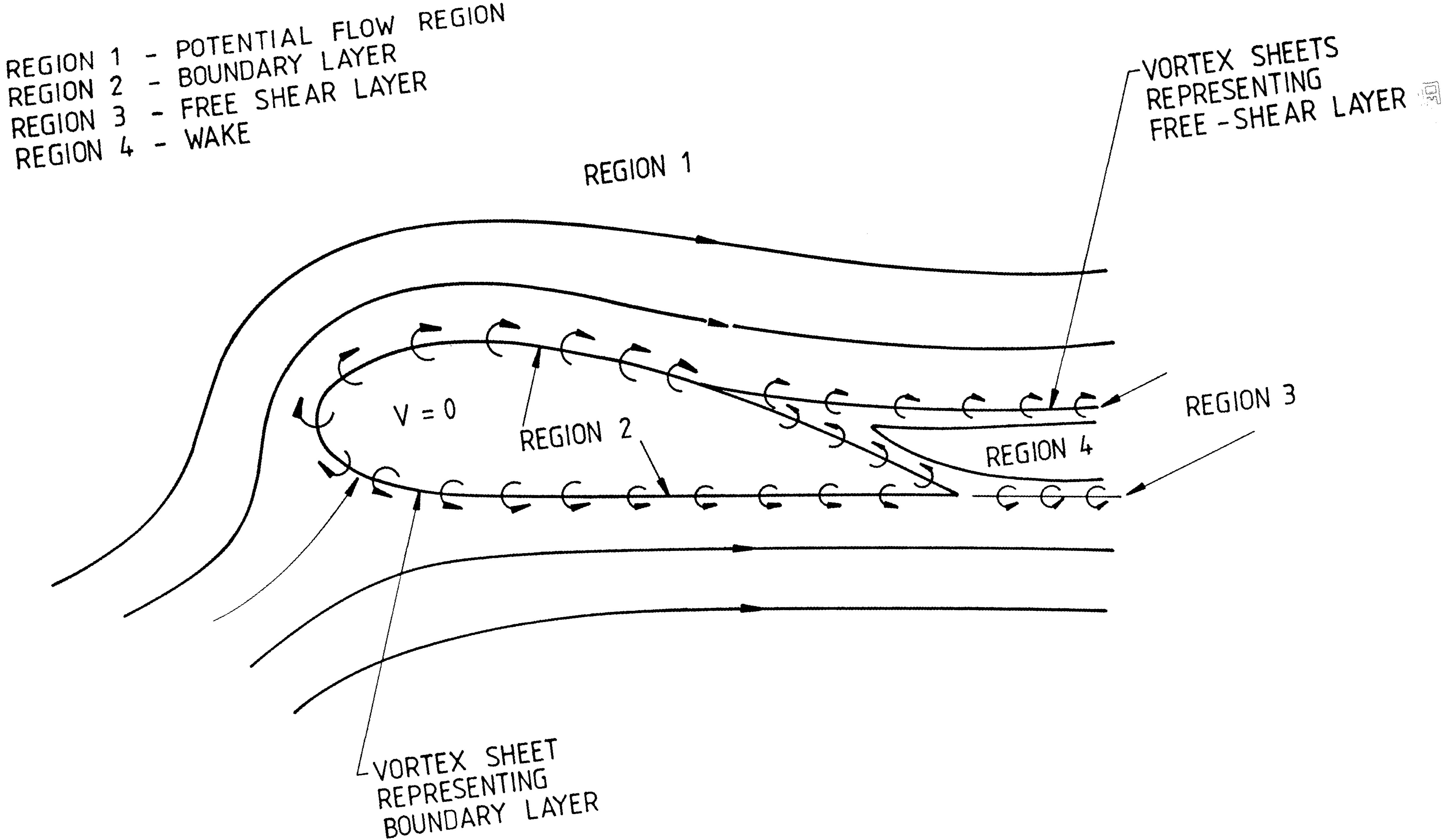

Figure 4.7 Mathematical Flow Model, [4.5]

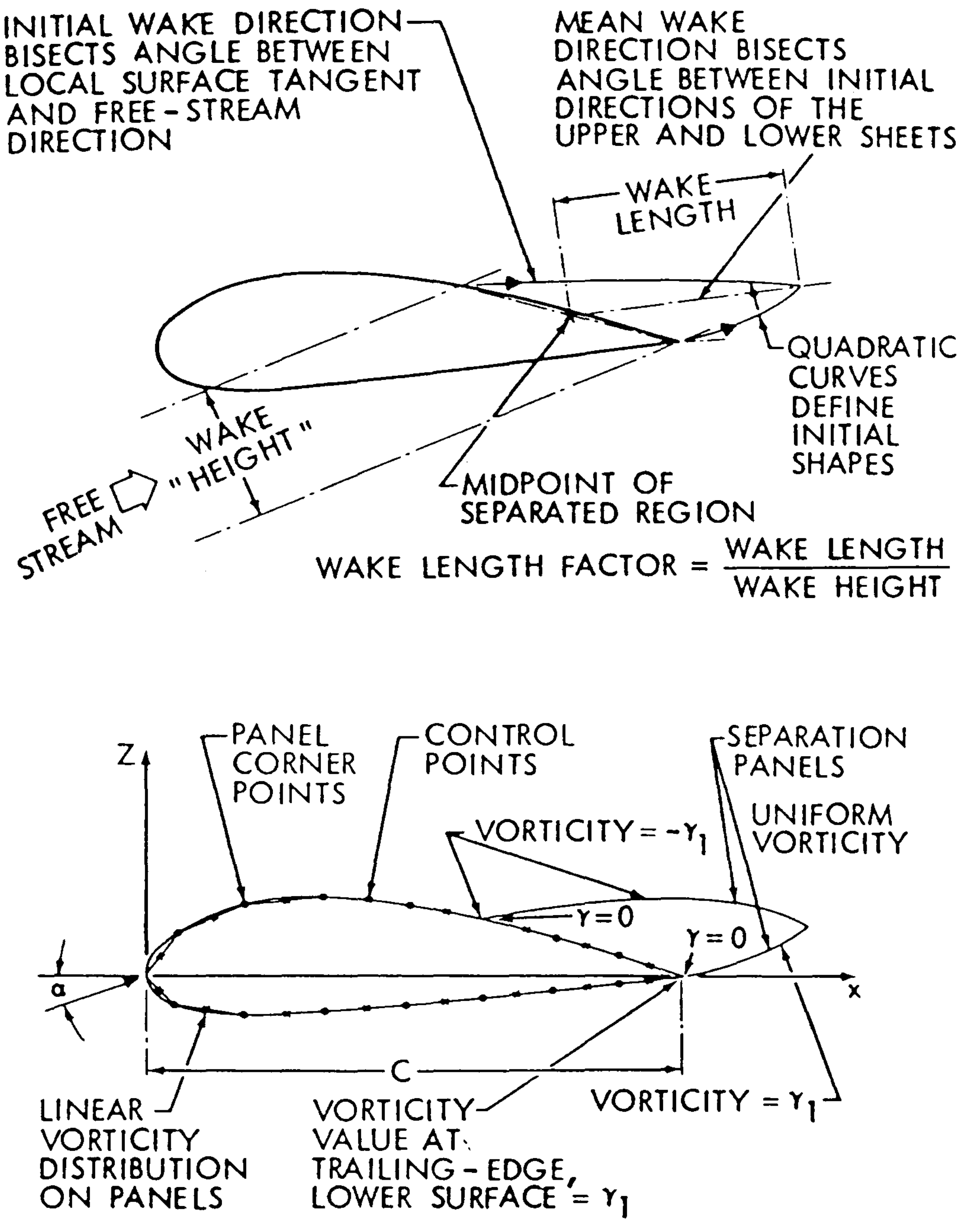

Figure 4.8(a) Model Geometry for Potential Flow With Free Shear Layer, [4.5]

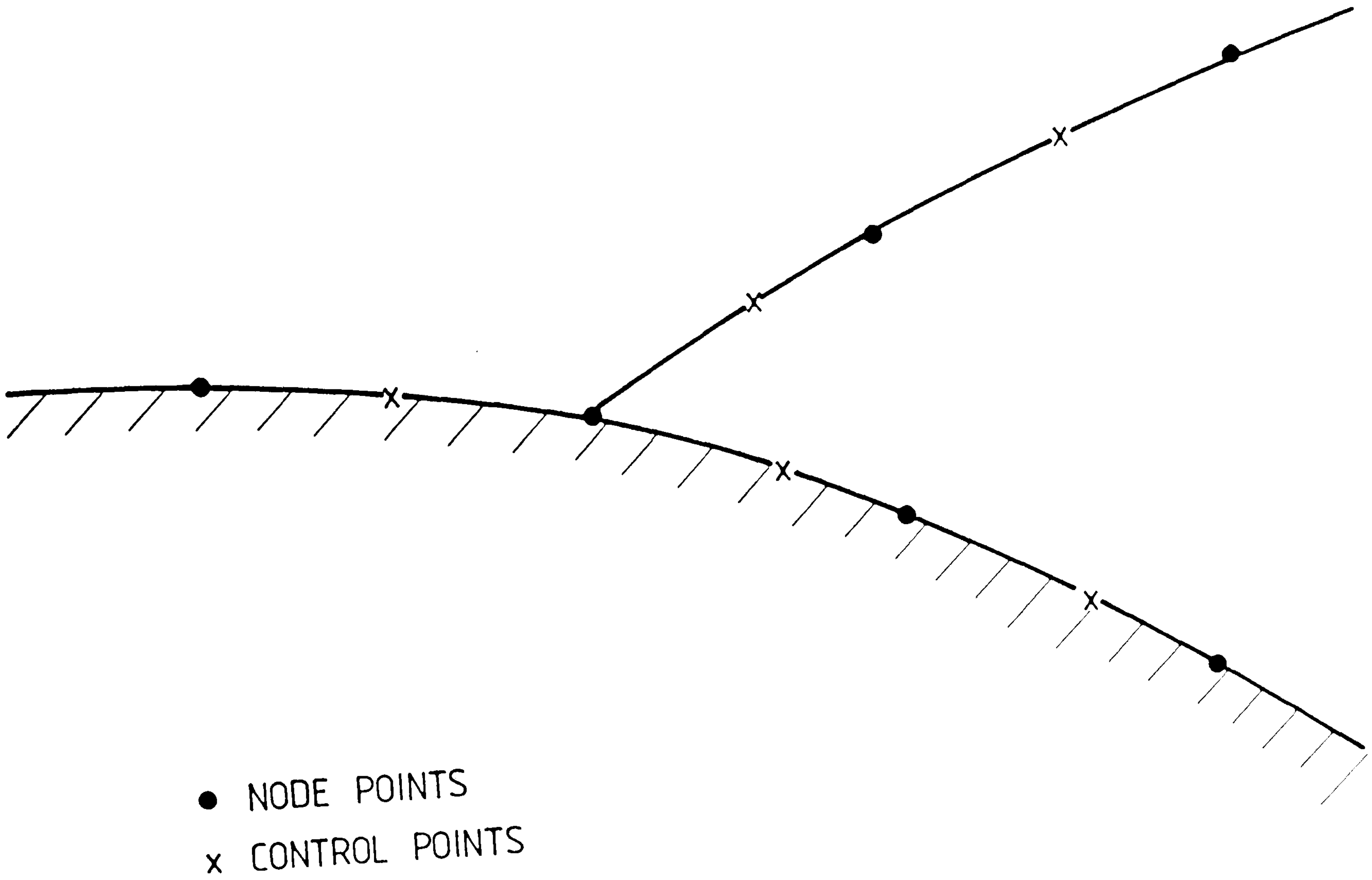

Figure 4.8(b) Model Geometry for Potential Flow with Free Shear Layers - detail around the point of separation

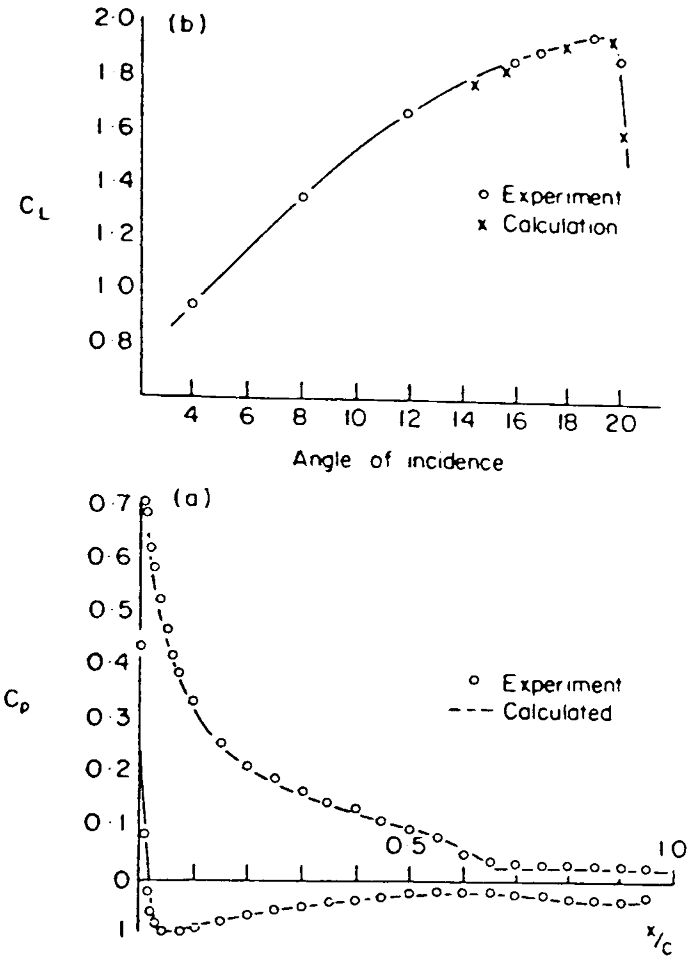

Figure 4.9 Illustration of Accuracy of a Vortex Based Free Shear Layer Model in Predicting Airfoil Lift, [4.1]

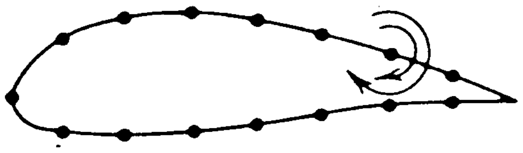

Figure 4.10 Velocity Field of Constant Strength Vortex Method, [4.7]

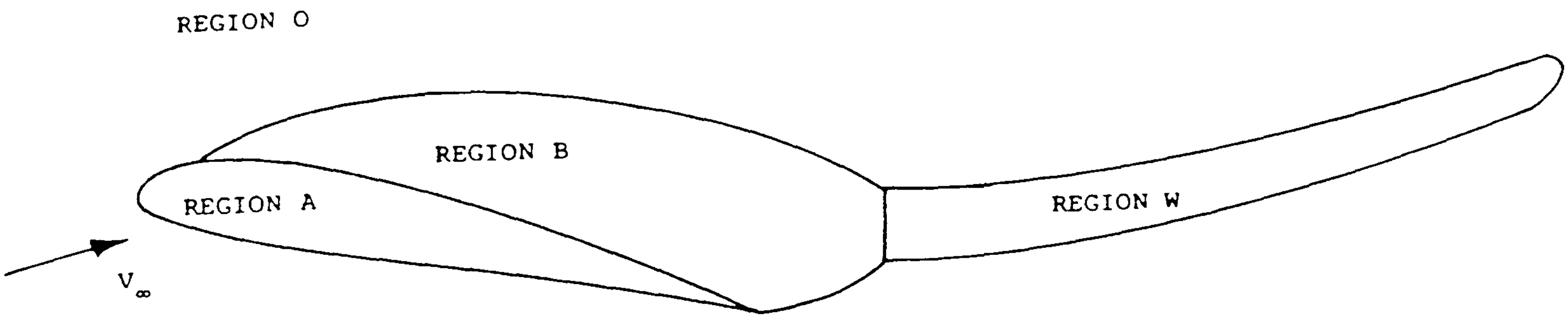

Figure 4.11 Idealised flow model - section through a wing and its wake, [4.12]

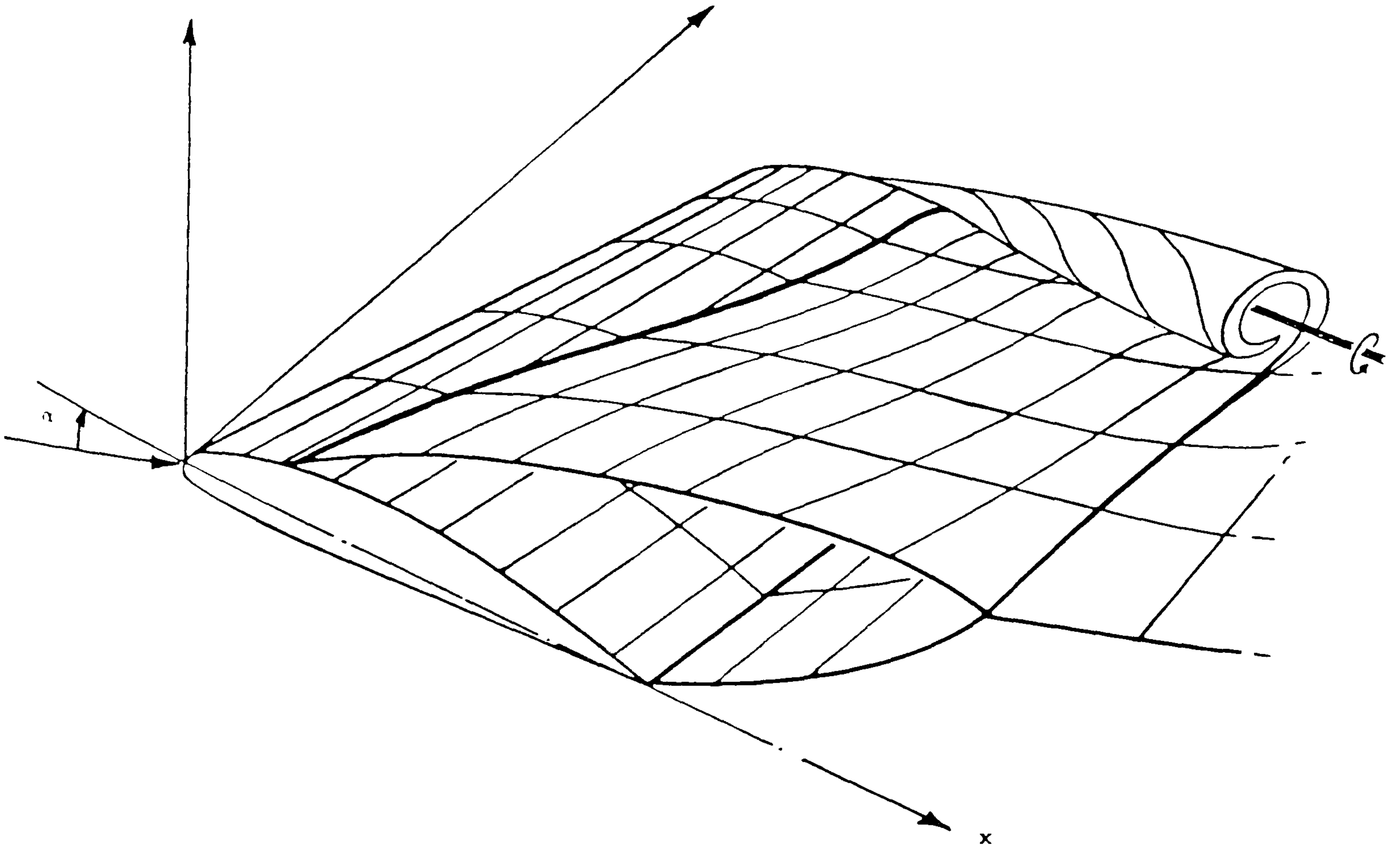

Figure 4.12 General arrangement of separation model, [4.12]

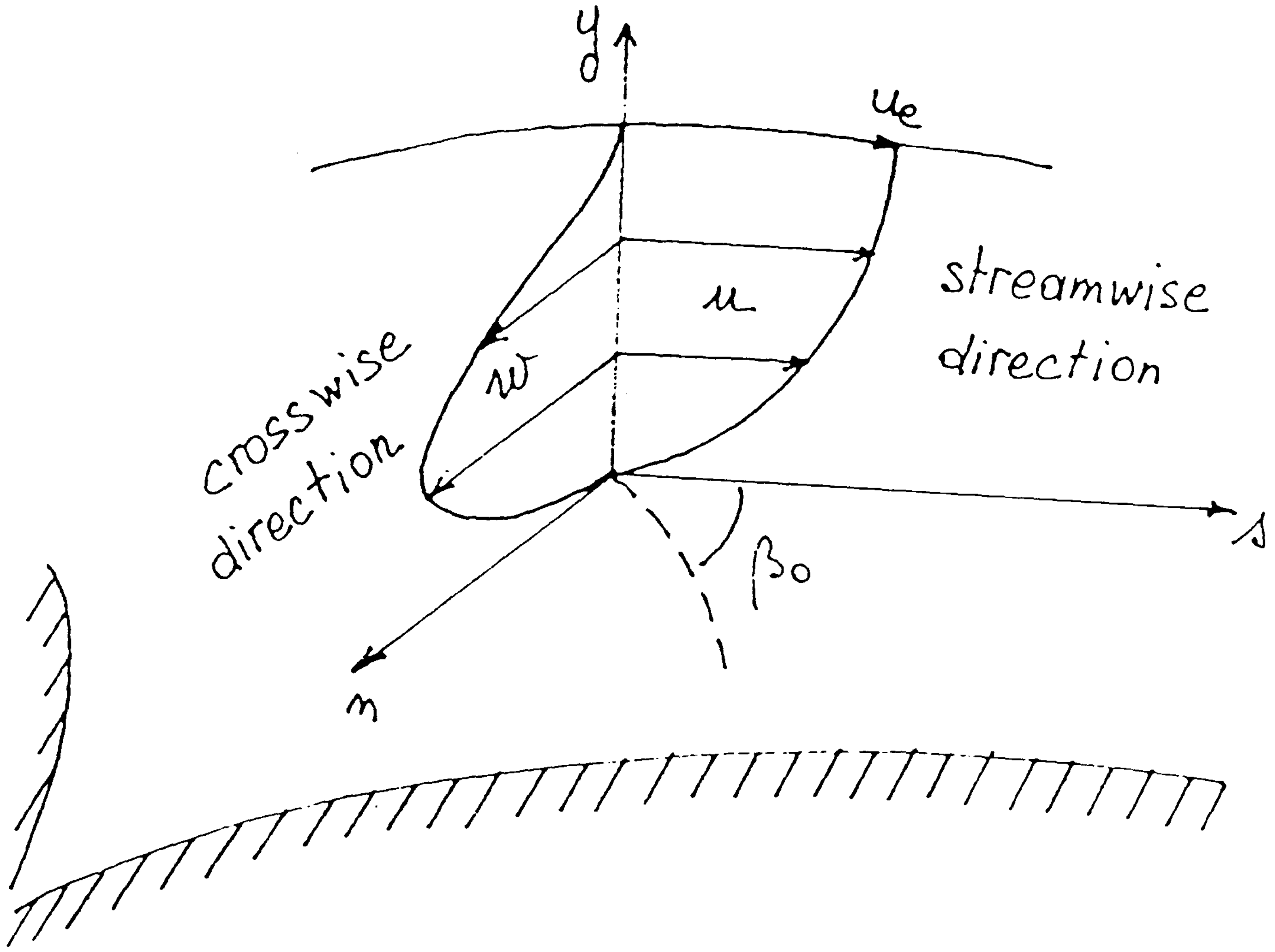

Figure 4.13 Boundary layer stream line coordinates, [4.11]

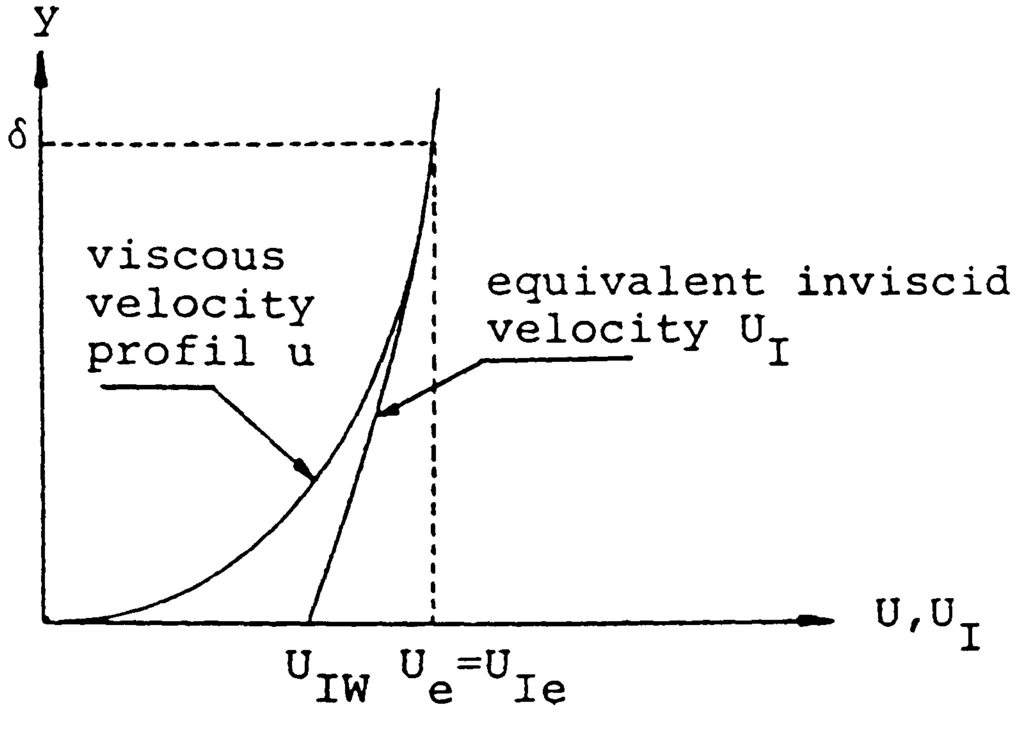

Figure 4.14 The equivalent inviscid flow concept, [2.50]

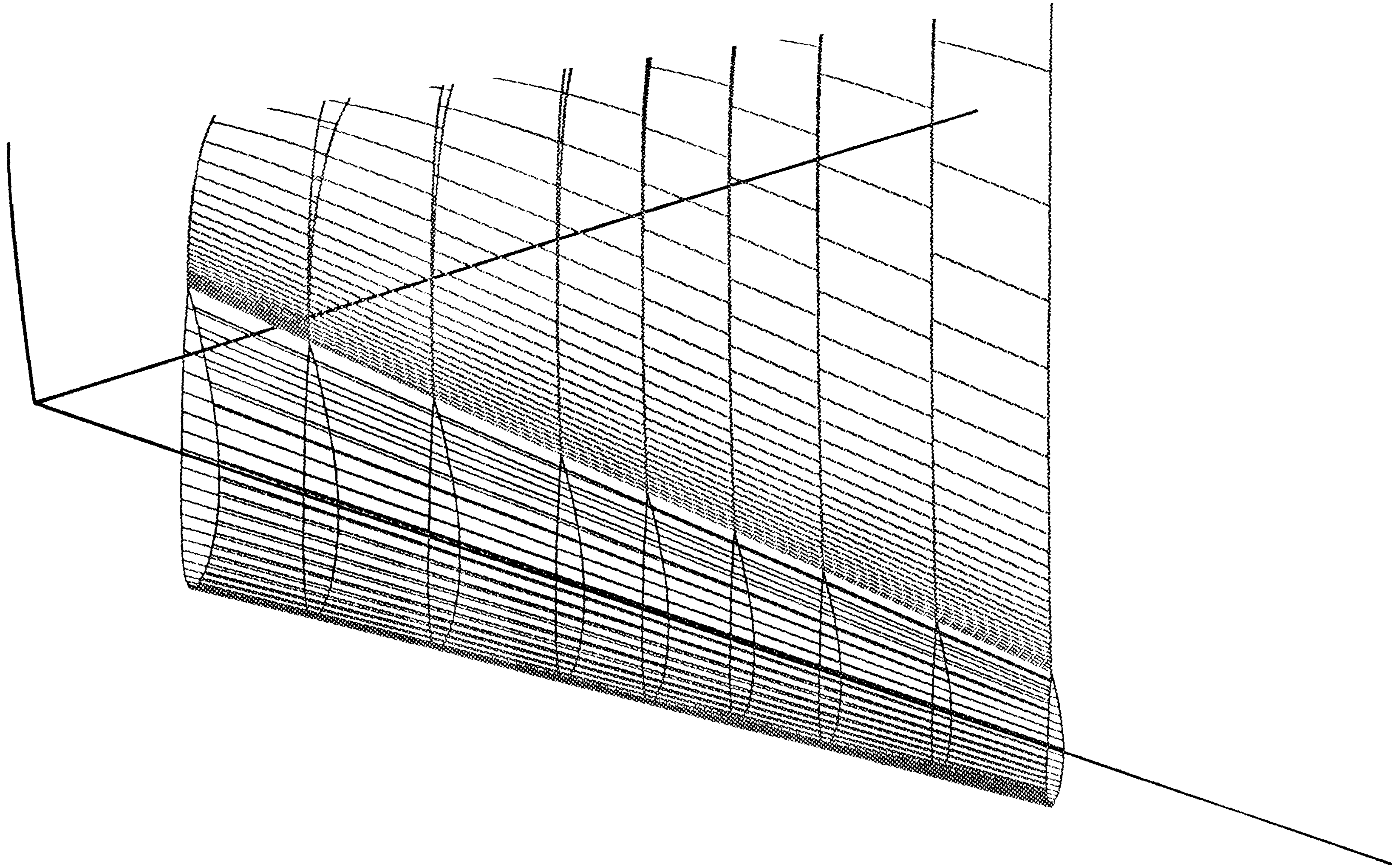

Figure 4.15   Panel representation of rotor blade and wake

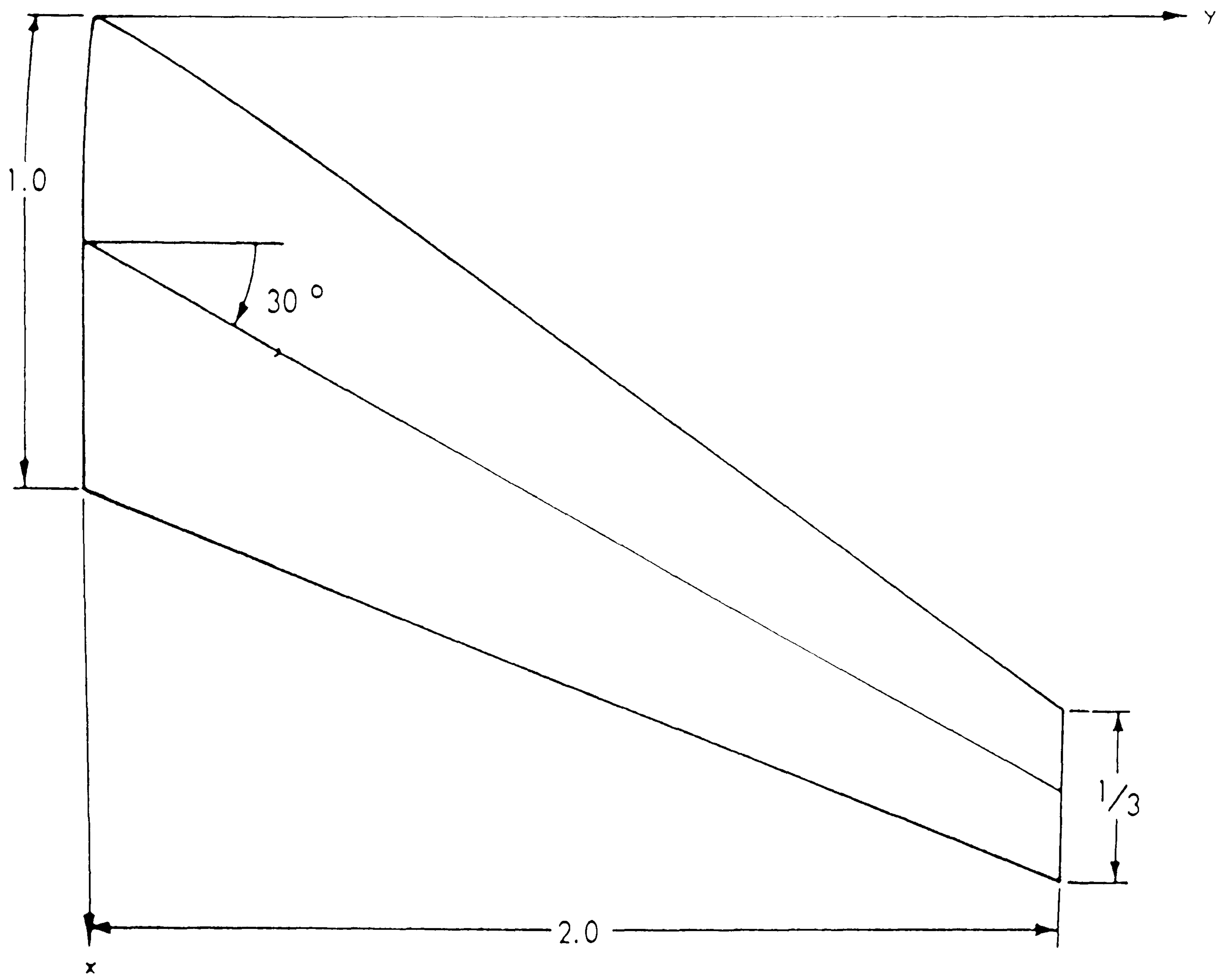

Figure 5.1 Planform of RAEWING test case, [5.1]

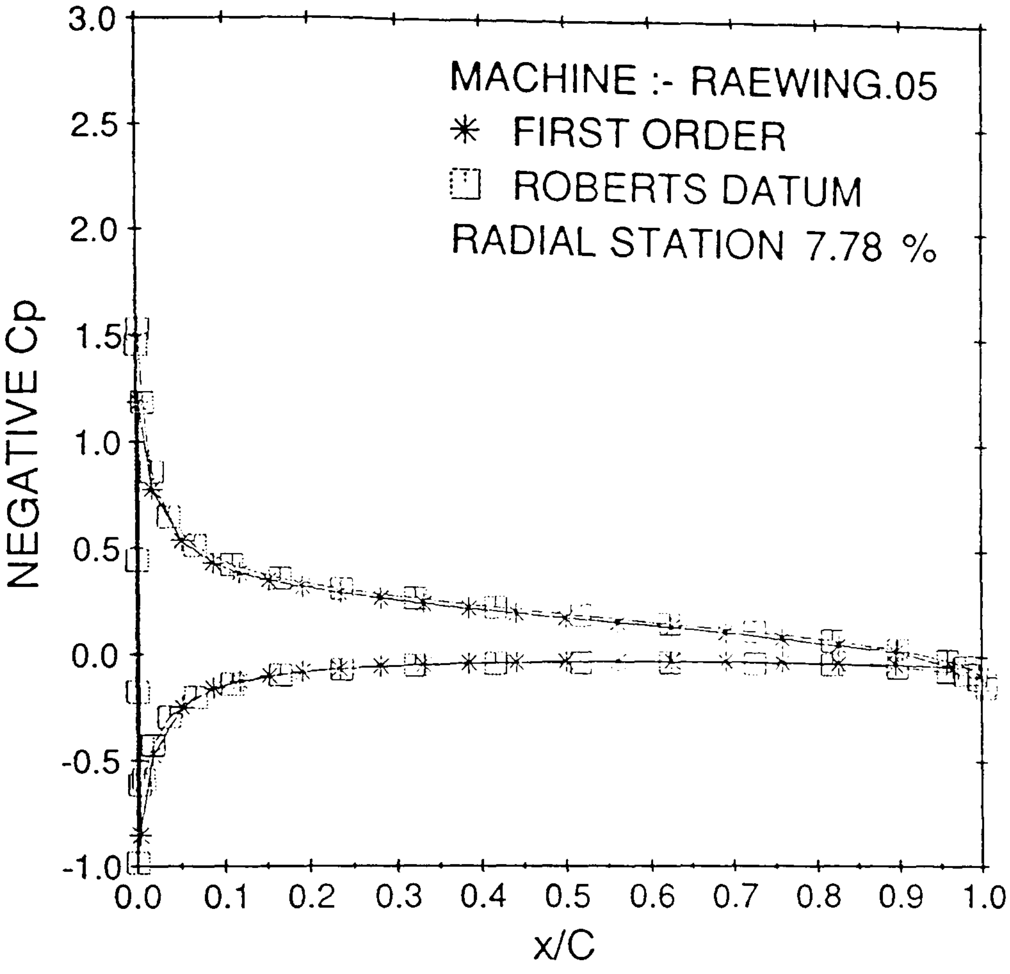

Figure 5.2 Pressure coefficient distribution for RAEWING at 8% span

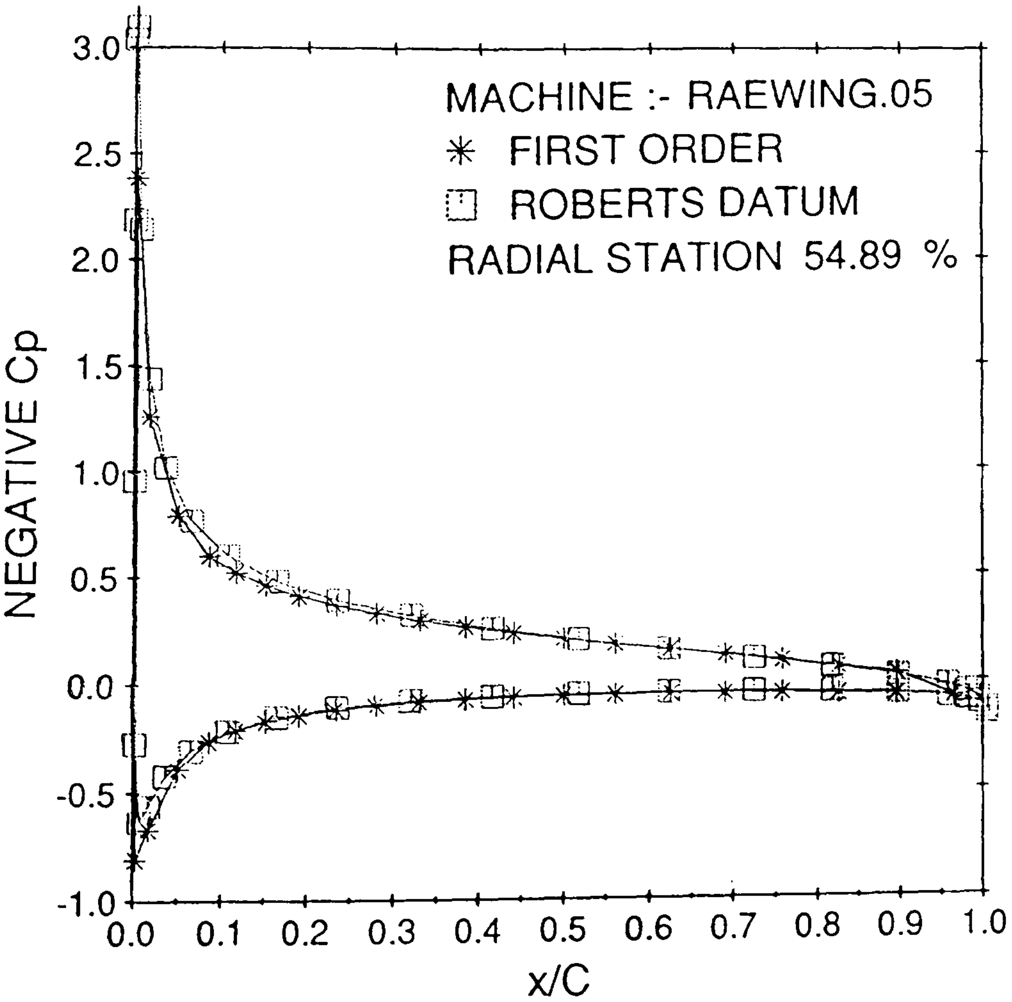

Figure 5.3 Pressure coefficient distribution for RAEWING at 55% span

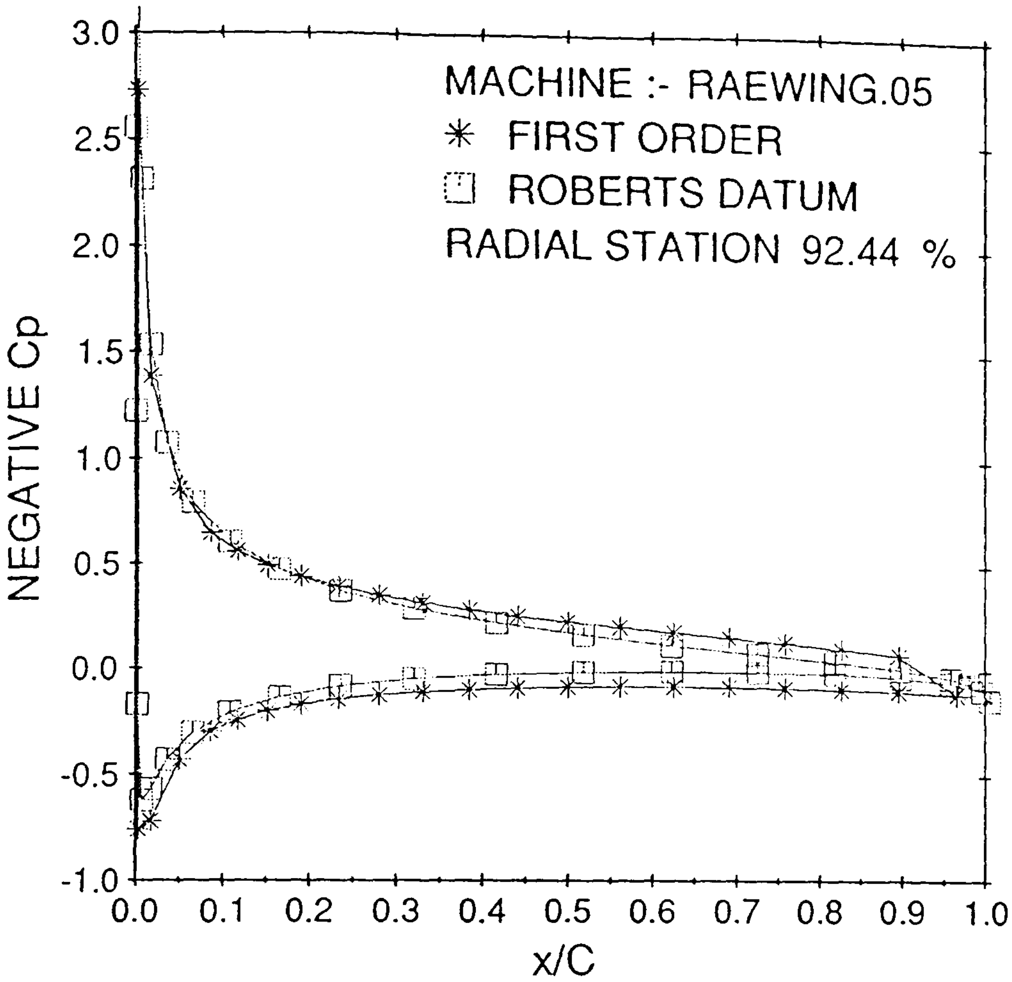

Figure 5.4 Pressure coefficient distribution for RAEWING at 92% span

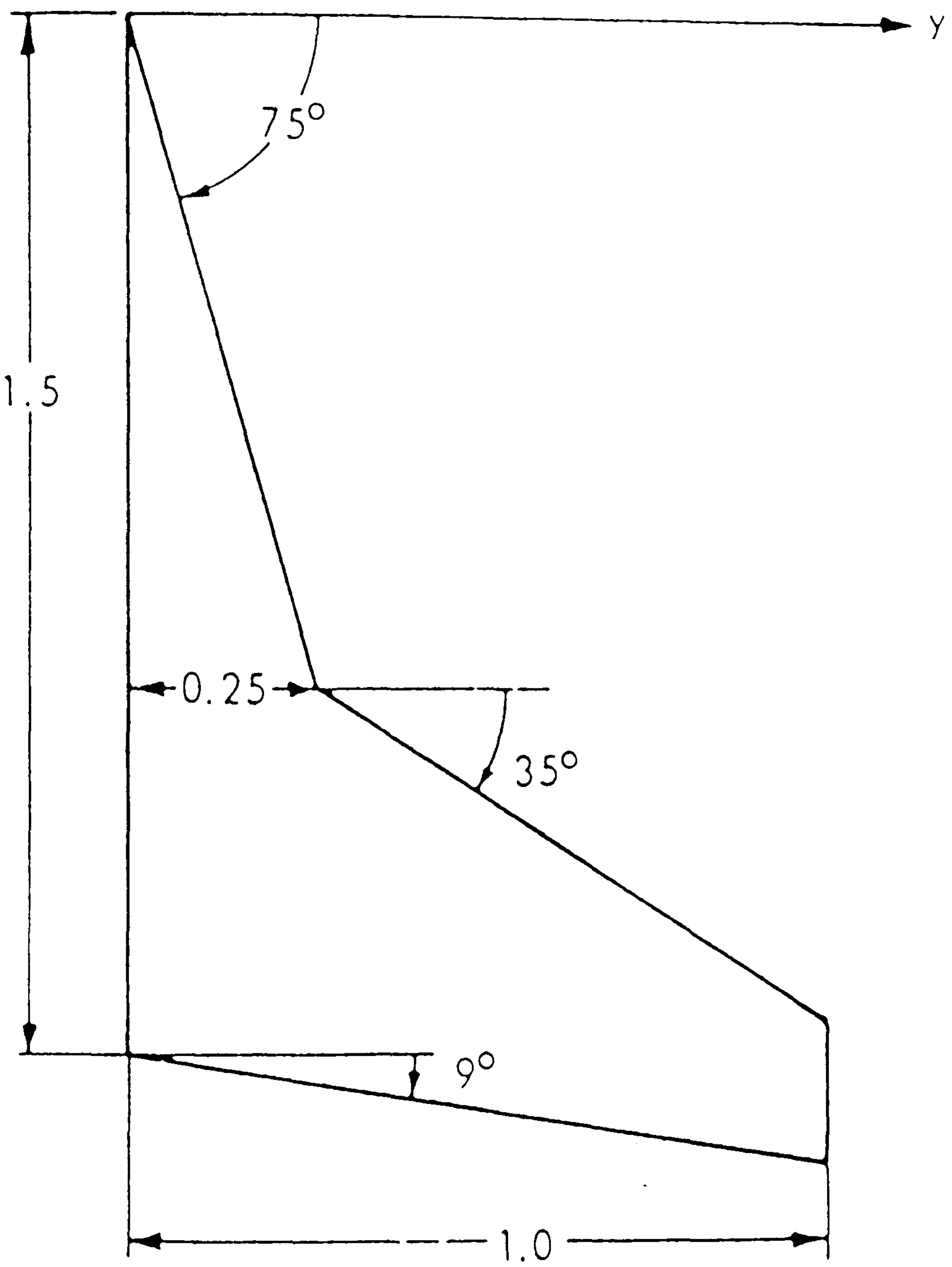

Figure 5.5 Planform of STRAKE test case, [5.1]

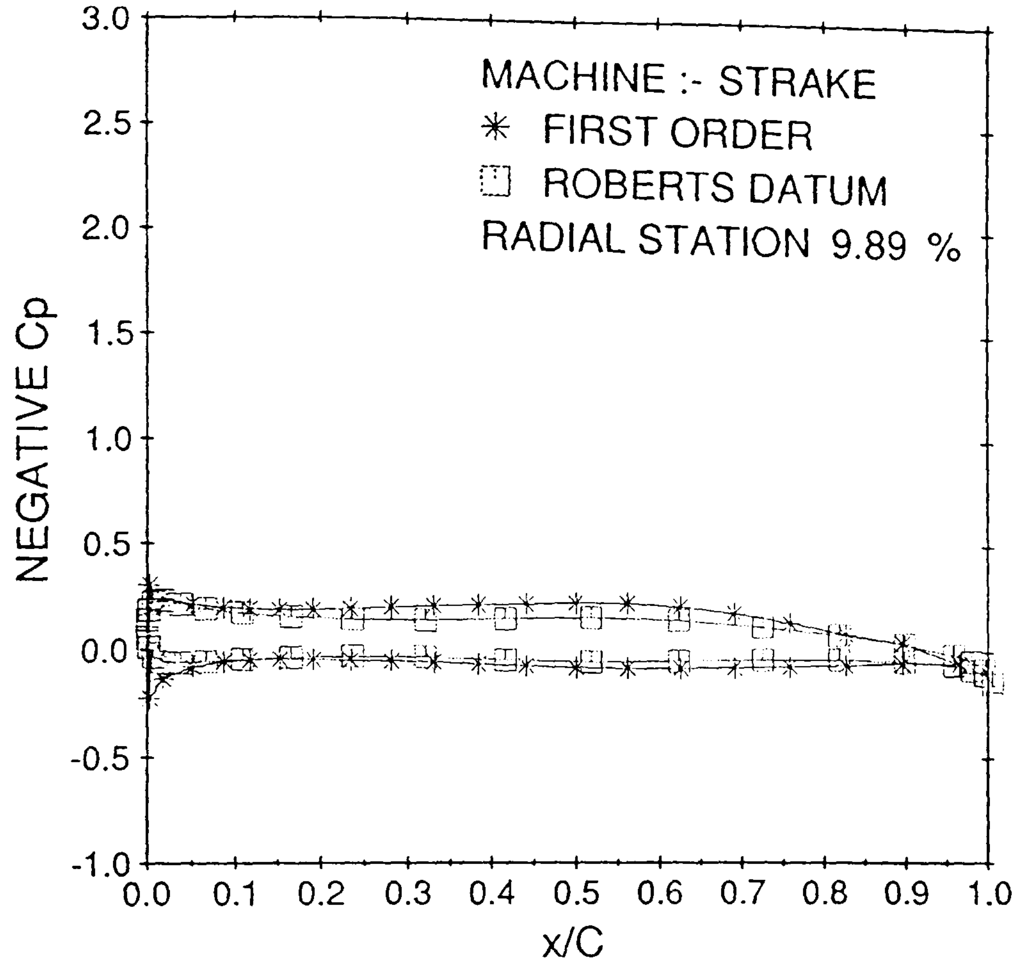

Figure 5.6 Pressure coefficient distribution for STRAKE at 10% span

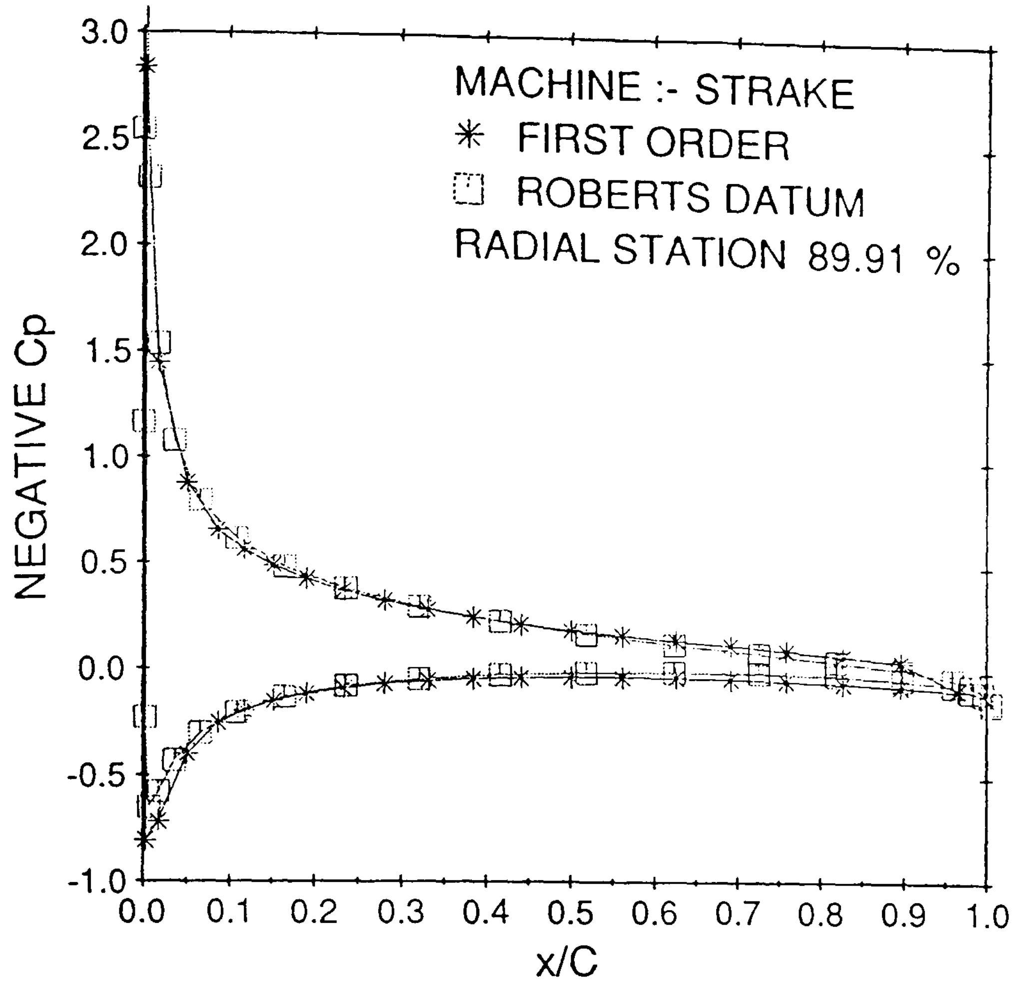

Figure 5.7 Pressure coefficient distribution for STRAKE at 90% span

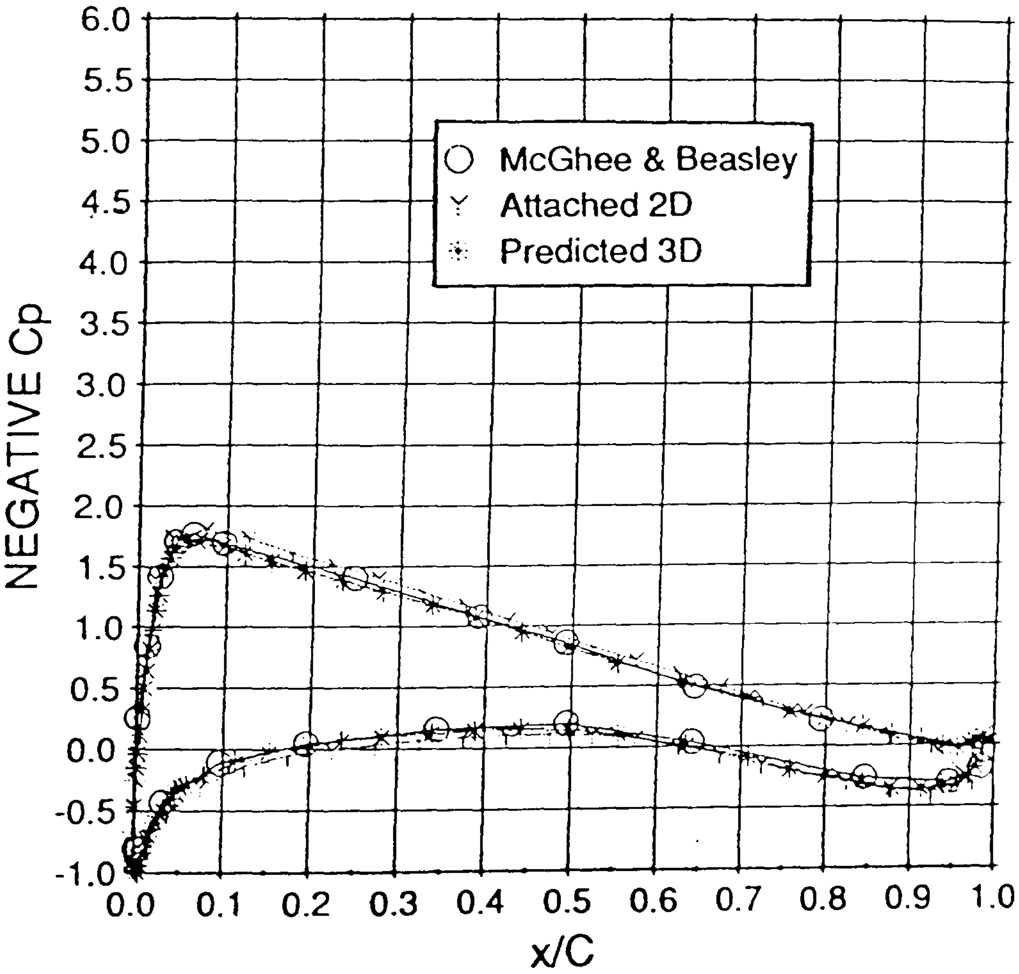

Figure 5.8 NASA LS(1) - 0421 Mod. Pressure Distribution at Incidence 3.9 degrees.

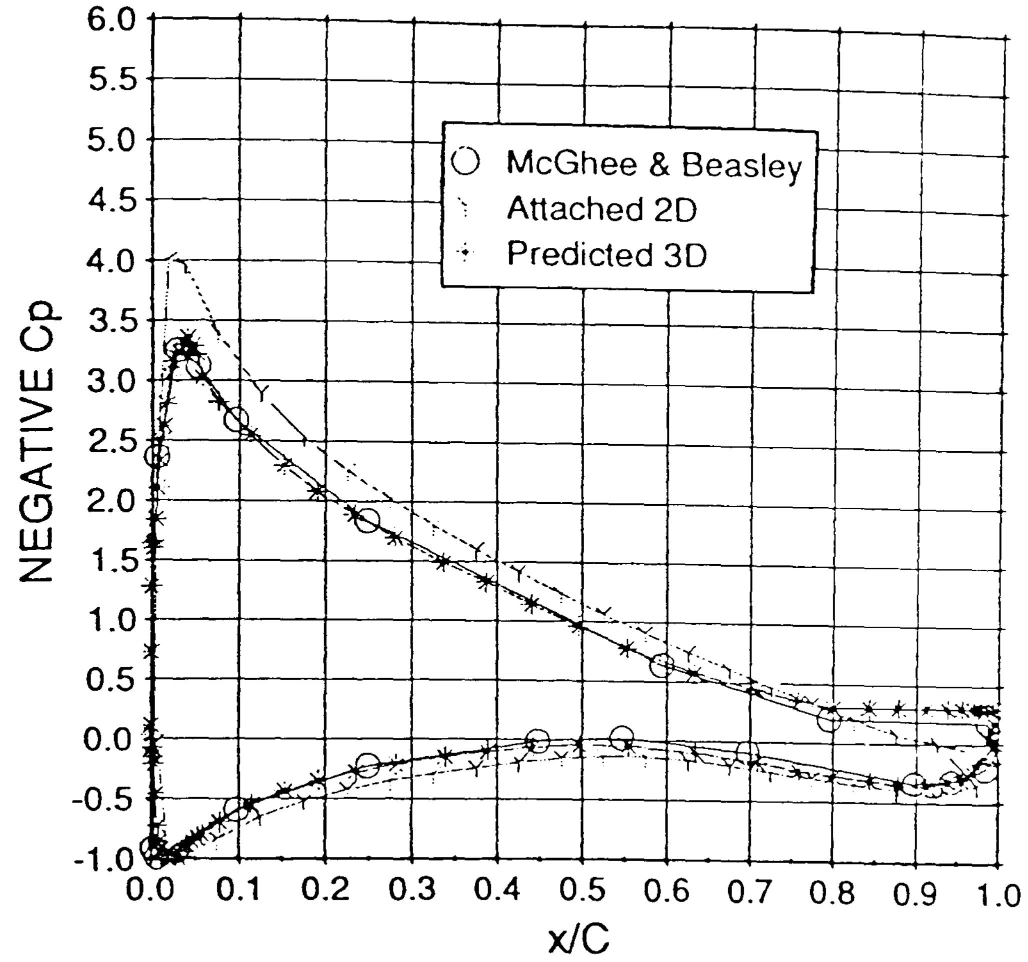

Figure 5.9 NASA LS(1) - 0421 Mod. Pressure Distribution at Incidence 10.1 degrees.

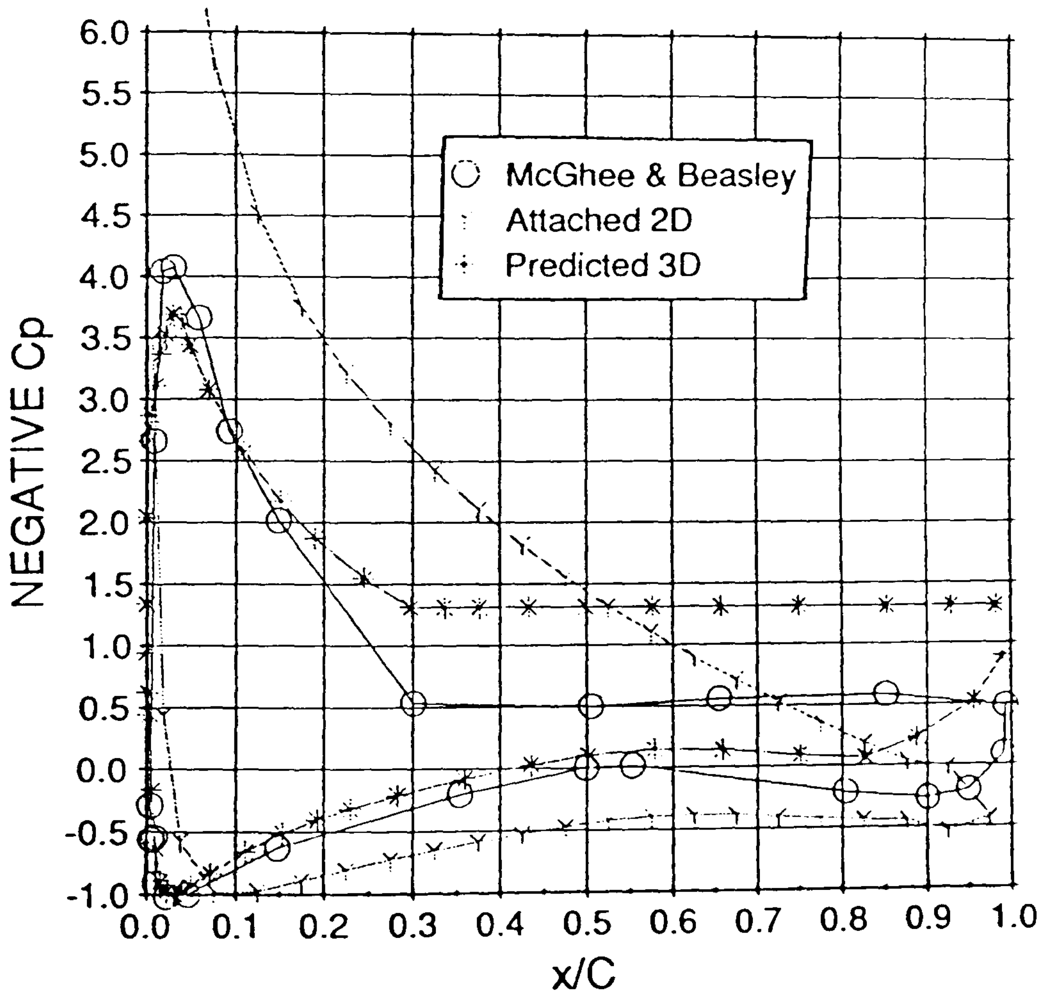

Figure 5.10 NASA LS(1) - 0421 Mod. Pressure Distribution at Incidence 18.0 degrees. First predictions.

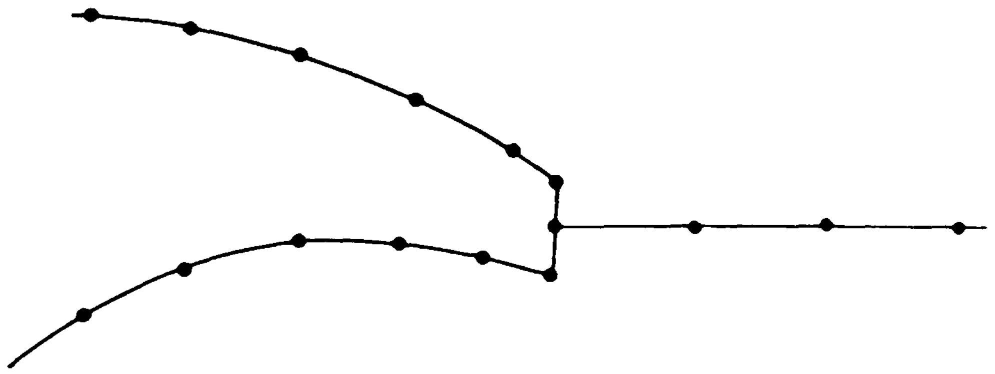

Figure 5.11(a) Trailing Edge Panel Distribution for Attached Flow.

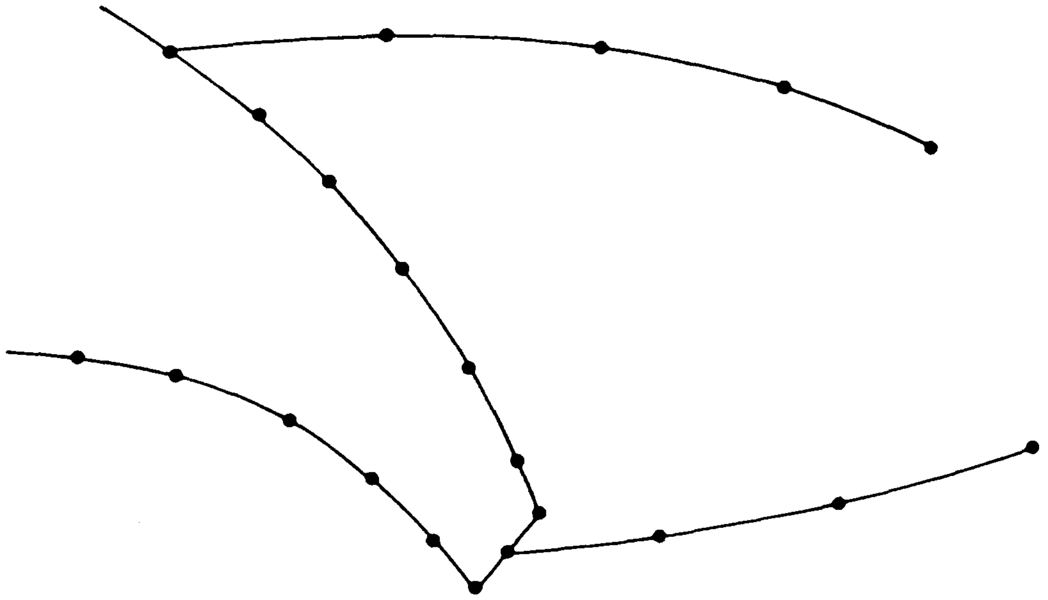

Figure 5.11(b) Initial Trailing Edge Panel Distribution for Separated Flow, Indicating Problem of Panel Interference.

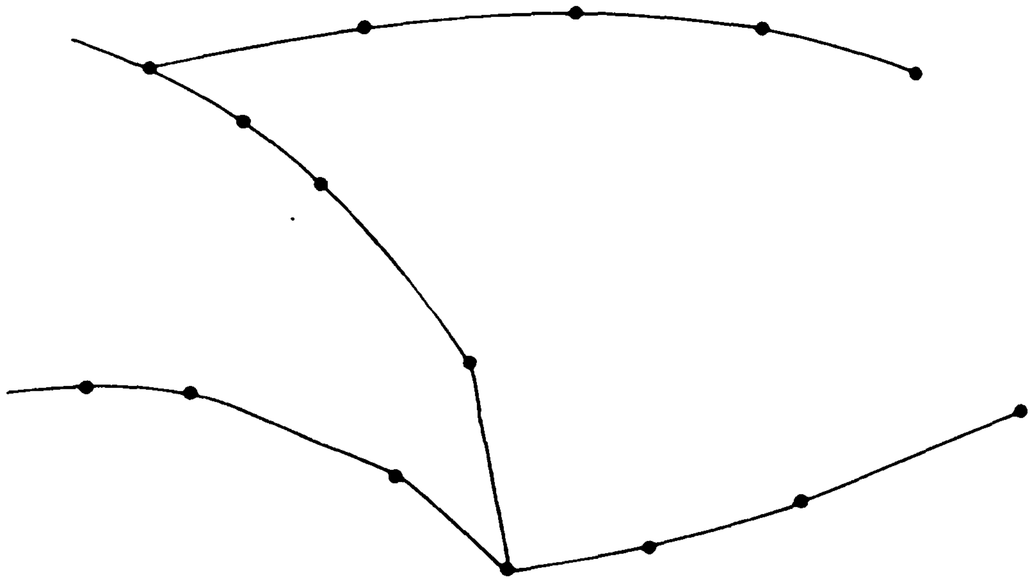

Figure 5.11(c) Modified Trailing Edge Panel Distribution for Separated Flow. Removes Problem of Interference

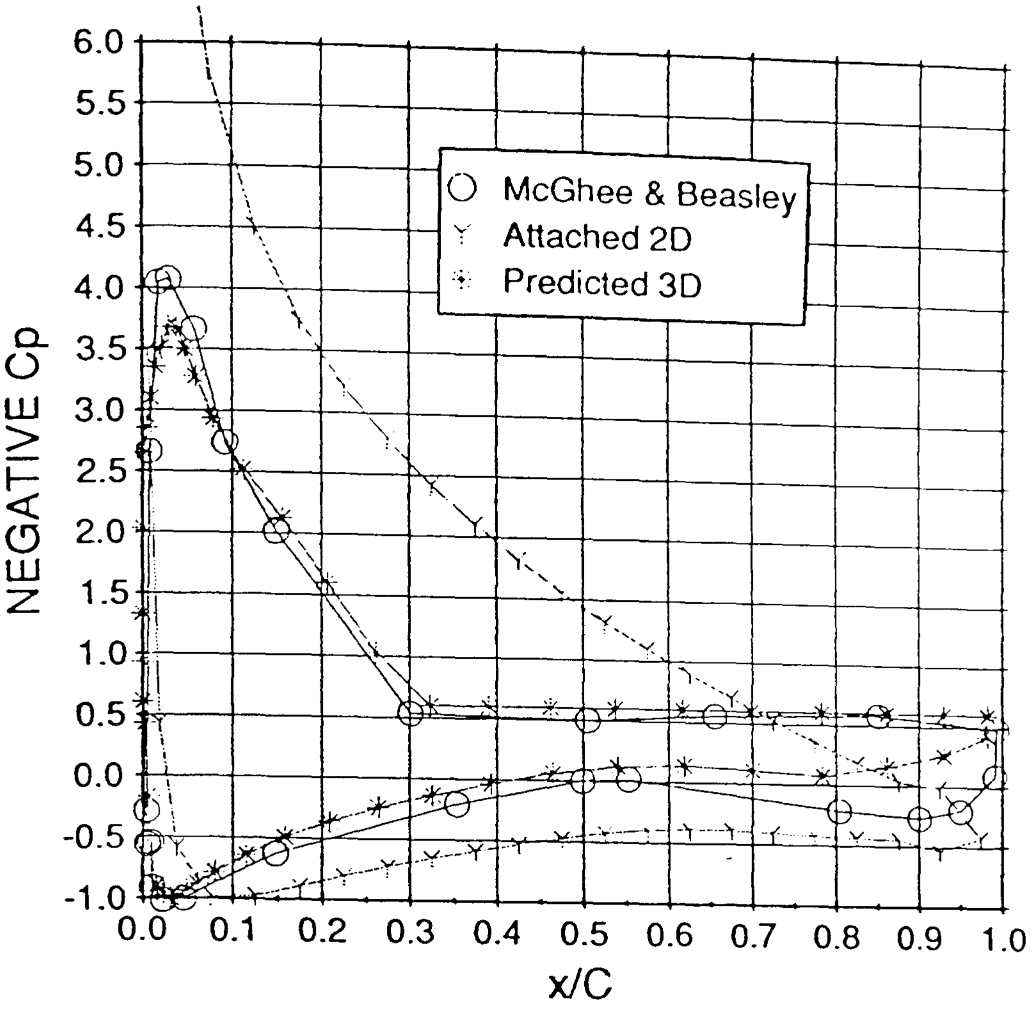

Figure 5.12 NASA LS(1) - 0421 Mod. Pressure Distribution at Incidence 18.0 degrees. Modified Predictions.

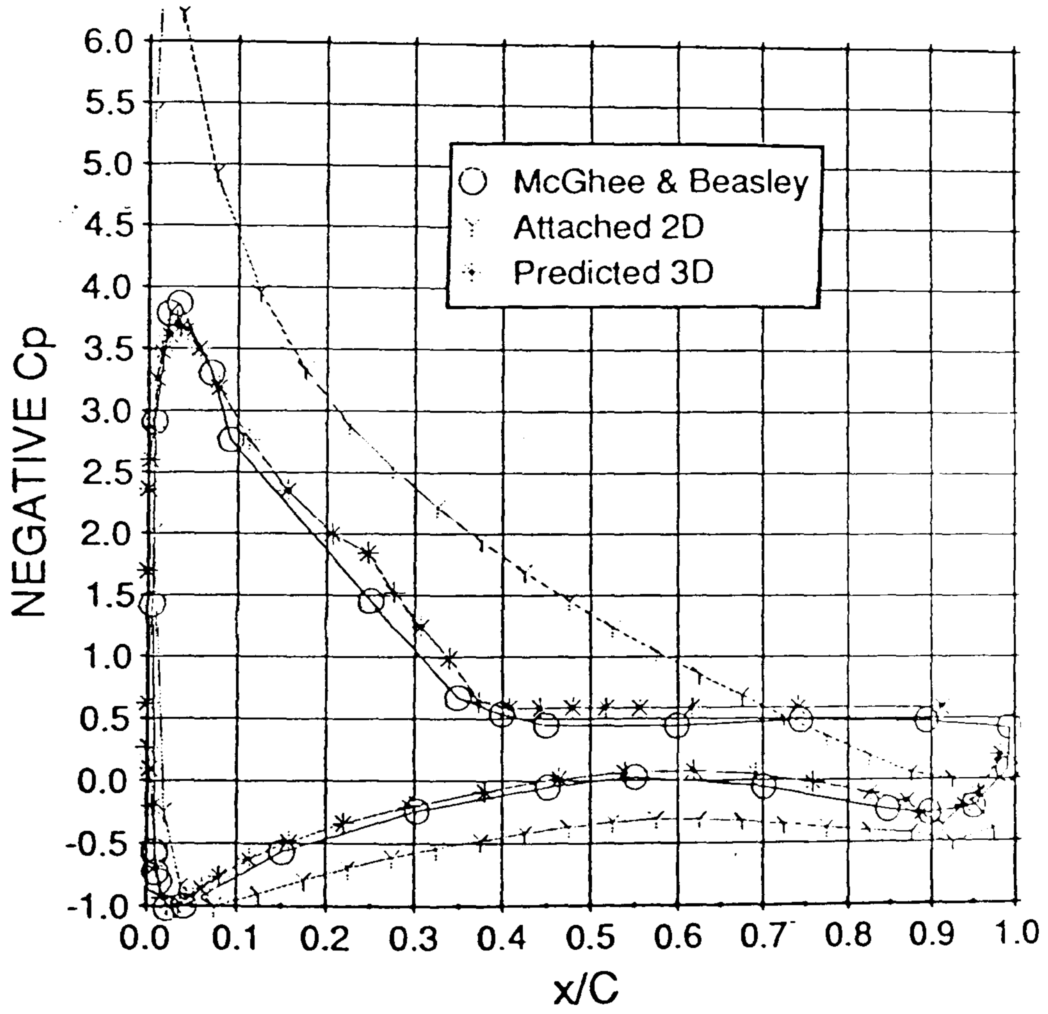

Figure 5.13 NASA LS(1) - 0421 Mod. Pressure Distribution at Incidence 15.3 degrees. Final Predictions.

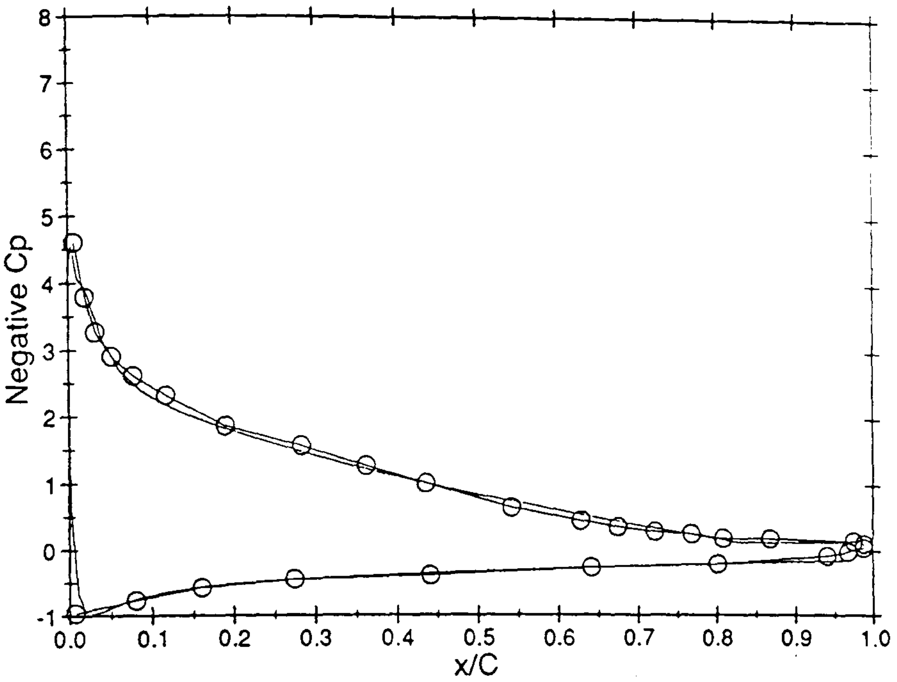

Figure 5.14 Two dimensional pressure profile for NACA 4412 aerofoil section near to maximum lift, solid line prediction, symbols measurement

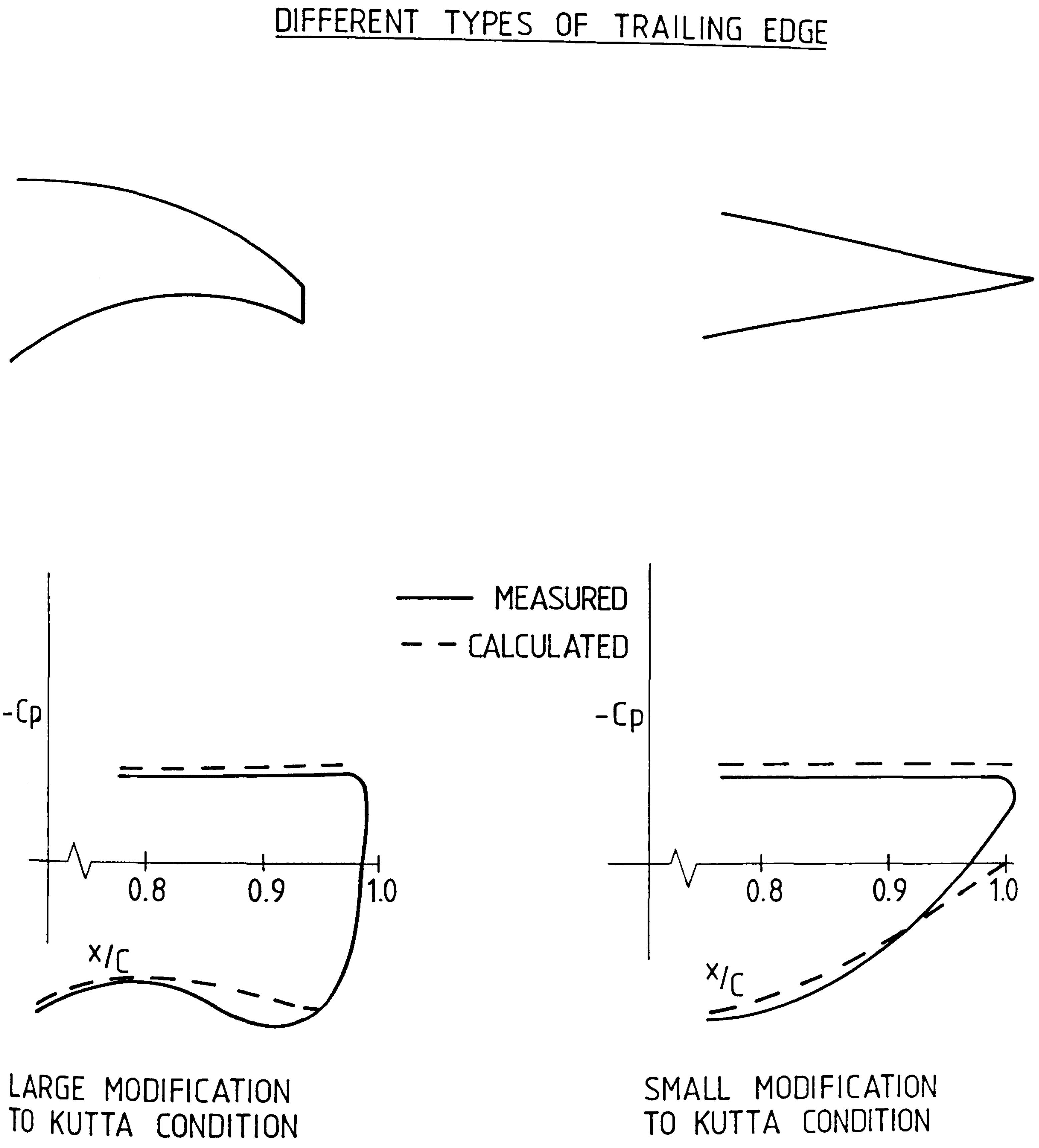

Figure 5.15 Illustration of how the modification to the Kutta condition might vary with aerofoil geometry

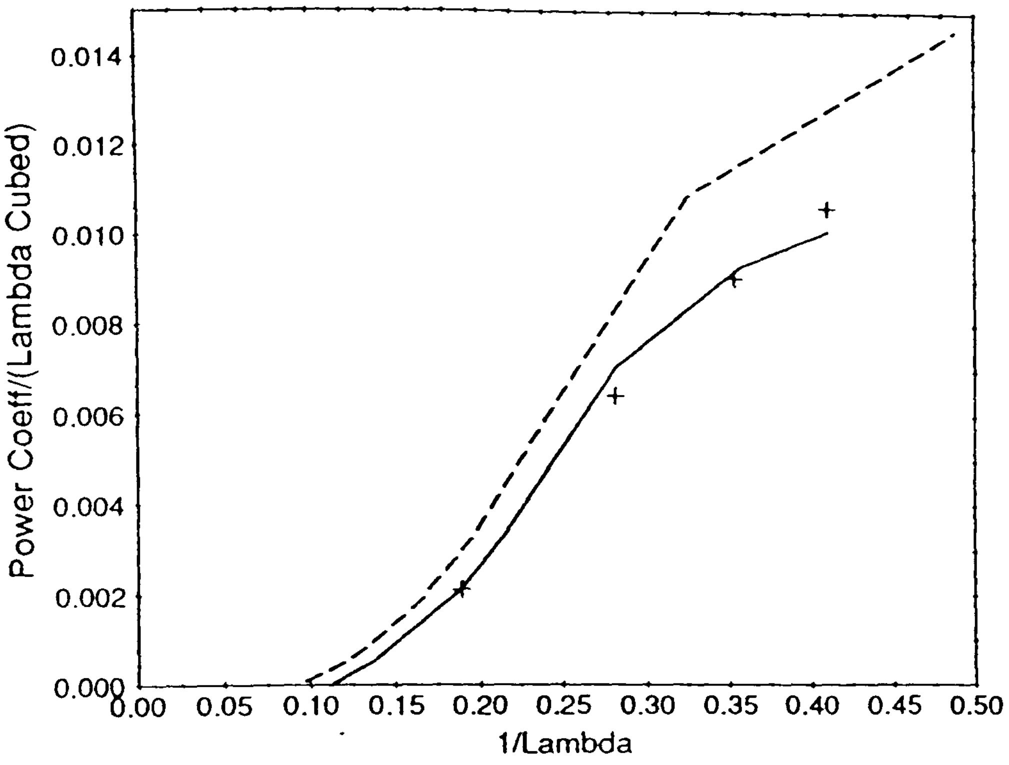

Figure 5.16 Measured and predicted power for the Cranfield turbine, solid line measurement, dashed strip theory, [18], symbols three dimensional prediction.

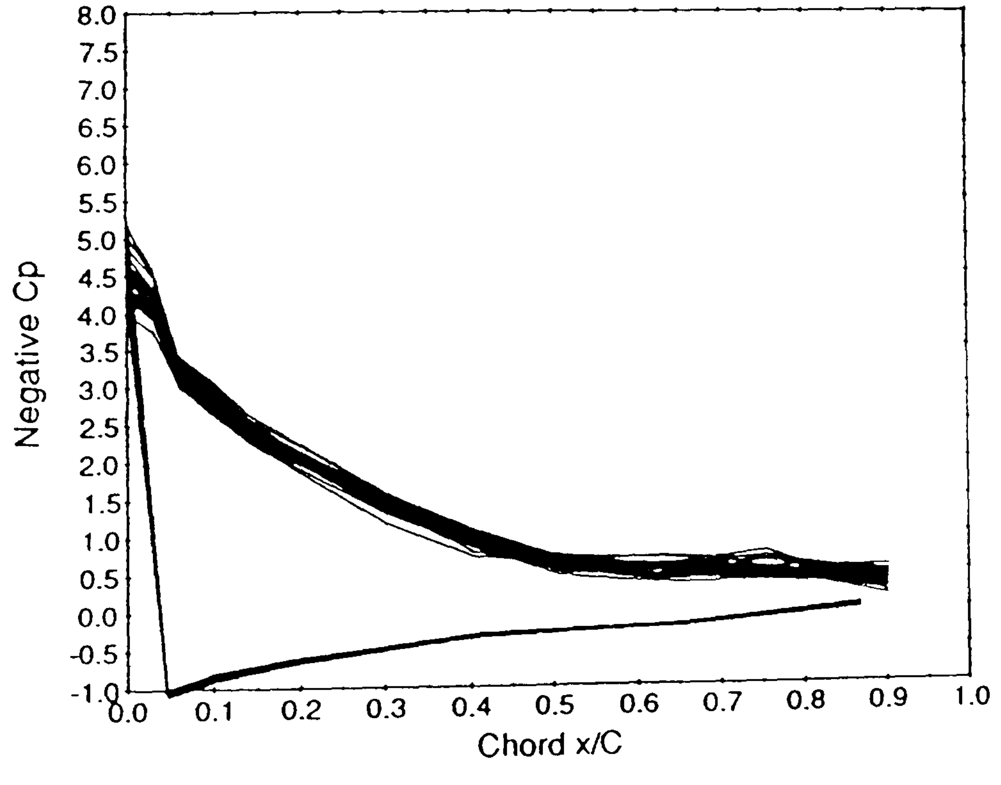

Figure 5.17 Measured pressure profiles for the 75%R station at tip speed ratio of 2.5, forty revs plotted.

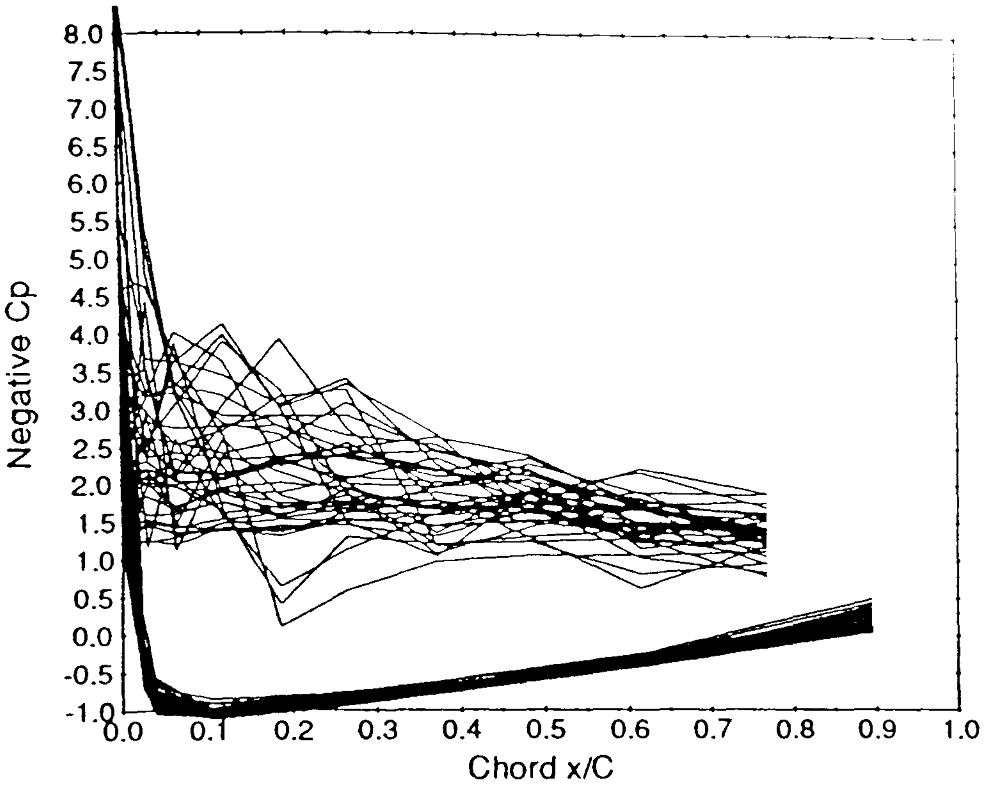

Figure 5.18 Measured pressure profiles for the 35%R station at tip speed ratio of 2.5, forty revs plotted.

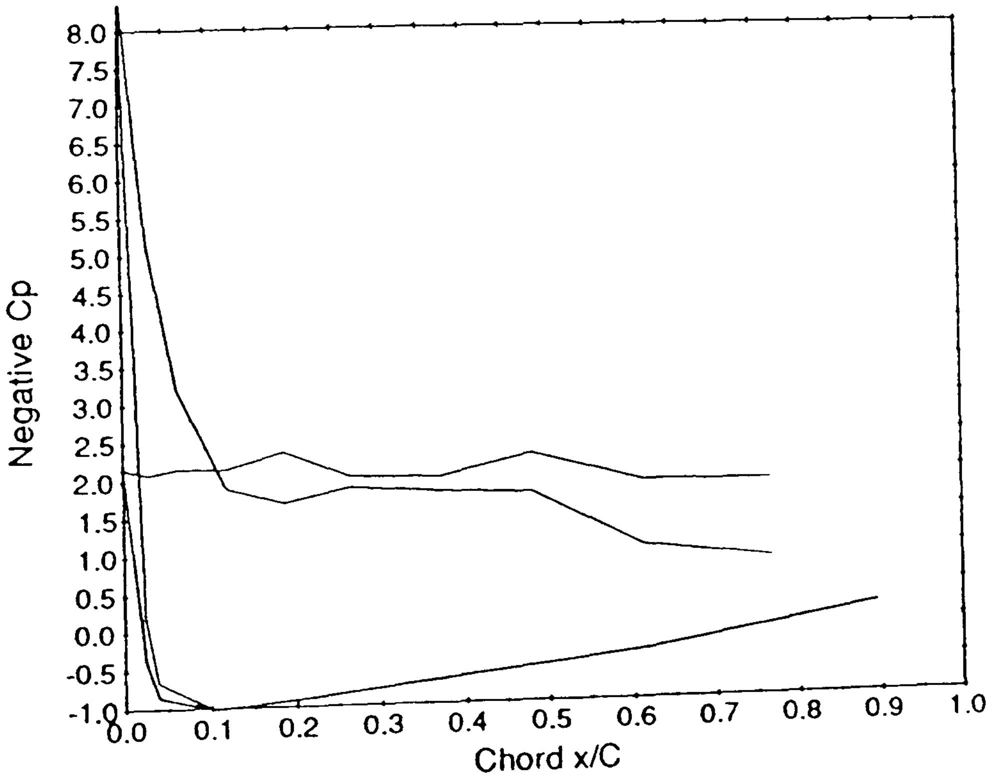

Figure 5.19 Measured pressure profile for the 35%R station at tip speed ratio of 2.5, revs 81 & 82.

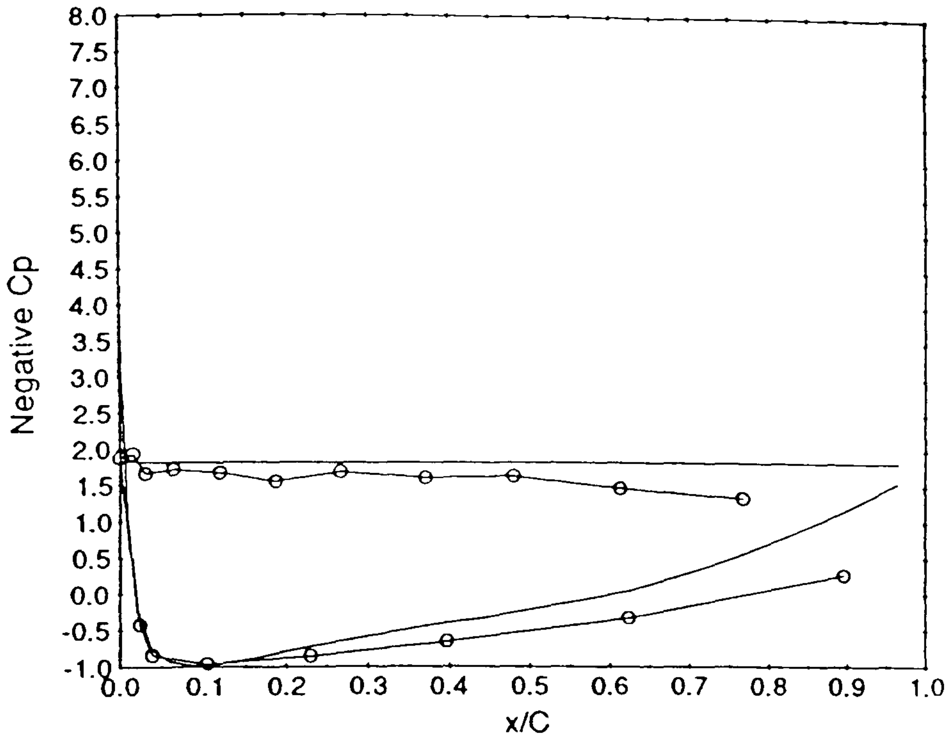

Figure 5.20 Measured and predicted pressure profiles for the 35%R station at tip speed ratio of 2.5, solid line predicted, symbols measured.

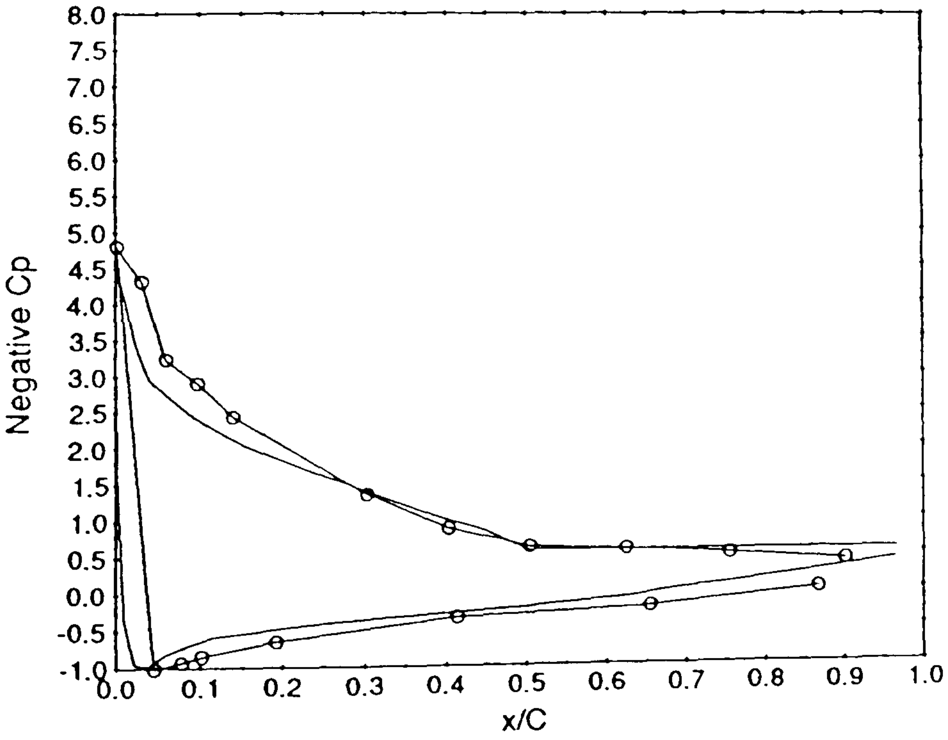

Figure 5.21 Measured and predicted pressure profiles for the 75%R station at tip speed ratio of 2.5, solid line predicted, symbols measured.

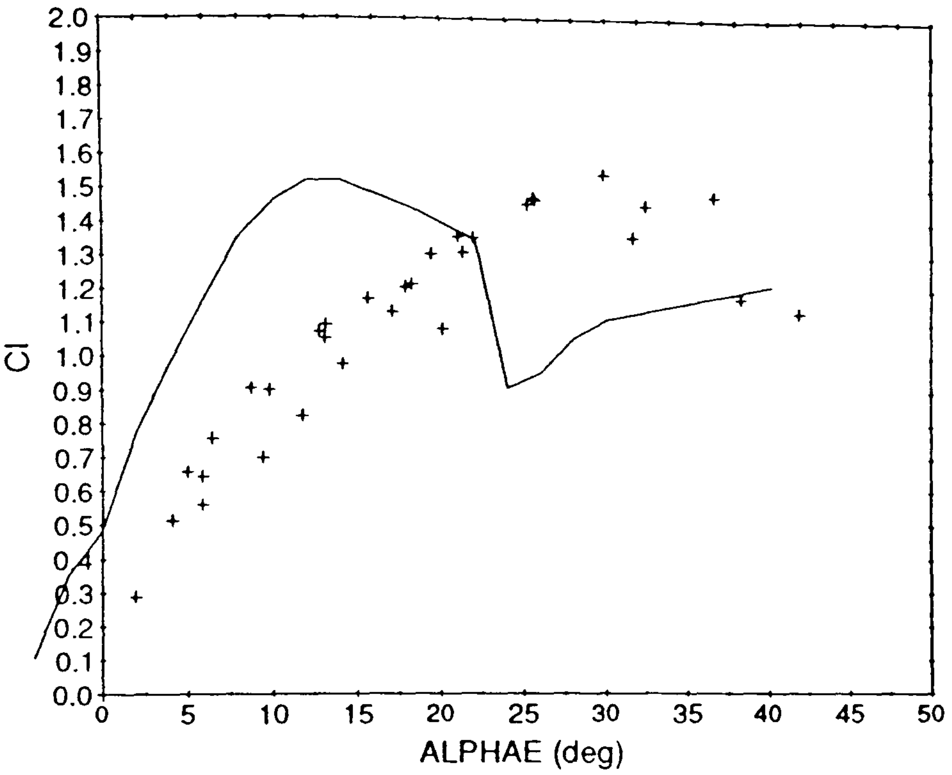

Figure 5.22 Predicted three dimensional (symbols), and measured two dimensional (solid line) lift coefficient.

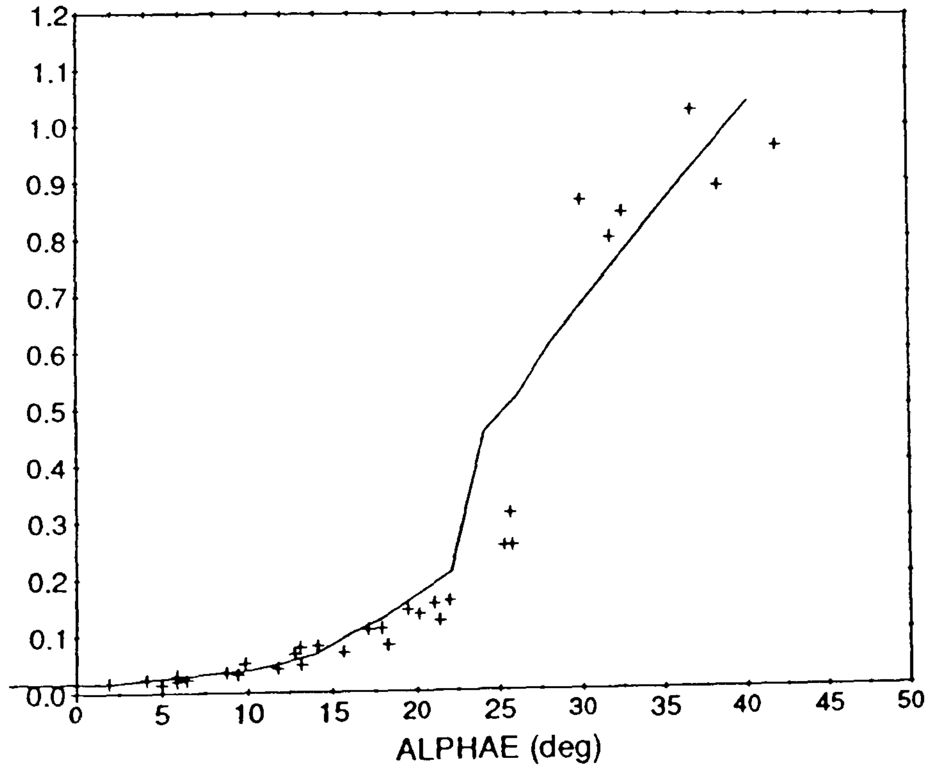

Figure 5.23 Predicted three dimensional (symbols), and measured two dimensional (solid line) drag coefficient.

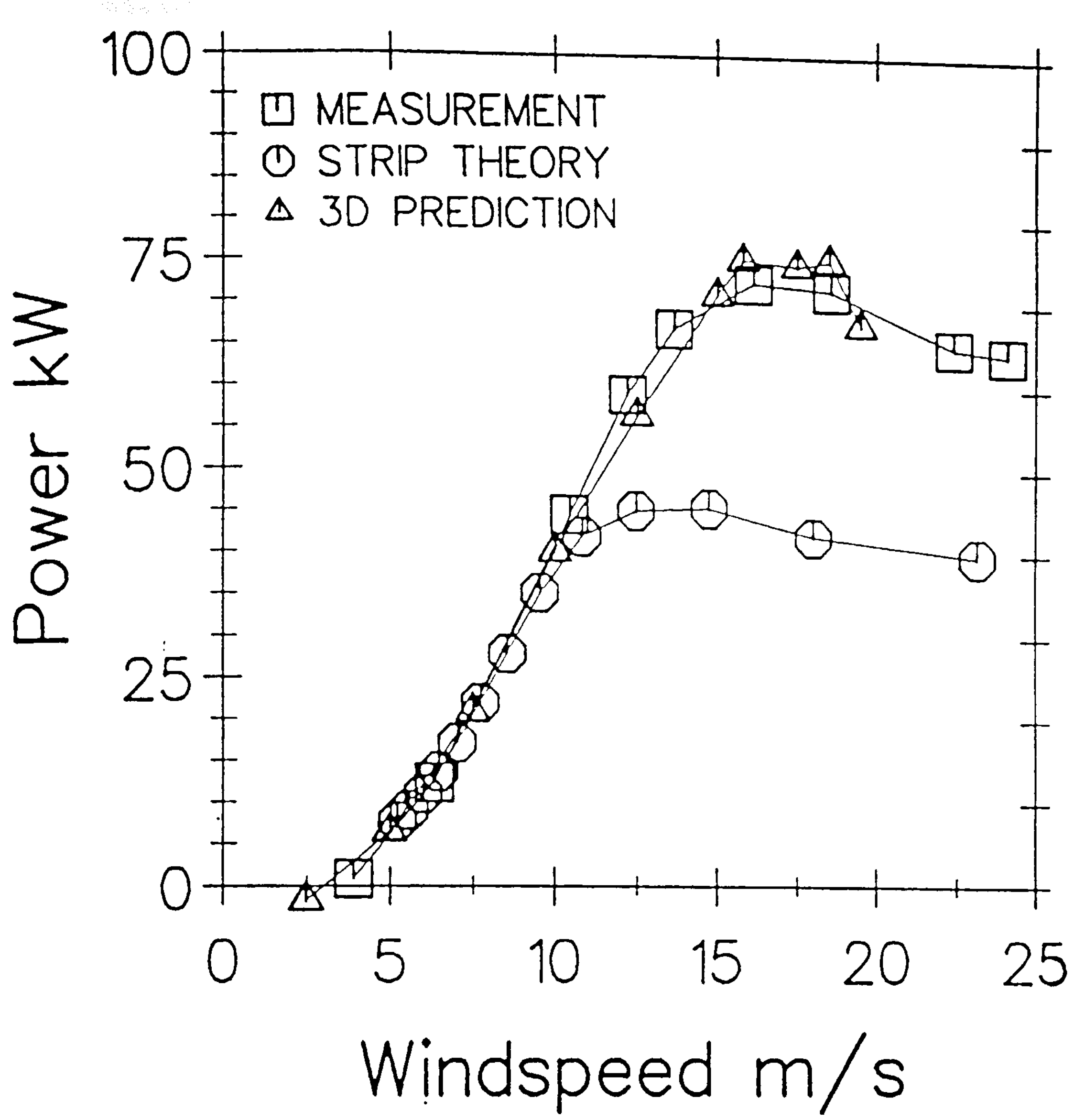

Figure 5.24 Predicted and measured power versus windspeed for the Vestas 15m diameter machine

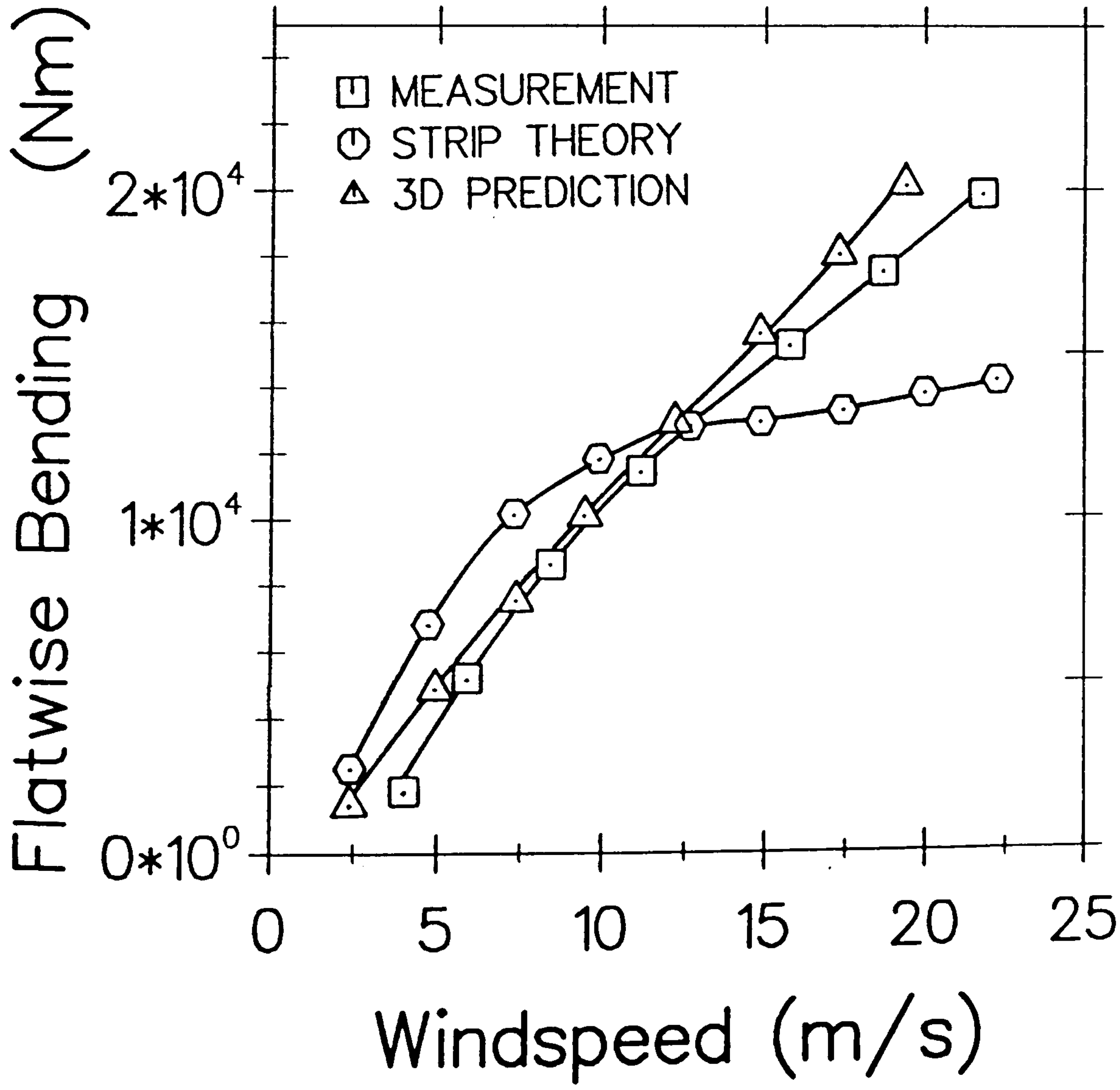

Figure 5.25 Predicted and measured root bending moment versus windspeed for the Vestas 15m diameter machine

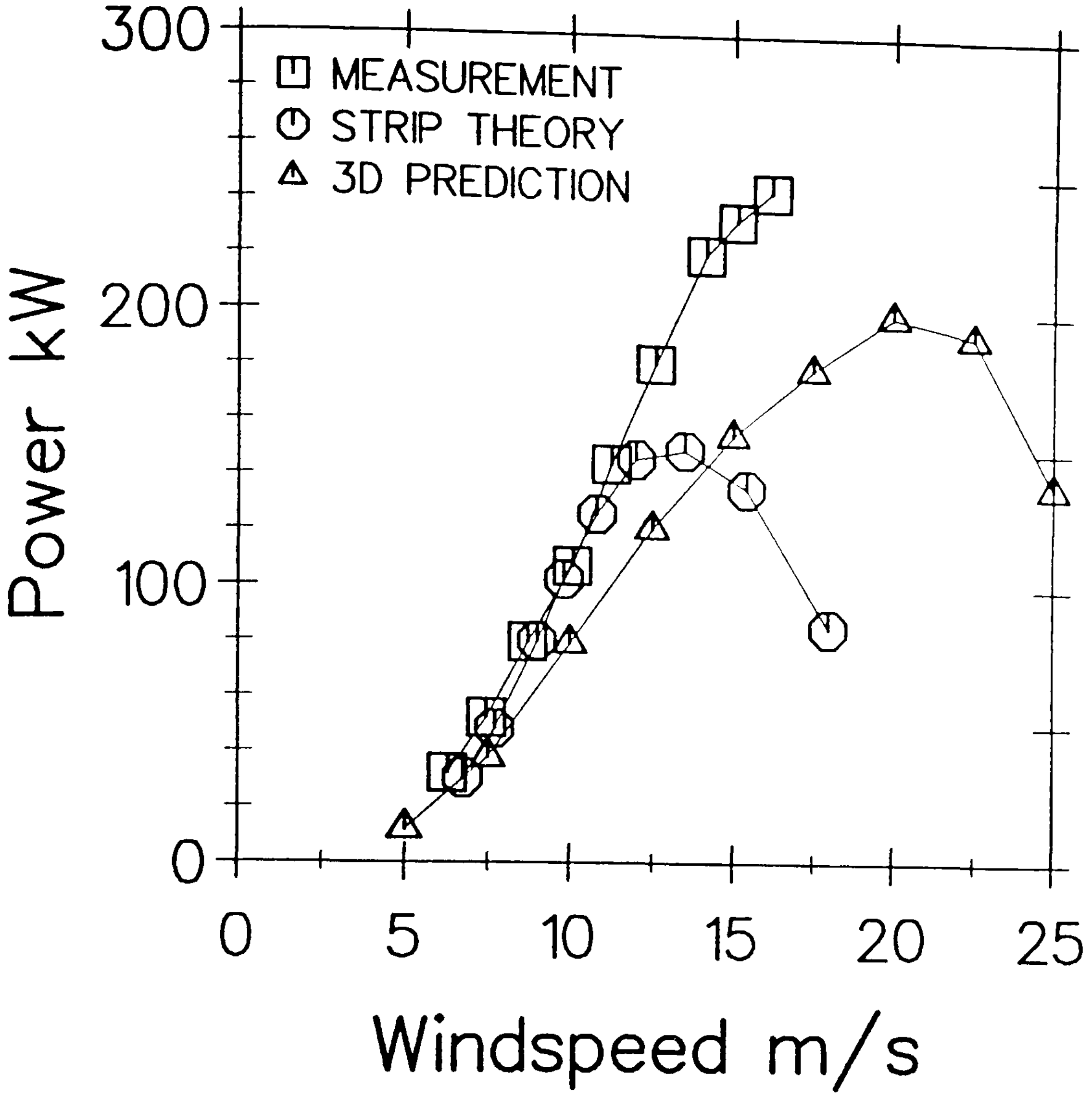

Figure 6.1 Power versus windspeed for the Danwin 22m diameter machine, initial panel method prediction

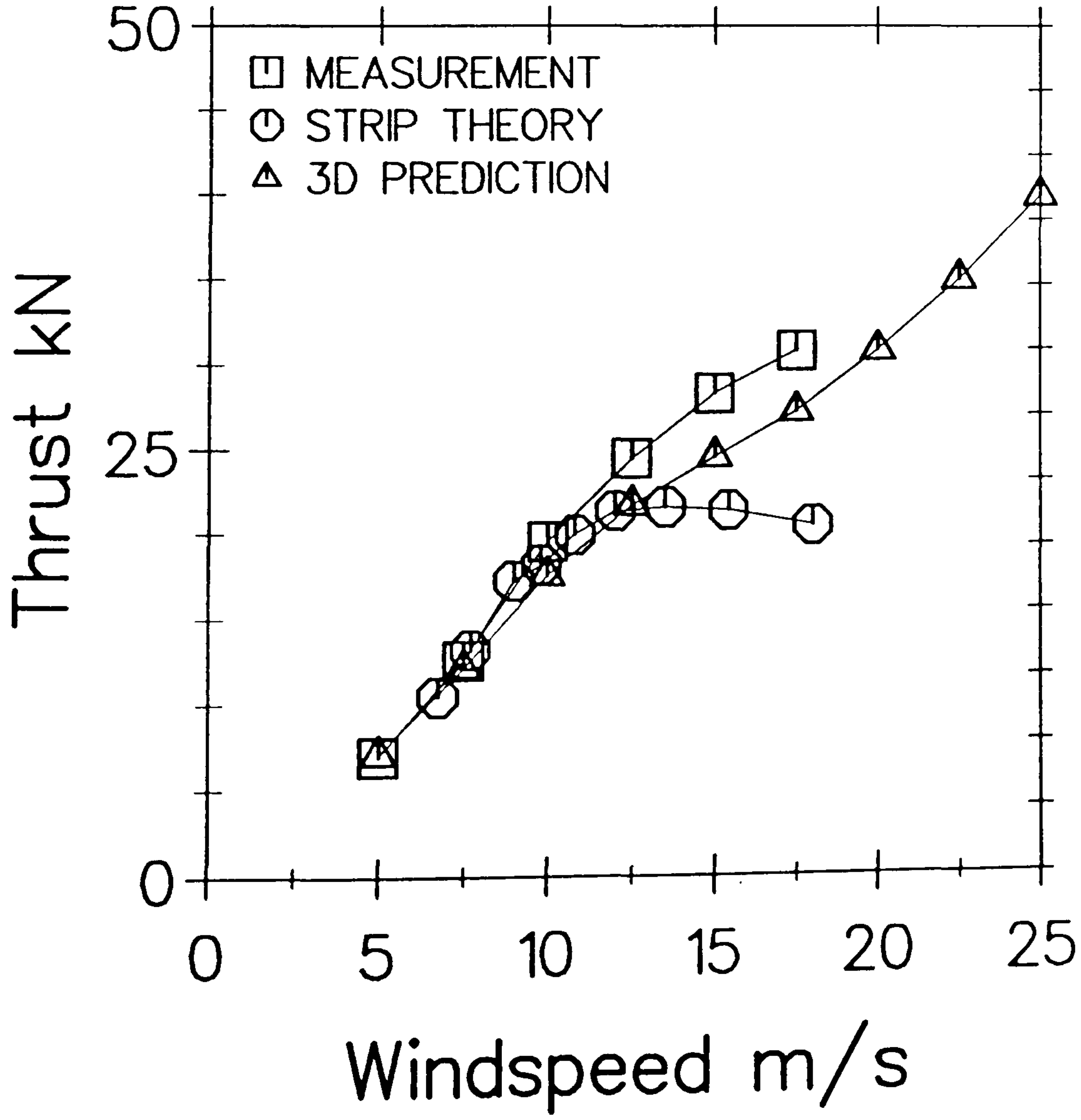

Figure 6.2 Thrust versus windspeed for the Danwin 22m diameter machine, initial panel method prediction

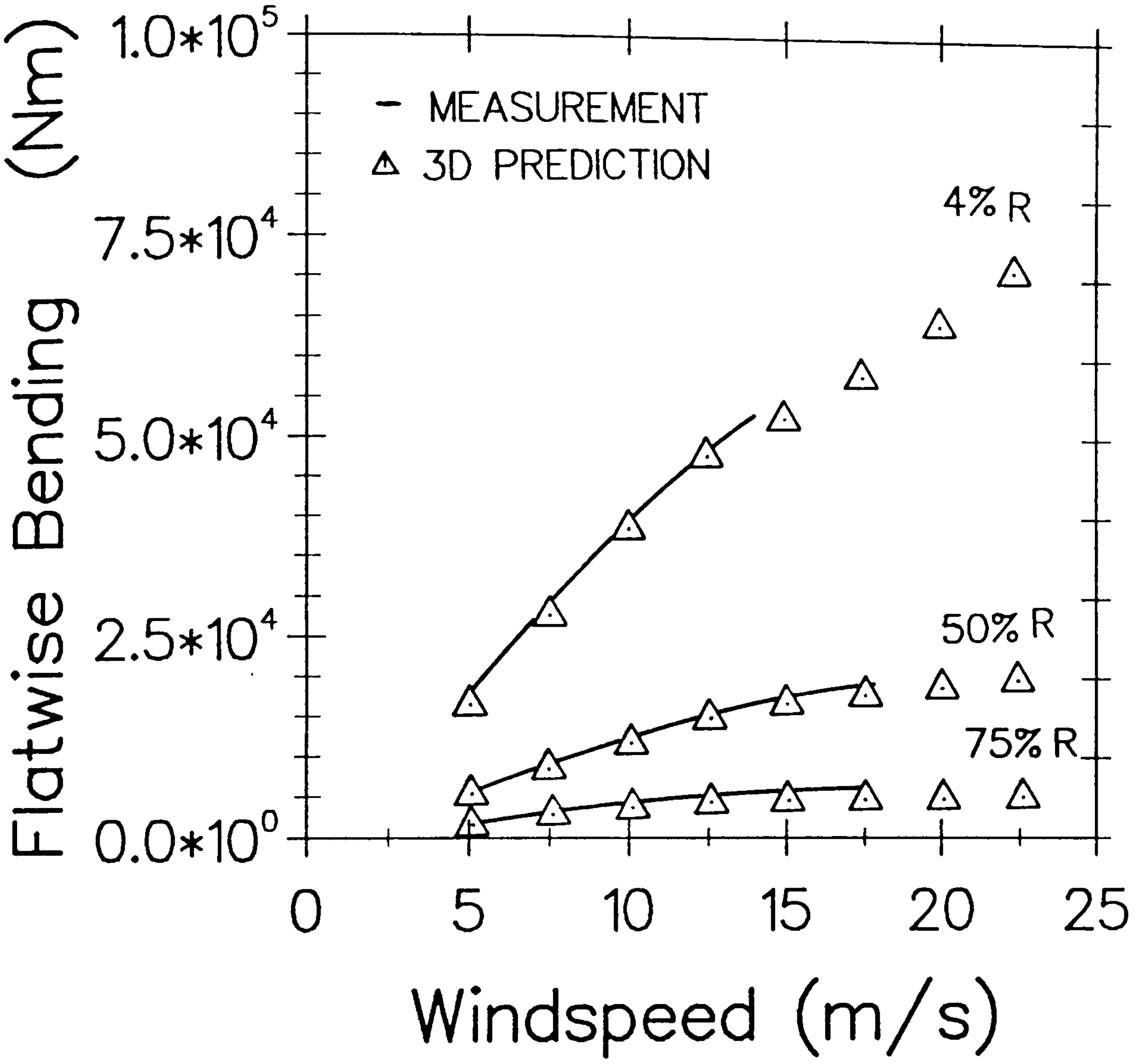

Figure 6.3 Bending moments versus windspeed for the Danwin 22m diameter machine, initial panel method prediction

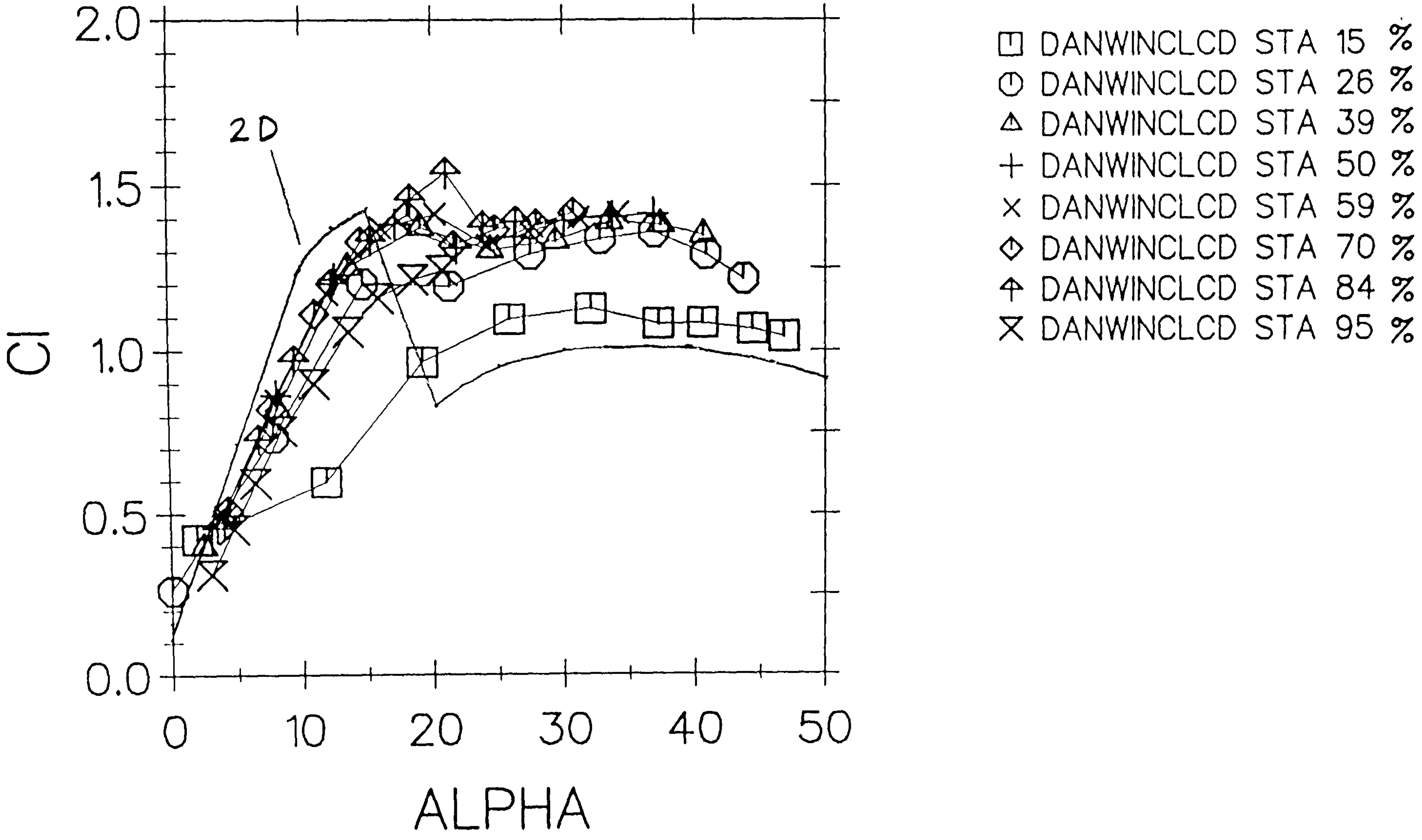

Figure 6.4 Derived lift cofficients for the Danwin 22m diameter machine

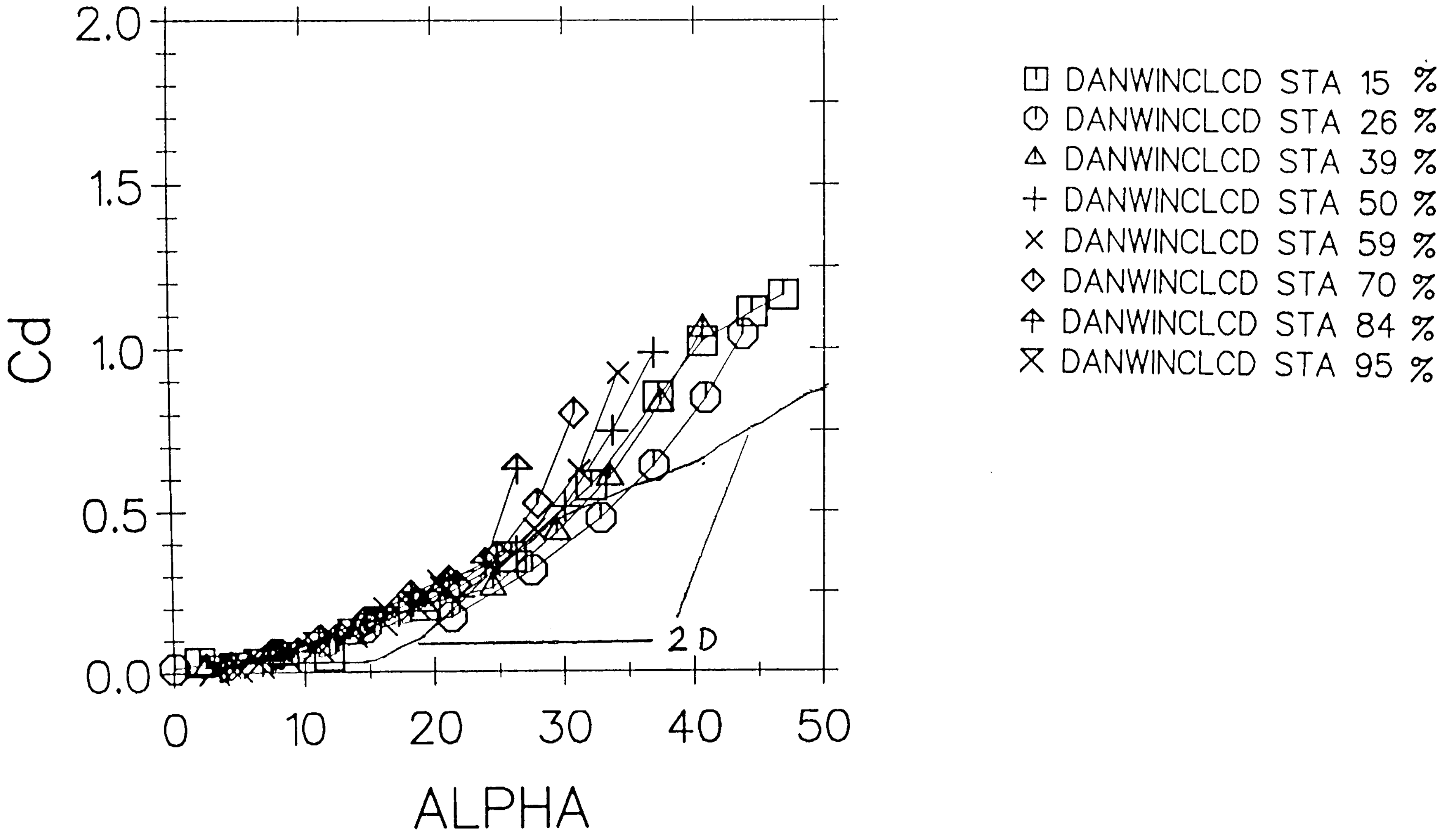

Figure 6.5 Derived drag cofficients for the Danwin 22m diameter machine

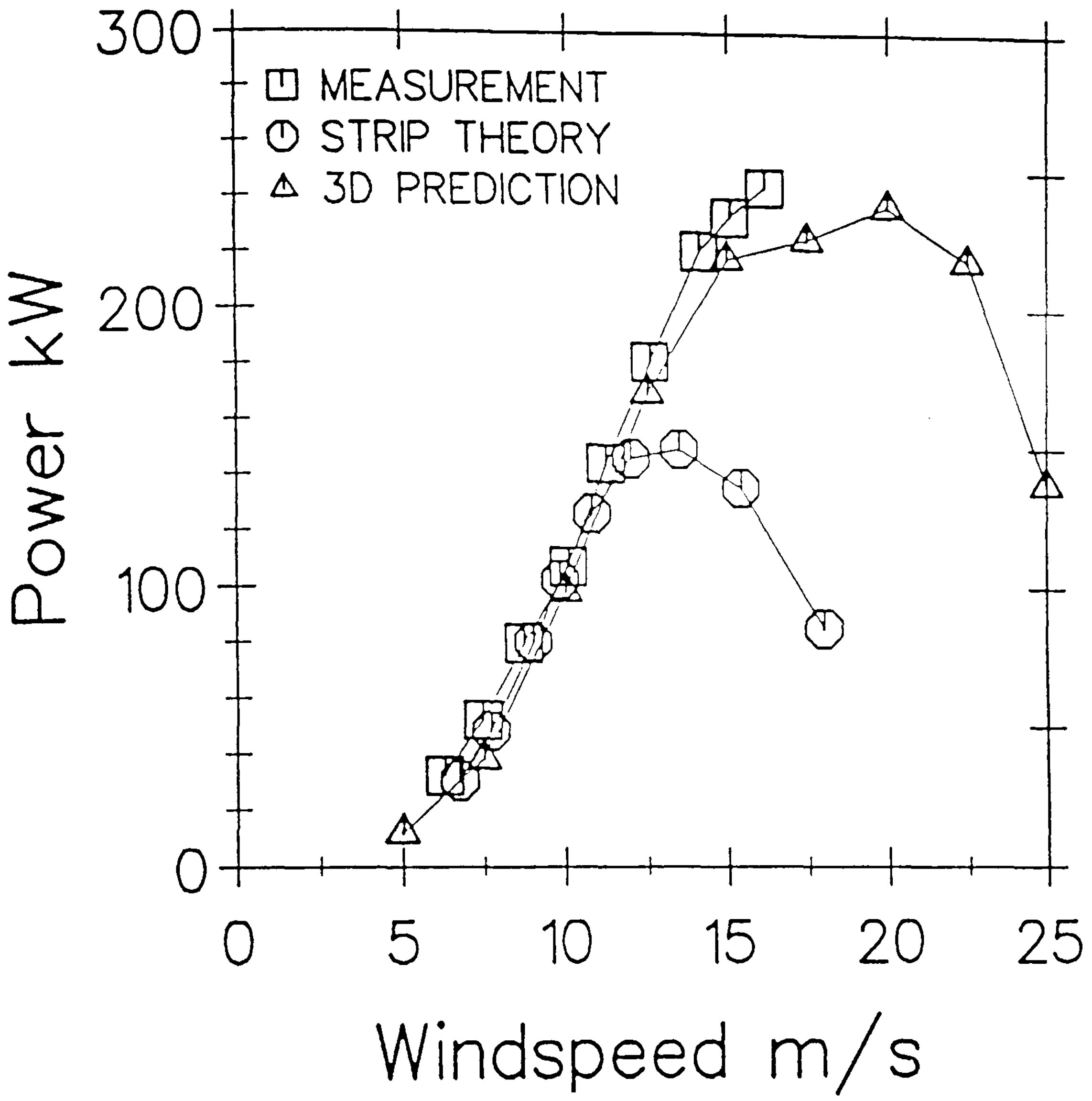

Figure 6.6 Power versus windspeed for the Danwin 22m diameter machine, after drag modification

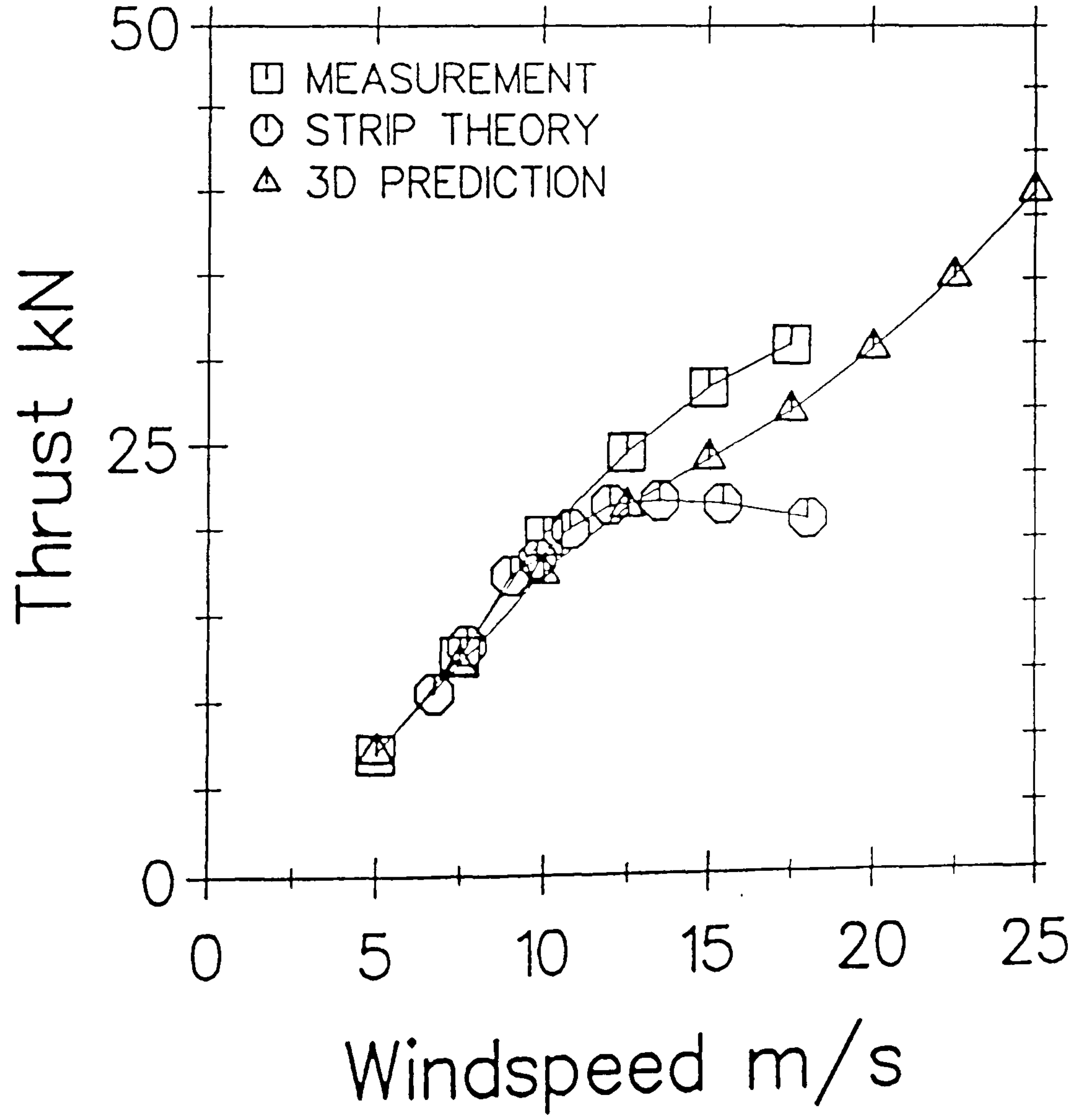

Figure 6.7 Thrust versus windspeed for the Danwin 22m diameter machine, after drag modification

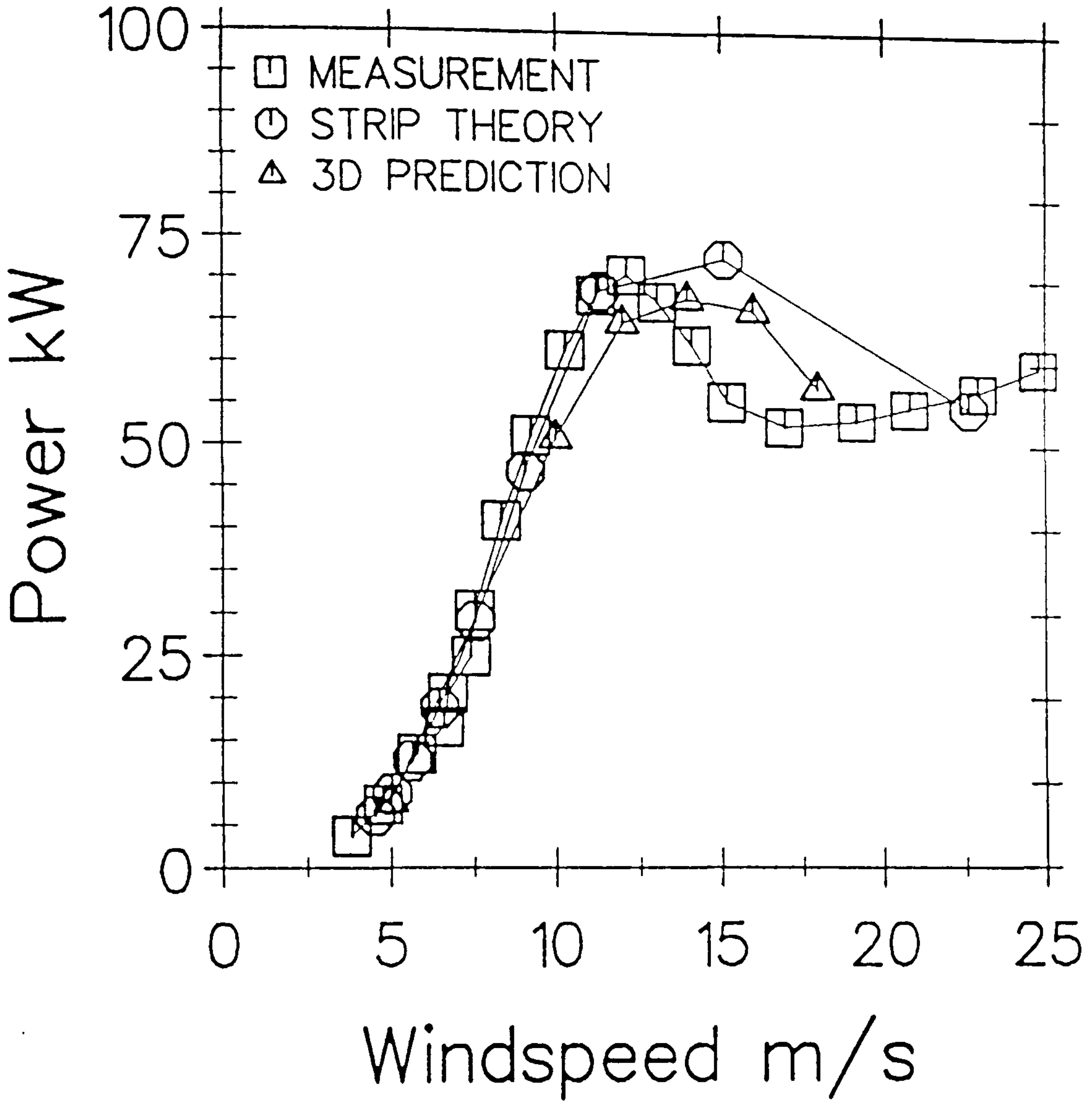

Figure 6.8 Power versus windspeed for the LM 17.2m diameter machine

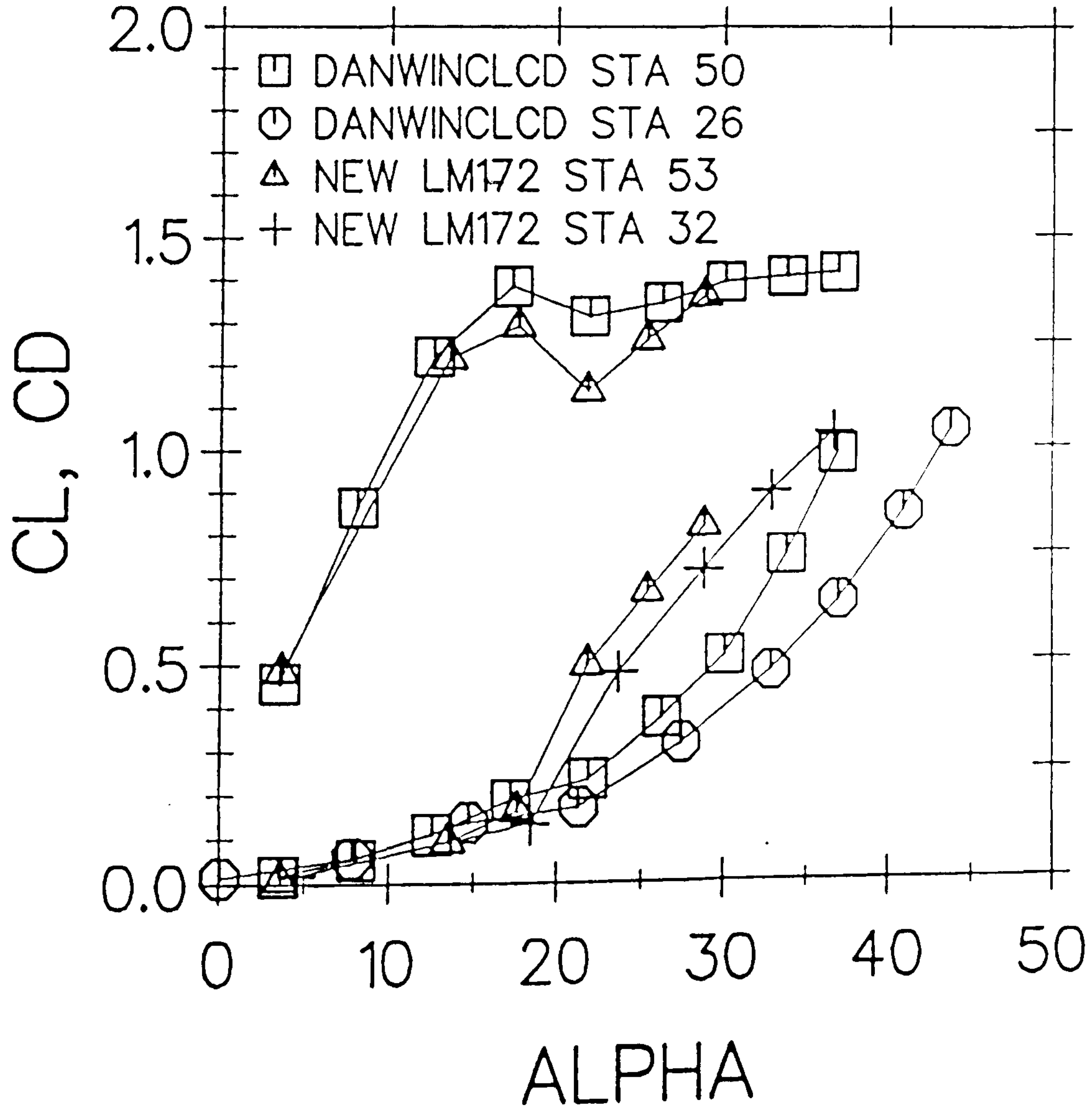

Figure 6.9 Derived lift and drag coefficients for Danwin 22m diameter machine and the LM 17.2m diameter machine

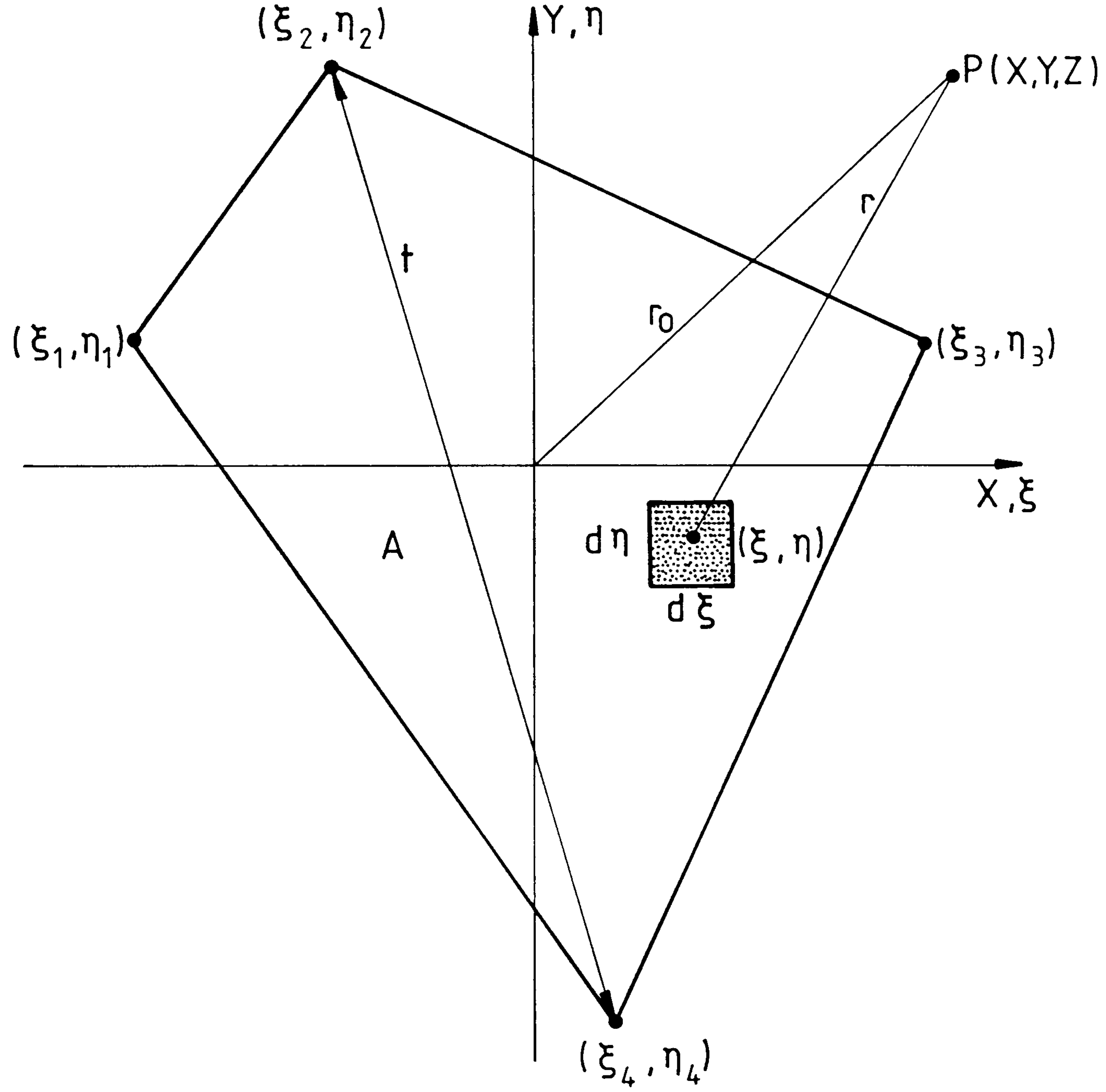

Figure A.1 A plane quadrilateral lying in the xy-plane

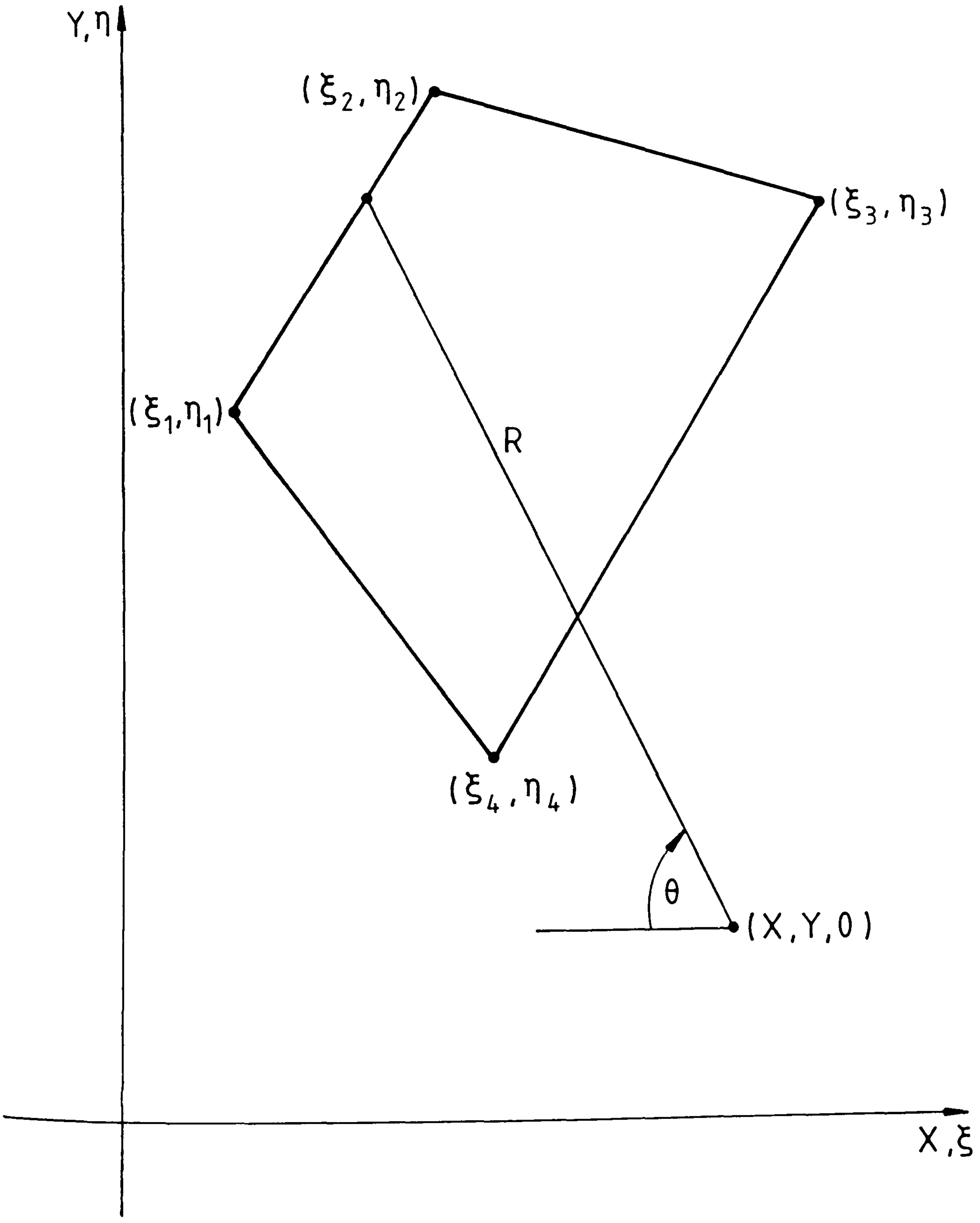

Figure A.2 Introduction of cylindrical coordinates

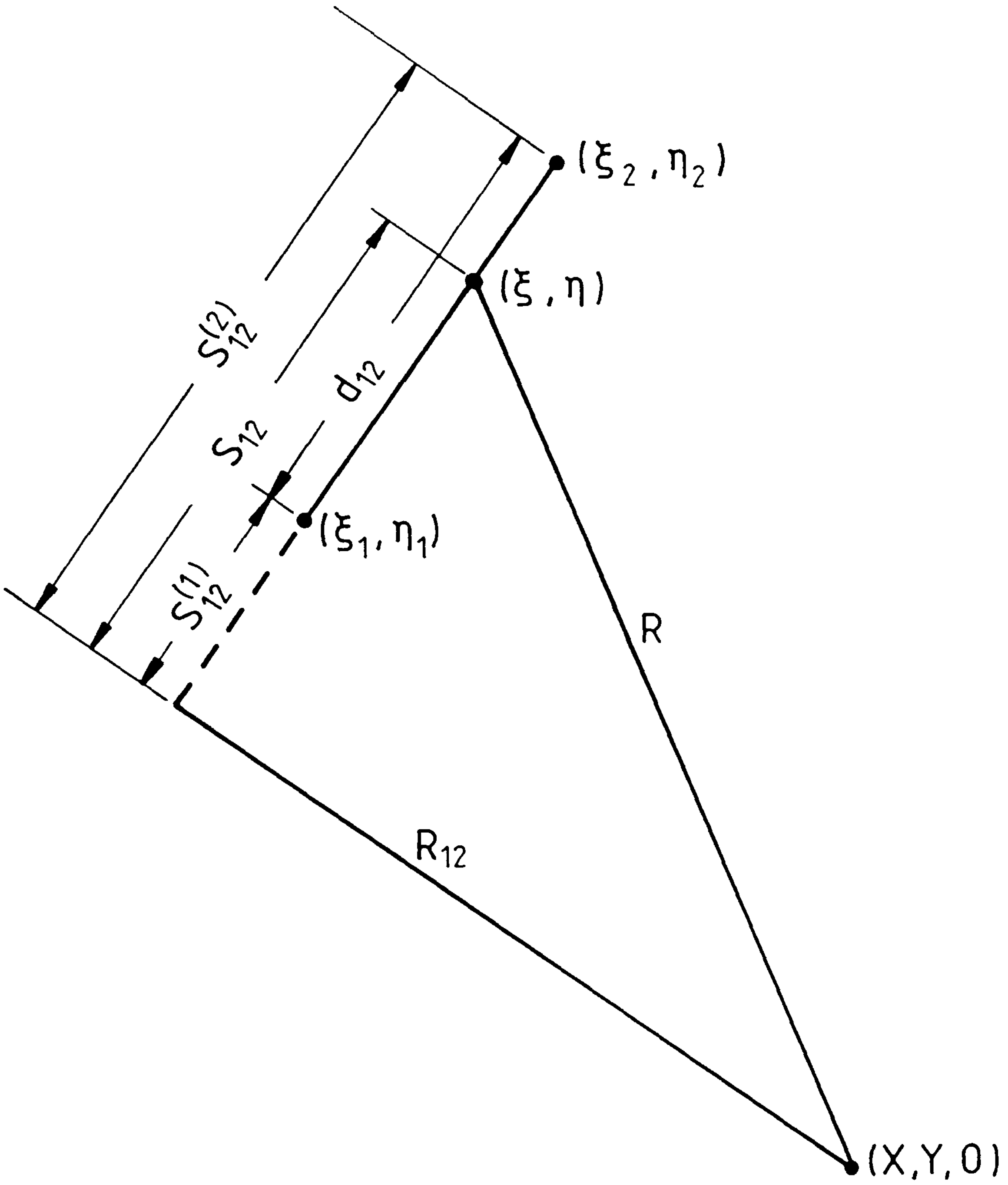

Figure A.3 Integration over a side of a quadrilateral

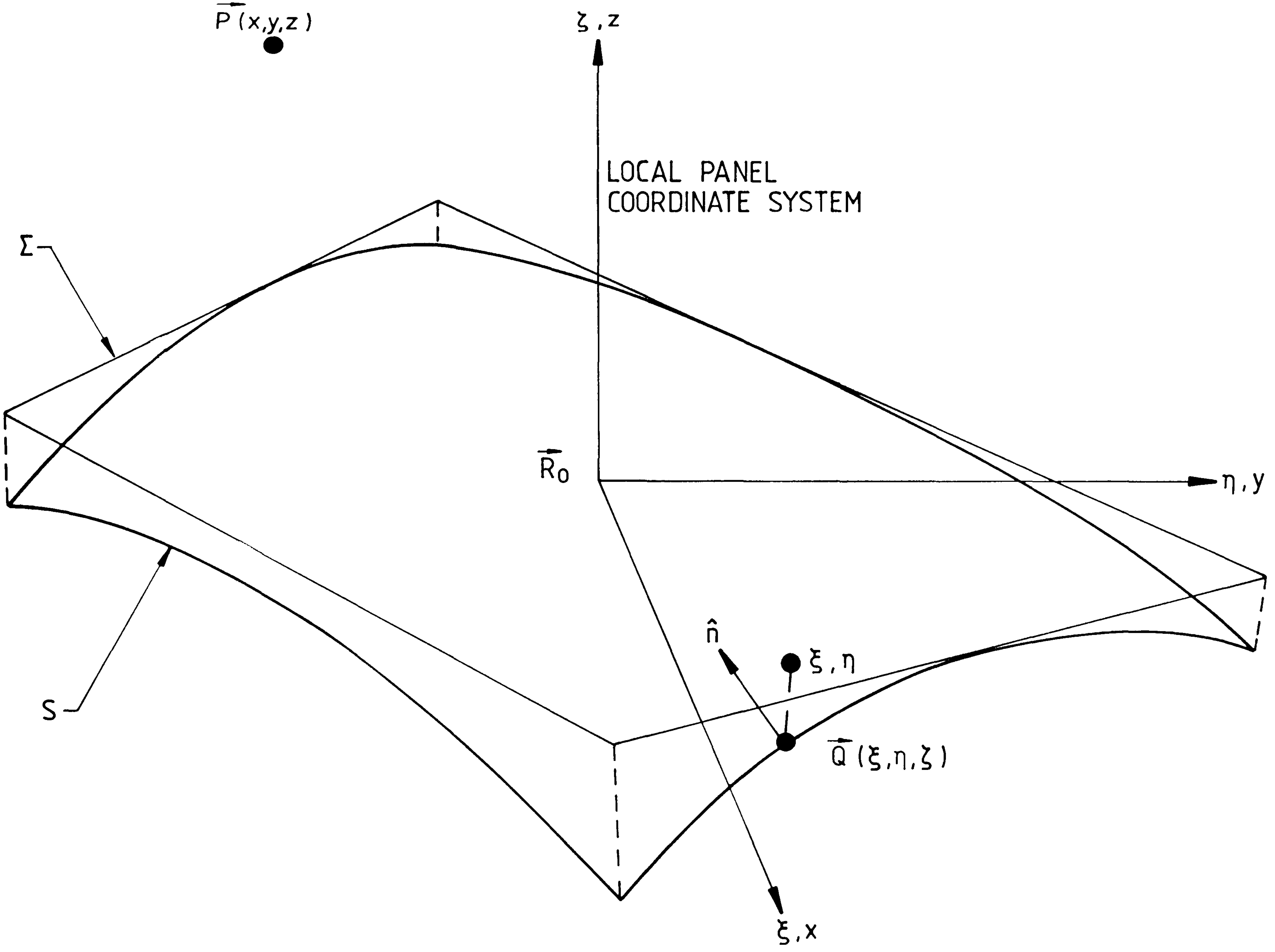

Figure B.1 Field point/Panel geometry

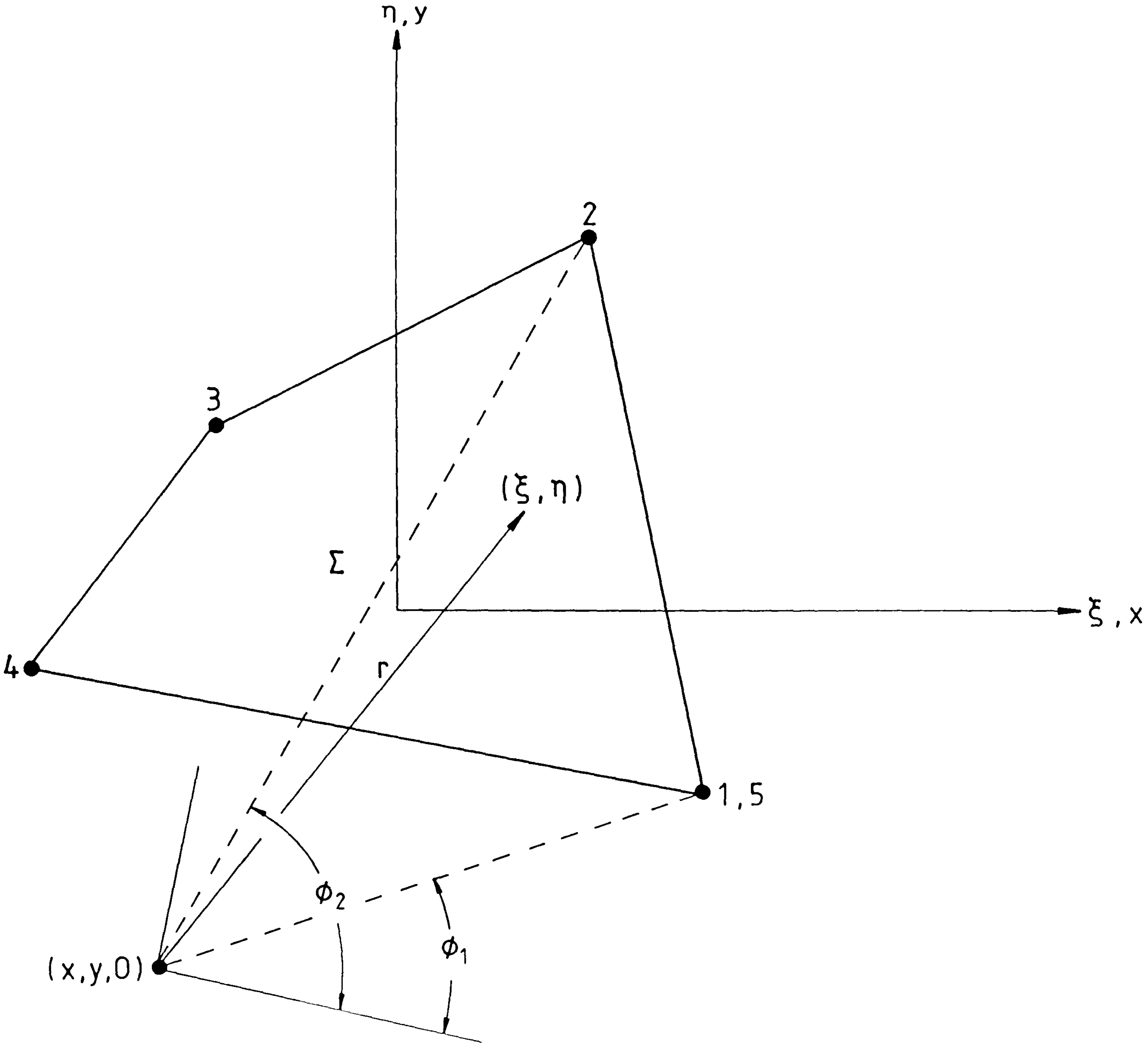

Figure B.2 Geometry relating to equation B.5

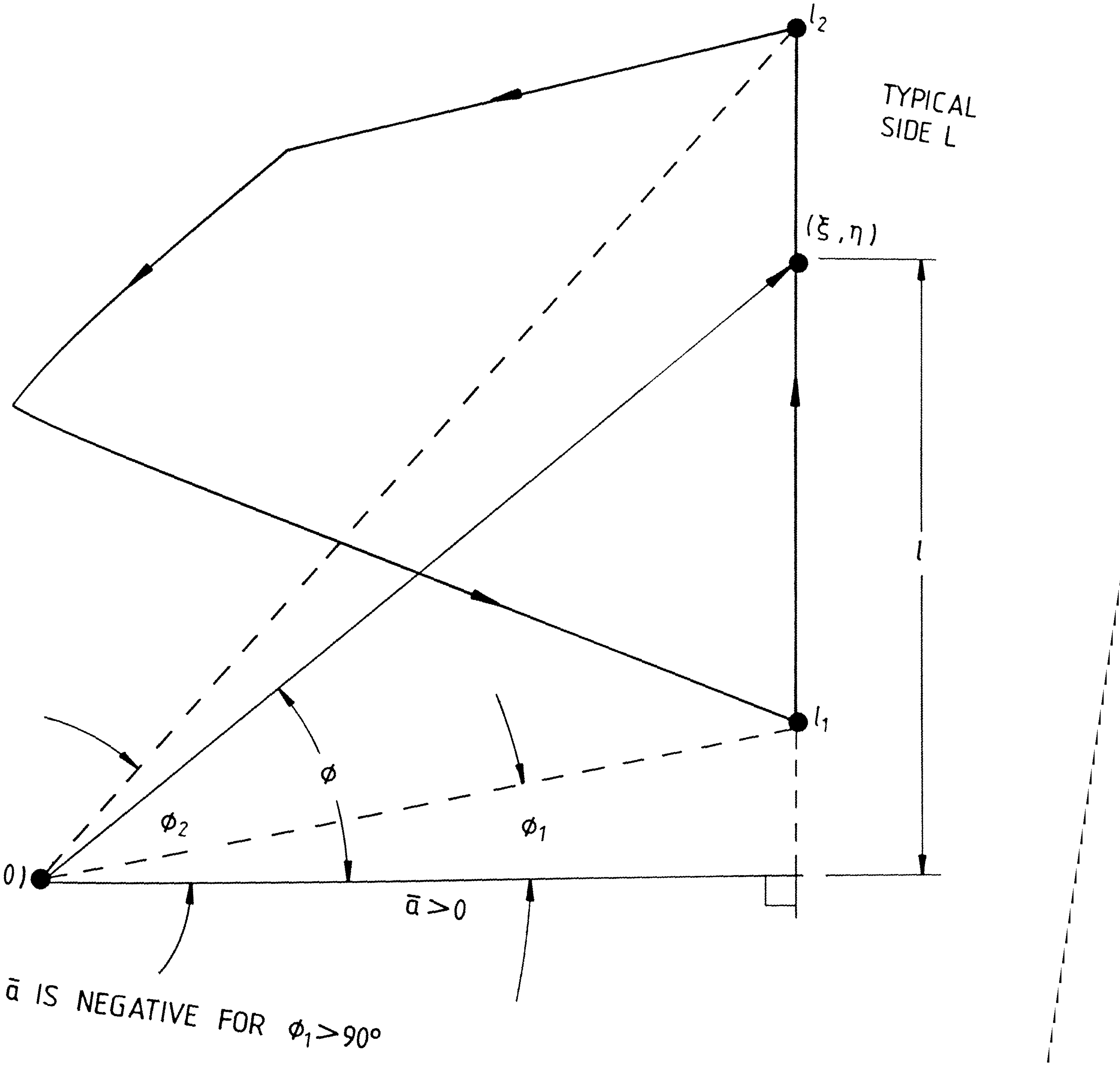

Figure B.3 Geometry relating to equation B.7

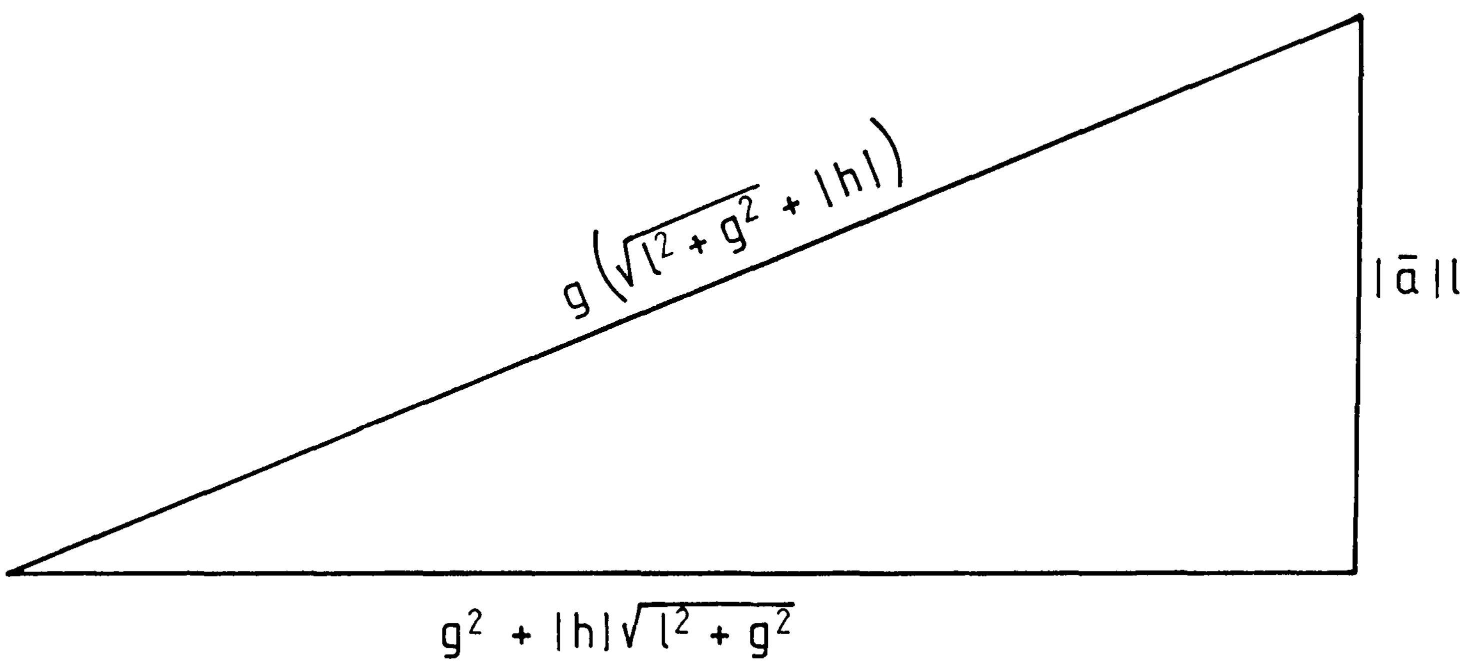

Figure B.4 Geometry relating to equation B.16

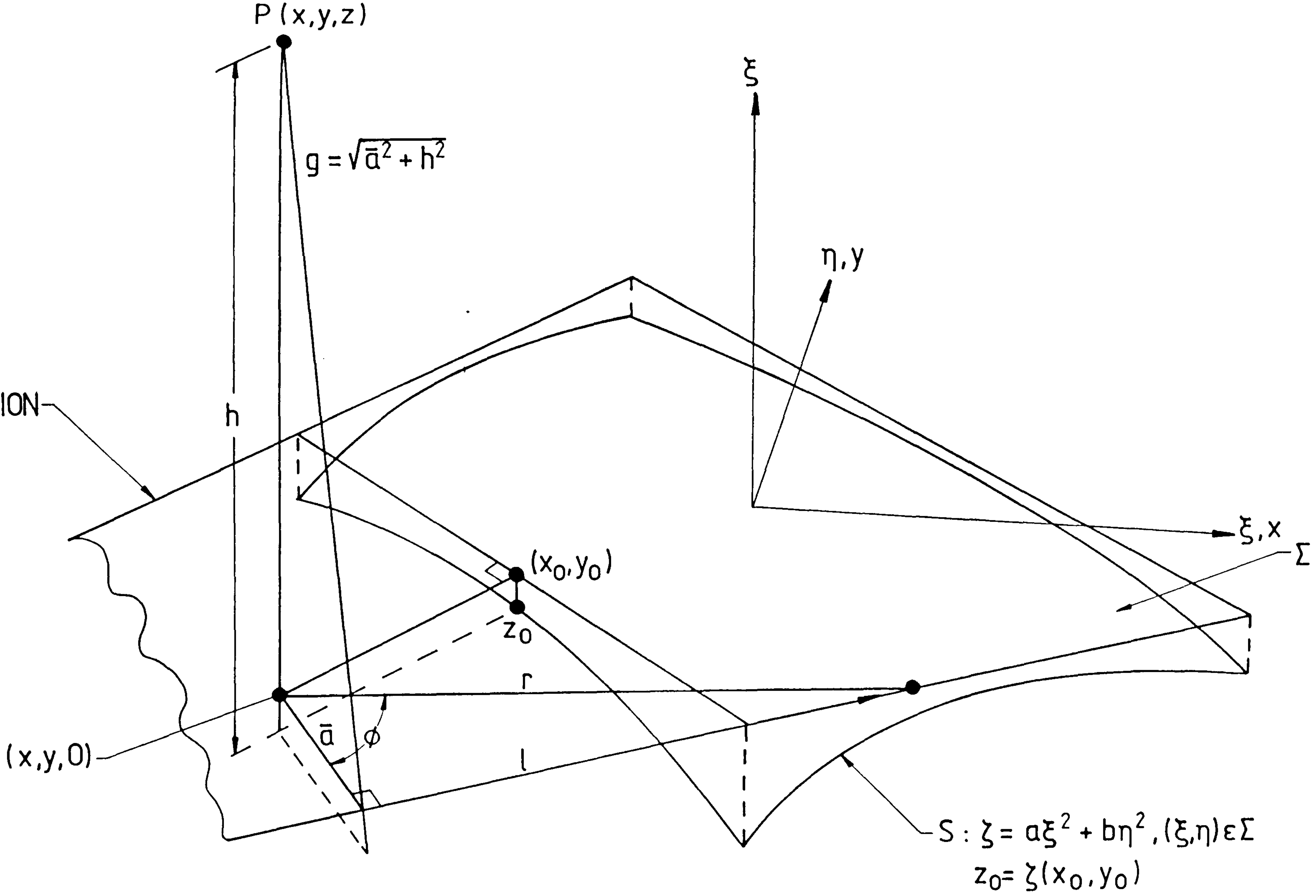

Figure B.5 The quantity $g = (a^2 + z^2)^{1/2}$ for point off the panel

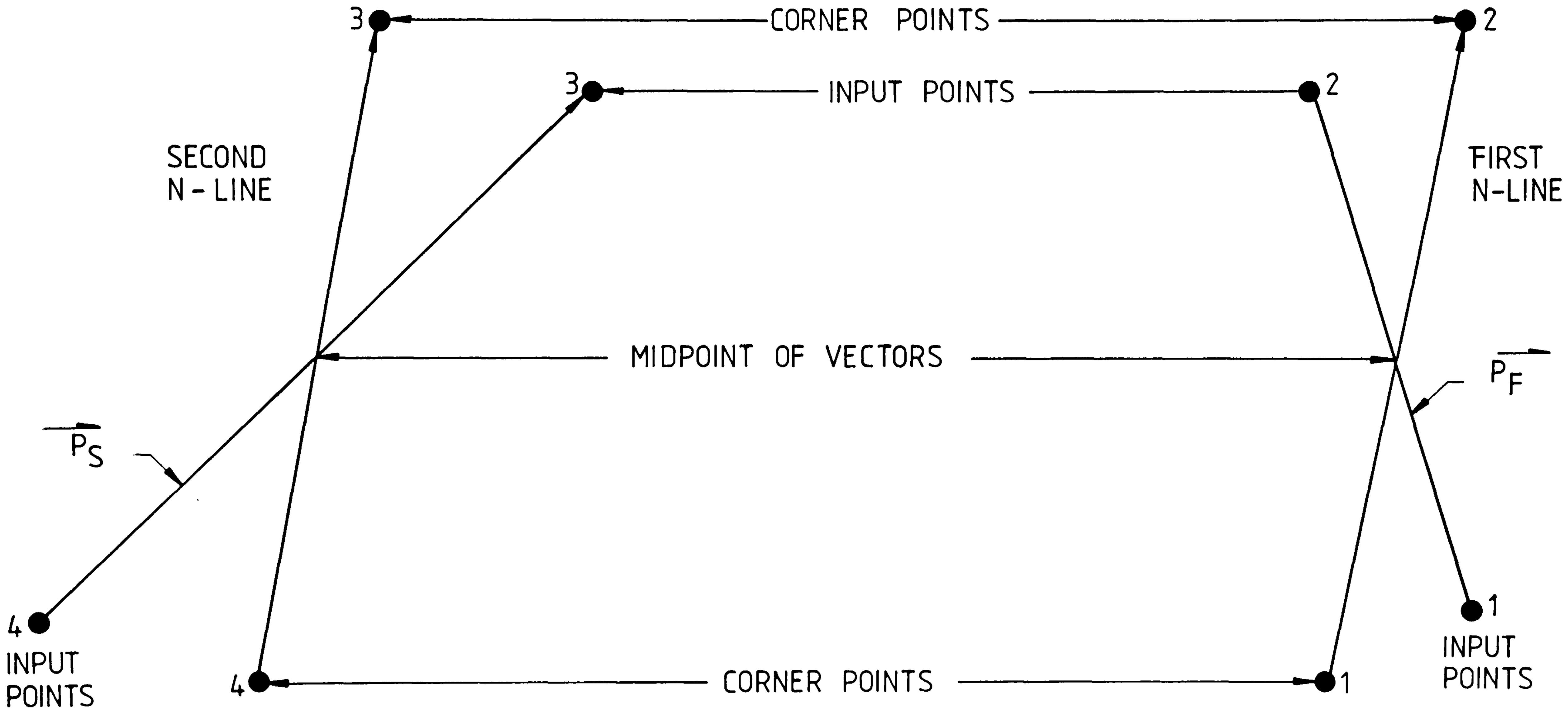

Figure C.1 Adjustment of the input points to form a plane trapezoidal element

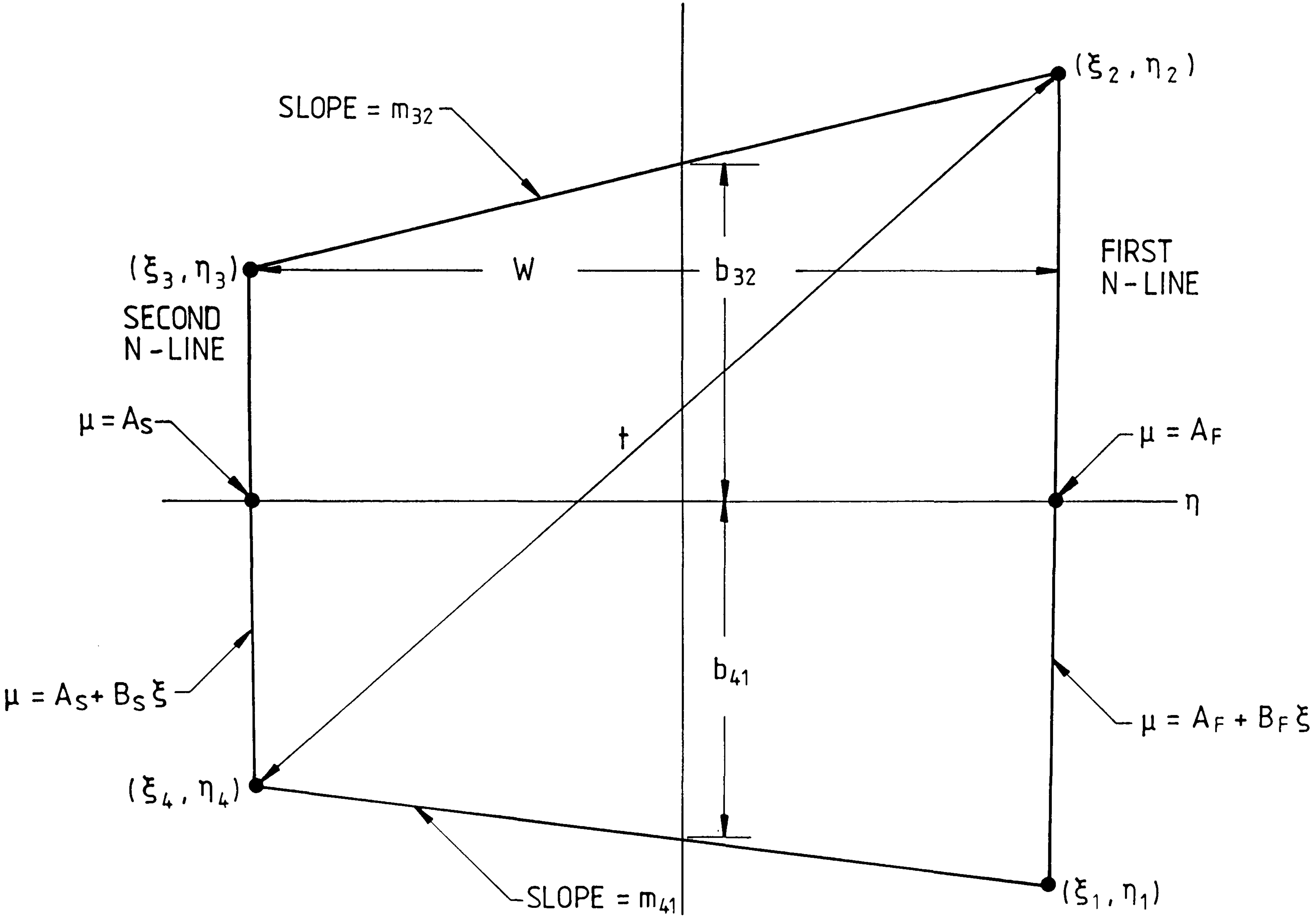

Figure C.2 A plane trapezoidal element

PAGINATION ERROR

(NO 'D' FIGS)

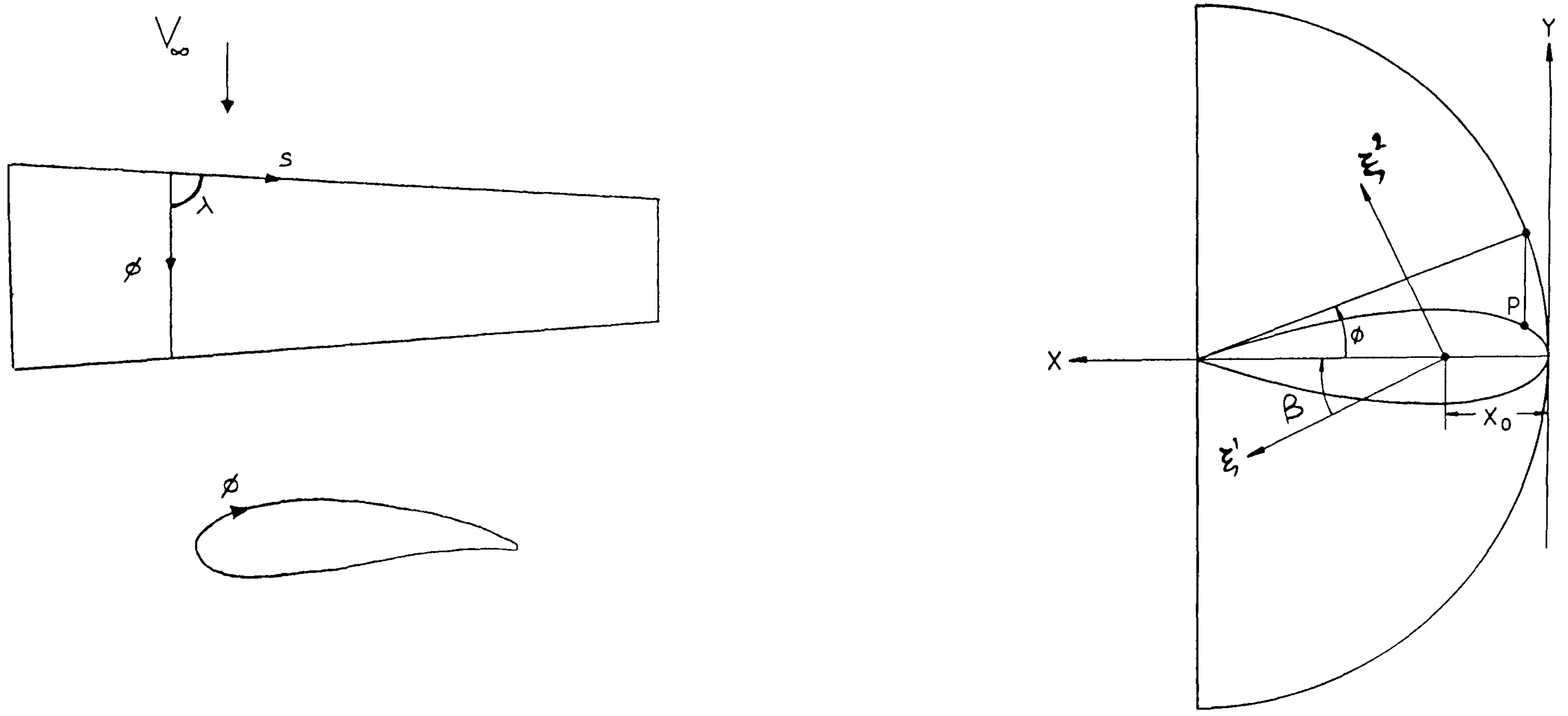

Figure E.1 Body fitted coordinate system

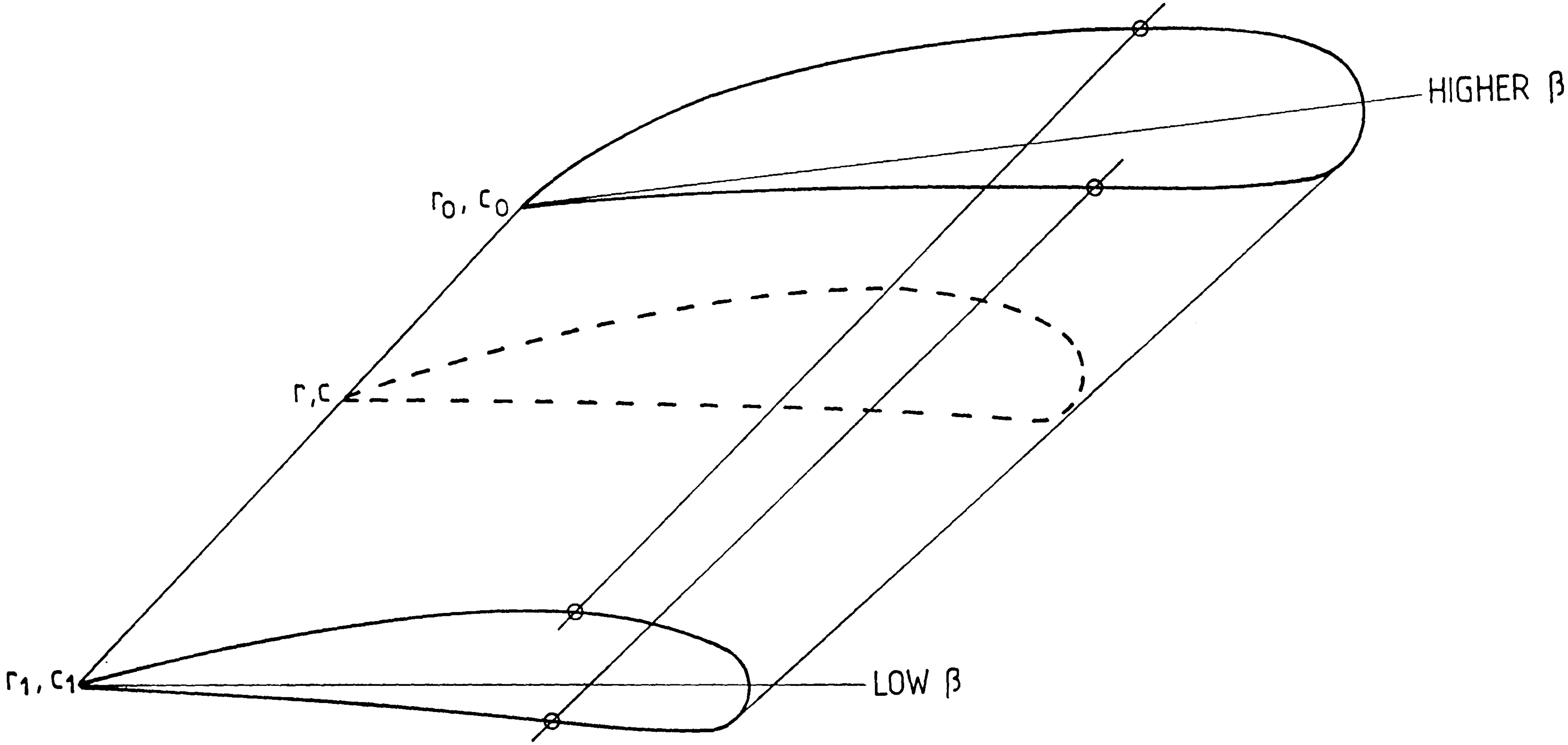

Figure E.2 Generation of metrical parameters required by the boundary layer calculation